Universidade do Minho
Escola de Engenharia

Beatriz Dias Cardoso

Evaluation of drug loaded magnetoliposomes as multifunctional platforms for advanced cell therapies

março de 2023

Evaluation of drug loaded magnetoliposomes as multifunctional platforms for advanced cell therapies

Beatrz Dias Cardoso

UMinho | 2023

Universidade do Minho
Escola de Engenharia

Beatriz Dias Cardoso

Evaluation of drug loaded magnetoliposomes as multifunctional platforms for advanced cell therapies

Tese de Doutoramento
Engenharia de Materiais

Trabalho efetuado sob a orientação do(a)
Professora Doutora Elisabete M. S. Castanheira Coutinho
Doutora Vanessa Fernandes Cardoso
Professor Doutor Senentxu Lanceros-Méndez

março de 2023

COPYRIGHTS AND TERMS OF USE OF WORK BY THIRD PARTIES

This is an academic work that can be used by others as long as the internationally accepted rules and good practices are respected, regarding copyright and related rights.
Thus, this work can be used under the terms set out in the license below.
If the user needs permission to be able to use the work under conditions not provided for in the indicated licensing, he must contact the author, through the RepositoriUM of the University of Minho.



Atribuição-NãoComercial-SemDerivações
CC BY-NC-ND

https://creativecommons.org/licenses/by-nc-nd/4.0/

Acknowledgments

Esta tese de doutoramento é o resultado refinado de um trabalho de colaboração e coordenação entre várias pessoas e entidades. Assim, e ciente do seu papel no alcance e sucesso dos meus objetivos, gostaria de expressar a minha sincera gratidão a todos os que me acompanharam nesta jornada e ajudaram a concluí-la.

Manifesto a minha profunda e sincera gratidão aos meus orientadores: Professora Doutora Elisabete Coutinho, Professor Doutor Senentxu Lanceros-Méndez e Doutora Vanessa Cardoso. Agradeço o sentido de oportunidade que ofereceram à minha vida quando, no dia zero, aceitaram materializar uma proposta de candidatura na ocupação profissional que sempre sonhei. Agradeço a liberdade para ser, pensar e fazer, que em muito contribuiu na tomada dos primeiros passos da minha independência científica. Agradeço, finalmente, a mentoria que garantiu o melhor desempenho das minhas funções e, assim, ter um papel ativo na construção do pensamento científico.

Este trabalho não seria possível sem a recetividade do Centro de Física da Universidade do Minho (CFUM) e da Unidade de Investigação em Microssistemas Eletromecânicos (CMEMS-UMinho) em disponibilizar os laboratórios, equipamentos e espaços de trabalho que me acolheram ao longo dos últimos anos. Deixo, também, as minha palavras de agradecimento a todos os seus colaboradores.

Ao "Basque Center on Materials, Applications and Nanostructures" (BCMaterials, Bilbao, Spain) e aos amigos que lá fiz por serem casa numa estadia internacional que me abriu os horizontes colaborativos e de visão científica. Agradeço, particularmente, à Carmen Rial Tubio pela instrução e auxílio na manipulação de equipamentos para a caracterização de materiais.

Expresso palavras de gratidão ao Nelson Pereira e à Clarisse Ribeiro pela contribuição do seu tempo, conhecimento científico e técnico que em muito ajudaram à progressão e alcance dos objetivos multidisciplinares deste trabalho.

Estendo palavras de agradecimento aos meus colegas (e amigos) de laboratório, em particular à Rita Rodrigues, Ricardo Fernandes, Maria João Faria e Eduarda Fernandes. Obrigada por me permitirem partilhar esta história convosco e trazerem ao local de trabalho um ambiente de liberdade de expressão, confiança e familiar.

Aos meus amigos de e para a vida! Maria, Mariana, Costeira, Lili, Ni, Nuno e Fru. Obrigada pela vossa presença ubíqua. Obrigada por haver sempre um plano de como ser e do que fazer. Agradeço a leveza das nossas partilhas, da razoabilidade das discussões, da gestão das expectativas e de todos os dias estarem disponíveis a relativizar os celeumas mútuos. Obrigada por serem a minha zona de conforto.

Sou imensamente grata à minha mãe, pai, irmã e irmão. Obrigada por acompanharem este trajeto sem deixarem de ser, SEMPRE, o caminho certo. Ao meus pais por serem os primeiros mentores da minha vida. Obrigada pelos valores que me transmitiram e pela confiança que sempre depositaram em mim e nas minhas capacidades. Acima de tudo, obrigada pelo amor (!) que sempre foi a minha força anímica. Uma palavra especial à minha irmã: Joana, obrigada por seres o maior e melhor exemplo da minha vida e seres o meu ser humano preferido, para sempre. Não esquecendo o meu cão, o Cãomarada, que é família, o meu amor e o sorriso de todas as horas.

This research was funded by the Portuguese Foundation for Science and Technology (FCT) under the PhD grant SFRH/BD/141936/2018, COVID/BD/153009/2022 and in the framework of the Strategic Funding UIDB/04650/2020, UIDB/04436/2020, UIDP/04436/2020 and through the research project PTDC/QUI-QFI/28020/2017 (POCI-01-0145-FEDER-028020), co-financed by European Fund of Regional Development (FEDER), COMPETE2020 and Portugal2020.



STATEMENT OF INTEGRITY

I hereby declare having conducted this academic work with integrity. I confirm that I have not used plagiarism or any form of undue use of information or falsification of results along the process leading to its elaboration.

I further declare that I have fully acknowledged the Code of Ethical Conduct of the University of Minho.

Assinado por: **Beatriz Dias Cardoso**
Num. de Identificação: 14581020
Data: 2023.03.15 11:27:45 +0000

_____

(Signature)

Resumo

O cancro é a principal causa de morte a nível mundial. Apesar dos avanços alcançados na área, a deterioração progressiva da qualidade de vida dos doentes urge a procura de novas estratégias de tratamento. Assim, este trabalho centrou-se no desenvolvimento e otimização de magnetolipossomas enquanto nanotransportadores de agentes quimioterápicos e na avaliação *in vitro* da seu desempenho terapêutica em meios miméticos ao ambiente tumoral e numa linha celular de interesse.

Inicialmente, sintetizaram-se nanopartículas (NPs) superparamagnéticas esféricas de ferrite de magnésio e cálcio ($Ca_xMg_{1-x}Fe_2O_4$, com x=0,25; 0,50 e 0,75) e estudaram-se os efeitos da variação destes elementos nas suas propriedades. O maior potencial das NPs de $Ca_{0.25}Mg_{0.75}Fe_2O_4$ instigou o desenvolvimento de uma nova metodologia de síntese com anisotropia de forma, de modo a potenciar a sua magnetização de saturação em relação às homólogas esféricas. Estas revelaram potencial em mediarem o estímulo térmico sob campo magnético alternado e irradiação de laser infravermelho. Posteriormente, testou-se a incorporação das NPs em magnetolipossomas aquosos (AMLs) e sólidos (SMLs), sendo que os SMLs se revelaram mais promissores. Da mesma forma, desenvolveu-se um novo método de síntese de SMLs para aumentar a quantidade de NPs por vesícula lipídica. Este método permitiu a reprodutibilidade de síntese de SMLs baseados em múltiplas combinações lipídicas com propriedades estruturais e coloidais adequadas para aplicação biomédica. A otimização de SMLs avançou no sentido de lhes conferir capacidade de libertar doxorrubicina (DOX) sob a presença de múltiplos estímulos (fusogénicos, temperatura e de pH). Assim, foram quantificados sistematicamente os efeitos de nove combinações lipídicas nos perfis de libertação da DOX sob condições miméticas às fisiológicas (37 °C e pH=7,4) e em condições terapêuticas (42 °C e/ou pH ácido). Este processo permitiu selecionar a combinação lipídica com maiores taxas de libertação nas condições terapêuticas. O efeito da DOX livre e encapsulada em SMLs (2 mg de NPs em 1 mM de formulação lipidica) foi avaliado na linha celular Sk-br-3 do cancro da mama, cultivada em diferentes níveis organizacionais celulares (2D e 3D). Por fim, plataformas microfluídicas foram fabricadas para retenção de esferóides de Sk-br-3 que visa a simulação de gradientes espacio-temporais do microambiente tumoral heterogéneo.

Em suma, este trabalho apresenta uma abordagem multidisciplinar no desenvolvimento e otimização de magnetolipossomas enquanto nanotransportadores multifuncionais para tratamento de tumores sólidos. Reforça ainda a importância de estabelecer métodos de cultura celular miméticos ao contexto *in vivo* na validação rigorosa de novas estratégias de tratamento.

Palavras-chave: nanopartículas superparamagnéticas; magnetolipossomas sólidos; doxorubicina; libertação controlada; cultura celular; microfluídica.

Abstract

Cancer is the leading cause of death worldwide. Despite the advances in the area, the progressive deterioration of patients' quality of life urges the search for new treatment strategies. Thus, this work focused on developing and optimizing magnetoliposomes as nanocarriers of chemotherapeutic agents and evaluating their *in vitro* therapeutic performance in tumoral mimetic environments in a suitable cell line.

Initially, spherical superparamagnetic nanoparticles (NPs) of magnesium and calcium ferrite ($Ca_xMg_{1-x}Fe_2O_4$, with x=0.25; 0.50 and 0.75) were synthesized, and the effects of varying these elements on their properties were studied. The more significant potential of $Ca_{0.25}Mg_{0.75}Fe_2O_4$ NPs prompted the development of a new synthesis methodology with shape-anisotropy to enhance its magnetic properties in relation to its spherical counterparts. The developed NPs demonstrated the potential to obtain a thermal stimulus under alternating magnetic fields and infrared laser irradiation. Subsequently, the incorporation of NPs in aqueous magnetoliposomes (AMLs) and solid magnetoliposomes (SMLs) was evaluated, and the SMLs proved to be more promising systems. Likewise, a new method of synthesizing SMLs was developed to increase the amount of NPs per lipid vesicle. This method allowed the synthesis reproducibility of SMLs based on multiple lipid combinations with structural and colloidal properties suitable for biomedical applications. Furthermore, the optimization of SMLs allowed to induce the ability to release doxorubicin (DOX) under the presence of multiple stimuli (fusogenic, temperature and pH). Thus, the effects of nine lipid combinations on DOX release profiles were systematically quantified under physiological conditions (37°C and pH=7.4) and under therapeutic conditions (42°C and/or acidic pH). This process allowed the selection of the lipid combination with the highest release rates under therapeutic conditions. Furthermore, the effect of free and encapsulated DOX in SMLs (2 mg of NPs in 1 mM of lipid formulation) was evaluated on the Sk-br-3 breast cancer cell line cultured at different cell organizational levels (2D and 3D). Finally, microfluidic platforms for the retention of Sk-br-3 spheroids were designed, aiming to simulate space-time gradients of the heterogeneous tumour microenvironment. Overall, this work presents a multidisciplinary approach to the development and optimization of magnetoliposomes as multifunctional nanosystems for the treatment of solid tumours. It also reinforces the importance of establishing mimetic cell culture methods to the *in vivo* context, allowing to validate the accuracy of new treatment strategies for the disease.

Keywords: superparamagnetic nanoparticles; solid magnetoliposomes; doxorubicin; controlled release; cell culture; microfluidics.

Table of Contents

Acknowledgments ..... **ii**

Resumo ..... **vi**

Abstract ..... **vii**

List of Figures ..... **xiv**

List of Tables ..... **xix**

List of Abbreviations ..... **xxii**

List of Symbols ..... **xxiv**

1. Introduction ***1***

1.1. Framework and main objectives **2**

1.2. Progress in theranostics with lipid-based nanosystems **5**

1.2.1. Liposomal drug delivery: design and classification 6

1.2.2. Superparamagnetic nanoparticles as theranostics mediators 9

1.2.3. Magnetic liposomes 11

1.2.4. Stimuli strategies for enhanced drug release 16

1.2.4.1. Alternating magnetic field-triggered release 16

1.2.4.2. Near-infrared-triggered release 19

1.2.5. Magnetoliposomes for ligand-mediated active targeted and combined therapy 21

1.2.6. Final Remarks 23

1.3. Cell culture platforms for *in vitro* nanodrug delivery systems development and screening **23**

1.3.1. Life science research and development: an overview of cell culture as a model for drug screening 26

1.3.1.1. Two-dimensional cell culture methods 27

1.3.1.2. Three-dimensional cell culture methods 30

1.3.2. The convergence between cell culture and microfluidic platforms 34

1.3.2.1. Overview of manufacturing processes and materials 34

1.3.2.2. Physical considerations in miniaturizing cell cultures 35

1.3.2.3. Implications in miniaturizing cell cultures 36
1.3.3. Final Remarks 39
1.4. Thesis oultine 39
1.5. References 41
2. Stealth magnetoliposomes based on spherical calcium-substituted magnesium ferrite nanoparticles 63
2.1. Overview 64
2.2. Introduction 64
2.3. Materials and Methods 67
2.3.1. Preparation of spherical $Ca_xMg_{1-x}Fe_2O_4$ ferrite nanoparticles 67
2.3.2. Preparation of aqueous and solid magnetoliposomes 68
2.3.3. Preparation of giant unilamellar vesicles 69
2.3.4. Spectroscopic measurements 69
2.3.5. Characterization of magnetic nanoparticles 71
2.3.6. Drug release studies 71
2.4. Results and Discussion 72
2.4.1. Characterization of magnetic nanoparticles 72
2.4.2. X-Ray Diffraction measurements 73
2.4.3. Sedimentation kinetics 75
2.4.4. Transmission Electron Microscopy 75
2.4.5. Magnetic Properties 76
2.4.6. Characterisation of magnetoliposomes 78
2.4.6.1. Aqueous magnetoliposomes 79
2.4.6.2. Solid magnetoliposomes 81
2.4.6.3. Curcumin release profile 84
2.5. Conclusions 86
2.6. References 88
3. Solid magnetoliposomes based on shape-anisotropic nanoparticles and pre-validation as anticancer drug nanocarriers 98

3.1. Overview 99

3.2. Introduction 99

3.3. Materials and Methods 101

3.3.1. Synthesis of cubic $Ca_{0.25}Mg_{0.75}Fe_2O_4$ nanoparticles 102

3.3.2. Solid magnetoliposomes preparation 102

3.3.3. Magnetic measurements and structural characterization 103

3.3.4. Magnetic hyperthermia measurements 104

3.3.5. Spectroscopic measurements 105

3.3.6. Drug Encapsulation efficiency and drug-loading capacity 105

3.3.7. Interaction with human serum albumin 106

3.3.8. Drug release kinetics and mathematical modelling of release profile 106

3.4. Results and Discussion 107

3.4.1. X-Ray diffraction analysis 107

3.4.2. Transmission electron microscopy 108

3.4.3. UV-Visible absorption 109

3.4.4. Magnetic properties 110

3.4.5. Magnetic hyperthermia 112

3.4.6. Photophysical properties of doxorubicin in solution 114

3.4.7. Characterisation of Magnetoliposomes 116

3.4.7.1. Synthesis of solid magnetoliposomes 116

3.4.7.2. Dynamic light scattering and transmission electron microscopy 117

3.4.7.3. Doxorubicin encapsulation in solid magnetoliposomes 120

3.4.7.4. Interaction with human serum albumin 124

3.4.7.5. Drug release kinetics and mathematical modelling of release profile 126

3.5. Conclusions 130

3.6. References 131

4. Advances towards an optimized multi-stimuli-responsive nanosystem for cancer therapy 138

4.1. Lipid formulation evaluation and optimization of magnetoliposomes as multi-stimuli-responsive vesicles for controlled doxorubicin release 139

4.1.1. Overview 140
4.1.2. Introduction 140
4.1.3. Materials and Methods 142
4.1.3.1. Solid magnetoliposomes preparation 143
4.1.3.2. Dynamic Light Scattering measurements 145
4.1.3.3. Fluorescence spectroscopy measurements 146
4.1.3.4. Differential Scanning Calorimetry 148
4.1.4. Results and discussion 148
4.1.4.1. Influence of formulation on structural, colloidal and thermodynamic parameters of doxorubin-loaded solid magnetoliposomes 148
4.1.4.2. Stability of liposomal aqueous suspensions upon storage at 4 °C 152
4.1.4.3. Interaction with human serum albumin 154
4.1.4.4. Implications of lipid formulation and pH on the location of doxorubicin 155
4.1.4.5. Effect of lipid formulations on doxorubicin release kinetics and profile 157
4.1.5. Conclusions 161
4.1.6. References 163

4.2. Investigation of superparamagnetic nanoparticles' potential for near infrared-derived hyperthermia 169

4.2.1. Overview 170
4.2.2. Introduction 170
4.2.3. Materials and Methods 172
4.2.3.1. Near infrared-induced photothermal hyperthermia 172
4.2.3.2. Solid magnetoliposomes preparation 173
4.2.3.3. Vibrating-sample magnetometer measurements 173
4.2.3.4. Lipid quantification in solid magnetoliposomes samples 174
4.2.3.5. Encapsulation efficiency of nanoparticles in solid magnetoliposomes 174
4.2.4. Results and Discussion 175
4.2.4.1. Near infrared-derived heating performance of $Ca_{0.25}Mg_{0.75}Fe_2O_4$ nanoparticles 175
4.2.4.2. Effects of increased magnetic nanoparticles inclusion on the properties of magnetoliposomes 177
4.2.5. Conclusions 180
4.2.6. References 181

5. In vitro evaluation of doxorubicin-loaded magnetoliposomes efficacy on breast cancer therapeutics 185

5.1. Overview 186

5.2. Introduction 186

5.3. *In vitro* preliminary evaluation of doxorubicin-loaded solid magnetoliposomes on different cell organisational levels 190

5.3.1. Materials and methods 191

5.3.1.1. Cell culture and spheroids formation 191

5.3.1.2. 2D, pseudo-3D and 3D cell culture assays 191

5.3.1.3. Image acquisition, processing and analysis 192

5.3.2. Statistical analysis 192

5.3.3. Results and discussion 192

5.3.3.1. Establishment of Sk-br-3 breast cancer cell culture on conventional adherent plates 192

5.3.3.2. Establishment of Sk-br-3 breast cancer cell culture on non-adherent plates 200

5.4. Design and fabrication of biomimetic microfluidic platforms for spheroids culture. 208

5.4.1. Materials and Methods 208

5.4.1.1. Microfluidic platform design and fabrication 208

5.4.1.2. Spheroids inclusion on microfluidic platforms 211

5.4.2. Results and discussion 211

5.4.2.1. Microfluidic platform design and fabrication validation 211

5.4.2.2. Evaluation of the microfluidic platform for spheroids inclusion and retention 213

5.4.3. Conclusions 215

5.5. References 217

6. Concluding remarks and future perspectives 220

6.1. Concluding remarks 221

6.2. Future perspectives 224

6.1. References 227

Appendices *228*

Appendix A: Supplementary information of chapter 3 ..... **229**

Appendix B: Supplementary information of sub-chapter 4.1 ..... **237**

Appendix C: Supplementary information of chapter 5 ..... **241**

References **243**

List of Figures

Figure 1.1 Schematic representation of liposome targeting strategies evolution. (A) Conventional liposomes. (B) Stealth liposomes, functionalized with hydrophilic polymeric conjugates. (C) Targeted liposomes, functionalized with glycoproteins, polysaccharides, or ligand of cell-specific receptors. (D) Immunoliposomes, functionalized with antibodies or antibody fragments. (E) Stimuli-responsive liposomes based on pH or temperature lipid formulations. 7

Figure 1.2 Categories and practical application of magnetic NPs in biomedicine. 9

Figure 1.3 Schematic representation of magnetic drug and gene delivery. The conjugated NPs (linked to the therapeutic agent or genes) are injected into the bloodstream near the target site. Simultaneously, magnetic fields force the NPs to extravasate to the target site (tumours). 11

Figure 1.4 Schematic representation of (A) AMLs, (B) SMLs, (C) liposomes with bilayer-embedded NPs, and (D) liposomes with surface-bound NPs. 12

Figure 1.5 (A) TEM of a single DPPC/DSPC-based AML containing 14 mg Fe/ml of Resovist, and (B) Fluorescence images of DOPC-loaded (red) magnetoliposomes loaded with CF (green), as a function of time, (i) without and (ii) with the action of an AMF (2 kHz, 20 mT). Adapted from [79]- 17

Figure 1.6 (A) TEM image of liposomes with surface-bound DMSA-coated nanoparticles and its schematic representation. (B) Representative confocal laser scanning microscopy images. (C) normalized survival after 24 h of MDA-MB-231 cells after exposure to different treatments (without (grey) and with the action of an AMF of 202 kHz and 30 mT for 1 h (red)). Adapted from [83]..... 19

Figure 1.7 (A) Schematic representation of DOX- Fe_3O_4–TSL synthesis and respective NIR-triggered DOX release. (B) *In vivo* anti-tumour efficacy, as tumour volume changes, in different treatment groups. Adapted from [85]. 20

Figure 1.8 Schematic representation of microfluidic-based devices as platforms for 2D and 3D cell culture. 25

Figure 1.9 Schematic representation of the drug discovery process from basic research (initiated by target identification) to its translation into an FDA-approved product. The arrows represent the quality assurance guides that guarantee the normal development of the process. The "good laboratory practices" are summarized in a list of individual laboratory contributions to drug discovery and development. ... 27

Figure 1.10 (A) Schematic representation of nonmalignant MECs and malignant MECs treated as monolayers on a thin coat of collagen (above) and their 3D structures embedded in rBM; and their respective (B) apoptotic labelling indices treated with Trail peptide (1 μg/ml), anti-FAS mAb (IgM CH-11, 2 μg/ml), TNF-α (100 nM), etoposide (50 μM), cytochalasin B (1 μM), or paclitaxel (120 nM). Results are the mean ± SEM of 3–5 experiments with duplicates or triplicates. Adapted from [155]. 28

Figure 1.11 SEM images of (A) LNCaP, (B) C4-2, and (C) C4-2B human prostate cancer cells grown on 2D culture plates, Matrigel® matrix, and CA scaffolds (bottom) for 15 days. Scale bars are 40 μm. Reproduced from [198]. 31

Figure 1.12 The fundamental differences between macroscale, μwells and microchannels concerning the total media volume, surface area/volume ratios and volume densities. μWells is a PDMS stencil placed on tissue culture plastic similar to microchannels. Adapted from [251]. 38

Figure 2.1 Absorption spectra of $Ca_{0.25}Mg_{0.75}Fe_2O_4$, $Ca_{0.50}Mg_{0.50}Fe_2O_4$ and $Ca_{0.75}Mg_{0.25}Fe_2O_4$ magnetic nanoparticles. Inset: Tauc plot for $Ca_{0.50}Mg_{0.50}Fe_2O_4$ nanoparticles, as an example (red line is the linear fitting). 73

Figure 2.2 XRD patterns with Miller indices of the synthesized calcium-substituted magnesium ferrite nanoparticles. (A) $Ca_{0.25}Mg_{0.75}Fe_2O_4$, (B) $Ca_{0.50}Mg_{0.50}Fe_2O_4$ and (C) $Ca_{0.75}Mg_{0.25}Fe_2O_4$. Grey lines: experimental patterns; black lines: fitted patterns; red dashed lines: background. 74

Figure 2.3 Sedimentation kinetics of $Ca_{0.50}Mg_{0.50}Fe_2O_4$ nanoparticles. 75

Figure 2.4 (A, B) TEM images of $Ca_{0.50}Mg_{0.50}Fe_2O_4$ nanoparticles with different magnifications. (C) Image A with outlined nanoparticles. (D) Size histogram of image A. (E) SAED image with indexed diffraction planes. 76

Figure 2.5 Magnetization hysteresis loops of calcium-substituted magnesium ferrite nanoparticles were measured at room temperature. Inset: Enlargement of the loops in the low field region. 77

Figure 2.6 Fluorescence spectra of curcumin encapsulated in liposomes and AMLs based on calcium-substituted magnesium ferrite nanoparticles. 80

Figure 2.7 Fluorescence spectra (λexc = 440 nm) of AMLs containing $Ca_{0.25}Mg_{0.75}Fe_2O_4$ nanoparticles (as an example), labelled with both curcumin (2×10^{-6} M) and Nile Red (2×10^{-6} M), before and after interaction with GUVs. (A) AMLs of Egg-PC; (B) AMLs of Egg-PC/DSPE-PEG2000 (0.95:0.05). 81

Figure 2.8 Fluorescence spectra (λexc= 440 nm) of curcumin in SMLs containing $Ca_{0.25}Mg_{0.75}Fe_2O_4$ nanoparticles (as an example), before and after interaction with GUVs. A: SMLs of DPPC; B: SMLs of DPPC/DSPE-PEG. 84

Figure 2.9 The drug release profile of curcumin from DPPC-based SMLs, with and without applying an AMF. 86

Figure 3.1 Schematic representation of the synthesis methodology of DOX-loaded SMLs. 103

Figure 3.2 XRD pattern of the $Ca_{0.25}Mg_{0.75}Fe_2O_4$ NPs and corresponding Rietveld analysis. 107

Figure 3.3 (A–C) HR-TEM images of $Ca_{0.25}Mg_{0.75}Fe_2O_4$ ferrite NPs at different magnifications. (D) Aspect ratio distribution histogram. (E) Size histogram and distribution fit ($R^2 = 0.96$) and (F) SAED image with indexed diffraction planes. 108

Figure 3.4 Tauc plot for shape-anisotropic $Ca_{0.25}Mg_{0.75}Fe_2O_4$ ferrite NPs (the red line corresponds to the linear fit). 109

Figure 3.5 Magnetisation hysteresis cycle of $Ca_{0.25}Mg_{0.75}Fe_2O_4$ ferrite NPs at 5 K and 300 K. Inset: enlargement of the hysteresis loop in the low field region. 111

Figure 3.6 Magnetically-induced thermal response curve (temperature variation vs time) of $Ca_{0.25}Mg_{0.75}Fe_2O_4$ NPs and SMLs for magnetic hyperthermia. 1 mg of NPs were dispersed in 1 mL of water and subjected to an AMF with different field frequencies and strengths over 30 min (1800 s). 113

Figure 3.7 (A) Molecular structure of DOX ($C_{27}H_{29}NO_{11}$). (B) Absorption spectra of DOX solutions, at 1×10^{-5} M, in several solvents. (C) Normalized fluorescence (at the peak of maximum emission) spectra of DOX (1×10^{-6} M, λexc = 480 nm) in several solvents. 114

Figure 3.8 Fluorescence spectra (λexc=470 nm) of SMLs with a DPPC bilayer labelled with only NBD-C_{12}-HPC, with only Rh-DOPE, and labelled with both NBD-C_{12}-HPC and Rh-DOPE. 117

Figure 3.9 Hydrodynamic diameter and PDI evolution of an aqueous solution of DPPC-based SMLs during storage at 4 °C for 30 days. 118

Figure 3.10 (A) HR-TEM image of a SML containing $Ca_{0.25}Mg_{0.75}Fe_2O_4$ ferrite NPs. (B) Schematic representation of a SML, characterised by the presence of a core (cluster of magnetic NPs) covered with a lipid bilayer. 120

Figure 3.11 Fluorescence spectra (λexc = 480 nm) of DOX (2×10^{-6} M) in liposomes (without magnetic NPs) and in SMLs containing $Ca_{0.25}Mg_{0.75}Fe_2O_4$ magnetic NPs. 120

Figure 3.12 Fluorescence spectra (λexc= 480 nm) of DOX in SMLs containing $Ca_{0.25}Mg_{0.75}Fe_2O_4$, before and after interaction with GUVs at 25 °C and 55 °C, for the different lipid formulations. A: DPPC; B: DPPC:DSPE-PEG; C: DPPC:Ch. 124

Figure 3.13 HSA fluorescence quenching (%) as a function of increasing DOX concentration in free form and loaded in DPPC/DSPE-PEG-based liposomes. According to **Equation 3.4**, a nonlinear fit is presented (red lines). 125

Figure 3.14 *In vitro* kinetic release profile of DOX encapsulated in SMLs at different conditions of temperatures and pH, with the triplicate mean fitted to the Weibull kinetic model. (A) DPPC-based SMLs. (B) DPPC/DSPE-PEG-based SMLs. 128

Figure 3.15 Size variation of DOX-loaded SMLs with increasing temperature at different pH values. (A) DPPC-based SMLs. (B) DPPC/DSPE-PEG-based SMLs. Mean size values and standard deviation are from triplicate assays. 129

Figure 4.1 Schematic representation of the lipid combinations used to prepare DOX-loaded SMLs.144

Figure 4.2 ζ-potential-pH profiles of DOX-loaded SMLs based on: (A) Group A, (B) Group B and (C) Group C lipid formulations. 150

Figure 4.3 DSC heating thermograms of DOX-loaded SMLs based on different lipid formulations. . 151

Figure 4.4 Stability data of DOX-loaded SMLs aqueous suspensions, based on (A) Group A, (B) Group B and (C) Group C lipid formulations, upon storage at 4 °C. The stability of the formulations is expressed as the mean size and PDI variations compared to the original values (measured on day 1). 153

Figure 4.5 HSA fluorescence quenching (%) as a function of increasing free DOX concentration (as a reference in Group A) and loaded in (A) Group A, (B) Group B and (C) Group C lipid formulations. A non-linear fit, according to **Equation 3.4**, is presented (corresponding lines). 154

Figure 4.6 (A) Fluorescence intensity and steady-state fluorescence anisotropy (r) variation with pH (from 2 to 11) of DOX-loaded SMLs based on different lipid formulations. Total lipid concentration: 1 mM; DOX: 2 μM. (B) Schematic representation of DOX molecules localisation in the lipid bilayer at different pH (predictive). 156

Figure 4.7 *In vitro* kinetic release profile of DOX encapsulated in SMLs is based on (a) Group A, (b) Group B, and (c) Group C lipid formulations at different conditions of temperature and pH. Triplicate mean fitted to the Weibull kinetic model. 158

Figure 4.8 Experimental setup for near infrared-induced photothermal hyperthermia measurements. 173

Figure 4.9 (A) Representative image of aqueous suspensions of the different $Ca_{0.25}Mg_{0.75}Fe_2O_4$ concentrations and (B) their corresponding UV/Visible absorption spectra. (C) Heating and cooling profiles of the tested samples during laser irradiation (808 nm, 1 W/cm^2). (D) Correlation between the photothermal capacity and NPs concentration. 176

Figure 4.10 (A) Representative image of aqueous dispersions of SMLs based on DPPC/DSPC/CHEMS/DSPE-PEG (1 mM) containing 1, 2 and 4 mg of magnetic NPs and (B) VSM measurements for dried samples of corresponding SMLs. (C) TEM image of several SMLs with the initial NPs/lipid formulation ratio of 2 mg/1 mM (scale bar: 500 nm; mean diameter of 146.07 ± 10 nm) and (D) TEM image of SMLs with the initial NPs/lipid formulation ratio of 2 mg/1 mM (scale bar: 100 nm). 178

Figure 5.1 Schematic representation of the heterogeneity in solid tumours. The continuous outgrowth of cells leads to the formation of gradients (such as nutrients and oxygen) that induce the generation of

tumour microenvironments. Proliferative tumour cells, which define the area closest to the tumour vasculature, receive the oxygen and nutrients needed to proliferate. Quiescent tumour cells represent a median region with viable but nonproliferating cells. In the area of greatest oxygen, nutrient deprivation and accumulation of toxic waste products, necrotic tumour cells are found. 188

Figure 5.2 Schematic representation of (A) Drug delivery of intravenously injected chemotherapeutic drugs into a tumour tissue by diffusion, binding and drug clearance from tumour tissue; and (B) Simulation of the tumour environment and the respective mechanisms involved in drug delivery on a microfluidic platform, where the microfluidic channel represents the tumour vasculature, and the microfluidic chamber allows the development of mimetic tumour tissue. 190

Figure 5.3 Roundness parameter variation of Sk-br-3 cells over 48 h when exposed to different treatment conditions. The histogram shows roundness mean values ± SD and the multiple comparisons with Dunnett's test. *$p < 0.05$; **$p < 0.01$; ***$p < 0.001$; ****$p < 0.0001$; by ANOVA followed by Dunnett's post-test. 196

Figure 5.4 Representation of the geometry and dimensions used to fabricate the two SU-8 master moulds using: (A) 3 round pillars with a diameter of ~85 µm; (B) 2 rectangles with a width and length of ~85 and ~100 µm, respectively, in order to trap the spheroids. 209

Figure 5.5 Representative SEM images of the microfluidic platforms designed with (A) 3 round pillars and (B) 2 rectangular pillars. The inset shows a zoom of the pillars. 212

Figure 5.6 Photograph of a PDMS microfluidic device composed of 3 replicas of the cell culture system. 213

Figure 5.7 Assembly scheme overview of (A) microfluidic platform connected to the flow pumping and image acquisition systems and (B) working device with microfluidic inlet and outlets tubbing and the corresponding valves coupled. 214

Figure 5.8 Sequential microscopy images of Sk-br-3 spheroids inclusion and retention on a microfluidic platform with rectangular pillars. 215

List of Tables

Table 1.1 Summary of magnetoliposomes types, lipid compositions, nanoparticles, encapsulated compounds, and triggers used to the aimed biomedical applications. 13

Table 1.2 Summary of the advantages and challenges of 2D and 3D cell culture methods. 33

Table 2.1 Selected Rietveld analysis parameters. 74

Table 2.2 The saturation magnetizations (M_s), remanant magnetisation (M_r), ratio M_r/M_s and coercive field (H_c) of calcium-substituted magnesium ferrite nanoparticles. 78

Table 2.3 Hydrodynamic diameter and PDI of egg-PC AMLs containing calcium-substituted magnesium ferrite nanoparticles. 79

Table 2.4 Steady-state fluorescence anisotropy (r) values for curcumin at 25 °C in AMLs containing $Ca_{0.25}Mg_{0.75}Fe_2O_4$. Values for curcumin in liposomes and glycerol are also shown for comparison. ... 80

Table 2.5 *FRET* efficiencies ($\Phi FRET$), Förster radii ($R0$) and donor-acceptor distances (rAD) calculated for the formation of the lipid bilayer in SMLs. 82

Table 2.6 Hydrodynamic diameter and polydispersity of DPPC SMLs containing calcium-substituted magnesium ferrite nanoparticles. 82

Table 2.7 Steady-state fluorescence anisotropy (r) values for curcumin at 25 °C and 55 °C in SMLs containing $Ca_{0.25}Mg_{0.75}Fe_2O_4$. Values for curcumin in DPPC liposomes are also shown for comparison. 83

Table 2.8 Obtained constant values by fitting the Korsmeyer-Peppas model to the curcumin' kinetic release data from SMLs in the presence and absence of an AMF, and respective coefficient of determination (R^2). 85

Table 3.1 H_C, M_s, M_r, and ratio M_r/M_s for cubic $Ca_{0.25}Mg_{0.75}Fe_2O_4$ ferrite NPs. 111

Table 3.2 Maximum absorption (λabs) and emission wavelengths (λem), molar absorption coefficients (ε), and fluorescence quantum yields (Φ_F) for DOX in several solvents. [a] Relative to fluorescein in 0.1 M NaOH aqueous solution. 115

Table 3.3 Hydrodynamic diameter and PDI of several SMLs lipid formulations at 25 °C. Results as mean ± SD. 119

Table 3.4 Steady-state fluorescence anisotropy values for DOX in SMLs with different lipid formulations, in SMLs upon interaction with GUVs and in GUVs (for comparison). Total lipid concentration: 1×10^{-3} M; DOX: 2×10^{-6} M. 121

Table 3.5 EE% and corresponding encapsulated DOX concentration (M) in SMLs containing $Ca_{0.25}Mg_{0.75}Fe_2O_4$ at different concentrations of DOX. The standard deviation is from triplicate drug encapsulation assays. 123

Table 3.6 The dissociation constant (kd), binding constant ($kb = 1/kd$), and the number of binding locations (n) of DOX, DPPC liposomes, and DPPC:DSPE-PEG liposomes to HSA. 126

Table 4.1 Lipid composition and the molar ratio of the lipids to synthesise SMLs with different types of action. 145

Table 4.2 Hydrodynamic diameter, PDI, EE%, pI and T_m of DOX-loaded SMLs based on different lipid formulations at 25 °C. 149

Table 4.3 Summary of release slope (m) values of DOX plotted in the first 5 h and ratio between the saturation release under 37 °C, pH 7.4 and the corresponding release conditions. 159

Table 4.4 M_s, D_H, PDI, encapsulated NPs (with the corresponding percentage of NPs encapsulation efficiency below), lipid with encapsulated NPs (with the corresponding percentage of lipids encapsulation efficiency below) and the final obtained NPs/lipid formulation ratio of SMLs samples starting from different initial NPs/lipid ratios. 179

Table 5.1 Representative bright-field and fluorescence microscopy images (merged) of free DOX, SMLs and DOX-loaded SMLs on Sk-br-3 breast cancer cells cultured in adherent conventional 2D cell plates over 48h. 194

Table 5.2 Representative bright-field and fluorescence microscopy images (merged) of free DOX, SMLs and DOX-loaded SMLs on 1-week dense Sk-br-3 breast cancer spheroids cultured on conventional adherent cell culture (pseudo-3D) plates over 48h. 198

Table 5.3 Representative bright-field and fluorescence microscopy images (merged) of free DOX, SMLs and DOX-loaded SMLs on Sk-br-3 breast cancer cells cultured on non-adherent cell culture plates (newly formed spheroids) over 48h. 202

Table 5.4 Representative bright-field and fluorescence microscopy images (merged) of free DOX, SMLs and DOX-loaded SMLs on one-week dense Sk-br-3 breast cancer spheroids cultured on non-adherent cell culture plates over 48h. 204

Table 5.5 Interactive 3D surface plots (front view and top view) of DOX-loaded SMLs effects on Sk-br-3 breast cancer cells seeded on non-adherent cell culture plates (newly formed spheroids) over 48 h. 206

Table 5.6 Interactive 3D surface plots (front view and top view) of DOX-loaded SMLs effects on 1-week dense Sk-br-3 breast cancer spheroids seeded on non-adherent cell culture plates over 48 h. 207

Table 5.7 Processing conditions used to obtain the SU-8 moulds [36]. 210

List of Abbreviations

2D	Two-Dimensional
3D	Three-Dimensional
AFP	Alpha-Fetoprotein
AMF	Alternating Magnetic Field
AMLs	Aqueous Magnetoliposomes
APTES	3-Aminopropyl)triethoxy Silane
BBB	Blood-Brain Barrier
CAFs	Cancer-Associated Fibroblasts
CF	Carboxyfluorescein
Ch	Cholesterol
CHEMS	Cholesteryl Hemisuccinate
CPR	Critical Perfusion Rate
CSC	Cancer Stem Cells
D_H	Hydrodynamic Diameter
DLS	Dynamic Light Scattering
DMEM	Dulbecco's Modified Eagle's Medium
DMSA	Dimercaptosuccinic Acid
DOPC	1,2-dioleoyl-sn-glycero-3-Phosphocholine
DOPE	Dioleoylphosphatidyl-Ethanolamine
DOX	Doxorubicin
DPPC	1,2-dipalmitoyl-sn-glycero-3-Phosphocholine
DSC	Differential scanning Calorimetry
DSPC	Distearoylphosphatidylcholine
ECM	Extracellular Matrix
e.g.	For Example
ECT	Effective Culture Time
EDS	Electron-Dispersive Spectroscopic Analyser
EE	Encapsulation Efficiency
EGFR	Epidermal Growth Factor Receptor
Egg-PC	Egg Yolk Phosphatidylcholine
EPR	Enhanced Permeability and Retention
FBS	Fetal Bovine Serum
FDA	Food and Drug Administration
FRET	Förster Resonance Energy Transfer
GF	Growth Factor
GUVs	Giant Unilamellar Vesicles
H	Magnetic Field
HA	Hyaluronic Acid
H_c	Coercive Field
HCL	Hydrochloric Acid
HLNCs	Hybrid Lipid-nanoparticle Complexes
HNSCC	Head and Neck Squamous Cell Carcinoma
HR-TEM	High-Resolution Transmission Electron Microscopy

HSA	Human Serum Albumin
HUVECs	Human Umbilical Vein Endothelial Cells
ILP	Intrinsic Loss Power
IONPs	Iron Oxide Nanoparticles
IPA	Isopropyl Alcohol
LF-AMF	Low-Frequency Alternating Magnetic Field
LUVs	Large Unilamellar Vesicles
MCSs	Multicellular Spheroids
MDR	Multi-drug Resistance
MFH	Magnetic Fluid Hyperthermia
MLV	Multilamellar Vesicles
MPS	Mononuclear Phagocyte System
M_r	Remnant Magnetisation
MRI	Magnetic Resonance Imaging
MTX	Methotrexate
MUL	Medium Unilamellar Vesicles
MVV	Multivesicular vesicles
NBD	Nitrobenzoxazole
NIR	Near-Infrared
NPs	Nanoparticles
OLV	Oligolamellar Vesicles
OSTE	Off-stoichiometric Thiol-ene
PDI	Polydispersity Index
PDMS	Polydimethylsiloxane
PEG	Polyethylene Glycol
PEGDA	Poly(ethylene glycol) Diacrylate
PGS	Poly(glycerol sebacate)
PLGA	Poly(DL-lactic-co-glycolide)
PTT	Photothermal Therapy
PVA	Polyvinyl Alcohol
r	Anisotropy
Re	*Reynolds* Number
RES	Reticuloendothelial System
Rh	Rhodamine
ROS	Reactive Oxygen Species
SAED	Small Area Electron Diffraction
SAR	Specific Absorption Rate
SAV	Surface Area-to-Volume
SD	Standard Deviation
SF	Silk Fibroin
SMLs	Solid Magnetoliposomes
SPIONs	Superparamagnetic Iron Oxide Nanoparticles
SQUID	Superconducting Quantum Interference Device
SUV	Small Unilamellar Vesicles
TEM	Transmission Electron Microscopy
ULV	Unilamellar Vesicles
UV	Ultraviolet
UV/Vis	Ultraviolet/Visible
VSM	Vibrating Sample Magnetometer
XRD	X-Ray Diffraction

List of Symbols

$\boldsymbol{\varepsilon}$	Absorption Coefficient
$\boldsymbol{\lambda_{abs}}$	Absorption Wavelength
$\boldsymbol{\lambda_{exc}}$	Excitation Wavelength
$\boldsymbol{\lambda_{em}}$	Emission Wavelength
$\boldsymbol{\theta}$	Angle
k_b	Binding Constant
$\boldsymbol{\chi^2}$	Chi-Square
$\boldsymbol{C_0}$	Concentrations at time 0
$\boldsymbol{C_t}$	Concentrations at time t
$\boldsymbol{R}$	Correlation Coefficient
°	Degrees
$\boldsymbol{k_d}$	Dissociation Constant
$\boldsymbol{r_{AD}}$	Donor-Acceptor Distances
$\boldsymbol{K}$	Drug Transport Constants
$\boldsymbol{I_{HH}}$	Emission intensities obtained with horizontal (for horizontally polarized excitation light)
$\boldsymbol{I_{HV}}$	Emission intensities obtained with vertical polarization (for horizontally polarized excitation light)
$\boldsymbol{H}$	Field Strength
$\boldsymbol{R_0}$	Förster Radius
$\boldsymbol{f}$	Frequency
$\boldsymbol{\Phi_{FRET}}$	*FRET* Efficiency
$\boldsymbol{I_{VH}}$	Intensities of the emission spectra obtained with horizontal polarization
$\boldsymbol{I_{VV}}$	Intensities of the emission spectra obtained with vertical polarization
$\boldsymbol{m_m}$	Mass of magnetic material
$\boldsymbol{m_s}$	Mass of suspension
Oe	Oersted
$\boldsymbol{E_g}$	Optical Band Gap
wt%	Percentage by Weight
$\boldsymbol{n}$	Refraction Index
$\boldsymbol{C}$	Specific Heat Capacity
$\boldsymbol{r}$	Steady-State Fluorescence Anisotropy
T	Temperature
ΔT	Temperature variation
t	Time
$\mathbf{T_m}$	Transition Temperature
$\boldsymbol{n}$	Transport Exponents
η	Viscosity
$\boldsymbol{\lambda}$	Wavelength

CHAPTER 1

Introduction

The following sections set out the motivations that support cancer research, particularly the relevance of this work in formulating new strategies for the controlled delivery of chemotherapeutic drugs. It also highlights the importance of cell culture techniques in drug screening and the establishment of microfluidic platforms for cell culture as *in vitro* mimetic approaches. The state-of-the-art in the research field is presented, showing recent advances in lipid-based magnetic nanosystems for delivery strategies in the biomedical field. The prospects of microfluidic technology as a practical tool for drug research and development are highlighted.

1.1. Framework and main objectives

Cancer is one of the biggest public health problems worldwide, representing one in six deaths. In the minute we read this sentence, 12 people died of cancer. The present work was carried out between 2018 and 2022. Therefore, looking at the evolution of cancer disease in this time frame becomes relevant. According to statistics carried out by the American Cancer Society for the United States of America, in 2018, ~1,735,350 new cancer cases and ~609,640 cancer deaths were estimated; while in 2022, ~1,918,030 new cancer cases and ~609,360 cancer deaths were projected. A straight forward analysis of these numbers reveals that the increase in new cases was not accompanied, in the same way, by the rise in the number of deaths. This trend has been observed since 1991, with a 32% drop in death risk between 1991 and 2019. This progress is fundamentally due to advances in early diagnosis, surgical techniques and the development of new targeted therapies that have taken place in the last decade. The millions of saved lives and the millions of lost lives validate the investment that has been made in the research and development of new advanced cancer therapies. They also highlight the importance of these new treatment approaches in the progress of medicine, public health, and society by improving patients' quality of life and increasing their life expectancy.

The investigation of new treatment approaches focuses on developing drugs for specific cancer targets and formulating new strategies to direct and control the delivery of drugs. Controlled drug delivery is one of the most ambitious concepts in pharmaceutical science, particularly for the selective treatment of cancer. Its main objective is based on the controlled delivery of chemotherapeutic agents in the pathological area, implying minimum side effects in non-target areas. Following these premises, liposomes (lipid bilayers enclosing an aqueous core) are the most widely used nanocarrier in the pharmaceutical industry [1]. Their success is due to their structural and compositional versatility, simplicity, cell membrane mimetic morphology, and ability to incorporate hydrophilic (in the aqueous core) and/or lipophilic (in the bilayers) compounds [2]. In addition, they also exhibit non-toxic, flexible, biocompatible, biodegradable, deformable, and non-immunogenic properties for systemic and non-systemic applications [3-5]. The primary goal of employing liposomes as drug carriers is to improve the pharmacokinetics and distribution of compounds in the target tissues. This can be accomplished through better cargo protection against early degradation, better targeting, a more sustained release, and enhanced internalisation of drugs in target cells [6-9].

Similarly, the potential of magnetic NPs in cancer treatment has also been explored in the last decades. The interest in using magnetic NPs as therapeutic agents emerged in 1957 after using magnetic metallic

NPs (Fe_2O_3) with a magnetic field to treat lymphatic nodes and metastases [10]. This class of materials is characterised by nanometric dimensions, whose inherent magnetism allows them to be magnetised, controlled, and produce heat under an external magnetic field or near-infrared (NIR) lasers. Furthermore, they have unique features such as a high surface area, tuneable size and magnetic properties, high chemical stability, high magnetic susceptibility, ability to functionalise their surface with specific molecules, biocompatibility with several cell types, and superparamagnetism [11-14].

Thus, this work mostly scrutinises the conjugation of magnetic NPs within liposomes, forming magnetoliposomes, which intends to formulate a drug delivery system for controlled drug release in space and time. Magnetoliposomes emerge as hybrid complexes that combine the advantages of the magnetic and lipid components, surpassing some limitations of their individual use and creating unique functionalities in a single system. The therapeutic functionality of magnetoliposomes is based on the cargo-controlled delivery and release under internal and external stimuli, their magnetophoretic mobility, and the synergy of drug action with induced thermally activated processes. Developing magnetoliposomes with therapeutic effectiveness demands an arduous and lengthy path of understanding, optimisation, and selection. As a result, a significant amount of time allocated to this work is dedicated to optimising magnetoliposomes.

The screening of magnetoliposomes is inseparable from cell culture techniques. Those are ubiquitously used to discover drug efficacy, delivery, pharmacological actions, and cytotoxicity. Most cell-based assays are based on two-dimensional (2D) models performed on multi-well plates that are easily monitored [15]. However, some limitations of 2D cell cultures, such as their difficulties in representing the three-dimensional (3D) structure of tissues *in vivo*, limit the ability of this method to predict the clinical response of drugs [16-18]. Therefore, in an attempt to establish more realistic biomechanical and biochemical microenvironments and avoid costly failures in the late stages of drug development, the scientific community has been favouring the development of 3D cell culture methods [19]. Nevertheless, considering that each model reflects different cellular organisational levels and behaviours, the extrapolated information of the screened drug depends on the method used. Thus, this work also explores differences in the cellular response of breast cancer cells as a model of the desease (to free drug and drug-loaded magnetoliposomes) cultured in 2D, pseudo-3D (tumour spheroids cultivated in adherent cell culture plates) and 3D (tumour spheroids). Aiming to establish an even more mimetic approach to physiological conditions, microfluidic platforms for cell culture weredesigned as a proof-of-concept. This platform is intended to reflect the continuous flow and the microenvironment gradients of solid tumours, allowing the comprehensive study of the nanosystems. Furthermore, the miniaturisation of cell culture

and supplementation processes bring these screening assays closer to mimetic conditions, reproducing the mechanisms that reduce drug efficacy with greater accuracy.

Thus, this thesis stands out for its multidisciplinarity and interdisciplinarity. Its main objective is to create knowledge and innovation for the application of nanotechnology in cancer therapy; specifically, it is devoted to developing optimised drug nanocarriers – magnetoliposomes – as multifunctional approaches to treating the disease. Furthermore, this work sought to understand the cellular response differences in cell-based assays that reflect several cellular organisational levels. Finally, microfluidic platforms for cell culture was designed as a proof-of-concept, intending to comprehensively evaluate the activity of the nanosystems in a more biomimetic *in vivo* context.

Accordingly, to fulfil this purpose, it was necessary to establish a set of subsequent goals, namely:

i) Understand the basic principles of superparamagnetic nanoparticles synthesis and the influence of different components on their properties;
ii) Understand the essential synthesis of different types of magnetoliposomes (namely, aqueous and solid) and their ability to encapsulate a drug model;
iii) Apply the acquired knowledge in the development of a methodology for the synthesis of nanoparticles with better magnetic properties;
iv) Apply the acquired knowledge in the development of a new methodology for the synthesis of drug-loaded magnetoliposomes with reproducible and improved properties;
v) Understand the effect of lipid formulations on structural, colloidal, and thermodynamic parameters of drug-loaded magnetoliposomes;
vi) Understand the mechanisms of induction of drug-controlled release under multi-stimuli (thermo/pH sensitivity);
vii) Integrate the acquired knowledge in the selection of the most promising lipid combination to study in physiologically relevant environments;
viii) Insight into the potential of superparamagnetic nanoparticles to combine magnetic hyperthermia and photothermal therapy;
ix) Establish the appropriate *in vitro* cell-based assays to validate the performance of the drug-loaded magnetoliposomes in several cellular organisational levels (2D, pseudo-3D and 3D cell culture methods);

x) Design and fabricate new microfluidic platforms that reflect the microenvironment gradients of breast cancer solid tumours to screen the effectiveness of drug-loaded magnetoliposomes as a new therapeutic approach in cancer.

Accordingly, the following sections describe concepts, fundamentals and the state-of-the-art in the research field. Thus, the evolutionary scheme of liposomes in the release and targeting strategies is detailed in **section 1.2**, as well as the applicability categories of magnetic NPs in biomedicine. Furthermore, the ability of the latter to modulate functionalities of lipid systems – forming magnetoliposomes – is exposed through a literature review of their use as stimuli strategies for enhanced drug release. Finally, **section 1.3** enunciates the importance of research and development in public health, and the active role that cell culture and microfluidics have in narrowing the path between developing and approving medicines.

1.2. Progress in theranostics with lipid-based nanosystems

Nanomedicine and smart delivery systems are part of the second generation of drug delivery systems and include, among others, dendrimers, carbon nanotubes, liposomes, micelles, and lipoplexes. The first United States Food and Drug Administration (US FDA)-approved nano-drug (Doxil®) [20] emerged in 1995, and it is an anti-cancer liposomal formulation encapsulating Doxorubicin (DOX). Since then, liposomes have been gaining recognition as biomimetic nanostructures for encapsulation and delivery of bioactive agents, with their efficiency proven by several lipid formulations FDA-approved for treating diseases. In addition to biocompatibility, biodegradability, and ability to encapsulate hydrophilic and hydrophobic drugs, their clinical applicability can be manipulated by varying preparation strategies, lipid formulations, surface modifications, and conjugation with other types of organic and inorganic materials. In recent years, superparamagnetic iron oxide NPs (SPIONs) have also opened a new horizon of applicability in biomedical sciences for diagnosis and therapeutics. Their inherent physicochemical properties give them the potential for tissue engineering, magnetic separation, *in vivo* cell tracking, magnetic hyperthermia, iron detection, magnetic resonance imaging (MRI), stem cell tracking, and targeted drug or gene delivery. Moreover, there are already FDA-approved magnetite-based nanoformulations, for instance, Feridex®/Endorem®, Nanotherm®, Feraheme™ /ferumoxytol, Umirem®, and GastroMARK™ [21]. Thus, the conjugation of lipids with SPIONs can give rise to

supramolecular hybrid structures that retain the properties of the materials singularly and new combined and synergistic therapeutic functions.

1.2.1. Liposomal drug delivery: design and classification

Liposomes are unilamellar or multilamellar spherical vesicles encapsulating an aqueous compartment, and they were discovered by A.D. Bangham in 1965 [22,23]. The vesicles are mainly formed by phospholipids – from plant or animal sources – amphiphilic molecules with a hydrophilic head and two non-polar hydrophobic chains. Its amphiphilic nature results in spontaneous self-assembly when in contact with aqueous solutions, forming membranes [24]. The lipid bilayer formation results from the preference of polar heads to interact with the aqueous component (facing the aqueous region outwards). In contrast, non-polar aliphatic chains interact with one another (facing each other).

One of the characteristics that most instigated the investigation of liposomes was the versatility to adapt their functionalities to specific applications. While the classical classification was limited to distinguishing liposomes according to their size and number of lamellae, nowadays, this classification includes their shape, structural and surface properties [6]. Based on their size, liposomes are classified into unilamellar liposomes (spherical vesicles confined by a single bilayer) and multilamellar liposomes (onion-like structures made by numerous unilamellar vesicles) [4,25]. Regarding their structural parameters, they are distinguished as (1) multilamellar vesicles (MLV)- consisting of more than five multiple lipid bilayers; (2) oligolamellar vesicles (OLV)- containing two to five concentric lamellae; (3) multivesicular vesicles (MVV)- contain internal, non-concentrically arranged smaller vesicles; and (4) unilamellar vesicles (ULV)- consisting of a single lipid bilayer and are categorized into four distinct groups based on vesicles size- small unilamellar vesicles (SUV), medium unilamellar vesicles (MUV), large unilamellar liposomes/vesicles (LUV) and giant unilamellar vesicles (GUV) [25].

The discovery and validation of new features and the need to provide liposomes with different functionalities resulted in the successive improvement of targeting strategies, mainly related to liposome composition and functionalisation with other molecules. Concerning the target strategies, liposomes are categorised into conventional liposomes, cationic liposomes, long-circulating liposomes, ligand-targeted liposomes, immune liposomes, and stimuli-sensitive liposomes (**Figure 1.1**) [26].

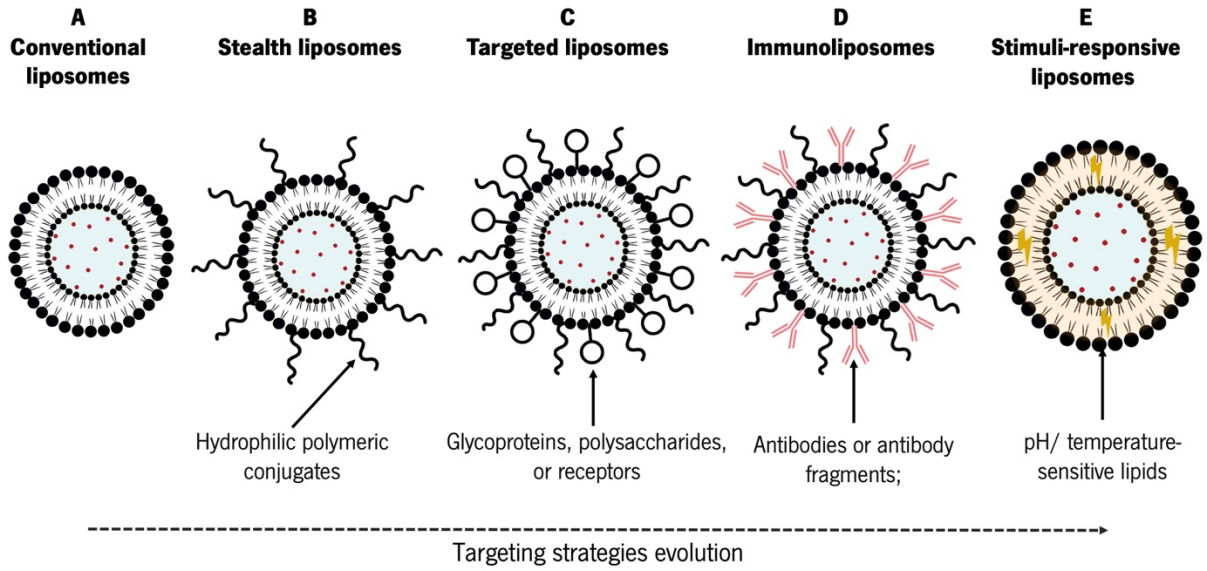


Figure 1.1 Schematic representation of liposome targeting strategies evolution. (A) Conventional liposomes. (B) Stealth liposomes, functionalized with hydrophilic polymeric conjugates. (C) Targeted liposomes, functionalized with glycoproteins, polysaccharides, or ligand of cell-specific receptors. (D) Immunoliposomes, functionalized with antibodies or antibody fragments. (E) Stimuli-responsive liposomes based on pH or temperature lipid formulations.

Conventional liposomes are the first generation of liposomes and correspond to the classic image of these structures. These liposomes do not have surface functionalisation and are only composed of phospholipids (usually neutral and/or negative) and/or cholesterol (Ch) [27]. Although controlling physicochemical properties (such as size, surface charge, lipid composition, and fluidity of the lipid bilayer) helps to modulate and predict the *in vivo* behaviour of liposomes, it is not sufficient to counteract the rapid elimination from circulation by the liver and spleen macrophages [28]. Also, their interaction with high (HDL) and low-density (LDL) lipoproteins result in a rapid release of the drugs into the plasma [29].

The development of long-circulating stealth liposomes was a significant step in liposomal drug delivery. The first strategy to develop this liposome was mimicking erythrocyte membranes through liposome functionalization with gangliosides and sialic acid derivatives (such as monosialoganglioside) [30]. The second strategy, and currently most used, is based on increasing the hydrophilicity of the liposome by functionalising it with hydrophilic polymers such as poly-(ethylene glycol) (PEG) [31,32]. Both strategies are based on the protective effect of the layer constituted by the flexible chains of these molecules, called the periliposomal layer, on the surface of liposomes [33]. This layer prevents the binding of

macromolecules such as blood plasma opsonins and, consequently, the binding of macrophages to liposomes.

Although this type of liposome has solved the reduced blood circulation half-life of conventional liposomes, its broad and non-specific tissue biodistribution has boosted the development of targeted liposomes [34]. This class of liposomes allows for increasing the specificity of drug delivery and accumulation at target sites through the functionalization of liposomes with specific targeting moieties (for instance: peptides, carbohydrates, vitamins, oligonucleotide aptamers, growth factors, and receptor ligands) [34-36]. The target cells recognize and bind to the corresponding targeting moieties, which results in liposome-specific internalization. Immunoliposomes, firstly prepared by Torchilin [37], are targeted liposomes that are functionalized with antibodies or antibody fragments that allow an active tissue targeting of cell-specific receptors. This liposome is part of the third generation of liposomal formulations and is one of the most used targeting approaches. Antibodies can be attached to liposomes simultaneously with PEG allowing for combined functionality with stealth liposomes [38]. Immunoliposomes are especially interesting in cancer therapy because they combine the advantages of drug encapsulation and passive and active targeting with the synergistic potential between the drug and signalling antibodies [36].

Due to some difficulties of conventional and long-circulating liposomes in releasing the cargo, and their inability to fuse with the endosome after internalization, stimuli-responsive liposomes were developed to achieve sustained release of drugs. The functionality of these liposomes is based on their ability to react to external stimuli (such as ultrasound, hyperthermia, and electromagnetic field) as well as internal stimuli characteristic of the microenvironment of the target tissues (redox potential, pH) [36,39]. pH-sensitive liposomes take advantage of the pH differences between pathological and normal tissues [40]. Although these liposomes are stable at physiological pH, the vesicles (containing pH-sensitive components) are destabilized after the acidification that follows the cellular internalization which impels cargo release [41-43]. On the other hand, redox potential-sensitive liposomes take advantage of the difference in redox potential between intracellular (reducing) and extracellular (oxidizing) spaces. These liposomes release cargo within cells when disulphide bonds present in lipids are reduced by glutathione to thiol groups [29]. The action mode of temperature-sensitive liposomes is a temperature increase above physiological temperature; when it exceeds the melting-phase transition temperature (T_m) of the bilayer, which is related to the T_m of the lipids that constitute it, the compound is released [44]. These liposomes have already achieved successful results in combination with heat-based thermal therapies, including ultrasound hyperthermia [45], microwave hyperthermia [46], or radiofrequency ablation [47]. The

recognition of the use of heat in clinical application dates to antiquity [48]. This type of therapy, called hyperthermia or thermotherapy, is characterized by a mean increase in body temperature (local, regional, or whole-body hyperthermia). It is recognized for its beneficial potential in cancer therapy when combined with other treatment modalities such as chemotherapy or radiotherapy, demonstrating the ability to shrink solid tumours and facilitate to kill cancer cells [49-51]. Currently, the scientific community has focused on using magnetic NPs for biomedical applications as mediators of magnetic hyperthermia.

1.2.2. Superparamagnetic nanoparticles as theranostics mediators

In 1962, Freeman *et al.* [52] discussed the potential of "the marriage of magnetism and medicine". In that work, they pointed out magnetism as a powerful technology in solving medical problems, such as its use in the treatment of cancer, magnetic analysis in biochemistry, treatment of mental disease, and magnetic analysis in diagnosis [52]. Currently, the use of magnetic NPs is already a reality in medicine (in clinical or pre-clinical stages), and their application can be classified into four general categories: diagnosis, imaging, movement, and treatment (**Figure 1.2**) [53].

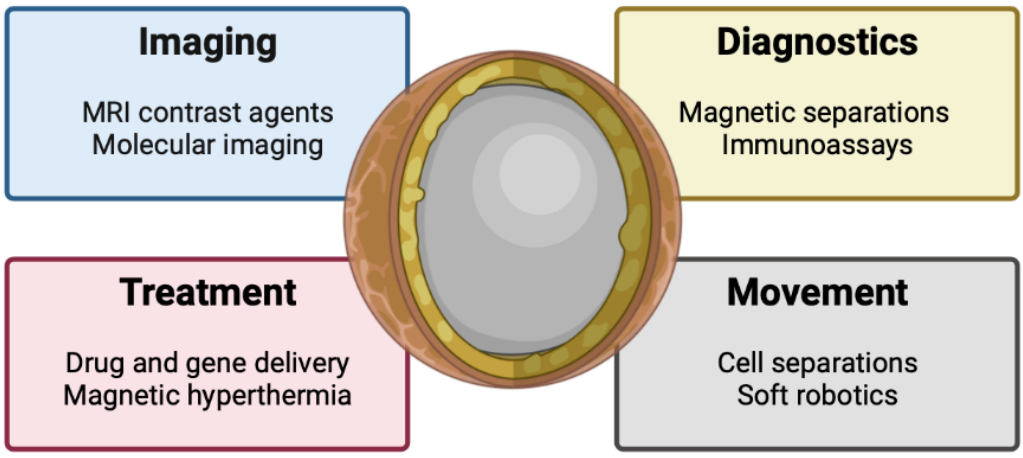


Figure 1.2 Categories and practical application of magnetic NPs in biomedicine.

Medicine assumes early diagnosis as one of the most determining (and challenging) factors for successfully treating a disease. Magnetic resonance imaging (MRI) is a widely used non-invasive diagnostic technique that allows obtaining images with spatial resolution, soft tissue contrast, and penetration depth [54]. Contrast agents (CAs) are injected into patients to increase the resolution and quality of MRI images [55]. However, CAs have demonstrated stability problems, toxicity, and mild

allergic-like reactions [56]. Therefore, magnetic NPs have been proposed as contrast agents for MRI as an alternative to conventional contrast agents [57]. SPIONs are the most intensively investigated due to their ability to be incorporated into iron metabolism (giving them greater biocompatibility), manipulation by remote magnetic fields, their superparamagnetism that induces high relaxivity (related to higher image contrast), and also the possibility of functionalizing the surfaces with specific molecules (as antibodies, folic acid and peptides) for accurate molecular imaging [58,59]. In addition to *in vivo* diagnosis resulting from imaging techniques, magnetic NPs can also be used for *in vitro* diagnosis. Some techniques include microfluidic magnetic separation of biomolecules [60-62] and the development of biosensors for detecting specific cancer biomarkers or inflammation biomarkers [63-65]. Magnetic NPs also offer the possibility to separate and concentrate specific biological entities from a collected sample. The first step is modifying the NPs' surface with biocompatible molecules (such as polyvinyl alcohol (PVA) or dextran) to increase their colloidal stability [66], with antibodies [67-69], or other macromolecules (such as folic acid or hormones) [70,71]. After adding the functionalized magnetic particles with the corresponding solution, it passes through a magnetic field gradient that immobilizes the NPs with attached specific biological entities of interest [72].

The application of magnetic particles in the treatment area is based on two premises of optimization: reducing the systemic distribution of drugs and their side effects in non-target tissues; reducing the necessary dose to be administered by making it more therapeutically efficient and localized. Magnetically targeted therapies can be used for gene therapies, drug delivery, magnetothermal heating, and as a catalyst for cancer therapies [53].

In magnetic gene and drug delivery, the functional mechanism starts with the functionalization of NPs with a protective coating (for instance, natural polymers, synthetic organic polymers, silica, or gold) that allows the binding of an organic linker (for example, carboxylic acid, amine, and aldehyde thiol) that creates solid binding interactions with the agents of therapeutic interest and also to induce their controlled release in specific microenvironments [73]. The ability to magnetically manipulate NPs with an external high-gradient magnetic field allows the concentration of the NPs (and the molecules attached) at the target site within the body. To address therapy needs, ideally, magnetic gene and drug delivery systems must meet specific criteria, such as [74]: (i) high biocompatibility and biodegradability; (ii) minimal toxicity and antigenicity; (iii) nanosized to allow their perfusion at the capillary level; (iv) ability to carry a wide range of molecules; (v) adequate magnetic responsiveness; and (vi) ability to be designed as a function of specific release triggers.

Clinical applications presupposes the injection of NPs into the bloodstream (either by intravenous or intra-arterial injection, preferably close to the target site), which are guided and concentrated at the therapeutic site under the action of external high-gradient magnetic fields (**Figure 1.3**) [75].

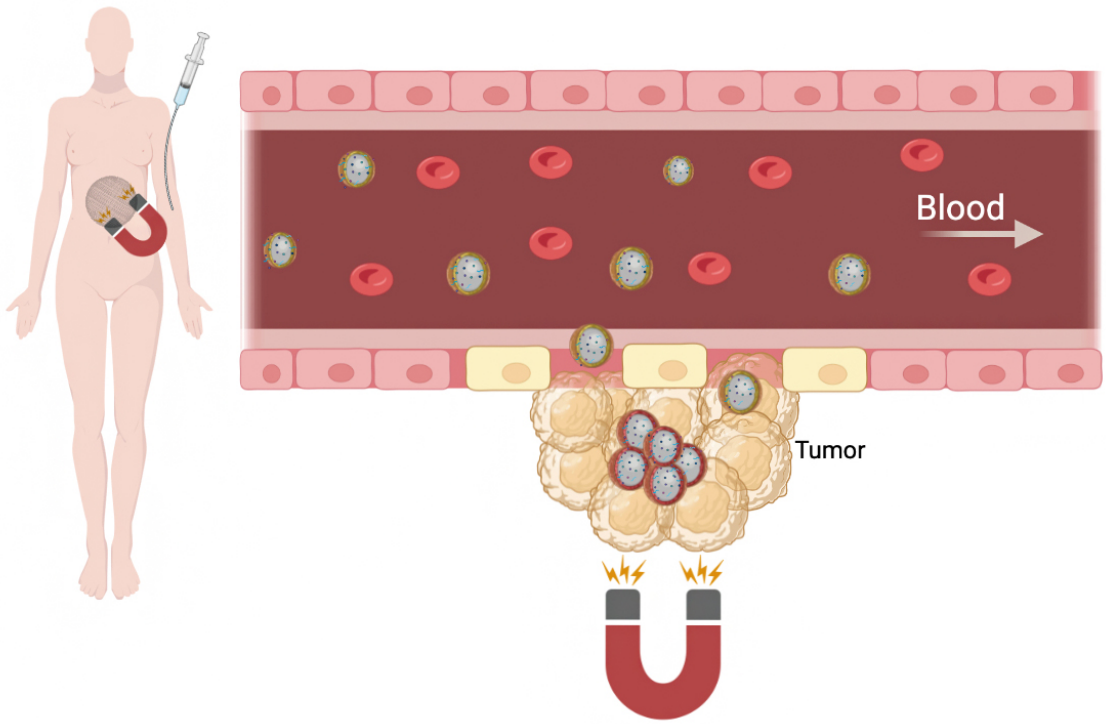


Figure 1.3 Schematic representation of magnetic drug and gene delivery. The conjugated NPs (linked to the therapeutic agent or genes) are injected into the bloodstream near the target site. Simultaneously, magnetic fields force the NPs to extravasate to the target site (tumours).

The charge is selectively released by different mechanisms, such as changes in physiological conditions (variations in osmolality, temperature, pH) or via enzymatic activity [76]. Magnetic NPs, like liposomes, play a leading role in biomedicine's greatest ambition: controlled and targeted delivery. The successive validation of both systems inevitably resulted in an interest in their combination into a single system with combined functionalities.

1.2.3. Magnetic liposomes

Hybrid lipid-nanoparticle complexes (HLNCs) are the general term used to describe lipid-nanoparticle conjugates. The conjugation of inorganic NPs with liposomes results in the formation of magnetoliposomes. Depending on the location of the NPs in the lipid structure, magnetoliposomes can be categorized into (A) aqueous magnetoliposomes (AMLs), when NPs are dispersed in the aqueous pool

of liposomes; (B) solid magnetoliposomes (SMLs), when a single particle or a cluster of particles is coated with a lipid membrane, without internal aqueous component; (C) liposomes with bilayer-embedded NPs; and (D) liposomes with surface-bound NPs (**Figure 1.4**).

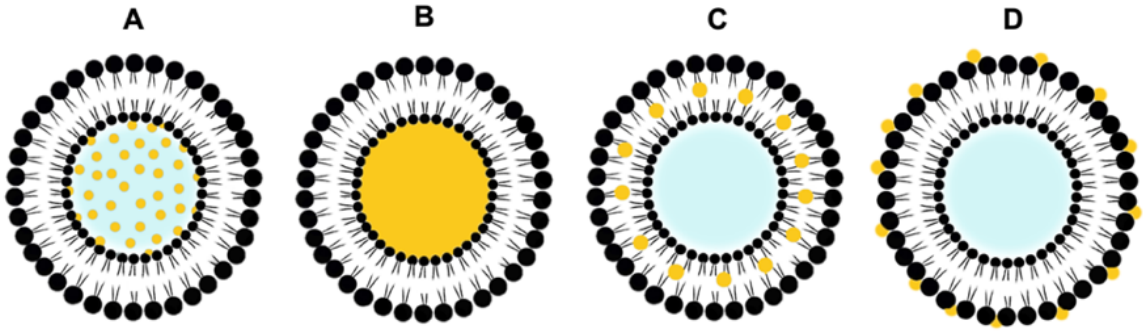


Figure 1.4 Schematic representation of (A) AMLs, (B) SMLs, (C) liposomes with bilayer-embedded NPs, and (D) liposomes with surface-bound NPs.

Since magnetoliposomes were first described by Margolis *et al.* [77] and De Cuyper and Joniau [78], the proposal has been to bring multifunctional combined properties of the two systems. The premise of using magnetoliposomes as controlled delivery strategies is based on the cargo-controlled delivery and release from liposomes under magnetic stimuli. The magnetophoretic mobility of magnetoliposomes adds to conventional liposomes the functionality of directing the cargo to a target area when a magnetic gradient is applied. On the other hand, by applying an alternating magnetic field (AMF), thermally activated processes are induced, which are associated with the controlled release of the encapsulated cargo, either by increasing the permeability or altering the lipid's diffusiveness bilayer. The possibility of choosing the lipid composition of bilayers over an extensive range of lipids with different functional characteristics allows for the applicability of magnetoliposomes for several biomedical applications and offers them additional targeting and controlled delivery strategies. **Table 1.1** summarizes the different types of magnetoliposomes designed and adjusted to specific features developed recently, which will be discussed in the following sections.

Table 1.1 Summary of magnetoliposomes types, lipid compositions, nanoparticles, encapsulated compounds, and triggers used to the aimed biomedical applications.

Magnetoliposomes type	Lipid composition	Nanoparticles	Encapsulated compound	Trigger	Aimed biomedical application	Ref.
AMLs	DPPC:Chol = 5:1 DPPC:DSPC:Chol = 10:5:3	Dextran-modified SPIONs (Resovist)	Carboxylfluorescein	AMF	Cancer therapy (not specified)	[79]
AMLs	DOPC	Citrate-modified SPIONs	Carboxyfluorescein	AMF	Cancer therapy (not specified)	[80]
Liposomes with bilayer-embedded nanoparticles	Soya bean Phosphatidyl Choline (PC)	SPIONs	Erythromycin	AMF	Bacterial infections	[81]
Liposomes with bilayer-embedded nanoparticles	DPPC POPC DSPC MPPC	Oleic acid-coated SPIONs	Calcein	AMF	Not specified	[82]
Liposomes with surface-bound nanoparticles Liposomes with bilayer-embedded nanoparticles AMLs	DPPC	DMSA[1]-coated SPIONs Oleic acid-coated SPIONs APS[2]-coated SPIONs	Doxorubicin	AMF	Cervical cancer and triple-negative breast cancer	[83]

AMLs	PC:chol: carboxymethyl dextran= 55:40:0 .5	Citrate-coated SPIONs	Doxorubicin	LF-AMF	Human neuroblastoma	[84]
SMLs	DPPC : Chol = 4 : 1	Oil-soluble SPIONs	Doxorubicin	NIR	human breast cancer	[85]
AMLs	DPPC:Chol:DSPE-PEG2000 = 80:20:5	Gold-coated SPIONs	Doxorubicin	NIR	breast cancer	[80]
SMLs	DOPG	Nickel Ferrite/Gold Core/Shell Nanoparticles Nickel Ferrite Nanoparticles Decorated with Gold	Not specified	NIR	Cancer therapy (not specified)	[86]
AMLs	DPPC/DDAB/CH	Citric-Acid-Coated SPIONs	Not specified	AMF NIR AMF-NIR	Glioblastoma	[87]
Methotrexate-functionalized Liposomes with bilayer-embedded nanoparticles	DPPC:Chol:SA:DSPE-MPEG2000:DSPE-PEG2000-MTX=67:17:13:1:2	Oleic acid-coated SPIONs	Doxorubicin	AMF-NIR and folate receptors	Human Cervical Carcinoma	[88]

Immuno (anti-LIBS)-AMLs	POPC:DPPC:Chol:m-PEG_{2000}DPPE	SPIONs	Not specified	GPIIb/IIIa receptor of platelets	Targeting Atherothrombosis	[89]
RGD-functionalized AMLs	DMPC:DMPG=9:1	SPIONs	Not specified	αvβ3 integrin	Targeting tumour cells and neovascularization	[90]
Cetuximab-functionalized	DPPC:MPPC: DSPE-mPEG-2000	Acid-coated SPIONs	Doxorubicin	NIR and EGFR	Breast Cancer	[91]
Glucose-functionalized Liposomes with bilayer-embedded nanoparticles	DPPC:L:CHOL=4:4:1	SPIONs	Fluorescein	AMF and glucose receptor (GLUTs)	Cancer therapy (not specified)	[92]
Transferrin-functionalized AMLs	EPC:Chol: mPEG2000-DSPE= 7:2:0.5	SPION	Not specified	Magnetic force and transferrin receptor	Blood-brain barrier transmigration	[93]
Cetuximab-functionalized AMLs	DPPC:Chol: DSPE-PEG2000-NH_2=90:5:5	citric acid-coated SPIONs	Camptosar (CPT-11)	AMF and EGFR	Brain tumour	[94]

1.2.4. Stimuli strategies for enhanced drug release

1.2.4.1. Alternating magnetic field-triggered release

The idea of using thermosensitive liposomes for controlled drug release under a tolerable local–regional hyperthermia (41–46 °C) dates to the '70s [44]. The premise of these systems is based on the lipids that undergo a solid-to-fluid phase transition at those temperatures, leading to enhanced permeability of membranes and controlled release of drugs. However, these systems preclude sustained drug delivery as its cargo is released in a single burst. The ability of magnetic nanoparticles to produce heat when subjected to appropriate AMF, whether by hysteresis losses or from Néel or Brownian relaxation processes, is named magnetic hyperthermia and makes magnetoliposomes excellent candidates for temperature-induced controlled release.

AMLs were the first developed magnetoliposome type [78]. Encapsulating inorganic nanoparticles in the aqueous core of liposomes gives the advantage of non-invasively stimulating the release of therapeutic molecules by AMF trigger. In addition, by spatially restricting the presence of nanoparticles in the lumen of liposomes, the heating source occurs within the liposome itself, which is another advantage over the strategy of using hyperthermia to induce the temperature phase transition in conventional thermosensitive liposomes. Tai *et al.* [79] monitored the release of carboxyfluorescein (CF) from AMLs loaded with dextran-coated iron oxide nanoparticles (Resovist®) with and without the stimulus from an AMF. 1,2-dipalmitoyl-sn-glycero-3-phosphocholine/distearoylphosphatidylcholine (DPPC/DSPC)-based AMLs containing 14 mg Fe/ml (transmission electron microscopy (TEM) representation in **Figure 1.5 A**) demonstrated significant CF release at 32 °C when subjected to an AMF, compared to the leaky temperature window (36 °C – 38 °C) of non-exposed nanosystems. It was also verified that the release profile depends on the encapsulated iron content, as the nanosystems containing 7 mg Fe/ml have been shown to induce release at 34 °C instead. The controlled release of CF was also proven after the injection of lipid systems in anaesthetized rats, which allowed us to conclude the suitability of these systems to controlled compounds released in living systems.

More recently, Bi and Han [80] studied the AMF thermal activation of citrate-modified magnetic nanoparticles encapsulated in dioleoylphosphatidylcholine (DOPC) AMLs, aiming for their use as safe drug delivery and stimulus-induced cancer treatment. Release profiles of CF from AMLs were recorded by fluorescence microscopy. **Figure 1.5 B** (where the green core corresponds to the CF solution while the red ring corresponds to the DOPC membrane) shows an evident release dependence on the AMF activation (2 kHz, 20 mT). The authors also studied how the AMF parameters (magnetic field frequency,

trigger time, and MNPs concentration) influence the release and concluded the proportional effect of these parameters on CF release.

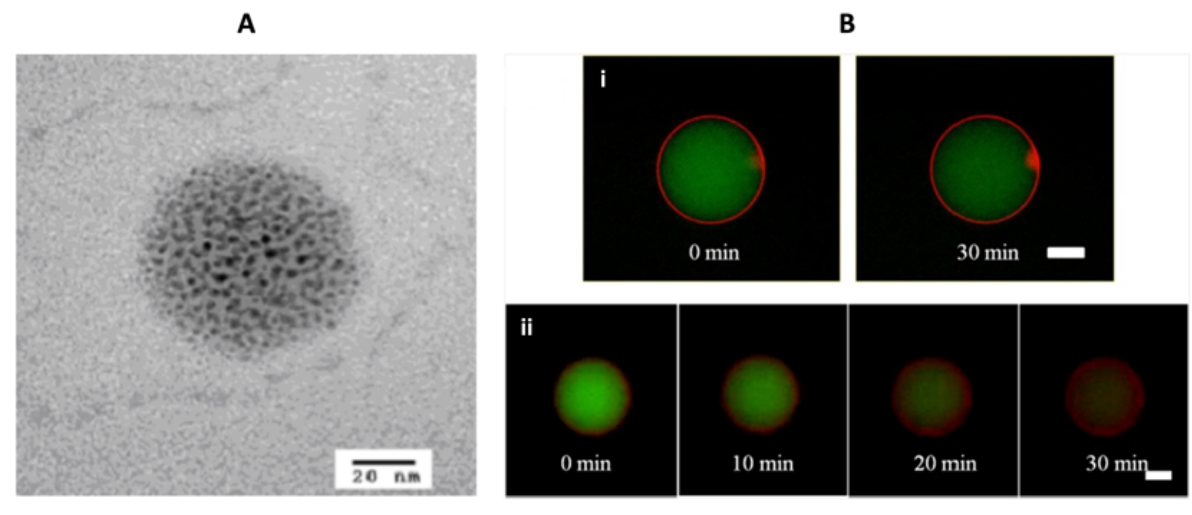


Figure 1.5 (A) TEM of a single DPPC/DSPC-based AML containing 14 mg Fe/ml of Resovist, and (B) Fluorescence images of DOPC-loaded (red) magnetoliposomes loaded with CF (green), as a function of time, (i) without and (ii) with the action of an AMF (2 kHz, 20 mT). Adapted from [79]-

Dong and coworkers [95] demonstrated that when applying an AMF, the local temperature around the magnetically heated nanoparticles, because of the Néel relaxation, is significantly higher than the bulk temperature. This fact supports the idea of placing nanoparticles in the lipid bilayer since the lipids near each SPION reach higher temperatures than the surrounding bulk. Furthermore, the enhanced membrane permeability can induce local triggered release when applying an AMF while stopping it upon removing the AMF. Salah *et al.* [81] developed erythromycin-loaded liposomes based on soybean phosphatidylcholine (SoyPC) with bilayer-embedded Fe_3O_4 nanoparticles as potential candidates to address antibiotic resistance. In the erythromycin-controlled release, they studied the influence of exposing magnetoliposomes over 30 min to 5 and 15 mT AMF at 100 kHz. The results revealed a substantially greater release of erythromycin from the systems when subjected to an external magnetic field. The mechanical forces exerted by the particles on the lipid bilayer ensure a controlled release of the antibiotic without causing the rupture of the lipid structure. Shaghasemi *et al.* [82] studied the same type of magnetoliposomes based on different phosphocholine lipids with varying chain lengths. Thus, they correlated the T_m of the magnetoliposomes and the susceptibility to thermally induce a local phase separation and increase the local permeability of the magnetoliposomes. They demonstrated that DPPC

(DPPC, T_m=41 °C) liposomes containing 4 wt% SPION released calcein whenever an AMF pulse was applied while that release was interrupted in the interval between pulses. However, in palmitoyloleoylphosphatidylcholine (POPC, T_m=−2 °C) magnetoliposomes in the liquid phase at room temperature, there was no calcein release (neither passive nor triggered). These results thus prove that the application of an AMF causes a distortion or local heating that leads to local phase separation at the T_m of the liposome membrane.

Recently, Brollo *et al.* [83] developed a strategy for synthesizing the different types of DPPC magnetoliposomes by controlling the nanoparticles' coating and studying the effect of nanoparticle spatial distribution on liposomes (membrane integrity, magnetic response, heating, and colloidal properties). The characterization results revealed that liposomes with dimercaptosuccinic acid (DMSA)-coated nanoparticles (negatively charged) attached outside (**Figure 1.6 A**) showed better stability and heating properties compared to their counterparts. DOX was encapsulated in these systems, and the ability to induce the controlled release of DOX by AMF was studied in MDA-MB-231 cell viability assays (cell line used in *in vitro* models of triple-negative breast cancer). It was found that after applying an AMF in the configuration of 202 kHz and 30 mT for 1 h, only magnetoliposomes loaded with DOX were found to induce cell death, which is qualitatively visible in images captured by confocal laser scanning microscopy in **Figure 1.6 B**, where live cells appear in green. **Figure 1.6 C** summarizes the normalized survival after 24 h of exposure to different treatments, with a cell survival of 17% after the application of AMF in DOX-loaded magnetoliposomes, which corresponds to a 70% reduction compared to non-exposed. AMF, as an external trigger, has gained value in the controlled release of therapeutic compounds from magnetoliposomes. In fact, magnetic hyperthermia-triggering is the most commonly used approach for controlled release.

However, the hyperthermic effect is unsuitable when leading with highly perfused organs or brain tissues [96]. Therefore, Guo *et al.* [84] developed carboxymethyl dextran (CMD)-coated magnetoliposomes as a non-hyperthermic DOX release and diagnostic strategy for brain cancers under low-frequency AMF (LF-AMF). The exposure of magnetoliposomes to a 45 mT-LF-AMF for 30 min led to a 74% DOX release (at pH 5), highly contrasting to the 35% released in the absence of the LF-AMF in the same conditions. Therefore, optimizing the requirements for this trigger is especially desired because it allows a non-invasive and controlled release (in time and space) while combining a synergistic effect of different therapies (e.g., magnetic hyperthermia with chemotherapy). Furthermore, in theory, this would reduce the systemic effects of the treatment and respective advantages of localized therapy (e.g., reducing resistance to antibiotics and chemotherapeutic drugs).

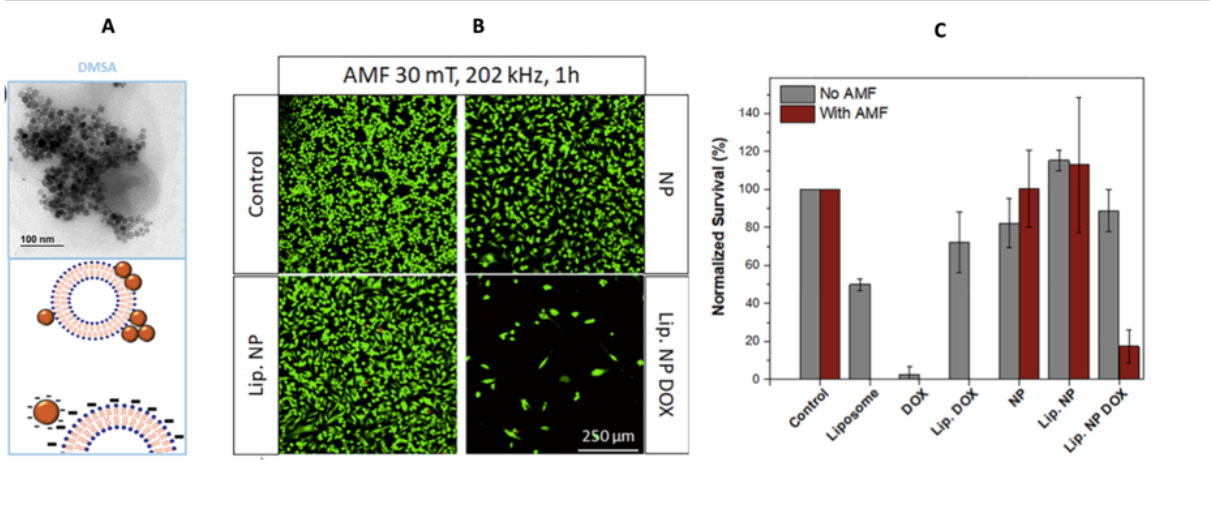


Figure 1.6 (A) TEM image of liposomes with surface-bound DMSA-coated nanoparticles and its schematic representation. (B) Representative confocal laser scanning microscopy images. (C) normalized survival after 24 h of MDA-MB-231 cells after exposure to different treatments (without (grey) and with the action of an AMF of 202 kHz and 30 mT for 1 h (red)). Adapted from [83].

1.2.4.2. Near-infrared-triggered release

NIR light (700–1000 nm) is another alternative to induce heat generation in nanoparticles with optical absorption in the NIR regions. Light-absorbing nanoparticles – called photothermal agents – transform the energy from a laser into heat in a process known as photothermal therapy [97]. The last few years have been extensively focused on developing or exploiting nanomaterials with strong optical absorption in the NIR region to address the limited optical penetration and the possible damage caused by laser illumination to healthy tissues. Some examples include, for instance, graphene nanocomposites [98], plasmonic-based nanorods [99], nanoshells [100] or nanostars [101]. Beyond an optimal and selective absorption region, photothermal agents should also present low toxicity and high solubility in biocompatible solutions and allow their functionalization [102], which is often incompatible with commonly used plasmonic gold nanoparticles or carbon-based materials. Iron oxide nanoparticles, particularly Fe_3O_4 [103,104], have been identified as the preferred photothermal agents due not only to their absorption in the NIR region but also to their biodegradability, easy clearance and biotransformation in the body [105]. Recently, Shen *et al.* [85] developed Fe_3O_4-loaded thermosensitive liposomes (Fe_3O_4–TSL) for NIR-laser-triggered DOX release and combined therapy. For that, oil-soluble Fe_3O_4 nanoparticles were coated with DPPC/Ch (4:1) lipid formulation, and DOX was loaded to the aqueous compartment by an ammonium sulfate gradient **(Figure 1.7 A)**. The NIR laser at a power density of 2 W/cm^2 for 5

min induced a total cumulative release of 41.6% at 12 h, while the samples irradiated twice (0 h and 6 h) were 66.7%. On the other hand, in the control sample (non-irradiated), only 10% of the drug was released simultaneously. These *in vitro* results were corroborated in tumour growth inhibition tests performed in rats. Only the DOX–Fe_3O_4–TSL+ NIR group induced a near disappearance of the tumour after a 12 day treatment (**Figure 1.7 B**), demonstrating a dual effect of photothermal chemotherapy in cancer treatment [85].

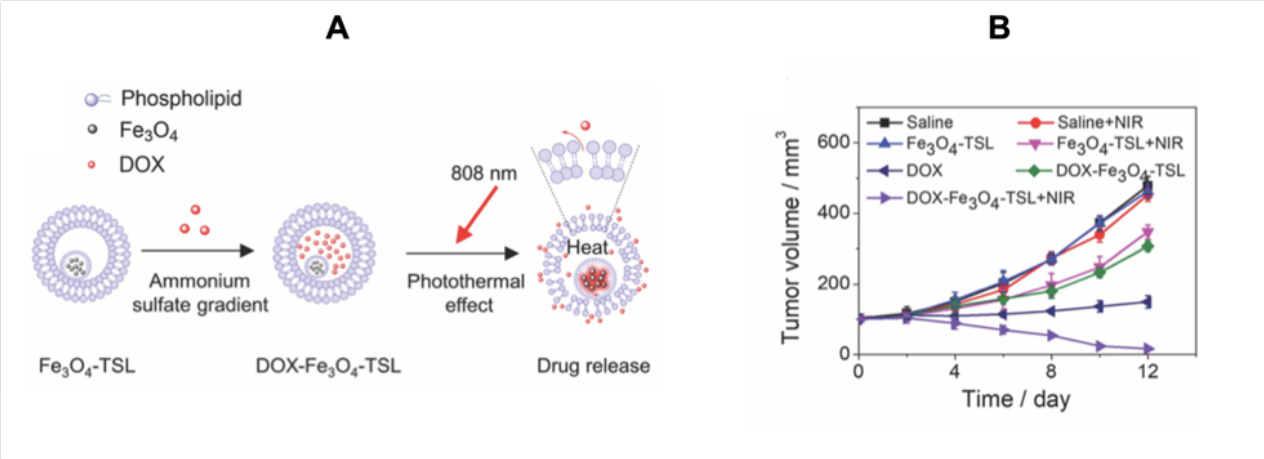


Figure 1.7 (A) Schematic representation of DOX- Fe_3O_4–TSL synthesis and respective NIR-triggered DOX release. (B) *In vivo* anti-tumour efficacy, as tumour volume changes, in different treatment groups. Adapted from [85].

So far, this type of trigger is most frequently used in liposomes coupled with plasmonic nanoparticles (usually gold-based nanoparticles), so they are no longer classified as magnetoliposomes. However, efforts have been made to develop nanoparticles that combine the plasmonic and magnetic modalities to combine magnetic hyperthermia and photothermal therapy in "all-in-one" nanoparticles [106].

This combined therapy may address some of the difficulties in magnetocaloric therapy (such as low heating efficiency), potentially facilitating its clinical translation. The systems that combine this type of nanoparticles with liposomes are called plasmonic magnetoliposomes or magnetoplasmonic liposomes and are relatively new in the magnetoliposomes state-of-art. Khosroshahi *et al.* [107] described DOX-loaded magnetoplasmonic thermosensitive liposomes (MPTL-DOX) and demonstrated the combined effect of magnetic drug targeting and laser hyperthermia-triggered drug release. The proposed system encloses polyvinyl pyrrolidone (PVP) stabilized magnetite/gold nanoshells in DPPC:chol:1,2-distearoyl-sn-glycero-3-phosphoethanolamine-N-[amino(polyethylene glycol)-2000] (DSPE-PEG2000) (80:20:5). The results revealed enhanced cell apoptosis of MCF-7 breast cancer cells induced by the synergistic

effect of chemotherapy and laser-mediated hyperthermia (at 350 mW for 5 min). Rodrigues *et al.* [108] developed manganese nanoparticles coated with gold ($MnFe_2O_4$/Au core/shell nanoparticles) to synthesize AMLs and SMLs, validating the potential use of both nanosystems for combined cancer therapy. This work was followed by Rio *et al.* [86], which developed nickel ferrite magnetic nanoparticles decorated with plasmonic gold nanoparticles and core/shell nanostructures (with a nickel ferrite core and a gold shell). The bimodal magneto-photothermal effect has proven to amplify heat generation compared to the single-mode magnetic hyperthermia or photothermia modalities. Cationic magnetoliposomes enclosing citric-acid-coated iron oxide magnetic nanoparticles demonstrated a synergy for dual therapy of human glioblastoma [87]. The action of AMF combined with NIR (at 4.5 mg/mL of magnetoliposomes) induced a reduction in cell viability of human glioblastoma U87 cells by 82%, compared to the reduction of 32-35% of single-mode treatments.

1.2.5. Magnetoliposomes for ligand-mediated active targeted and combined therapy

Magnetoliposomes, as multifunctional nanosystems, increase the bioavailability of drugs, enhance their local accumulation (either by magnetic action or passive targeting) and induce a controlled release through external stimuli. Drug delivery strategies have evolved towards precision nanomedicine, which seeks to control the release of the drug in quantity, time, and space. Surface modification of liposomes with various targeting ligands (e.g., aptamers, antibodies, peptides) has been validated to achieve more efficient targeting, improve systems endocytosis and improve the general therapeutic response [109]. These advances have been applied to develop more functional magnetoliposomes with enhanced precise targeting. The use of functionalized magnetoliposomes as a strategy for precise targeting of certain types of cells is predominant in research and development in the cancer field. This fact is due not only to the ambition in this area but also to the functional application of the knowledge generated over the years in molecular genetics.

Folate-mediated receptor targeting is one of the most promising targeting strategies for drug delivery due to the overexpression of folate receptors on the surface of several cancer types of cells. Methotrexate (MTX) is an antifolate therapeutic agent that targets folate receptors and acts as an anticancer drug [110]. As a result, Guo and coworkers [88] proposed thermosensitive magnetoliposomes functionalized with MTX (MTX-magnetoliposomes) for light/magnetic hyperthermia triggered for precise cervical cancer therapy. The targeting capabilities of the magnetoliposomes were evaluated in cervical cancer HeLa tumour-bearing nude mice using NIR optical imaging technique. The authors demonstrated a much

higher accumulation of MTX-magnetoliposomes in tumours when applying a constant magnetic field than biodistribution in other organs.

Furthermore, biodistribution assays demonstrated a much higher accumulation of magnetoliposomes in the tumour under the action of a local constant magnetic field (CMF), which revealed the importance of magnetic-biological dual targeting. These results were corroborated by the *in vivo* anti-tumour activity studies. Furthermore, these studies also demonstrated the importance of the dual effect of AMF with NIR laser irradiation, revealing greater tumour inhibition efficiency when both stimuli were applied simultaneously [88]. Furthermore, the functionalization of magnetoliposomes with alpha-fetoprotein (AFP) antibodies also demonstrated the importance and validity of dual-targeting (magnetic targeting and antibody targeting) for high specificity for early liver cancer diagnosis [111]. Also, the potential of immuno-magnetoliposomes is being studied to detect platelets involved in atherosclerotic plaque rupture and thrombosis [89].

Integrins are a molecular family involved in tumour angiogenesis, and signalling blockade has been demonstrated to be efficient in inhibiting tumour growth, angiogenesis, and metastasis. Due to the overexpression of $\alpha_v\beta_3$ integrin on tumour neovascularization, the functionalization of anionic magnetoliposomes, the cyclic arginine-glycine-aspartate (cRGD), was proposed to target the $\alpha_v\beta_3$ integrin [90]. Dorjsuren *et al.* [91] developed DOX-loaded thermosensitive magnetoliposomes functionalized with cetuximab (CET), a monoclonal antibody against the epidermal growth factor receptor (EGFR). In this work, the authors corroborated the selective binding of functionalized magnetoliposomes in cells with overexpression of EGFR. They also demonstrated the synergistic effect between chemotherapy and photothermia by reducing breast cancer cell viability when the treatment was combined with hyperthermia induced by NIR laser irradiation. Recently, glucose-modified liposomes loaded with Fe_3O_4 nanoparticles also demonstrated potential for cancer cell-targeting and controlled release under the action of an AMF [92].

The efficient transport of drugs to the brain is an application that can highly benefit from the action of an external magnetic field in combination with functionalized magnetoliposomes. For example, Ding *et al.* [93] demonstrated the synergistic effect of transferrin receptor-mediated transportation with magnetic activity on the transmigration of magnetoliposomes across the blood-brain barrier (BBB), which is resistant to the passage of various drugs. In turn, Lu *et al.* [94] demonstrated the ability of surface-conjugated AMLs with CET in the enhanced recognition of EGFR receptors and intracellular uptake of the human primary glioblastoma cells (U87). In addition, the citric acid-coated magnetic Fe_3O_4 encapsulated

in the aqueous lumen of thermosensitive nanosystems induced the controlled release of the drug camptosar (CPT-11) and enhanced cytotoxicity in human glioblastoma U87 cells [94].

1.2.6. Final Remarks

The importance of liposomes is already clinically proven, and their role in current medicine is indisputable. Even so, its application potential continues on an upward curve due to accumulated knowledge, the development of new materials, and the combined functionalities of those materials. Therefore, the combination of inorganic nanoparticles and liposomes or magnetoliposomes could be the next extension of their use in numerous biomedical applications. Undoubtedly, magnetoliposomes have proven to be good controlled drug delivery systems and add dual and synergistic therapies to their conventional counterparts.

The promising results obtained in *in vitro* and even *in vivo* assays have aroused the interest of more researchers from different specialized areas. The multidisciplinarity involved in the development of magnetoliposomes (such as physics, biology, materials engineering, chemistry, and pharmacology) makes it demanding to reach a fully integrated knowledge, but, on the other hand, it allows the scientific community to overlap areas of knowledge and even create new ones (e.g., biophysics). In conclusion, the miscibility of scientific concepts could be fundamental in the efficient clinical translation of magnetoliposomes as a new smart material for controlled and precise drug release.

1.3. Cell culture platforms for *in vitro* nanodrug delivery systems development and screening

Microfluidics is the term used to describe the science and technology that deals with the fabrication of miniaturized devices and the manipulation of fluids (10^{-9}-10^{-18} L) confined in channels with dimensions in the micrometre range [112]. The embrace of microfluidics technology, as it is recognized today, was introduced in 1990 [113] by the term "Miniaturized Total Chemical Analysis Systems" – μTAS – which defines a single device that comprises multiple laboratory steps. The basic concept of μTAS is based on the transformation of (bio)chemical information (such as the activity of particles and chemical concentrations) into electronic data in a fully automated system with the size of a chip [113]. The cumulative comprehension of the behaviour and control of fluid flow at the microscale allowed the rapid advancement of this area [114]. As a result, the state-of-the-art integrates several reviews articles that explore concepts such as the fluidic behaviour in a variety of devices [115], the physics behind the fluid

phenomena [116], the fundamental kinematics of microparticles inside microchannels [117], and the small-scale mixing [118], among others.

Furthermore, the versatility of microfluidic devices in integrating multiple components (e.g., micropumps, mixers, separation columns, reactors) [119] and their combination with existing macrodevices makes them excellent for high parallelization [120]. The knowledge consolidation combined with the technology's stated potential has allowed extending their applicability to several fields [121]. As a result, microfluidics is currently implemented in the analysis of residual antibiotics in food [122], production of monodisperse emulsions in cosmetics [123,124], fertility testing [125,126], monitoring of blood glucose [127] and onsite environmental detection [128], as representative examples. Among the different application possibilities, healthcare is one of the fields that can take the most advantage of microfluidics in the entire spectrum of research, development, diagnosis, and therapeutics. Several diseases' societal and economic impact requires accelerating the clinical translation of nanomedicines and drugs in a research and development line that allows a more precise, faster, and accurate discovery and evaluation. In this aspect, microfluidics can be highly beneficial for the initial drug discovery stage, especially for production and screening using cell-based platforms.

The establishment of *in vitro* cell culture [129,130] is still one of the breakthroughs of the 20th century. Conventional 2D cell culture is a laboratory approach in pharmaceutical research and fills the knowledge gap between biochemical assays and animal model testing [131]. Although 2D cell culture is an informative and relevant approach, the microenvironment in the conventional cell culture plates distances itself from physiological conditions, making this method simplistic in describing the biological complexity [132]. Additionally, testing in animal models raises ethical and monetary questions [133]. As a result, 3D cell culture has asserted its importance in cell biology research, providing a platform that ensures an enhanced simulation of the *in vivo* microenvironment and its complex interactions [16].

Although the advantages of conventional 2D and 3D cell culture in pharmaceutical research should not be overlooked, they face challenges that lead to misleading information resulting in inconsistent *in vivo* responses [131]. Thus, the window of opportunities and accuracy of cell culture methods (2D and 3D) can be widened through their convergence with microfluidics platforms (**Figure 1.8**). The use of microfluidic-based 2D and 3D cell culture systems that better mimic *in vivo* microenvironment and the dynamic fluid flow conditions enable access to mechanisms and physical phenomena that, otherwise, would become unnoticed.

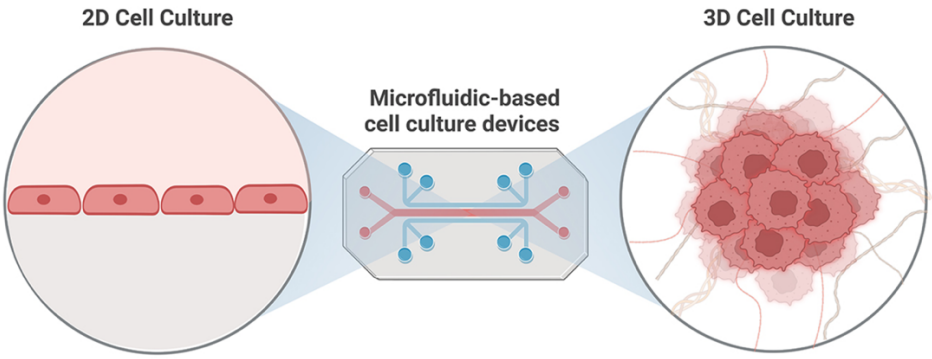


Figure 1.8 Schematic representation of microfluidic-based devices as platforms for 2D and 3D cell culture.

The reproducible and quicker screening of drugs at an early stage of development can actively contribute to reducing the late-stage failure risk while reducing animal experimentation [134]. The accurate validation of the potential of new medicines can thus be supported by understanding how the microenvironments created on microfluidic platforms influence cellular behaviour and functions and how those microenvironments can be adjusted for better *in vitro* control. As a result, relevant review articles address the technical challenges that limit the widespread accessibility of microfluidics [135], the understanding of molecular and cell biology that can be enhanced by precision microfluidic approaches [136], as well as the role of microfluidics in high-throughput drug screening applications [137]. Furthermore, recent literature explores the application of microfluidic devices in anti-cancer and personalized cancer drug screening [138-141], organoid-based disease models combined with microfluidics [142], as well as the advances in the application of specific types of microfluidic devices in biomedicine, such as single-cell droplet microfluidics [143], and concentration gradient microfluidics [144].

This section addresses the most relevant practical considerations of the topics mentioned above in this context while explicitly highlighting cell culture's essential role in drug screening. It explores the advantages that make 2D and 3D cell culture essential methods in the drug research scenario and the challenges that limit them from being more effective in drug validation. Furthermore, the complementarity of cell culture methods with microfluidic platforms toward a more reliable and simplified drug screening is also explored. For that, this work describes the most relevant physicochemical and operational considerations that miniaturization entails and how this technology represents a suitable approach for *in vitro* control of cells' physiological context.

1.3.1. Life science research and development: an overview of cell culture as a model for drug screening

Healthcare is highly dependent on drug research and development; therefore, it is essential to promote drug innovation on an ongoing basis. The human body is a highly dynamic, multilevel, and complex biological system, hindering the accurate prediction of a drug's entire spectrum of influences and effects. The drug discovery paradigm must be continuously updated due to its social impact. It is also an estimated time and money-consuming process that typically takes over 12 years or longer from the target identification until the market approval [145].

The complex, long and expensive process requires methodical planning, which Mohs and Greig [146] summarized in a list of individual laboratory contributions to drug discovery and development (**Figure 1.9**). It is organized as follows: (i) target identification; (ii) target validation; (iii) finding new molecule; (iv) screening assays; (v) data on drug-like characteristics; (vi) development tools; (vii) efficacy measures; and (viii) technologies to improve the efficiency of trial completion [146]. However, there is no predefined key to success, and it is often necessary to step back in the development line. Actually, in the cancer therapeutics area, the overall success rate for products in clinical development is approximately 10% [147]. Understanding the reasons for the failure requires efficient collaborations between different expertise areas (e.g., toxicology, biology, physics, and chemistry) [148]. This knowledge must be followed by a continuous review (or even renewal) of the production processes, analysis, and quantification techniques.

For over a century, cell cultures have been used to understand *in vivo* cell behaviour and its mechanisms [149]. Cell-based assays are one of the most comprehensive approaches to data-harvest quantitative and physiologically relevant information in drug-screening processes [150,151]. The daily scientific articles evidence this relevance, showing its role in research and development. It is estimated that $135 billion [152] are spent yearly on screening medicines. As an *in vitro* model, the cells used in cell-based assays must accurately represent the system to be studied and express relevant factors and signalling intermediates [151]. Although 2D cell culture methods are the most commonly used cell-based assays, their limitations in mimetically reflecting the 3D cellular organization found *in vivo* have encouraged the scientific community to move towards 3D models. As a result, in the following section, some considerations for using 2D and 3D cell cultures in drug screening are detailed, as well as their respective advantages and challenges.

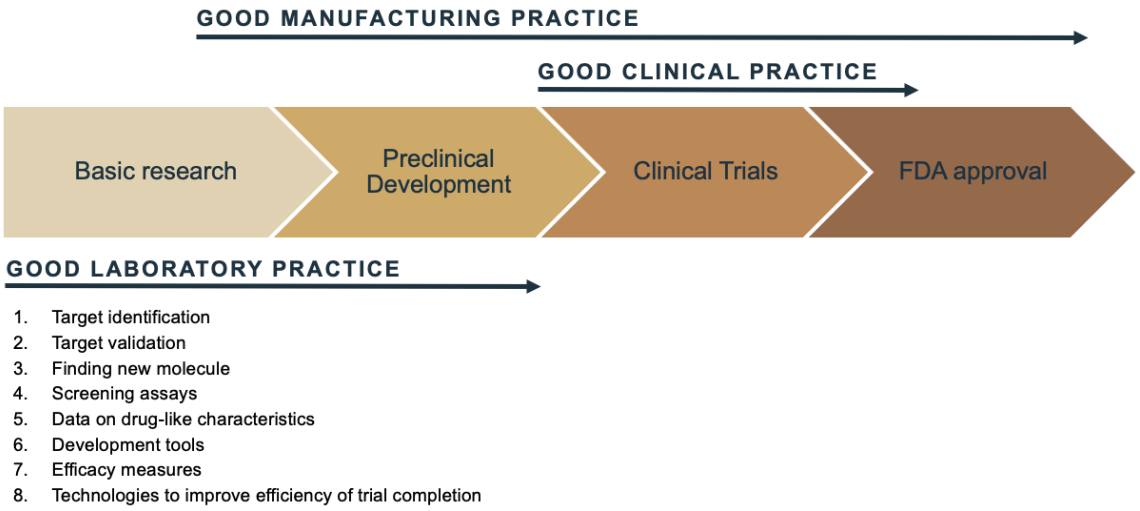


Figure 1.9 Schematic representation of the drug discovery process from basic research (initiated by target identification) to its translation into an FDA-approved product. The arrows represent the quality assurance guides that guarantee the normal development of the process. The "good laboratory practices" are summarized in a list of individual laboratory contributions to drug discovery and development.

1.3.1.1. Two-dimensional cell culture methods

The conventional cell culture is commonly referred to as 2D due to its inherent dependence on adhesion to a planar and rigid surface, which provides mechanical support for anchorage-dependent cells (meaning that cells need to adhere to a solid) in a monolayer. Besides the well-established methods for culturing, expanding, differentiating, and de-differentiating cells, 2D cell culture is also a simple and low-cost maintenance method [153]. Furthermore, this method ensures a homogeneous growth and proliferation of cells since the monolayer cells have uniform access to the components of the medium (such as growth factors and nutrients) [154].

Although it remains the most used *in vitro* study model worldwide, it has been showing significant limitations that compromise the achievement of reliable biomedical information. These limitations are mainly due to monolayer cultures' inability to simulate the *in vivo* microenvironment and the cellular architecture. For example, Weaver *et al.* [155] demonstrated that tissue architecture could regulate the mammary epithelial cells (MECs) sensibility to exogenous apoptotic stimuli. The authors used nonmalignant S-1 cells of MECs and their tumorigenic progeny (T4-2), grown as 2D monolayers on a thin coat of collagen I; and their respective 3D structures embedded in the reconstituted basement membrane (rBM). As a result, nonmalignant cells formed growth-arrested 3D organoids (acini), while malignant MECs continued to proliferate to form nonpolar, multicellular, and disorganized 3D aggregates (**Figure**

1.10 A). One of the trials aimed to test whether the presence of rBM and malignant transformation can modulate the sensitivity of extracellular matrix (ECM) to apoptotic stimuli. For that, the authors measured the apoptotic labelling indices of the cell cultures when treated with different apoptotic agents (**Figure 1.10 B**). The results of apoptotic sensitivity of cell cultures grown as 2D monolayers revealed similar responses in all apoptotic agents. In turn, the nonmalignant MEC acini were the only cell cultures demonstrating apoptosis resistance, while the nonmalignant MEC acini showed no apoptosis resistance after malignant transformation. Furthermore, the ligand-activated β4 integrin induces tissue polarity in mammary epithelial acini and it is involved in apoptosis resistance to several chemical and receptor-linked stimuli [155]. These differences are reflected in profound changes regarding their proliferation, cell-cell connections, cell-matrix connections, migration, survival, adhesion, and differentiation [156,157].

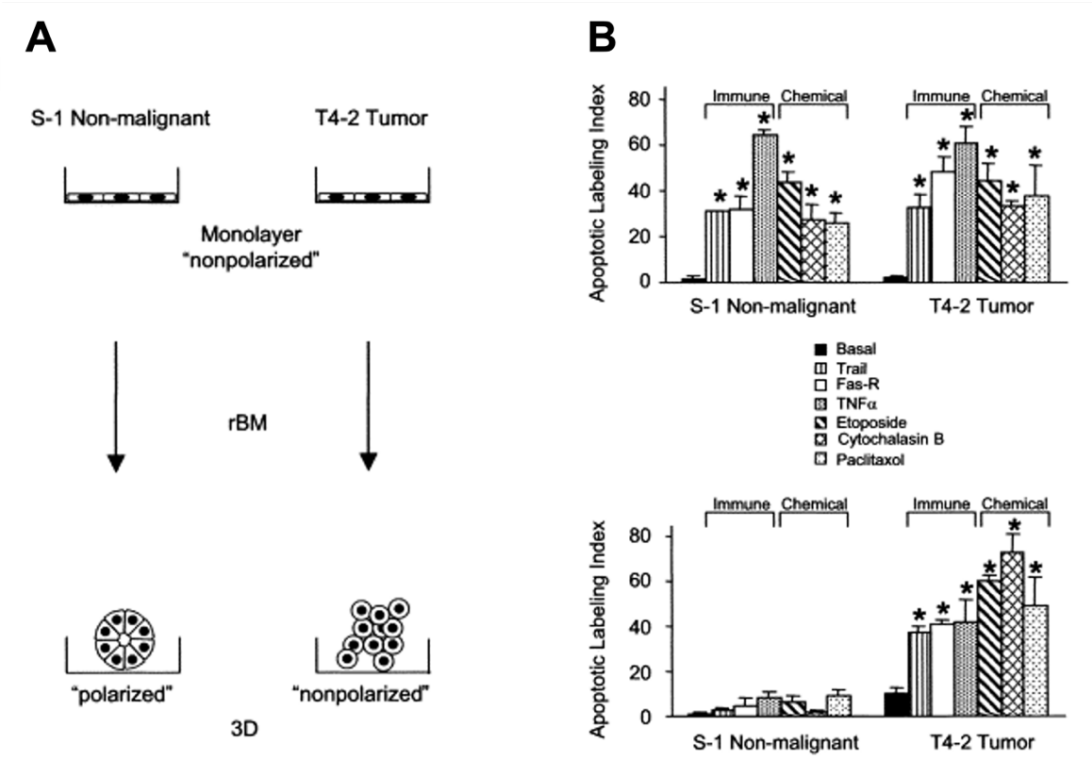


Figure 1.10 (A) Schematic representation of nonmalignant MECs and malignant MECs treated as monolayers on a thin coat of collagen (above) and their 3D structures embedded in rBM; and their respective (B) apoptotic labelling indices treated with Trail peptide (1 μg/ml), anti-FAS mAb (IgM CH-11, 2 μg/ml), TNF-α (100 nM), etoposide (50 μM), cytochalasin B (1 μM), or paclitaxel (120 nM). Results are the mean ± SEM of 3–5 experiments with duplicates or triplicates. Adapted from [155].

Monolayer cultures do not allow the simulation of oxygen or nutrient gradients that occur naturally *in vivo* and highly influence cell behaviour (cell migration, cell signalling, and cell motility) [158]. Furthermore, ECM proteins (composed of around 300 different proteins in mammals) significantly mediate cellular functions [159]. In addition to the ECM, *in vivo* cells are also in contact with stromal cells, which include glial cells (in neuronal tissue), mesenchymal supporting cells (in epithelial tissue), immune system cells, and cells of the surrounding vasculature [157]. Regarding cancer drug research, the extrapolated biomedical information from 2D cell cultures is subject to more inconsistencies due to the inherently complex nature of the tumour microenvironment. It consists of a heterogeneous mixture of tumour and stromal cells that, in turn, include growth factors (GF), macrophages, cytokines, and inflammatory cells [160,161]. Cancer-associated fibroblasts (CAFs) are a component with significant abundance in the tumour stroma [158], presenting highly significant tumour-restraining/promoting roles, such as CAF-mediated therapy resistance and tumour progression (for detailed information, see reference [162]). One of the mechanisms involved in CAF-mediated therapy resistance is the release of cytokines under therapeutic pressure, which activates different signalling cascades in tumour cells. The deoxyribonucleic acid (DNA) damage of CAFs induced by chemotherapeutic drugs has already been shown to trigger a boost of pro-survival pathways in tumour cells. In addition, CAFs support cancer stem cells (CSC) in maintaining stemless features [163,164]. CSCs have a slow-cycling or quiescent state (meaning the cell division process is interrupted), which makes them resistant to chemotherapy drugs which usually target dividing cells [165,166]. As 2D cell cultures cannot review all these contexts, this method is shown to modify their transcriptional regulation, receptor expression, cell invasion [167,168], cell proliferation, apoptosis and anti-apoptosis [169,170].

Some strategies have been used to create models that recapitulate cell behaviour *in vivo* to provide control of cell shape in 2D cell culture. Those techniques include cell-patterning methods, tailoring of substrate stiffness, and sandwich culture. In cell patterning, the conventional homogeneous surface that cells adhere to and grow is replaced by an engineered geometric surface with variable microtopography, allowing control of cells' size and shape [171]. Cell patterning techniques are divided into physical methods [172-175] and biochemical methods [176-179]. These strategies have been used to study fundamental principles of cell biology (such as differentiation, proliferation, and migration) [180,181] and in drug screening [182,183]. In addition, since most tissue cells are anchorage-dependent [184], the stiffness of substrates also influences cell behaviour [185]. Stiffness variation in cell culture has been shown, for instance, to regulate cell behaviour and the resulting chondrogenic fate of human

mesenchymal stem cells (MSC) and cartilage phenotype [186], as well as in the regenerative response of neural stem cells [187].

These strategies are essential in overcoming some of the limitations of conventional 2D cell culture, providing this method with functionalities that bring artificial conditions closer to real ones. However, they are pseudo-3D microenvironments that do not accurately translate the 3D microenvironment and, as such, the complex properties and architecture of *in vivo* tissues. As a result, the scientific community has favoured the development of 3D cell culture methods [19] to improve predictability in drug discovery.

1.3.1.2. Three-dimensional cell culture methods

3D cell culture creates an artificial environment that allows cells to grow and interact with each other and the surrounding space in the three dimensions. As a result, 3D cell culture has increased interest in cell biology research for drug development and screening due to the improved simulations of *in vivo* microenvironment and its complex interactions [19,188,189].

To create accurate *in vivo* spatiotemporal conditions for cell development and the mechanically active microenvironment, several 3D cell culture techniques have been established. Those strategies include 3D non-scaffold-based cellular aggregates, hydrogel-based cell cultures, and insert scaffold-based cellular cultures [19,161,190,191]. Different biodegradable polymers have been explored as supporting matrices (scaffolds) for vascularized tissue engineering, including poly(DL-lactic-co-glycolic acid) (PLGA), poly(glycerol sebacate) (PGS), silk fibroin (SF) and poly(1,3-diamino-2-hydroxypropane-co-polyol sebacate) (APS) [192-195]. Cells can also be encapsulated and immobilized into hydrogels that act as scaffolding materials [196]. Using hydrogels as scaffolding materials allows the encapsulation of cells into the hydrogel while permitting diffusive permeability to oxygen and the mass transport of nutrients to encapsulated cells [196,197]. Native ECM proteins have been employed as hydrogel scaffolding basis, including fibrin, hyaluronic acid (HA), collagen, fibronectin, agarose, Matrigel®, and poly(ethylene glycol) diacrylate (PEGDA) [196]. Gel-free 3D cell culture is another suitable approach to culture cells that proliferate with low ECM ratios and high cell densities, such as multicellular tumour spheroids. Another consideration must be deliberated is that cell morphology highly depends on the culture environment, even among different 3D cell culture techniques. Florcyk and colleagues [198] demonstrated these differences by culturing human prostate cancer (PCa) cells (LNCaP, C4-2, and C4-2B) in 2D, seeded on Matrigel® matrix and 3D porous chitosan–alginate (CA) scaffolds for 15 days (**Figure 1.11**). Cells grown in 2D revealed to form flat layers. In the case of the Matrigel®, samples had a linear and elongated

morphology and created dense, thick cell sheets in some regions. Finally, the CA scaffold samples demonstrated tumour spheroid formation within the scaffold pores.

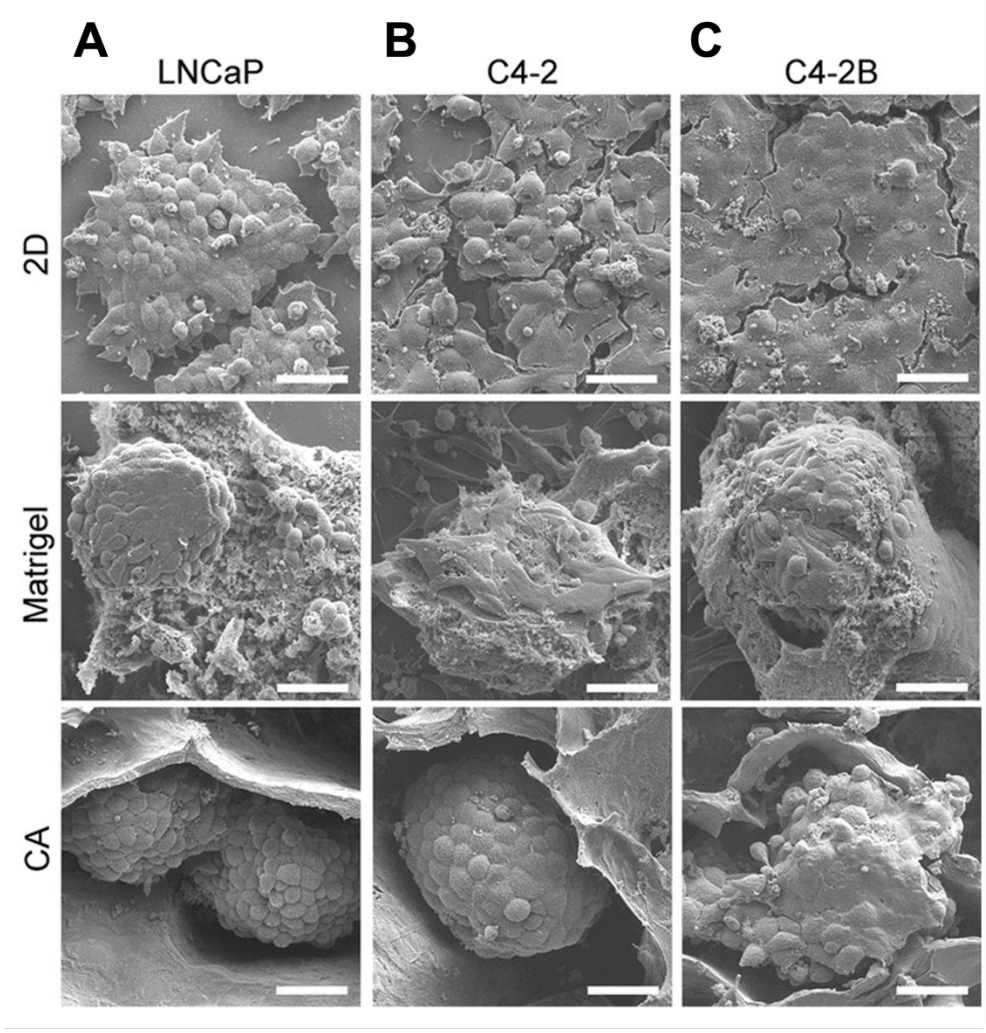


Figure 1.11 SEM images of (A) LNCaP, (B) C4-2, and (C) C4-2B human prostate cancer cells grown on 2D culture plates, Matrigel® matrix, and CA scaffolds (bottom) for 15 days. Scale bars are 40 μm. Reproduced from [198].

ECM's fundamental role in regulating cell-to-cell interactions, cell differentiation and growth [199] requires understanding how its composition and structure influence biological mechanisms, as these influence the therapeutic effects of drugs. Cultured cells in a 3D microenvironment with ECM components were revealed not only to induce the expression of genes not expressed in 2D cultures [200,201], but also to synthesize the ECM components themselves, as happens in *in vivo* regeneration [199,202]. Advances in this area have been followed by the development of biomaterials that better resemble ECM and enhance cell culture efficiency and cellular functions. Some of these biomaterials include hydrogels [203-205], decellularized native tissue [206-208], ultra-low attachment surface [209,210], and solid

scaffolds [205,211]. Thus, 3D cell culture has been used in regenerative medicine [212-214], disease modelling [215-217], and drug screening [218-221].

The access to functional differences of 2D monolayers compared to 3D microenvironments has been carried out, mainly in cancer research. Hickman *et al.* [222] reviewed human cancer models that aim to reproduce the heterogeneity and complexity of human cancer *in situ.* Imamura *et al.* [223] demonstrated that some breast cancer cell lines (namely, BT-549, BT-474, and T-47D) formed dense 3D multicellular spheroids (MCSs), and those spheroids decreased the sensitivity to the chemotherapeutic drugs DOX and paclitaxel when compared to 2D cultured cells. The results revealed that chemoresistance might result from MCSs hypoxia, associated with an increased G_0 phase cell population and/or a downregulation of pro-apoptotic molecules [223]. Recently, similar results were observed in head and neck squamous cell carcinoma (HNSCC) cell lines (namely, LK0902, LK0917, and LK1108), revealing that 3D cultured cells are less sensitive to cisplatin when compared to the 2D counterparts [224]. In the same study, the expression of CSC-associated transcription factors (such as NANOG and SOX2) increased in all the studied cell lines cultured in 3D. No specific pattern was found between epithelial-mesenchymal transition (EMT)-associated protein expression and drug response. Still, the increase in EMT protein expression led to increased migration of tumour cells growing in spheroids [224].

Although this method brings clear advantages concerning conventional methods, there are some challenges and limitations in the widespread use of 3D models. It is pointed to a low reproducibility and an increased difficulty in data interpretation [225]. Despite all the advances, it is a growing area, still lacking an intensive characterization and validation of models for the different pathologies, leaving some biological properties (such as gene expression, growth kinetics, and signalling cascades) with no comprehensive understanding [222]. Some other limitations are related to restricted cell observation and extraction for further analyses, difficulties in obtaining some 3D systems types, and the time and money-consuming process implicated in maintaining the cultures [226]. Furthermore, some 3D culture approaches do not address the static nature of 2D culture since it also requires regular media changes to remove cell wastes and nutrient restoration. These extra steps are associated with an increased risk of experimental errors and sample contamination. **Table 1.2** summarizes the advantages and challenges of 2D and 3D cell culture methods.

Table 1.2 Summary of the advantages and challenges of 2D and 3D cell culture methods.

Cell culture method	Advantages	Challenges
2D	Long-term culture, high reproducibility, simple and easy to interpret	Inability to simulate *the in vivo* microenvironment and the cellular architecture
	Homogeneous growth and proliferation of cells	The morphology of tissues or organs is changed
	Relatively low-cost maintenance	Loss of multiple phenotypes and polarity expression
	Well-established methods with commercially available media	Changes in the proliferation, cell-cell connections, cell-matrix connections, migration, survival, adhesion, and differentiation
	Homogeneous growth and proliferation of cells	Do not allow the simulation of oxygen or nutrient gradients that occur naturally *in vivo*
3D	Improved simulations *of in vivo* microenvironment and its complex interactions	Long-term culture is difficult, with lower reproducibility, and more significant difficulties in interpreting results
	The morphology of tissues or organs is preserved	Still lacking an intensive characterization and validation of models for the different pathologies
	Polarity differences and multiple phenotypes	Money-consuming process and time-consuming
	Accurate *in vivo* spatiotemporal conditions for cell development and the mechanically active microenvironment	Restricted cell observation
	Allow the simulation of oxygen or nutrient gradients that occur naturally *in vivo*	

Notwithstanding the limitations that both 2D and 3D cell cultures offer, their importance as essential laboratory approaches to pharmacology and therapeutic research must be highlighted again. The challenges in each technique have also encouraged to development of solutions that can increasingly

provide more complex and accurate pharmacological profiles. Furthermore, the parallel advances in biomaterials science and microengineering allowed the researchers to refine some approaches by regulating *in vitro* microstructure and mechanical properties, aiming to mimic the biochemical functions of living organisms [227]. Integrating knowledge from these areas resulted in microfluidic cell culture systems as a new dimension for understanding cell behaviour in drug screening.

1.3.2. The convergence between cell culture and microfluidic platforms

1.3.2.1. Overview of manufacturing processes and materials

The use of microfluidic devices in life science research has increased mainly upon the invention of soft lithography [228] and large-scale microfluidic integration [229]. These achievements allowed the establishment of a more straightforward, versatile, and sophisticated method of producing devices, enabling the adjustment of prototypes to the complexity of biological organisms. The fabrication of disposable microfluidic devices includes several techniques, such as photolithography, soft lithography, hot embossing, *in situ* construction, laser ablation, injection moulding, micromachining, wet etching, and reactive ion etching [230,231]. Soft lithography is a set of techniques for fabricating micro- and nanostructures based on printing, moulding and embossing with an elastomeric stamp [232] and it is the most popular technique for fabricating microfluidic devices. This technique allows the development of structures from μm to less than 100 nm. The resolution limit is determined by the balance of the wetting, *van der Waals*, and kinetic factors [232]. Detailed information about soft lithography fabrication methods, materials and the integration of microfluidic systems with physical micro/nanostructures fabricated by soft lithography is reviewed in [233].

Polydimethylsiloxane (PDMS) is the most used material in this technique due to its functional and physical properties. The fabrication of PDMS microfluidic devices consists of two main steps: the fabrication of the stamp by a photolithography process and the moulding [231]. This elastomer presents practical advantages, including fast processing, low cost, reusability of the masters (e.g. resin SU-8), and easy sealing and bonding to different substrates [231]. Furthermore, PDMS is an excellent material for cell-based assays as it is gas permeable, presents favourable biochemical reliability, is non-toxic, presents appropriate optical properties (such as optical transparency and low autofluorescence), is autoclavable, and allows the easy integration of fluidics interconnects (as valves and pumps to control the fluid flow) [231]. However, PDMS faces challenges driving the use of PDMS-alternative materials to fabricate the

devices. In addition to device manufacturing aspects, the successful convergence of microfluidics with cell culture is a complex process that requires consideration of several other operational and biological considerations. Thus, the following sections integrate knowledge concerning the effects of miniaturization, the integration of components to control cell seeding, the pump of media to cells, the transport of fluids between regions, and the control of fluid flow. All these elements must be considered individually and together when designing, using, and analysing results from a microfluidic cell culture platform.

1.3.2.2. Physical considerations in miniaturizing cell cultures

The general idea of using microengineering devices is to condense conventional chemical and biological laboratories into a single device. However, scaling down standard laboratory procedures by a factor of 1000 or more implies physical changes that require a rebuild in our critical and analytical view [234]. At the micrometre scale, fundamental physical and chemical scaling effects occur since different forces dominate. This phenomenon ensures that, at the microscale, the physical parameters are very similar to those naturally occurring under physiological conditions, namely the surface area-to-volume (SAV) ratio, laminar flow, and an effective culture volume [230,234,235].

At the macroscale, the inertia force effect dominates the flow action. As the scale is reduced, the viscous force effect becomes dominant, leading to a small number of *Reynolds* and dominating the laminar flow [236]. *Reynolds* number (Re) is a dimensionless number defined as the ratio of inertial force to viscous force that describes a fluid flow regime – laminar or turbulent. A laminar flow results from the channel dimensions, fluid properties, and flow velocity [230]. This behaviour is numerically indicated by $Re < 2300$, in which the velocity of a particle in a fluid is not a random function of time [230]. The small dimension of microchannels results in a low Re number (e.g., $10 > Re > 0.001$) [237], making the flow regime almost always laminar with no turbulence. As a result, the dominant mass transport type changes from convection to diffusion [236]. This behaviour allows for performing a set of chemical manipulations, such as solvent extraction and phase separation [238]. In the laminar flow context, diffusion can be a process with substantial influence on the movement of soluble components through the microchannels. Since diffusion is a slow process at the microscale, microchannels can create concentration gradients with complex profiles. Dertinger *et al.* [239] explored microfluidic networks to describe the generation of gradients with complex shapes in solution, demonstrating that gradients are maintained across a broad channel (900-2100 μm width) over several tens of seconds. The miniaturization is also accompanied by a significant increase in the SAV ratio, dominating the surface and edge effects from viscous force and

surface tension on thermal transmission [236]. The enhanced SAV ratio reduces the diffusion distance and the mass and heat transfer time, decreasing the reaction times [240]. High heat-exchange efficiency allows rapid heat or cools the mixture, ensuring isothermal conditions with accurately defined residence times [241]. Detailed information about the fundamental laws and theoretical principles underlying the operation of microfluidic devices can be found in [234] and [236].

1.3.2.3. Implications in miniaturizing cell cultures

These scaling effects in microfluidic channels are well suited to cells' biological and physical context in a living organism [242]. Thus, the small dimensions of microfluidic devices are the leading cause of direct and indirect advantages that these platforms offer to perform biological experiments compared to traditional cell cultures in well plates or Petri dishes. The main benefit microfluidic technology offers to cell culture is its ability to provide personalized control over culture conditions, the fluids flow, and the chemical and physical microenvironment *in vitro* [243]. Microfluidic devices can create spatiotemporal gradients, and dynamic fluid flows, control the delivery of nutrients and chemical cues to cells [112], and patterned cell culture substrates inside the device [244]. They also control cell counts and density in a specific area or volume while placing cells in complex geometries [245], individual recovery during or after studies, and high spatial and temporal resolution monitoring. As detailed in the 3D cell culture section, this approach also allows structuring cells in 3D geometries and, thus, creating conditions even more similar to physiological ones [246].

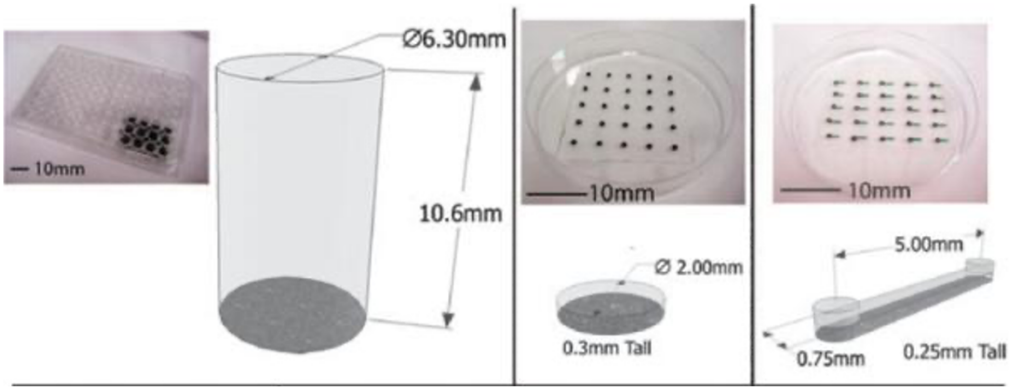
Furthermore, each microfluidic device can be designed for specific cell types as monoculture and can also implement the co-culture of different cell lines due to the flexibility in the device design [237]. Since the microchannels scale meets the scale found in the cellular microenvironment and the ratio between cell volume and extracellular fluid volume is more significant than one, a more similar cellular context is ensured [247]. In turn, miniaturization reduces the volume of reagents, samples, and cells used per assay, which is advantageous for waste reduction [248], but requires the consideration of other effects. It is also an alternative to limited resources and costly growth factors or inhibitors, reducing the overall cost of cell culture studies compared to 96-well plates [249]. The cell population in the microfluidic strategy comprises a few hundred cells (or even a single cell [250]), highly contrasting with the 10^4–10^7 cells of macroscopic cell cultures [235]. This reduction in cell number increases the spatial and temporal resolution of the assays since it allows the capture of changes in the behaviour of cells to the individual level that otherwise would become unnoticed in a larger group of cells [235]. Ren *et al.* [250] reported a microfluidic device composed of multi-constriction channels able to differentiate a human breast cancer

cell line (MDA-MB-231) and a non-tumorigenic human breast cell line (MCF-10A). The work was based on the principle that non-neoplastic and neoplastic cells present different velocity profiles due to the lower membrane stiffness and cytoskeleton of cancer cells [250].

As previously mentioned, reducing the volume of reagents has clear advantages; however, it is also necessary to consider the differences and limitations of the change in volumetry. The miniaturization increases the susceptibility to liquid evaporations, which, in turn, results in a significant increase in osmolality. For instance, while in macroscale cultures, the evaporative loss of 1 mL corresponds to a 0.5% shift in osmolality, in microfluidic culture, the osmolarity shift deviates to a 33% increase [251]. An increase in osmolality is translated into changes in cellular growth, signalling, gene expression, metabolism, and cellular growth [252]. Evaporation losses are particularly challenging when using PDMS-based microfluidic devices since it is a vapour-permeable material. Heo *et al.* [252] characterized the problem using PDMS membranes with varying thicknesses, concluding that the evaporation-mediated osmolality shifts are faster with thin PDMS membranes. Also, humidified and non-humidified cell culture incubators prevented mouse embryo and human endothelial cell growth and development. The authors proposed a PDMS-parylene-PDMS membrane, which has proven effective in preventing evaporation, resulting in the development of single-cell embryos to the blastocyst stage and culture of human endothelial cells under a non-humidified environment [252].

Additionally, the volume density of microfluidic-based cell culture significantly differs from other cultures. Conventional cell culture techniques present reduced volume density, meaning that large media volumes cover few cells compared to microfluidic devices. It is estimated that, for the same cell surface density, a slightly large microchannel (with dimensions of 750 mm wide, 5 mm long, and 250 mm tall) present a volume density 2 to 4 times higher than the macroscopic 6-well plates while using 250 times fewer cells, and 500–1000 times fewer media and costly reagents [253]. Higher volume density means reducing the total amount of the media components available for each cell and a higher rate of accumulation of waste products. Even though lowering the available medium "*per*" cell possibly affects cell behaviour, those effects on cellular functions are unclear [253]. Paguirigan and Beebe [251] analysed the effects of media supplementation (varying serum and glucose concentrations) and the effects of volume density on cell proliferation in microchannel and macroscale cultures. For this, the authors used three culture devices (macroscale, μWells, and microchannels) to identify how the variation of different characteristics, such as small volume, volume density differences and interactions with PDMS, impact cell behaviour. The fundamental differences between macro and microculture devices are represented in **Figure 1.12**. The results revealed a significant proliferation reduction in microchannel

culture at 2.5 and 5 times the density of typical macroscale cultures compared to the macroscopic counterparts. However, in contrast to macroscale cultures, microchannel culture did not show a significant variation in the proliferation rate in the different volume density variations. The results suggest that volume density is not a predominating factor in regulating proliferation rates. Those effects can partially relate to the continuous nutrient supply and waste removal in microfluidic systems [251].



Per Well or Channel Values	Macroscale	µWells	Microchannels
Volume of Media	200 µL	4 µL	5 µL
Total Surface Area/Volume Ratio	0.79 mm^{-1}	1.3 mm^{-1}	2.3mm^{-1}
PDMS Surface Area/Volume Ratio	0 mm^{-1}	~0.5 mm^{-1}	~2 mm^{-1}
Volume density	80 cells/µL	400 cells/µL	400 cells/µL

Figure 1.12 The fundamental differences between macroscale, µwells and microchannels concerning the total media volume, surface area/volume ratios and volume densities. µWells is a PDMS stencil placed on tissue culture plastic similar to microchannels. Adapted from [251].

In addition to scaling out effects, the manufacturing methods, the fabrication materials, integrated components, and the geometry of the cell culture sites also highly differentiate the microfluidic cell cultures from other cell culture techniques. Therefore, the design of microfluidic-based cell culture devices must consider the effect of those factors singularly and combined since small changes in the approaches or features of the devices can be translated into different cellular responses. Kim *et al.* [197] were pioneers in the systematic discussion of the design principles of microfluidic perfusion culture systems and the practical issues that the operation of these systems raises in biomedical applications.

Understanding the physical and biological processes that follow miniaturization and the development and integration of functional components have driven the rapid growth of microfluidic-based drug screening platforms in recent years. They are already established as a low-cost, reproducible, and fast alternative, allowing high throughput drug screening and playing an important role in reducing animal testing and associated ethical issues. Relevant microfluidic-based cell culture devices for drug screening and cell therapies include gradient-based microfluidics [254-258], droplet microfluidics [259-261], printed-based microfluidics [262-264], digital microfluidics [265-267], SlipChip [268-270] and paper microfluidics [271-273].

1.3.3. Final Remarks

The potential that microfluidic cell culture adds to the well-established macroscopic cell culture is undoubted. It allows the scientific community to gain insights into molecular and cellular biology and perform high-throughput drug screening that would otherwise be extremely difficult with macroscopic cell culture techniques. However, there is still a long way to go to understand all the differences in cellular behaviour between microfluidic and macroscopic cell cultures since science is, until now, mainly supported by the knowledge generated in macroscopic methods. Moreover, although microfluidic devices already allow a good mimicry of the physiological microenvironment, this area must continually grow to increase the simulation of the human body in a holistic and consolidated way. These developments must be monitored multidisciplinary, and engineering must play a key role in developing detectors or automatic analysis systems integrated into the devices for real-time analysis of cellular responses. It is intended that future generations of microfluidic devices for pharmaceutical research will allow replacing ethically and monetarily questionable *in vivo* assays and bring society closer to personalized medicine.

1.4. Thesis oultine

This PhD thesis results from accomplishing and refining the main objectives detailed in section 1.1. It is organised into 6 chapters describing the addressed problematics and how those aims were validated, most corresponding to manuscripts published or in preparation for submission to specialised journals. Thus, the following chapters bring together the developments in synthesising, characterising, and screening functionalised magnetic-based nanocarriers for chemotherapeutic drug delivery for cell therapies.

For getting new insights into ferrite nanoparticle properties, **Chapter 2** explores the synthesis of superparamagnetic spherical calcium-substituted magnesium ferrite nanoparticles ($Ca_xMg_{1-x}Fe_2O_4$, with x = 0.25, 0.50, 0.75) and the effects of varying the magnesium and calcium in the ferrite structure. These nanoparticles were included in the core of PEGylated and non-PEGylated liposomes, forming aqueous and SMLs. These were validated as encapsulation systems and magnetic nanocarriers for a model drug – curcumin. Considering the functional role that magnetic nanoparticles play in magnetoliposome responsiveness, **Chapter 3** explores the development of a new method for preparing $Ca_{0.25}Mg_{0.75}Fe_2O_4$ shape-anisotropic ferrites with enhanced magnetic properties. It also describes the development of a new methodology for synthesising SMLs comprising a magnetic core with an insignificant amount of water. These new magnetoliposomes were designed to increase the nanoparticle/lipid ratio compared to the previous method and, thus, enhance the magnetic contribution of the systems. Furthermore, it explores the ability of magnetoliposomes to encapsulate and protect a relevant drug in cancer therapy – DOX – and takes a first look at its controlled release under therapeutically relevant conditions. **Chapter 4** applies the acquired knowledge in optimising the lipid formulation and the inclusion of magnetic nanoparticles to obtain multi-stimuli-responsive systems and is divided into two subchapters. **Chapter 4.1** presents a comprehensive study of the effect of nine lipid formulations on structural, colloidal, thermodynamic, stability, and controlled drug release kinetics. This section emphasises the implications of lipid combinations on the phase transition temperature of magnetoliposomes and the pH variations on drug-lipid interplay as a predictive model of temperature and pH stimulus sensitivity. In turn, **Chapter 4.2** explores the potential of $Ca_{0.25}Mg_{0.75}Fe_2O_4$ superparamagnetic nanoparticles to photothermal therapy and their effects upon inclusion in lipid vesicles.

Chapter 5 evaluates the differential effects of DOX and DOX-loaded SMLs in four different cell organizational levels. For this, Sk-br-3 breast cancer cell culture was established on conventional adherent and non-adherent plates by seeding Sk-br-3 cells and 1-week dense Sk-br-3 spheroids on each plate in assays independently. Furthermore, it involves the design and manufacture of microfluidic platforms based on microenvironment gradient as a proof-of-concept to establish a model for drug screening that better mimic to the physiological context.

Finally, **Chapter 6** summarises the key points and conclusions of the explored works throughout each chapter and how they contributed to getting new insights into the development of magnetoliposomes for cancer therapy. It also acknowledges the limitations of the research while highlighting prospects for future research.

1.5. References

1. Daraee, H.; Etemadi, A.; Kouhi, M.; Alimirzalu, S.; Akbarzadeh, A. Application of liposomes in medicine and drug delivery. *Artificial cells, nanomedicine, and biotechnology* **2016**, *44*, 381-391.

2. Johnston, M.J.; Semple, S.C.; Klimuk, S.K.; Ansell, S.; Maurer, N.; Cullis, P.R. Characterization of the drug retention and pharmacokinetic properties of liposomal nanoparticles containing dihydrosphingomyelin. *Biochimica et Biophysica Acta (BBA)-Biomembranes* **2007**, *1768*, 1121-1127.

3. Nakhaei, P.; Margiana, R.; Bokov, D.O.; Abdelbasset, W.K.; Kouhbanani, M.A.J.; Varma, R.S.; Marofi, F.; Jarahian, M.; Beheshtkhoo, N. Liposomes: Structure, Biomedical Applications, and Stability Parameters With Emphasis on Cholesterol. *Frontiers in Bioengineering and Biotechnology* **2021**, *9*.

4. Akbarzadeh, A.; Rezaei-Sadabady, R.; Davaran, S.; Joo, S.W.; Zarghami, N.; Hanifehpour, Y.; Samiei, M.; Kouhi, M.; Nejati-Koshki, K. Liposome: classification, preparation, and applications. *Nanoscale research letters* **2013**, *8*, 1-9.

5. Salimi, A. Liposomes as a novel drug delivery system: fundamental and pharmaceutical application. *Asian Journal of Pharmaceutics (AJP)* **2018**, *12*.

6. Del Amo, E.M.; Rimpelä, A.-K.; Heikkinen, E.; Kari, O.K.; Ramsay, E.; Lajunen, T.; Schmitt, M.; Pelkonen, L.; Bhattacharya, M.; Richardson, D. Pharmacokinetic aspects of retinal drug delivery. *Progress in retinal and eye research* **2017**, *57*, 134-185.

7. Gabizon, A.; Dagan, A.; Goren, D.; Barenholz, Y.; Fuks, Z. Liposomes as in vivo carriers of adriamycin: reduced cardiac uptake and preserved antitumor activity in mice. *Cancer research* **1982**, *42*, 4734-4739.

8. Gabizon, A.; Tzemach, D.; Mak, L.; Bronstein, M.; Horowitz, A.T. Dose dependency of pharmacokinetics and therapeutic efficacy of pegylated liposomal doxorubicin (DOXIL) in murine models. *Journal of drug targeting* **2002**, *10*, 539-548.

9. Geng, S.; Yang, B.; Wang, G.; Qin, G.; Wada, S.; Wang, J.-Y. Two cholesterol derivative-based PEGylated liposomes as drug delivery system, study on pharmacokinetics and drug delivery to retina. *Nanotechnology* **2014**, *25*, 275103.

10. Gilchrist, R.; Medal, R.; Shorey, W.D.; Hanselman, R.C.; Parrott, J.C.; Taylor, C.B. Selective inductive heating of lymph nodes. *Annals of surgery* **1957**, *146*, 596.

11. Ban, I.; Stergar, J.; Maver, U. NiCu magnetic nanoparticles: review of synthesis methods, surface functionalization approaches, and biomedical applications. *Nanotechnology reviews* **2018**, *7*, 187-207.

12. Malhotra, N.; Lee, J.-S.; Liman, R.A.D.; Ruallo, J.M.S.; Villaflores, O.B.; Ger, T.-R.; Hsiao, C.-D. Potential toxicity of iron oxide magnetic nanoparticles: A review. *Molecules* **2020**, *25*, 3159.

13. Gryparis, E.C.; Hatziapostolou, M.; Papadimitriou, E.; Avgoustakis, K. Anticancer activity of cisplatin-loaded PLGA-mPEG nanoparticles on LNCaP prostate cancer cells. *European journal of pharmaceutics and biopharmaceutics* **2007**, *67*, 1-8.

14. Choi, J.; Wang, N.S. Nanoparticles in biomedical applications and their safety concerns. *Biomedical engineering from theory to applications* **2011**, *29*, 486.

15. Sundberg, S.A. High-throughput and ultra-high-throughput screening: solution-and cell-based approaches. *Current opinion in biotechnology* **2000**, *11*, 47-53.

16. Pampaloni, F.; Reynaud, E.G.; Stelzer, E.H. The third dimension bridges the gap between cell culture and live tissue. *Nature reviews Molecular cell biology* **2007**, *8*, 839-845.

17. Yang, S.; Ng, R. 3D cultures for growing and studying cells. *Materials Today* **2007**, *10*, 56.

18. Jensen, C.; Teng, Y. Is it time to start transitioning from 2D to 3D cell culture? *Frontiers in molecular biosciences* **2020**, *7*, 33.

19. Duval, K.; Grover, H.; Han, L.-H.; Mou, Y.; Pegoraro, A.F.; Fredberg, J.; Chen, Z. Modeling physiological events in 2D vs. 3D cell culture. *Physiology* **2017**, *32*, 266-277.

20. Barenholz, Y.C. Doxil®—the first FDA-approved nano-drug: lessons learned. *Journal of controlled release* **2012**, *160*, 117-134.

21. Bobo, D.; Robinson, K.J.; Islam, J.; Thurecht, K.J.; Corrie, S.R. Nanoparticle-based medicines: a review of FDA-approved materials and clinical trials to date. *Pharmaceutical research* **2016**, *33*, 2373-2387.

22. Bangham, A.D.; Horne, R. Negative staining of phospholipids and their structural modification by surface-active agents as observed in the electron microscope. *Journal of molecular biology* **1964**, *8*, 660-IN610.

23. Bangham, A.D.; Hill, M.W.; Miller, N. Preparation and use of liposomes as models of biological membranes. In *Methods in membrane biology*, Springer: **1974**; pp. 1-68.

24. Papahadjopoulos, D.; Kimelberg, H.K. Phospholipid vesicles (liposomes) as models for biological membranes: their properties and interactions with cholesterol and proteins. *Progress in surface science* **1974**, *4*, 141-232.

25. Sharma, A.; Sharma, U.S. Liposomes in drug delivery: progress and limitations. *International journal of pharmaceutics* **1997**, *154*, 123-140.

26. Nisini, R.; Poerio, N.; Mariotti, S.; De Santis, F.; Fraziano, M. The multirole of liposomes in therapy and prevention of infectious diseases. *Frontiers in Immunology* **2018**, *9*, 155.

27. Storm, G.; Crommelin, D.J. Liposomes: quo vadis? *Pharmaceutical Science & Technology Today* **1998**, *1*, 19-31.

28. Euliss, L.E.; DuPont, J.A.; Gratton, S.; DeSimone, J. Imparting size, shape, and composition control of materials for nanomedicine. *Chemical Society Reviews* **2006**, *35*, 1095-1104.

29. Bozzuto, G.; Molinari, A. Liposomes as nanomedical devices. *International Journal of Nanomedicine* **2015**, *10*, 975.

30. Gabizon, A.; Papahadjopoulos, D. Liposome formulations with prolonged circulation time in blood and enhanced uptake by tumors. *Proceedings of the National Academy of Sciences* **1988**, *85*, 6949-6953.

31. Allen, T.; Hansen, C.; Martin, F.; Redemann, C.; Yau-Young, A. Liposomes containing synthetic lipid derivatives of poly (ethylene glycol) show prolonged circulation half-lives in vivo. *Biochimica et Biophysica Acta (BBA)-Biomembranes* **1991**, *1066*, 29-36.

32. Allen, T.M.; Hansen, C.; Rutledge, J. Liposomes with prolonged circulation times: factors affecting uptake by reticuloendothelial and other tissues. *Biochimica et Biophysica Acta (BBA)-Biomembranes* **1989**, *981*, 27-35.

33. Drummond, D.C.; Meyer, O.; Hong, K.; Kirpotin, D.B.; Papahadjopoulos, D. Optimizing liposomes for delivery of chemotherapeutic agents to solid tumors. *Pharmacological reviews* **1999**, *51*, 691-744.

34. Torchilin, V.P. Recent advances with liposomes as pharmaceutical carriers. *Nature reviews Drug discovery* **2005**, *4*, 145-160.

35. Medina, O.P.; Zhu, Y.; Kairemo, K. Targeted liposomal drug delivery in cancer. *Current pharmaceutical design* **2004**, *10*, 2981-2989.

36. Sapra, P.; Allen, T. Ligand-targeted liposomal anticancer drugs. *Progress in lipid research* **2003**, *42*, 439-462.

37. Torchilin, V.; Khaw, B.A.; Smirnov, V.; Haber, E. Preservation of antimyosin antibody activity after covalent coupling to liposomes. *Biochemical and biophysical research communications* **1979**, *89*, 1114-1119.

38. Bendas, G. Immunoliposomes. *BioDrugs* **2001**, *15*, 215-224.

39. Perche, F.; Torchilin, V.P. Recent trends in multifunctional liposomal nanocarriers for enhanced tumor targeting. *Journal of drug delivery* **2013**, *2013*.

40. Gullino, P.M.; Grantham, F.H.; Smith, S.H.; Haggerty, A.C. Modifications of the acid-base status of the internal milieu of tumors. *Journal of the National Cancer Institute* **1965**, *34*, 857-869.

41. Simões, S.; Moreira, J.N.; Fonseca, C.; Düzgüneş, N.; De Lima, M.C.P. On the formulation of pH-sensitive liposomes with long circulation times. *Advanced drug delivery reviews* **2004**, *56*, 947-965.

42. Venugopalan, P.; Jain, S.; Sankar, S.; Singh, P.; Rawat, A.; Vyas, S. pH-sensitive liposomes: mechanism of triggered release to drug and gene delivery prospects. *Die Pharmazie* **2002**, *57*, 659-671.

43. Ellens, H.; Bentz, J.; Szoka, F.C. pH-induced destabilization of phosphatidylethanolamine-containing liposomes: role of bilayer contact. *Biochemistry* **1984**, *23*, 1532-1538.

44. Yatvin, M.B.; Weinstein, J.N.; Dennis, W.H.; Blumenthal, R. Design of liposomes for enhanced local release of drugs by hyperthermia. *Science* **1978**, *202*, 1290-1293.

45. Dromi, S.; Frenkel, V.; Luk, A.; Traughber, B.; Angstadt, M.; Bur, M.; Poff, J.; Xie, J.; Libutti, S.K.; Li, K.C. Pulsed-high intensity focused ultrasound and low temperature–sensitive liposomes for enhanced targeted drug delivery and antitumor effect. *Clinical cancer research* **2007**, *13*, 2722-2727.

46. Jin, Y.; Liang, X.; An, Y.; Dai, Z. Microwave-triggered smart drug release from liposomes co-encapsulating doxorubicin and salt for local combined hyperthermia and chemotherapy of cancer. *Bioconjugate chemistry* **2016**, *27*, 2931-2942.

47. Gasselhuber, A.; Dreher, M.R.; Negussie, A.; Wood, B.J.; Rattay, F.; Haemmerich, D. Mathematical spatio-temporal model of drug delivery from low temperature sensitive liposomes during radiofrequency tumour ablation. *International Journal of Hyperthermia* **2010**, *26*, 499-513.

48. Hornback, N. Historical aspects of hyperthermia in cancer therapy. *Radiologic Clinics of North America* **1989**, *27*, 481-488.

49. van der Zee, J.; González, D.; van Rhoon, G.C.; van Dijk, J.D.; van Putten, W.L.; Hart, A.A. Comparison of radiotherapy alone with radiotherapy plus hyperthermia in locally advanced pelvic tumours: a prospective, randomised, multicentre trial. *The Lancet* **2000**, *355*, 1119-1125.

50. Habash, R.W.; Bansal, R.; Krewski, D.; Alhafid, H.T. Thermal therapy, part 2: hyperthermia techniques. *Critical Reviews™ in Biomedical Engineering* **2006**, *34*.

51. Lee, S.-Y.; Fiorentini, G.; Szasz, A.M.; Szigeti, G.; Szasz, A.; Minnaar, C.A. Quo vadis oncological hyperthermia (2020)? *Frontiers in Oncology* **2020**, *10*, 1690.

52. Freeman, M.; Arrott, A.; Watson, J. Magnetism in medicine. *Journal of Applied Physics* **1960**, *31*, S404-S405.

53. Stueber, D.D.; Villanova, J.; Aponte, I.; Xiao, Z.; Colvin, V.L. Magnetic nanoparticles in biology and medicine: Past, present, and future trends. *Pharmaceutics* **2021**, *13*, 943.

54. Singh, A.; Jain, S.; Sahoo, S.K. Magnetic nanoparticles for amalgamation of magnetic hyperthermia and chemotherapy: An approach towards enhanced attenuation of tumor. *Materials Science and Engineering: C* **2020**, *110*, 110695.

55. Beckett, K.R.; Moriarity, A.K.; Langer, J.M. Safe use of contrast media: what the radiologist needs to know. *Radiographics* **2015**, *35*, 1738-1750.

56. Katayama, H.; Yamaguchi, K.; Kozuka, T.; Takashima, T.; Seez, P.; Matsuura, K. Adverse reactions to ionic and nonionic contrast media. A report from the Japanese Committee on the Safety of Contrast Media. *Radiology* **1990**, *175*, 621-628.

57. Okuhata, Y. Delivery of diagnostic agents for magnetic resonance imaging. *Advanced drug delivery reviews* **1999**, *37*, 121-137.

58. Xie, W.; Guo, Z.; Gao, F.; Gao, Q.; Wang, D.; Liaw, B.-s.; Cai, Q.; Sun, X.; Wang, X.; Zhao, L. Shape-, size-and structure-controlled synthesis and biocompatibility of iron oxide nanoparticles for magnetic theranostics. *Theranostics* **2018**, *8*, 3284.

59. Zhang, C.; Yan, Y.; Zou, Q.; Chen, J.; Li, C. Superparamagnetic iron oxide nanoparticles for MR imaging of pancreatic cancer: Potential for early diagnosis through targeted strategies. *Asia-Pacific Journal of Clinical Oncology* **2016**, *12*, 13-21.

60. Catarino, S.O.; Rodrigues, R.O.; Pinho, D.; Miranda, J.M.; Minas, G.; Lima, R. Blood cells separation and sorting techniques of passive microfluidic devices: From fabrication to applications. *Micromachines* **2019**, *10*, 593.

61. Liang, W.; Liu, J.; Yang, X.; Zhang, Q.; Yang, W.; Zhang, H.; Liu, L. Microfluidic-based cancer cell separation using active and passive mechanisms. *Microfluidics and Nanofluidics* **2020**, *24*, 1-19.

62. Yan, S.; Zhang, J.; Yuan, D.; Li, W. Hybrid microfluidics combined with active and passive approaches for continuous cell separation. *Electrophoresis* **2017**, *38*, 238-249.

63. Haun, J.B.; Yoon, T.J.; Lee, H.; Weissleder, R. Magnetic nanoparticle biosensors. *Wiley Interdisciplinary Reviews: Nanomedicine and Nanobiotechnology* **2010**, *2*, 291-304.

64. Lee, H.; Sun, E.; Ham, D.; Weissleder, R. Chip–NMR biosensor for detection and molecular analysis of cells. *Nature medicine* **2008**, *14*, 869-874.

65. Cristofanilli, M.; Budd, G.T.; Ellis, M.J.; Stopeck, A.; Matera, J.; Miller, M.C.; Reuben, J.M.; Doyle, G.V.; Allard, W.J.; Terstappen, L.W. Circulating tumor cells, disease progression, and survival in metastatic breast cancer. *New England Journal of Medicine* **2004**, *351*, 781-791.

66. Pardoe, H.; Chua-Anusorn, W.; Pierre, T.G.S.; Dobson, J. Structural and magnetic properties of nanoscale iron oxide particles synthesized in the presence of dextran or polyvinyl alcohol. *Journal of Magnetism and Magnetic Materials* **2001**, *225*, 41-46.

67. Morisada, S.; Miyata, N.; Iwahori, K. Immunomagnetic separation of scum-forming bacteria using polyclonal antibody that recognizes mycolic acids. *Journal of microbiological methods* **2002**, *51*, 141-148.

68. Tibbe, A.G.; Grooth, B.G.d.; Greve, J.; Liberti, P.A.; Dolan, G.J.; Terstappen, L.W. Optical tracking and detection of immunomagnetically selected and aligned cells. *Nature biotechnology* **1999**, *17*, 1210-1213.

69. Ramanaviciene, A.; Popov, A.; Baliunaite, E.; Brasiunas, B.; Kausaite-Minkstimiene, A.; Tamer, U.; Kirdaite, G.; Bernotiene, E.; Mobasheri, A. Magneto-Immunoassay for the Detection and Quantification of Human Growth Hormone. *Biosensors* **2022**, *12*, 65.

70. Levy, L.; Sahoo, Y.; Kim, K.-S.; Bergey, E.J.; Prasad, P.N. Nanochemistry: synthesis and characterization of multifunctional nanoclinics for biological applications. *Chemistry of Materials* **2002**, *14*, 3715-3721.

71. Angelopoulou, A.; Kolokithas-Ntoukas, A.; Fytas, C.; Avgoustakis, K. Folic acid-functionalized, condensed magnetic nanoparticles for targeted delivery of doxorubicin to tumor cancer cells overexpressing the folate receptor. *Acs Omega* **2019**, *4*, 22214-22227.

72. Materón, E.M.; Miyazaki, C.M.; Carr, O.; Joshi, N.; Picciani, P.H.; Dalmaschio, C.J.; Davis, F.; Shimizu, F.M. Magnetic nanoparticles in biomedical applications: A review. *Applied Surface Science Advances* **2021**, *6*, 100163.

73. McBain, S.C.; Yiu, H.H.; Dobson, J. Magnetic nanoparticles for gene and drug delivery. *International Journal of Nanomedicine* **2008**, *3*, 169.

74. Senyei, A.; Widder, K.; Czerlinski, G. Magnetic guidance of drug-carrying microspheres. *Journal of Applied Physics* **1978**, *49*, 3578-3583.

75. Al-Jamal, K.T.; Bai, J.; Wang, J.T.-W.; Protti, A.; Southern, P.; Bogart, L.; Heidari, H.; Li, X.; Cakebread, A.; Asker, D. Magnetic drug targeting: preclinical in vivo studies, mathematical modeling, and extrapolation to humans. *Nano letters* **2016**, *16*, 5652-5660.

76. Rahim, M.A.; Jan, N.; Khan, S.; Shah, H.; Madni, A.; Khan, A.; Jabar, A.; Khan, S.; Elhissi, A.; Hussain, Z. Recent advancements in stimuli responsive drug delivery platforms for active and passive cancer targeting. *Cancers* **2021**, *13*, 670.

77. Margolis, L.B.; Namiot, V.A.; Kljukin, L.M. Magnetoliposomes: another principle of cell sorting. *Biochimica et Biophysica Acta (BBA)-Biomembranes* **1983**, *735*, 193-195.

78. De Cuyper, M.; Joniau, M. Magnetoliposomes. Formation and structural characterization. *European biophysics journal: EBJ* **1988**, *15*, 311-319.

79. Tai, L.-A.; Tsai, P.-J.; Wang, Y.-C.; Wang, Y.-J.; Lo, L.-W.; Yang, C.-S. Thermosensitive liposomes entrapping iron oxide nanoparticles for controllable drug release. *Nanotechnology* **2009**, *20*, 135101.

80. Bi, H.; Han, X. Magnetic field triggered drug release from lipid microcapsule containing lipid-coated magnetic nanoparticles. *Chemical Physics Letters* **2018**, *706*, 455-460.

81. Salah, B.M.; Rady, M.; Abdel-Halim, M.; Fahmy, H.M.; El-Din, N.S.; Gaber, M.H. Alternating Magnetic Field Induced Membrane Permeability in Erythromycin Magneto-Liposomes A Potential Solution to Antibiotic Resistance. *Biophysics* **2021**, *66*, 264-272.

82. Shaghasemi, B.S.; Virk, M.M.; Reimhult, E. Optimization of magneto-thermally controlled release kinetics by tuning of magnetoliposome composition and structure. *Scientific reports* **2017**, *7*, 1-10.

83. Fortes Brollo, M.E.; Domínguez-Bajo, A.; Tabero, A.; Domínguez-Arca, V.; Gisbert, V.; Prieto, G.; Johansson, C.; Garcia, R.; Villanueva, A.; Serrano, M.C. Combined magnetoliposome formation and drug loading in one step for efficient alternating current-magnetic field remote-controlled drug release. *ACS applied materials & interfaces* **2020**, *12*, 4295-4307.

84. Guo, H.; Chen, W.; Sun, X.; Liu, Y.-N.; Li, J.; Wang, J. Theranostic magnetoliposomes coated by carboxymethyl dextran with controlled release by low-frequency alternating magnetic field. *Carbohydrate polymers* **2015**, *118*, 209-217.

85. Shen, S.; Huang, D.; Cao, J.; Chen, Y.; Zhang, X.; Guo, S.; Ma, W.; Qi, X.; Ge, Y.; Wu, L. Magnetic liposomes for light-sensitive drug delivery and combined photothermal–chemotherapy of tumors. *Journal of Materials Chemistry B* **2019**, *7*, 1096-1106.

86. Rio, I.S.; Rodrigues, A.R.O.; Rodrigues, C.P.; Almeida, B.G.; Pires, A.; Pereira, A.; Araújo, J.; Castanheira, E.; Coutinho, P.J. Development of novel magnetoliposomes containing nickel ferrite nanoparticles covered with gold for applications in thermotherapy. *Materials* **2020**, *13*, 815.

87. TS, A.; Lu, Y.-J.; Chen, J.-P. Optimization of the preparation of magnetic liposomes for the combined use of magnetic hyperthermia and photothermia in dual magneto-photothermal cancer therapy. *International Journal of Molecular Sciences* **2020**, *21*, 5187.

88. Guo, Y.; Zhang, Y.; Ma, J.; Li, Q.; Li, Y.; Zhou, X.; Zhao, D.; Song, H.; Chen, Q.; Zhu, X. Light/magnetic hyperthermia triggered drug released from multi-functional thermo-sensitive

magnetoliposomes for precise cancer synergetic theranostics. *Journal of controlled release* **2018**, *272*, 145-158.

89. Meier, S.; Pütz, G.; Massing, U.; Hagemeyer, C.; Von Elverfeldt, D.; Meißner, M.; Ardipradja, K.; Barnert, S.; Peter, K.; Bode, C. Immuno-magnetoliposomes targeting activated platelets as a potentially human-compatible MRI contrast agent for targeting atherothrombosis. *Biomaterials* **2015**, *53*, 137-148.

90. Ribeiro, R.S.G.; Belderbos, S.; Danhier, P.; Gallo, J.; Manshian, B.B.; Gallez, B.; Bañobre, M.; De Cuyper, M.; Soenen, S.J.; Gsell, W. Targeting tumor cells and neovascularization using RGD-functionalized magnetoliposomes. *International journal of nanomedicine* **2019**, *14*, 5911.

91. Dorjsuren, B.; Chaurasiya, B.; Ye, Z.; Liu, Y.; Li, W.; Wang, C.; Shi, D.; Evans, C.E.; Webster, T.J.; Shen, Y. Cetuximab-coated thermo-sensitive liposomes loaded with magnetic nanoparticles and doxorubicin for targeted egfr-expressing breast cancer combined therapy. *International journal of nanomedicine* **2020**, *15*, 8201.

92. Cvjetinović, Đ.; Milanović, Z.; Mirković, M.; Petrović, J.; Vesković, A.; Popović-Bijelić, A.; Prijović, Ž.; Janković, D.; Vranješ-Đurić, S. Magnetically induced controlled release from glucose-modified liposomes loaded with Fe3O4 nanoparticles. *Journal of Nanoparticle Research* **2021**, *23*, 1-10.

93. Ding, H.; Sagar, V.; Agudelo, M.; Pilakka-Kanthikeel, S.; Atluri, V.S.R.; Raymond, A.; Samikkannu, T.; Nair, M.P. Enhanced blood–brain barrier transmigration using a novel transferrin embedded fluorescent magneto-liposome nanoformulation. *Nanotechnology* **2014**, *25*, 055101.

94. Lu, Y.-J.; Chuang, E.-Y.; Cheng, Y.-H.; Anilkumar, T.; Chen, H.-A.; Chen, J.-P. Thermosensitive magnetic liposomes for alternating magnetic field-inducible drug delivery in dual targeted brain tumor chemotherapy. *Chemical Engineering Journal* **2019**, *373*, 720-733.

95. Dong, J.; Zink, J.I. Taking the temperature of the interiors of magnetically heated nanoparticles. *ACS nano* **2014**, *8*, 5199-5207.

96. Jordan, A.; Scholz, R.; Wust, P.; Fähling, H.; Felix, R. Magnetic fluid hyperthermia (MFH): Cancer treatment with AC magnetic field induced excitation of biocompatible superparamagnetic nanoparticles. *Journal of Magnetism and Magnetic materials* **1999**, *201*, 413-419.

97. Riley, R.S.; Day, E.S. Gold nanoparticle-mediated photothermal therapy: applications and opportunities for multimodal cancer treatment. *Wiley Interdisciplinary Reviews: Nanomedicine and Nanobiotechnology* **2017**, *9*, e1449.

98. Chen, Y.-W.; Su, Y.-L.; Hu, S.-H.; Chen, S.-Y. Functionalized graphene nanocomposites for enhancing photothermal therapy in tumor treatment. *Advanced drug delivery reviews* **2016**, *105*, 190-204.

99. Robinson, R.; Gerlach, W.; Ghandehari, H. Comparative effect of gold nanorods and nanocages for prostate tumor hyperthermia. *Journal of controlled release* **2015**, *220*, 245-252.

100. Bardhan, R.; Lal, S.; Joshi, A.; Halas, N.J. Theranostic nanoshells: from probe design to imaging and treatment of cancer. *Accounts of chemical research* **2011**, *44*, 936-946.

101. Kumar, P.S.; Pastoriza-Santos, I.; Rodríguez-González, B.; De Abajo, F.J.G.; Liz-Marzán, L.M. High-yield synthesis and optical response of gold nanostars. *Nanotechnology* **2007**, *19*, 015606.

102. Jaque, D.; Maestro, L.M.; Del Rosal, B.; Haro-Gonzalez, P.; Benayas, A.; Plaza, J.; Rodríguez, E.M.; Solé, J.G. Nanoparticles for photothermal therapies. *nanoscale* **2014**, *6*, 9494-9530.

103. Shen, S.; Wang, S.; Zheng, R.; Zhu, X.; Jiang, X.; Fu, D.; Yang, W. Magnetic nanoparticle clusters for photothermal therapy with near-infrared irradiation. *Biomaterials* **2015**, *39*, 67-74.

104. Chu, M.; Shao, Y.; Peng, J.; Dai, X.; Li, H.; Wu, Q.; Shi, D. Near-infrared laser light mediated cancer therapy by photothermal effect of Fe3O4 magnetic nanoparticles. *Biomaterials* **2013**, *34*, 4078-4088.

105. Kolosnjaj-Tabi, J.; Lartigue, L.; Javed, Y.; Luciani, N.; Pellegrino, T.; Wilhelm, C.; Alloyeau, D.; Gazeau, F. Biotransformations of magnetic nanoparticles in the body. *Nano Today* **2016**, *11*, 280-284.

106. Yan, H.; Shang, W.; Sun, X.; Zhao, L.; Wang, J.; Xiong, Z.; Yuan, J.; Zhang, R.; Huang, Q.; Wang, K. "All-in-one" nanoparticles for trimodality imaging-guided intracellular photo-magnetic hyperthermia therapy under intravenous administration. *Advanced Functional Materials* **2018**, *28*, 1705710.

107. Khosroshahi, M.E.; Ghazanfari, L.; Hassannejad, Z.; Lenhert, S. In-vitro application of doxorubicin loaded magnetoplasmonic thermosensitive liposomes for laser hyperthermia and chemotherapy of breast cancer. *J Nanomed Nanotechnol* **2015**, *6*, 2.

108. Rodrigues, A.R.O.; Matos, J.O.; Nova Dias, A.M.; Almeida, B.G.; Pires, A.; Pereira, A.M.; Araújo, J.P.; Queiroz, M.-J.R.; Castanheira, E.; Coutinho, P.J. Development of multifunctional liposomes containing magnetic/plasmonic MnFe2O4/Au core/shell nanoparticles. *Pharmaceutics* **2019**, *11*, 10.

109. Marqués-Gallego, P.; de Kroon, A.I. Ligation strategies for targeting liposomal nanocarriers. *BioMed research international* **2014**, *2014*.

110. Wong, P.T.; Choi, S.K. Mechanisms and implications of dual-acting methotrexate in folate-targeted nanotherapeutic delivery. *International Journal of Molecular Sciences* **2015**, *16*, 1772-1790.

111. Chen, Y.; Lu, J.; Yang, J.; Hao, K.; Li, M. Investigation of Alpha-Fetoprotein Antibody Modified Fluorescent Magnetic Probe on HepG2 Cell and Cancer Model Mouse. *Journal of nanoscience and nanotechnology* **2020**, *20*, 5147-5150.

112. Whitesides, G.M. The origins and the future of microfluidics. *Nature* **2006**, *442*, 368-373.

113. Manz, A.; Verpoorte, E.; Raymond, D.E.; Effenhauser, C.S.; Burggraf, N.; Widmer, H.M. μ-TAS: miniaturized total chemical analysis systems. In Proceedings of the Micro Total Analysis Systems, **1995**; pp. 5-27.

114. Stone, H.A.; Stroock, A.D.; Ajdari, A. Engineering flows in small devices: microfluidics toward a lab-on-a-chip. *Annu. Rev. Fluid Mech.* **2004**, *36*, 381-411.

115. Gravesen, P.; Branebjerg, J.; Jensen, O.S. Microfluidics-a review. *Journal of micromechanics and microengineering* **1993**, *3*, 168.

116. Squires, T.M.; Quake, S.R. Microfluidics: Fluid physics at the nanoliter scale. *Reviews of Modern Physics* **2005**, *77*, 977-1026, doi:10.1103/RevModPhys.77.977.

117. Zhang, J.; Yan, S.; Yuan, D.; Alici, G.; Nguyen, N.-T.; Warkiani, M.E.; Li, W. Fundamentals and applications of inertial microfluidics: A review. *Lab on a Chip* **2016**, *16*, 10-34.

118. Li, Z.; Zhang, B.; Dang, D.; Yang, X.; Yang, W.; Liang, W. A review of microfluidic-based mixing methods. *Sensors and Actuators A: Physical* **2022**, 113757.

119. Lee, C.-C.; Sui, G.; Elizarov, A.; Shu, C.J.; Shin, Y.-S.; Dooley, A.N.; Huang, J.; Daridon, A.; Wyatt, P.; Stout, D. Multistep synthesis of a radiolabeled imaging probe using integrated microfluidics. *Science* **2005**, *310*, 1793-1796.

120. Lombardi, D.; Dittrich, P.S. Advances in microfluidics for drug discovery. *Expert opinion on drug discovery* **2010**, *5*, 1081-1094.

121. Buguin, A.; Chen, Y.; Silberzan, P. Microfluidics: Concepts and applications to the life sciences. In *Nanoscience*; Springer: **2009**; pp. 743-774.

122. Jin, Y.; Dou, M.; Zhuo, S.; Li, Q.; Wang, F.; Li, J. Advances in microfluidic analysis of residual antibiotics in food. *Food Control* **2022**, 108885.

123. Park, D.; Kim, H.; Kim, J.W. Microfluidic production of monodisperse emulsions for cosmetics. *Biomicrofluidics* **2021**, *15*, 051302.

124. Lee, M.-H.; Oh, S.-G.; Moon, S.-K.; Bae, S.-Y. Preparation of silica particles encapsulating retinol using O/W/O multiple emulsions. *Journal of Colloid and Interface Science* **2001**, *240*, 83-89.

125. Sarabi, M.R.; Yigci, D.; Alseed, M.M.; Mathyk, B.A.; Ata, B.; Halicigil, C.; Tasoglu, S. Disposable paper-based microfluidics for fertility testing. *Iscience* **2022**, 104986.

126. Yager, P.; Edwards, T.; Fu, E.; Helton, K.; Nelson, K.; Tam, M.R.; Weigl, B.H. Microfluidic diagnostic technologies for global public health. *nature* **2006**, *442*, 412-418.

127. Gong, M.M.; Sinton, D. Turning the page: advancing paper-based microfluidics for broad diagnostic application. *Chemical reviews* **2017**, *117*, 8447-8480.

128. Zhang, D.; Li, C.; Ji, D.; Wang, Y. Based Microfluidic Sensors for Onsite Environmental Detection: A Critical Review. *Critical Reviews in Analytical Chemistry* **2022**, *52*, 1432-1449.

129. Carrel, A. Pure cultures of cells. *The Journal of experimental medicine* **1912**, *16*, 165-168.

130. Jacoby, W.; Pasten, I. Methods in Enzymology: Cell Culture. Vol. 58. **1979**.

131. Jaroch, K.; Jaroch, A.; Bojko, B. Cell cultures in drug discovery and development: The need of reliable in vitro-in vivo extrapolation for pharmacodynamics and pharmacokinetics assessment. *J Pharm Biomed Anal* **2018**, *147*, 297-312, doi:10.1016/j.jpba.2017.07.023.

132. Bhatt, S.M. *Animal cell culture: concept and application*; Alpha Science International Ltd: 2011.

133. Andersen, M.L.; Winter, L.M. Animal models in biological and biomedical research-experimental and ethical concerns. *Anais da Academia Brasileira de Ciências* **2017**, *91*.

134. Sibbitts, J.; Sellens, K.A.; Jia, S.; Klasner, S.A.; Culbertson, C.T. Cellular analysis using microfluidics. *Analytical chemistry* **2017**, *90*.

135. Battat, S.; Weitz, D.A.; Whitesides, G.M. An outlook on microfluidics: the promise and the challenge. *Lab on a Chip* **2022**, *22*, 530-536.

136. Duncombe, T.A.; Tentori, A.M.; Herr, A.E. Microfluidics: reframing biological enquiry. *Nature reviews Molecular cell biology* **2015**, *16*, 554-567.

137. De Stefano, P.; Bianchi, E.; Dubini, G. The impact of microfluidics in high-throughput drug-screening applications. *Biomicrofluidics* **2022**, *16*, 031501.

138. Menon, N.V.; Lim, S.B.; Lim, C.T. Microfluidics for personalized drug screening of cancer. *Current Opinion in Pharmacology* **2019**, *48*, 155-161.

139. Shi, Y.; Cai, Y.; Cao, Y.; Hong, Z.; Chai, Y. Recent advances in microfluidic technology and applications for anti-cancer drug screening. *TrAC Trends in Analytical Chemistry* **2021**, *134*, 116118.

140. Radhakrishnan, J.; Varadaraj, S.; Dash, S.K.; Sharma, A.; Verma, R.S. Organotypic cancer tissue models for drug screening: 3D constructs, bioprinting and microfluidic chips. *Drug discovery today* **2020**, *25*, 879-890.

141. Dabbagh Moghaddam, F.; Romana Bertani, F. Application of microfluidic platforms in cancer therapy. *Materials Chemistry Horizons* **2022**, *1*, 69-88.

142. Kim, S.K.; Kim, Y.H.; Park, S.; Cho, S.-W. Organoid engineering with microfluidics and biomaterials for liver, lung disease, and cancer modeling. *Acta biomaterialia* **2021**, *132*, 37-51.

143. Liu, D.; Sun, M.; Zhang, J.; Hu, R.; Fu, W.; Xuanyuan, T.; Liu, W. Single-cell droplet microfluidics for biomedical applications. *Analyst* **2022**.

144. Fangjuan, Z.; Haibing, L.; Mengqi, G.; Defu, W.; Yanbing, N.; Shaofei, S. Concentration-gradient microfluidic chips for drug screening. *Progress in Chemistry* **2021**, *33*, 1138.

145. DiMasi, J.A.; Feldman, L.; Seckler, A.; Wilson, A. Trends in risks associated with new drug development: success rates for investigational drugs. *Clinical Pharmacology & Therapeutics* **2010**, *87*, 272-277.

146. Mohs, R.C.; Greig, N.H. Drug discovery and development: Role of basic biological research. *Alzheimer's & Dementia: Translational Research & Clinical Interventions* **2017**, *3*, 651-657.

147. Hait, W.N. Anticancer drug development: the grand challenges. *Nature reviews Drug discovery* **2010**, *9*, 253-254.

148. Drews, J. Drug discovery: a historical perspective. *science* **2000**, *287*, 1960-1964.

149. Harrison, R.G.; Greenman, M.; Mall, F.P.; Jackson, C. Observations of the living developing nerve fiber. *The Anatomical Record* **1907**, *1*, 116-128.

150. Michelini, E.; Cevenini, L.; Mezzanotte, L.; Coppa, A.; Roda, A. Cell-based assays: fuelling drug discovery. *Analytical and bioanalytical chemistry* **2010**, *398*, 227-238.

151. Zang, R.; Li, D.; Tang, I.-C.; Wang, J.; Yang, S.-T. Cell-based assays in high-throughput screening for drug discovery. *International Journal of Biotechnology for Wellness Industries* **2012**, *1*, 31-51.

152. DiMasi, J.A.; Grabowski, H.G.; Hansen, R.W. Innovation in the pharmaceutical industry: new estimates of R&D costs. *Journal of health economics* **2016**, *47*, 20-33.

153. Bonassar, L.J.; Vacanti, C.A. Tissue engineering: the first decade and beyond. *Journal of cellular biochemistry* **1998**, *72*, 297-303.

154. Edmondson, R.; Broglie, J.J.; Adcock, A.F.; Yang, L. Three-dimensional cell culture systems and their applications in drug discovery and cell-based biosensors. *Assay and drug development technologies* **2014**, *12*, 207-218.

155. Weaver, V.M.; Lelièvre, S.; Lakins, J.N.; Chrenek, M.A.; Jones, J.C.; Giancotti, F.; Werb, Z.; Bissell, M.J. β4 integrin-dependent formation of polarized three-dimensional architecture confers resistance to apoptosis in normal and malignant mammary epithelium. *Cancer cell* **2002**, *2*, 205-216.

156. Weigelt, B.; Ghajar, C.M.; Bissell, M.J. The need for complex 3D culture models to unravel novel pathways and identify accurate biomarkers in breast cancer. *Advanced drug delivery reviews* **2014**, *69*, 42-51.

157. Langhans, S.A. Three-dimensional in vitro cell culture models in drug discovery and drug repositioning. *Frontiers in pharmacology* **2018**, *9*, 6.

158. Prieto-Vila, M.; Takahashi, R.-u.; Usuba, W.; Kohama, I.; Ochiya, T. Drug resistance driven by cancer stem cells and their niche. *International Journal of Molecular Sciences* **2017**, *18*, 2574.

159. Bonnans, C.; Chou, J.; Werb, Z. Remodelling the extracellular matrix in development and disease. *Nature reviews Molecular cell biology* **2014**, *15*, 786-801.

160. Han, B.; Qu, C.; Park, K.; Konieczny, S.F.; Korc, M. Recapitulation of complex transport and action of drugs at the tumor microenvironment using tumor-microenvironment-on-chip. *Cancer letters* **2016**, *380*, 319-329.

161. Li, S.; Yang, K.; Chen, X.; Zhu, X.; Zhou, H.; Li, P.; Chen, Y.; Jiang, Y.; Li, T.; Qin, X. Simultaneous 2D and 3D cell culture array for multicellular geometry, drug discovery and tumor microenvironment reconstruction. *Biofabrication* **2021**, *13*, 045013.

162. Fiori, M.E.; Di Franco, S.; Villanova, L.; Bianca, P.; Stassi, G.; De Maria, R. Cancer-associated fibroblasts as abettors of tumor progression at the crossroads of EMT and therapy resistance. *Molecular cancer* **2019**, *18*, 1-16.

163. Das, S.; Shapiro, B.; Vucic, E.A.; Vogt, S.; Bar-Sagi, D. Tumor Cell–Derived IL1β Promotes Desmoplasia and Immune Suppression in Pancreatic CancerIL1β Promotes Immune Suppression in Pancreatic Cancer. *Cancer research* **2020**, *80*, 1088-1101.

164. Qiao, Y.; Zhang, C.; Li, A.; Wang, D.; Luo, Z.; Ping, Y.; Zhou, B.; Liu, S.; Li, H.; Yue, D. IL6 derived from cancer-associated fibroblasts promotes chemoresistance via CXCR7 in esophageal squamous cell carcinoma. *Oncogene* **2018**, *37*, 873-883.

165. Bradford, G.B.; Williams, B.; Rossi, R.; Bertoncello, I. Quiescence, cycling, and turnover in the primitive hematopoietic stem cell compartment. *Experimental hematology* **1997**, *25*, 445-453.

166. Fiori, M.E.; Villanova, L.; De Maria, R. Cancer stem cells: at the forefront of personalized medicine and immunotherapy. *Current Opinion in Pharmacology* **2017**, *35*, 1-11.

167. Migone, C. Three-dimensional polymeric systems for cancer cells studies. **2014**.

168. Debnath, J.; Brugge, J.S. Modelling glandular epithelial cancers in three-dimensional cultures. *Nature reviews cancer* **2005**, *5*, 675-688.

169. Kievit, F.M.; Florczyk, S.J.; Leung, M.C.; Wang, K.; Wu, J.D.; Silber, J.R.; Ellenbogen, R.G.; Lee, J.S.; Zhang, M. Proliferation and enrichment of CD133+ glioblastoma cancer stem cells on 3D chitosan-alginate scaffolds. *Biomaterials* **2014**, *35*, 9137-9143.

170. Liu, C.; Liu, Y.; Xu, X.-x.; Wu, H.; Xie, H.-g.; Chen, L.; Lu, T.; Yang, L.; Guo, X.; Sun, G.-w. Potential effect of matrix stiffness on the enrichment of tumor initiating cells under three-dimensional culture conditions. *Experimental cell research* **2015**, *330*, 123-134.

171. Yang, W.; Wang, Z.; Yu, T.; Chen, Y.; Ge, Z. Recent advance in cell patterning techniques: Approaches, applications and future prospects. *Sensors and Actuators A: Physical* **2021**, 113229.

172. Maramizonouz, S.; Tao, X.; Rahmati, M.; Jia, C.; Tao, R.; Torun, H.; Zheng, T.; Jin, H.; Dong, S.; Luo, J. Flexible and bendable acoustofluidics for particle and cell patterning. *International Journal of Mechanical Sciences* **2021**, *202*, 106536.

173. Cao, Q.; Fan, Q.; Chen, Q.; Liu, C.; Han, X.; Li, L. Recent advances in manipulation of micro-and nano-objects with magnetic fields at small scales. *Materials Horizons* **2020**, *7*, 638-666.

174. Chen, Y.-S.; Tung, C.-K.; Dai, T.-H.; Wang, X.; Yeh, C.-T.; Fan, S.-K.; Liu, C.-H. Liver-lobule-mimicking patterning via dielectrophoresis and hydrogel photopolymerization. *Sensors and Actuators B: Chemical* **2021**, *343*, 130159.

175. Song, Y.; Tian, Q.; Liu, J.; Guo, W.; Sun, Y.; Zhang, S. A reusable single-cell patterning strategy based on an ultrathin metal microstencil. *Lab on a Chip* **2021**, *21*, 1590-1597.

176. Yang, W.; Yu, H.; Wang, Y.; Liu, L. Regulation of cell adhesion to poly (ethylene glycol) diacrylate film by modification with polystyrene nano-spheres. In Proceedings of the 2016 IEEE 16th International Conference on Nanotechnology (IEEE-NANO), 2016; pp. 508-510.

177. Garcia-Hernando, M.; Calatayud-Sanchez, A.; Etxebarria-Elezgarai, J.; de Pancorbo, M.M.; Benito-Lopez, F.; Basabe-Desmonts, L. Optical single cell resolution cytotoxicity biosensor based on single cell adhesion dot arrays. *Analytical chemistry* **2020**, *92*, 9658-9665.

178. Park, J.; Choi, J.H.; Kim, S.; Jang, I.; Jeong, S.; Lee, J.Y. Micropatterned conductive hydrogels as multifunctional muscle-mimicking biomaterials: Graphene-incorporated hydrogels directly patterned with femtosecond laser ablation. *Acta biomaterialia* **2019**, *97*, 141-153.

179. Piya, R.; Zhu, Y.; Soeriyadi, A.H.; Silva, S.M.; Reece, P.J.; Gooding, J.J. Micropatterning of porous silicon B ragg reflectors with poly (ethylene glycol) to fabricate cell microarrays: Towards single cell sensing. *Biosensors and Bioelectronics* **2019**, *127*, 229-235.

180. Hou, Y.; Xie, W.; Achazi, K.; Cuellar-Camacho, J.L.; Melzig, M.F.; Chen, W.; Haag, R. Injectable degradable PVA microgels prepared by microfluidic technology for controlled osteogenic differentiation of mesenchymal stem cells. *Acta biomaterialia* **2018**, *77*, 28-37.

181. Zhang, J.; Luo, Y.; Poh, C.L. Blue light-directed cell migration, aggregation, and patterning. *Journal of molecular biology* **2020**, *432*, 3137-3148.

182. Li, M.; Liu, L.; Xi, N.; Wang, Y. Applications of micro/nano automation technology in detecting cancer cells for personalized medicine. *IEEE Transactions on Nanotechnology* **2017**, *16*, 217-229.

183. Zhong, H.; Xuan, L.; Wang, D.; Zhou, J.; Li, Y.; Jiang, Q. Generation of a co-culture cell micropattern model to simulate lung cancer bone metastasis for anti-cancer drug evaluation. *RSC advances* **2017**, *7*, 21837-21847.

184. Hadden, H.L.; Henke, C.A. Induction of lung fibroblast apoptosis by soluble fibronectin peptides. *American journal of respiratory and critical care medicine* **2000**, *162*, 1553-1560.

185. Discher, D.E.; Janmey, P.; Wang, Y.-l. Tissue cells feel and respond to the stiffness of their substrate. *Science* **2005**, *310*, 1139-1143.

186. Lee, J.; Jeon, O.; Kong, M.; Abdeen, A.A.; Shin, J.-Y.; Lee, H.N.; Lee, Y.B.; Sun, W.; Bandaru, P.; Alt, D.S. Combinatorial screening of biochemical and physical signals for phenotypic regulation of stem cell–based cartilage tissue engineering. *Science advances* **2020**, *6*, eaaz5913.

187. Stukel, J.M.; Willits, R.K. The interplay of peptide affinity and scaffold stiffness on neuronal differentiation of neural stem cells. *Biomedical Materials* **2018**, *13*, 024102.

188. Kapałczyńska, M.; Kolenda, T.; Przybyła, W.; Zajączkowska, M.; Teresiak, A.; Filas, V.; Ibbs, M.; Bliźniak, R.; Łuczewski, Ł.; Lamperska, K. 2D and 3D cell cultures–a comparison of different types of cancer cell cultures. *Archives of Medical Science* **2018**, *14*, 910-919.

189. Justice, B.A.; Badr, N.A.; Felder, R.A. 3D cell culture opens new dimensions in cell-based assays. *Drug discovery today* **2009**, *14*, 102-107.

190. Costa, E.C.; Moreira, A.F.; de Melo-Diogo, D.; Gaspar, V.M.; Carvalho, M.P.; Correia, I.J. 3D tumor spheroids: an overview on the tools and techniques used for their analysis. *Biotechnology advances* **2016**, *34*, 1427-1441.

191. Suri, S.; Schmidt, C.E. Cell-laden hydrogel constructs of hyaluronic acid, collagen, and laminin for neural tissue engineering. *Tissue Engineering Part A* **2010**, *16*, 1703-1716.

192. King, K.R.; Wang, C.C.J.; Kaazempur-Mofrad, M.R.; Vacanti, J.P.; Borenstein, J.T. Biodegradable microfluidics. *Advanced Materials* **2004**, *16*, 2007-2012.

193. Bettinger, C.J.; Weinberg, E.J.; Kulig, K.M.; Vacanti, J.P.; Wang, Y.; Borenstein, J.T.; Langer, R. Three-dimensional microfluidic tissue-engineering scaffolds using a flexible biodegradable polymer. *Advanced Materials* **2006**, *18*, 165-169.

194. Borenstein, J.T.; Tupper, M.M.; Mack, P.J.; Weinberg, E.J.; Khalil, A.S.; Hsiao, J.; García-Cardeña, G. Functional endothelialized microvascular networks with circular cross-sections in a tissue culture substrate. *Biomedical microdevices* **2010**, *12*, 71-79.

195. Wang, J.; Bettinger, C.J.; Langer, R.S.; Borenstein, J.T. Biodegradable microfluidic scaffolds for tissue engineering from amino alcohol-based poly (ester amide) elastomers. *Organogenesis* **2010**, *6*, 212-216.

196. Li, X.; Valadez, A.V.; Zuo, P.; Nie, Z. Microfluidic 3D cell culture: potential application for tissue-based bioassays. *Bioanalysis* **2012**, *4*, 1509-1525.

197. Kim, L.; Toh, Y.-C.; Voldman, J.; Yu, H. A practical guide to microfluidic perfusion culture of adherent mammalian cells. *Lab on a Chip* **2007**, *7*, 681-694.

198. Florczyk, S.J.; Liu, G.; Kievit, F.M.; Lewis, A.M.; Wu, J.D.; Zhang, M. 3D porous chitosan–alginate scaffolds: a new matrix for studying prostate cancer cell–lymphocyte interactions in vitro. *Advanced healthcare materials* **2012**, *1*, 590-599.

199. Frantz, C.; Stewart, K.M.; Weaver, V.M. The extracellular matrix at a glance. *Journal of cell science* **2010**, *123*, 4195-4200.

200. Sepantafar, M.; Maheronnaghsh, R.; Mohammadi, H.; Radmanesh, F.; Hasani-Sadrabadi, M.M.; Ebrahimi, M.; Baharvand, H. Engineered hydrogels in cancer therapy and diagnosis. *Trends in biotechnology* **2017**, *35*, 1074-1087.

201. Debnath, T.; Ghosh, S.; Potlapuvu, U.S.; Kona, L.; Kamaraju, S.R.; Sarkar, S.; Gaddam, S.; Chelluri, L.K. Proliferation and differentiation potential of human adipose-derived stem cells grown on chitosan hydrogel. *PloS one* **2015**, *10*, e0120803.

202. Benoit, D.S.; Schwartz, M.P.; Durney, A.R.; Anseth, K.S. Small functional groups for controlled differentiation of hydrogel-encapsulated human mesenchymal stem cells. *Nature materials* **2008**, *7*, 816-823.

203. Caliari, S.R.; Burdick, J.A. A practical guide to hydrogels for cell culture. *Nature methods* **2016**, *13*, 405-414.

204. Hunt, N.C.; Hallam, D.; Karimi, A.; Mellough, C.B.; Chen, J.; Steel, D.H.; Lako, M. 3D culture of human pluripotent stem cells in RGD-alginate hydrogel improves retinal tissue development. *Acta biomaterialia* **2017**, *49*, 329-343.

205. Hochleitner, G.; Chen, F.; Blum, C.; Dalton, P.D.; Amsden, B.; Groll, J. Melt electrowriting below the critical translation speed to fabricate crimped elastomer scaffolds with non-linear extension behaviour mimicking that of ligaments and tendons. *Acta biomaterialia* **2018**, *72*, 110-120.

206. Zhao, C.; Li, Y.; Peng, G.; Lei, X.; Zhang, G.; Gao, Y. Decellularized liver matrix-modified chitosan fibrous scaffold as a substrate for C3A hepatocyte culture. *Journal of Biomaterials Science, Polymer Edition* **2020**, *31*, 1041-1056.

207. Taylor, D.A.; Lee, P.-F.; Barac, Y.; Hochman-Mendez, C.; Sampaio, L.C. Decellularization of whole hearts for cardiac regeneration. In *Emerging Technologies for Heart Diseases*; Elsevier: **2020**; pp. 291-310.

208. Seo, Y.; Jung, Y.; Kim, S.H. Decellularized heart ECM hydrogel using supercritical carbon dioxide for improved angiogenesis. *Acta biomaterialia* **2018**, *67*, 270-281.

209. Daly, A.C.; Davidson, M.D.; Burdick, J.A. 3D bioprinting of high cell-density heterogeneous tissue models through spheroid fusion within self-healing hydrogels. *Nature communications* **2021**, *12*, 1-13.

210. Cesarz, Z.; Tamama, K. Spheroid culture of mesenchymal stem cells. *Stem cells international* **2016**, *2016*.

211. Aldemir Dikici, B.; Claeyssens, F. Basic principles of emulsion templating and its use as an emerging manufacturing method of tissue engineering scaffolds. *Frontiers in Bioengineering and Biotechnology* **2020**, *8*, 875.

212. Bejleri, D.; Streeter, B.W.; Nachlas, A.L.; Brown, M.E.; Gaetani, R.; Christman, K.L.; Davis, M.E. A bioprinted cardiac patch composed of cardiac-specific extracellular matrix and progenitor cells for heart repair. *Advanced healthcare materials* **2018**, *7*, 1800672.

213. Jain, P.; Kathuria, H.; Dubey, N. Advances in 3D bioprinting of tissues/organs for regenerative medicine and in-vitro models. *Biomaterials* **2022**, *287*, 121639.

214. Chang, P.-H.; Chao, H.-M.; Chern, E.; Hsu, S.-h. Chitosan 3D cell culture system promotes naïve-like features of human induced pluripotent stem cells: A novel tool to sustain pluripotency and facilitate differentiation. *Biomaterials* **2021**, *268*, 120575.

215. Subia, B.; Dahiya, U.R.; Mishra, S.; Ayache, J.; Casquillas, G.V.; Caballero, D.; Reis, R.L.; Kundu, S.C. Breast tumor-on-chip models: From disease modeling to personalized drug screening. *Journal of controlled release* **2021**, *331*, 103-120.

216. Nuciforo, S.; Heim, M.H. Organoids to model liver disease. *JHEP Reports* **2021**, *3*, 100198.

217. Zhang, L.; Liu, F.; Weygant, N.; Zhang, J.; Hu, P.; Qin, Z.; Yang, J.; Cheng, Q.; Fan, F.; Zeng, Y. A novel integrated system using patient-derived glioma cerebral organoids and xenografts for disease modeling and drug screening. *Cancer letters* **2021**, *500*, 87-97.

218. Gebeyehu, A.; Surapaneni, S.K.; Huang, J.; Mondal, A.; Wang, V.Z.; Haruna, N.F.; Bagde, A.; Arthur, P.; Kutlehria, S.; Patel, N. Polysaccharide hydrogel based 3D printed tumor models for chemotherapeutic drug screening. *Scientific reports* **2021**, *11*, 1-15.

219. Groveman, B.R.; Ferreira, N.C.; Foliaki, S.T.; Walters, R.O.; Winkler, C.W.; Race, B.; Hughson, A.G.; Zanusso, G.; Haigh, C.L. Human cerebral organoids as a therapeutic drug screening model for Creutzfeldt–Jakob disease. *Scientific reports* **2021**, *11*, 1-9.

220. Qian, L.; Tcw, J. Human iPSC-based modeling of central nerve system disorders for drug discovery. *International journal of molecular sciences* **2021**, *22*, 1203.

221. Barros, A.S.; Costa, A.; Sarmento, B. Building three-dimensional lung models for studying pharmacokinetics of inhaled drugs. *Advanced drug delivery reviews* **2021**, *170*, 386-395.

222. Hickman, J.A.; Graeser, R.; de Hoogt, R.; Vidic, S.; Brito, C.; Gutekunst, M.; van der Kuip, H. Three-dimensional models of cancer for pharmacology and cancer cell biology: capturing tumor complexity in vitro/ex vivo. *Biotechnology journal* **2014**, *9*, 1115-1128.

223. Imamura, Y.; Mukohara, T.; Shimono, Y.; Funakoshi, Y.; Chayahara, N.; Toyoda, M.; Kiyota, N.; Takao, S.; Kono, S.; Nakatsura, T. Comparison of 2D-and 3D-culture models as drug-testing platforms in breast cancer. *Oncology reports* **2015**, *33*, 1837-1843.

224. Melissaridou, S.; Wiechec, E.; Magan, M.; Jain, M.V.; Chung, M.K.; Farnebo, L.; Roberg, K. The effect of 2D and 3D cell cultures on treatment response, EMT profile and stem cell features in head and neck cancer. *Cancer cell international* **2019**, *19*, 1-10.

225. Bissell, M.J.; LaBarge, M.A. Context, tissue plasticity, and cancer: are tumor stem cells also regulated by the microenvironment? *Cancer cell* **2005**, *7*, 17-23.

226. Kapałczyńska, M.; Kolenda, T.; Przybyła, W.; Zajączkowska, M.; Teresiak, A.; Filas, V.; Ibbs, M.; Bliźniak, R.; Łuczewski, Ł.; Lamperska, K. 2D and 3D cell cultures–a comparison of different types of cancer cell cultures. *Archives of medical science: AMS* **2018**, *14*, 910.

227. Yliperttula, M.; Chung, B.G.; Navaladi, A.; Manbachi, A.; Urtti, A. High-throughput screening of cell responses to biomaterials. *european journal of pharmaceutical sciences* **2008**, *35*, 151-160.

228. Xia, Y.; Whitesides, G.M. Soft lithography. *Annual review of materials science* **1998**, *28*, 153-184.

229. Thorsen, T.; Maerkl, S.J.; Quake, S.R. Microfluidic large-scale integration. *science* **2002**, *298*, 580-584.

230. Beebe, D.J.; Mensing, G.A.; Walker, G.M. Physics and applications of microfluidics in biology. *Annual review of biomedical engineering* **2002**, *4*, 261-286.

231. Fiorini, G.S.; Chiu, D.T. Disposable microfluidic devices: fabrication, function, and application. *BioTechniques* **2005**, *38*, 429-446.

232. Nur, O.; Willander, M. Low Temperature Chemical Nanofabrication: Recent Progress, Challenges and Emerging Technologies. **2019**.

233. Kim, P.; Kwon, K.W.; Park, M.C.; Lee, S.H.; Kim, S.M.; Suh, K.Y. Soft lithography for microfluidics: a review. **2008**.

234. Bruus, H. *Theoretical microfluidics*; Oxford university press Oxford: 2008; Volume 18.

235. Halldorsson, S.; Lucumi, E.; Gómez-Sjöberg, R.; Fleming, R.M. Advantages and challenges of microfluidic cell culture in polydimethylsiloxane devices. *Biosensors and Bioelectronics* **2015**, *63*, 218-231.

236. Song, Y.; Zhao, X.; Tian, Q.; Liang, H. Fundamental concepts and physics in microfluidics. *Microfluidics: Fundamentals, Devices, and Applications* **2018**.

237. Wu, M.-H.; Huang, S.-B.; Lee, G.-B. Microfluidic cell culture systems for drug research. *Lab on a Chip* **2010**, *10*, 939-956.

238. Sato, K.; Tokeshi, M.; Sawada, T.; Kitamori, T. Molecular transport between two phases in a microchannel. *Analytical sciences* **2000**, *16*, 455-456.

239. Dertinger, S.K.; Chiu, D.T.; Jeon, N.L.; Whitesides, G.M. Generation of gradients having complex shapes using microfluidic networks. *Analytical chemistry* **2001**, *73*, 1240-1246.

240. Teh, S.-Y.; Lin, R.; Hung, L.-H.; Lee, A.P. Droplet microfluidics. *Lab on a Chip* **2008**, *8*, 198-220.

241. Abou-Hassan, A.; Sandre, O.; Cabuil, V. Microfluidics in inorganic chemistry. *Angewandte Chemie International Edition* **2010**, *49*, 6268-6286.

242. Bruzewicz, D.A.; McGuigan, A.P.; Whitesides, G.M. Fabrication of a modular tissue construct in a microfluidic chip. *Lab on a Chip* **2008**, *8*, 663-671.

243. Novo, P.; Volpetti, F.; Chu, V.; Conde, J.P. Control of sequential fluid delivery in a fully autonomous capillary microfluidic device. *Lab on a Chip* **2013**, *13*, 641-645.

244. Takayama, S.; McDonald, J.C.; Ostuni, E.; Liang, M.N.; Kenis, P.J.; Ismagilov, R.F.; Whitesides, G.M. Patterning cells and their environments using multiple laminar fluid flows in capillary networks. *Proceedings of the National Academy of Sciences* **1999**, *96*, 5545-5548.

245. Chiu, D.T.; Jeon, N.L.; Huang, S.; Kane, R.S.; Wargo, C.J.; Choi, I.S.; Ingber, D.E.; Whitesides, G.M. Patterned deposition of cells and proteins onto surfaces by using three-dimensional microfluidic systems. *Proceedings of the National Academy of Sciences* **2000**, *97*, 2408-2413.

246. Gottwald, E.; Giselbrecht, S.; Augspurger, C.; Lahni, B.; Dambrowsky, N.; Truckenmüller, R.; Piotter, V.; Gietzelt, T.; Wendt, O.; Pfleging, W. A chip-based platform for the in vitro generation of tissues in three-dimensional organization. *Lab on a Chip* **2007**, *7*, 777-785.

247. Liu, A.; Islam, M.; Stone, N.; Varadarajan, V.; Jeong, J.; Bowie, S.; Qiu, P.; Waller, E.K.; Alexeev, A.; Sulchek, T. Microfluidic generation of transient cell volume exchange for convectively driven intracellular delivery of large macromolecules. *Materials Today* **2018**, *21*, 703-712.

248. Agresti, J.J.; Antipov, E.; Abate, A.R.; Ahn, K.; Rowat, A.C.; Baret, J.-C.; Marquez, M.; Klibanov, A.M.; Griffiths, A.D.; Weitz, D.A. Ultrahigh-throughput screening in drop-based microfluidics for directed evolution. *Proceedings of the National Academy of Sciences* **2010**, *107*, 4004-4009.

249. Yeo, L.Y.; Chang, H.C.; Chan, P.P.; Friend, J.R. Microfluidic devices for bioapplications. *Small* **2011**, *7*, 12-48.

250. Ren, X.; Ghassemi, P.; Babahosseini, H.; Strobl, J.S.; Agah, M. Single-cell mechanical characteristics analyzed by multiconstriction microfluidic channels. *ACS sensors* **2017**, *2*, 290-299.

251. Paguirigan, A.L.; Beebe, D.J. From the cellular perspective: exploring differences in the cellular baseline in macroscale and microfluidic cultures. *Integrative Biology* **2009**, *1*, 182-195.

252. Heo, Y.S.; Cabrera, L.M.; Song, J.W.; Futai, N.; Tung, Y.-C.; Smith, G.D.; Takayama, S. Characterization and resolution of evaporation-mediated osmolality shifts that constrain microfluidic cell culture in poly (dimethylsiloxane) devices. *Analytical chemistry* **2007**, *79*, 1126-1134.

253. Paguirigan, A.L.; Beebe, D.J. Microfluidics meet cell biology: bridging the gap by validation and application of microscale techniques for cell biological assays. *BioEssays* **2008**, *30*, 811-821.

254. Shourabi, A.Y.; Kashaninejad, N.; Saidi, M.S. An integrated microfluidic concentration gradient generator for mechanical stimulation and drug delivery. *Journal of Science: Advanced Materials and Devices* **2021**, *6*, 280-290.

255. Shen, S.; Zhang, X.; Zhang, F.; Wang, D.; Long, D.; Niu, Y. Three-gradient constructions in a flow-rate insensitive microfluidic system for drug screening towards personalized treatment. *Talanta* **2020**, *208*, 120477.

256. Lee, R.; Lee, J.; Kim, K.-B.; Kim, J. Microfluidic system with light intensity filters facilitating the application of photodynamic therapy for high-throughput drug screening. *Photodiagnosis and Photodynamic Therapy* **2022**, *38*, 102812.

257. Azizi, M.; Davaji, B.; Nguyen, A.V.; Zhang, S.; Dogan, B.; Simpson, K.W.; Abbaspourrad, A. Gradient-Based Microfluidic Platform for One Single Rapid Antimicrobial Susceptibility Testing. *ACS sensors* **2021**, *6*, 1560-1571.

258. Lin, X.; Su, J.; Zhou, S. Microfluidic chip of concentration gradient and fluid shear stress on a single cell level. *Chinese Chemical Letters* **2022**, *33*, 3133-3138.

259. Klein, A.M.; Mazutis, L.; Akartuna, I.; Tallapragada, N.; Veres, A.; Li, V.; Peshkin, L.; Weitz, D.A.; Kirschner, M.W. Droplet barcoding for single-cell transcriptomics applied to embryonic stem cells. *Cell* **2015**, *161*, 1187-1201.

260. Matuła, K.; Rivello, F.; Huck, W.T. Single-cell analysis using droplet microfluidics. *Advanced Biosystems* **2020**, *4*, 1900188.

261. Chan, H.F.; Zhang, Y.; Ho, Y.-P.; Chiu, Y.-L.; Jung, Y.; Leong, K.W. Rapid formation of multicellular spheroids in double-emulsion droplets with controllable microenvironment. *Scientific reports* **2013**, *3*, 1-8.

262. Dafale, N.A.; Semwal, U.P.; Rajput, R.K.; Singh, G. Selection of appropriate analytical tools to determine the potency and bioactivity of antibiotics and antibiotic resistance. *Journal of pharmaceutical analysis* **2016**, *6*, 207-213.

263. Chen, X.; Chen, H.; Wu, D.; Chen, Q.; Zhou, Z.; Zhang, R.; Peng, X.; Su, Y.-C.; Sun, D. 3D printed microfluidic chip for multiple anticancer drug combinations. *Sensors and Actuators B: Chemical* **2018**, *276*, 507-516.

264. Liu, P.; Fu, L.; Song, Z.; Man, M.; Yuan, H.; Zheng, X.; Kang, Q.; Shen, D.; Song, J.; Li, B. Three dimensionally printed nitrocellulose-based microfluidic platform for investigating the effect of oxygen gradient on cells. *Analyst* **2021**, *146*, 5255-5263.

265. Shah, G.J.; Ding, H.; Sadeghi, S.; Chen, S.; van Dam, R.M. On-demand droplet loading for automated organic chemistry on digital microfluidics. *Lab on a Chip* **2013**, *13*, 2785-2795.

266. Ng, A.H.; Li, B.B.; Chamberlain, M.D.; Wheeler, A.R. Digital microfluidic cell culture. *Annual review of biomedical engineering* **2015**, *17*, 91-112.

267. Zhang, Y.; Liu, Y. A digital microfluidic device integrated with electrochemical impedance spectroscopy for cell-based immunoassay. *Biosensors* **2022**, *12*, 330.

268. Yang, J.; Deng, Y.; Zhang, M.; Feng, S.; Peng, S.; Yang, S.; Liu, P.; Cai, G.; Ge, G. Construction and Manipulation of Serial Gradient Dilution Array on a Microfluidic Slipchip for Screening and Characterizing Inhibitors against Human Pancreatic Lipase. *Biosensors* **2023**, *13*, 274.

269. Li, X.; Liu, X.; Yu, Z.; Luo, Y.; Hu, Q.; Xu, Z.; Dai, J.; Wu, N.; Shen, F. Combinatorial screening SlipChip for rapid phenotypic antimicrobial susceptibility testing. *Lab on a Chip* **2022**, *22*, 3952-3960.

270. Chang, C.-W.; Peng, C.-C.; Liao, W.-H.; Tung, Y.-C. Polydimethylsiloxane SlipChip for mammalian cell culture applications. *Analyst* **2015**, *140*, 7355-7365.

271. Zhai, J.; Yi, S.; Jia, Y.; Mak, P.-I.; Martins, R.P. Cell-based drug screening on microfluidics. *TrAC Trends in Analytical Chemistry* **2019**, *117*, 231-241.

272. Mao, K.; Min, X.; Zhang, H.; Zhang, K.; Cao, H.; Guo, Y.; Yang, Z. based microfluidics for rapid diagnostics and drug delivery. *Journal of controlled release* **2020**, *322*, 187-199.

273. Fu, S.x.; Zuo, P.; Ye, B.C. A novel wick-like paper-based microfluidic device for 3D cell culture and anti-cancer drugs screening. *Biotechnology Journal* **2021**, *16*, 2000126.

CHAPTER 2

Stealth magnetoliposomes based on spherical calcium-substituted magnesium ferrite nanoparticles

This chapter describes the preparation of spherical calcium-substituted magnesium ferrite nanoparticles ($Ca_xMg_{1-x}Fe_2O_4$) with different ratios of magnesium and calcium and the influence that the partial replacement of magnesium by calcium in the ferrite structure has on its properties. These particles were used to synthesise stealth solid and aqueous magnetoliposomes as nanocarriers of a model drug – curcumin – as a proof-of-concept of biocompatible nanosystems with potential application in cancer therapy. The results were published in *International Journal of Molecular Sciences*.

Cardoso, B.D.; Rodrigues, A.R.O.; Almeida, B.G.; Amorim, C.O.; Amaral, V.S.; Castanheira, E.M.; Coutinho, P.J. Stealth magnetoliposomes based on calcium-substituted magnesium ferrite nanoparticles for curcumin transport and release. *International journal of molecular sciences* **2020**, *21*, 3641.

2.1. Overview

Despite the promising pharmacological properties of curcumin, the transport and effective release of this drug is still a challenge. The advances in functionalised nanocarriers for curcumin have also been motivated by the anticancer activity of this natural compound, aiming at controlled release therapies. Here, stealth (aqueous and solid) magnetoliposomes containing calcium-substituted magnesium ferrite nanoparticles, $Ca_xMg_{1-x}Fe_2O_4$ (with x = 0.25, 0.50, 0.75) were developed as nanocarriers for curcumin. The magnetic nanoparticles exhibit superparamagnetic properties and crystalline structure, with sizes below 10 nm. The magnetoliposomes based on these nanoparticles have hydrodynamic diameters around or below 150 nm and a low polydispersity. The influence of an AMF on drug release over time was evaluated and compared with curcumin released by diffusion. The results suggest the potential of drug-loaded magnetoliposomes as nanocarriers that can be magnetically guided to the tumour and act as agents for a synergistic effect combining magnetic hyperthermia and controlled drug release.

2.2. Introduction

Curcumin is a polyphenolic compound that can be extracted from Turmeric Curcuma longa rhizomes [1]. This phytochemical is a liposoluble compound showing many promising pharmacological properties that result from its ability to regulate different immunomodulators, which are substances that can boost or suppress the host defence [2]. This property is especially relevant in cancer therapy as the development of different types of cancer results from genomic instabilities often potentiated by infectious diseases and chronic inflammation disorders [3]. The induced inflammatory processes produce and release pro-inflammatory molecules involved in tumour initiation and growth [4]. These molecules include the transcription factor activator protein-1 (AP-1) [5], cyclooxygenase-2 (COX-2) [6,7], nuclear factor kappa-light-chain-enhancer of activated B cells (NF-Kb) [8,9], and reactive oxygen species (ROS) [10,11]. The regulation of these immunomodulators and, consequently, the anticancer activity of curcumin results from its antioxidant, anti-inflammatory, anti-angiogenesis, induction of apoptosis and anti-metastasis effect [12-15]. Furthermore, consuming this compound at levels up to 20 mg as a food additive is considered safe by the United States Food and Drug Administration (US FDA) [16].

However, despite its safety and multiple biological activities, this compound has several challenges that limit its therapeutic use. Curcumin is chemically unstable, mainly associated with solvolysis and oxidative degradation that results in the production of some degradation products (e.g., vanillin, ferulic acid, and

diferuloylmethane) [17]. It is also sensitive to type I and II reactions with molecular oxygen, resulting in photochemical degradation [18]. In addition, it presents a low water solubility (456 μg/L), poor absorption, rapid metabolism, and elimination, which limit its biomedical use and therapeutic effect, justifying the lack of success in clinical trials [19,20]. In recent years, the scientific community has focused on developing strategies to improve curcumin ADMET properties (absorption, distribution, metabolism, excretion and toxicology) and its specificity [21]. Some of these drawbacks can be minimized by curcumin encapsulation in suitable nanosystems.

Drug delivery systems are one of the most employed and practical strategies to address drug bioavailability issues by protecting and carrying payloads to the target site [22,23]. The nanocarriers include, for instance, micelles [24-26], microemulsions [27-29], nanogels [30,31], polymeric nanoparticles [32-34], carbon nanotubes [35,36], magnetic nanoparticles [37,38], and liposomes [39,40]. Liposomes are layered lipid vesicles that can encapsulate a wide range of compounds and improve their solubility while showing high biocompatibility, low toxicity, and immunogenicity (detailed in **section 1.1.2**). The liposome preparation method and composition variations allow for modifying their inherent features, such as size, circulation time in biological conditions, responsiveness to specific external and internal stimuli, and control of payload release [41,42]. All the modifications must be accurately thought out to take advantage of the uniqueness of physiological cancer features since they include chemical (such as enzyme concentration and pH) and structural (capillary structure) differences compared to normal cells/tissues [43-47].

One of the structural features most widely explored by liposomal nanomedicine is the leaky nature of tumour blood vessels, characterized by the presence of gaps within the range of 100-780 nm between the endothelial cells of tumour capillaries and contrary to the 5-10 nm of typical normal endothelium [48]. This is the most critical feature that ensures the liposomes as an effective strategy for passive targeting. This phenomenon, known as the Enhanced Permeability and Retention (EPR) effect, allows the extravasation of liposomes smaller than 400 nm, but it is more effective at sizes below 200 nm [49-52]. However, it is recognized that intravenously injected liposomes are opsonized by plasma components (opsonins) and uptaken by the mononuclear phagocyte system (MPS) [53,54]. The surface modifications of the nanocarrier's surface can significantly affect its circulation time [55]. Polyethylene glycol (PEG) is a highly hydrophilic polymer that forms a hydrophilic shield on the surface of the liposome and has been used to obtain sterically stabilized liposomes. PEGylated liposomes (also known as stealth liposomes) contribute to a prolonged systemic circulation by protecting the active moiety from the immune system, changing its physicochemical properties (as the hydrodynamic size) and providing hydrophilicity to

hydrophobic drugs without changing their mechanism of action. Yet, it is reported that the liposomes' ability to interact and release drugs in the target is reduced [56], and the associated inadequate blood perfusion in tumours leads to a low pH and oxygen (hypoxia) inside the solid tumours and surrounding tissues [57]. These conditions difficult the therapeutic effect of either radiotherapy (based on the creation of ROS) [58] or chemotherapy (since the drugs cannot concentrate in the tumour at the therapeutic dosage). Therefore, many efforts are being made to improve liposomes' further therapeutic effectiveness. Superparamagnetic nanoparticles are single-domain magnetic materials that can be entrapped in liposomes- forming magnetoliposomes- asserting themselves as a controlled delivery strategy for cargo-controlled delivery and release from liposomes under magnetic stimuli (detailed information in **section 1.1.3, 1.1.4,** and **1.1.5**). However, even though Fe_3O_4 and maghemite (γ-Fe_2O_3) are the most studied nanoparticles for magnetic hyperthermia [59], they have been associated with a tendency to react with oxygen, resulting in the production of free radicals as ROS, leading to oxidative damage in the human body [60].

As a result, the synthesis of nanoparticles without transition metals has been explored as a more biocompatible alternative. Spinel ferrites, MFe_2O_4 (where M = Fe, Mn, Zn, Co, Mg, Cu, Ni) present unique electric, optical and magnetic properties [61,62]. Magnesium ferrite ($MgFe_2O_4$) is a class of compounds that crystalize into an inverse spinel structure with tetrahedral (A) and octahedral (B) sites, where cations distribution occurs [63]. This type of particle is an excellent candidate to improve the biocompatibility associated with nanoparticles since magnesium ions are related to genomic stability, are involved in energy generation through ATP hydrolysis, and in the catalytic activity of enzymatic systems in DNA processing [64]. In addition, a specific absorption rate (SAR) potentiation has been reported due to an increase in momentum and magnetic susceptibility induced by particle dipole interaction energy [65,66]. Since the spinel structure allows a high diffusibility of M^{2+} ions, the distribution of cations in the crystal lattice sites is susceptible to heat treatments [64,67]. In turn, the magnitude of magnetism is highly sensitive to the synthesis methodology, the distribution of magnetic ions in tetrahedral and octahedral sites, and grain size and shape [65]. The substitution of transition and diamagnetic metal ions is a strategy that can be followed to improve spinel ferrites' magnetization [68]. Calcium ferrite ($CaFe_2O_4$) nanoparticles are also biocompatible, eco-friendly and present high thermal stability [69]. Calcium-substituted magnesium ferrite nanoparticles ($Ca_xMg_{1-x}Fe_2O_4$) can increase ferrites' biocompatibility and improve magnetic properties [70,71]. It is reported that magnesium ferrite nanoparticles showed an enhanced magnetization upon doping with nonmagnetic Zn^{2+} ions, resulting from changes in the ion's site distribution [72,73].

Taking all this into account, the following subsection detail the synthesis of magnesium and calcium-based mixed ferrites and their inclusion as a central part of the magnetoliposomes. Thus, three different proportions of calcium and magnesium were used to synthesize $Ca_xMg_{1-x}Fe_2O_4$ nanoparticles (x = 0.75, 0.25, 0.50), and their optical, structural, morphological, and magnetic properties were characterized. The mixed ferrites were included in magnetoliposomes, forming the magnetic core, either within an aqueous phase (AMLs) or surrounded by a lipid bilayer without water (SMLs). Curcumin was encapsulated in these novel nanosystems, and its release rate was evaluated under an AMF. In addition, the influence of magnetoliposomes PEGylation in curcumin location and release was also investigated. The developed nanosystems are promising for applications as curcumin nanocarriers for synergistic cancer therapy (using a combined approach of magnetic hyperthermia and chemotherapy), considering curcumin's already reported antitumor properties.

2.3. Materials and Methods

Ultrapure water Milli-Q grade (MilliporeSigma, St. Louis, MO, USA) and spectroscopic grade solvents were used in all preparation steps.

To synthesize magnetic nanoparticles, the following chemicals were used: magnesium sulfate ($MgSO_4$, from Sigma-Aldrich, St. Louis, MO, USA); calcium acetate hydrate $(CH_3COO)_2Ca \cdot x\ H_2O$, from Sigma-Aldrich, St. Louis, MO, USA); and iron (III) chloride hexahydrate ($FeCl_3 \cdot 6\ H_2O$, from Sigma-Aldrich, St. Louis, MO, USA).

The following chemicals were used to synthesize lipid bilayers: egg yolk phosphatidylcholine (Egg-PC, from Sigma-Aldrich, St. Louis, MO, USA); DPPC (1,2-dipalmitoyl-sn-glycero-3-phosphocholine, from Sigma-Aldrich, St. Louis, MO, USA); Soybean lecithin (L-α-Phosphatidylcholine), from Sigma-Aldrich St. Louis, MO, USA; N-(lissamine rhodamine B sulfonyl)-1,2-dioleoyl-sn-3-phosphatidylethanolamine (Rh-DOPE) (ammonium salt) (from Avanti Polar Lipids, Birmingham, AL, USA)); and nitrobenzoxazole labelled lipid NBD-C12-HPC (from Avanti Polar Lipids, Birmingham, AL, USA).

2.3.1. Preparation of spherical $Ca_xMg_{1-x}Fe_2O_4$ ferrite nanoparticles

Calcium-substituted magnesium ferrite nanoparticles ($Ca_xMg_{1-x}Fe_2O_4$) were prepared by the co-precipitation method. First, 10 mL of an aqueous solution containing magnesium sulfate, calcium acetate hydrate at the corresponding molarity (for x = 0.25, 0.50, or 0.75), and iron (III) chloride hexahydrate

were prepared in a 1:2 molar ratio. The corresponding masses were weighed on an analytical microbalance (Sartorius, M2P microbalance). The raw materials were dissolved in water and stirred on a hot-plate magnetic stirrer (IKA, C-MAG HS 4) at 75 °C until a clear solution was obtained. Then, the resulting mixture was added, drop by drop, to a 15 mL aqueous solution containing sodium hydroxide at 5 M at 90 °C, under constant and vigorous magnetic stirring on a hot-plate for 15 min. After that, the solution was cooled to room temperature, resulting in a black precipitation. Next, the precipitated nanoparticles were washed by several cycles of centrifugation (Hettich, UNIVERSAL 320) at 5000 rpm for 5 min and redispersed in water. Finally, to obtain a crystalline phase, the nanoparticles were calcined at 600 °C for 30 min.

2.3.2. Preparation of aqueous and solid magnetoliposomes

For AMLs preparation, where magnetic nanoparticles are encapsulated in liposomes, an ethanolic solution of Egg-PC was injected, under vortex, onto 3 mL of an aqueous solution containing 0.1 mM of nanoparticles, to a final lipid concentration of 1 mM (ethanolic injection method [74,75]). Then, the ferrofluid was washed with water by magnetic decantation to eliminate the non-encapsulated nanoparticles. Finally, curcumin was incorporated into AMLs by the co-injection method, as previously described by [76].

The preparation methodology of SMLs, consisting of a lipid bilayer surrounding a cluster of magnetic nanoparticles, and the ability to synthesize SMLs has been proven in previous works [76] using the lipid DPPC. First, 10 µl of the previously synthesized $Mg_{1-x}Fe_2O_4$ ferrite nanoparticles were dispersed in 3 ml of water and centrifuged (7000 rpm for 5 min). Next, the deposited nanoparticles were dispersed in 10 µl of water, ultrasonicated for 1 min at 189 W, and then dispersed in 3 ml of chloroform, forming nanoparticles clusters. To form the first lipid layer, the solution containing the clusters was heated up to 55°C (above the melting temperature of DPPC, 41°C [77]), and a DPPC ethanolic lipid solution (at 1 mM) was injected to 3 mL of nanoparticles aqueous solution under vortex stirrer (LBX, V05 series). Next, magnetic decantation was performed for SMLs purification, removing lipid aggregates and liposomes without a magnetic core, and washed with ultrapure water. For the second lipid layer formation, the purified SMLs aqueous solution was heated up to 55°C, and a DPPC ethanolic solution (at 1 mM) was injected under vorte stirrer. Finally, 1 µM of curcumin was dissolved in 150 µL of ethanol (96%) and which was injected to the SMLs, under vortexing, right before forming the second lipid layer.

Hydrodynamic diameters and polydispersity index (PDI) of the prepared SMLs were determined in a dynamic light scattering (DLS) equipment NANO ZS Malvern Zetasizer (Malvern Panalytical Ltd., Malvern,

UK), at 25 °C, using a He-Ne laser of λ = 632.8 nm and a detector angle of 173°. Five independent measurements were performed for each sample.

2.3.3. Preparation of giant unilamellar vesicles

Soybean lecithin (L-α-Phosphatidylcholine), from Sigma-Aldrich St. Louis, MO, USA, was used for GUVs preparation using a procedure described by Tamba *et al.* [78,79]. First, 100 ml of soybean lecithin solution (1 mM) were dried under an argon stream to produce a thin and homogeneous lipid film of soybean lecithin. Next, 40 mL of water was added to the film and incubated in a drying over (Raypa) at 45 °C for 30 min. Then, 3 mL of 0.1 M glucose aqueous solution were added, and the resulting mixture was again incubated at 37 °C for 2 h. Finally, after incubation, the GUVs suspension was centrifuged at 14 000 rpm for 30 min at 20 °C to remove multilamellar vesicles and lipid aggregates.

2.3.4. Spectroscopic measurements

Absorption spectra were obtained in a Shimadzu UV-3101PC UV-Vis-NIR (Shimadzu Corporation, Kyoto, Japan) spectrophotometer using a 1 cm optical path length. Fluorescence spectra were acquired by a Fluorolog 3 (HORIBA Jobin Yvon IBH Ltd., Glasgow, UK) spectrofluorimeter equipped with Glan-Thompson polarisers and double monochromators in excitation and emission all spectra being corrected for the instrumental response.

The steady-state fluorescence anisotropy, *r*, was measured in the latter equipment using Glan-Thompson polarisers and calculated using

Equation 2.1.

Equation 2.1

$$r = \left(\frac{I_{VV} - GI_{VH}}{I_{VV} + 2GI_{VH}}\right)$$

where, I_{VV} and I_{VH} are the intensities of the emission spectra obtained with vertical and horizontal polarization, respectively (for vertically polarized excitation light), and $G = I_{HV}/I_{HH}$ is the instrument correction factor, where I_{HV} and I_{HH} are the emission intensities obtained with vertical and horizontal polarization (for horizontally polarized excitation light).

Förster resonance energy transfer (*FRET*) assays were carried out to confirm the formation of the double lipid layer in SMLs and the interactions with model membranes. For that, the first lipid layer included the energy acceptor rhodamine B labelled lipid, *N*-(lissamine rhodamine B sulfonyl)-1,2-dioleoyl-*sn*-3-phosphatidylethanolamine (Rh-DOPE) (ammonium salt) (from Avanti Polar Lipids, Birmingham, AL, USA)), and the second lipid layer included the energy donor nitrobenzoxazole labelled lipid NBD-C_{12}-HPC (also from Avanti Polar Lipids, Birmingham, AL, USA) [80,81]. The latter was used as a reference, with Φ_r = 0.32 at 25 °C [82]. *FRET* occurs when a donor fluorophore in the excited state transfers energy to an acceptor moiety in the ground state in a non-radiative process. *FRET* efficiency (Φ_{FRET}) is defined as the proportion of donor molecules transferring their excess energy to acceptor molecules. Experimentally, it can be calculated by taking the ratio of the donor integrated fluorescence intensities in the presence of an acceptor (F_{DA}) and the absence of an acceptor (F_D), following **Equation 2.2** [83],

Equation 2.2

$$\Phi_{FRET} = 1 - \frac{F_{DA}}{F_D}.$$

In turn, the values of *FRET* efficiency allow calculating the distance between the donor molecules and the acceptor ones (**Equation 2.3**) [83],

Equation 2.3

$$r_{AD} = R_0 \left[\frac{1 - \Phi_{FRET}}{\Phi_{FRET}}\right]^{1/6}$$

where R_0 is the Förster radius (critical distance), which the spectral overlap can obtain, $J(\lambda)$, between the donor emission and the acceptor absorption, according to the following relations (**Equation 2.4** and **Equation 2.5**) with R_0 in Å, λ in nm, $\varepsilon_A(\lambda)$ in M^{-1} cm^{-1}):

Equation 2.4

$$R_0 = 0.2108\,[k^2\,\Phi_D^0\,n^{-4}\,J(\lambda)]^{1/6}$$

Equation 2.5

$$J(\lambda) = \int_0^\infty I_D(\lambda)\varepsilon_A(\lambda)\lambda^4 d\lambda$$

where $k^2 = 2/3$ is the orientational factor assuming random orientation of the dyes, Φ_D^0 is the fluorescence quantum yield of the donor in the absence of energy transfer, n is the refraction index of the medium, $I_D(\lambda)$ is the fluorescence spectrum of the donor normalized so that $\int_0^\infty I_D(\lambda)d\lambda = 1$, and $\varepsilon_A(\lambda)$ is the molar absorption coefficient of the acceptor.

2.3.5. Characterization of magnetic nanoparticles

Magnetization measurements were carried out in an MPMS3 SQUID magnetometer MPMS5XL (Quantum Design Inc., San Diego, CA, USA). The curves were obtained by initially cooling the sample under an applied magnetic field of H = 100 Oe (field cooled, FC) and then measuring its magnetization with increasing temperature (applied field of H = 50 Oe). The magnetization hysteresis loop measurements were made by fixing the temperature and measuring the magnetization at a series of different applied magnetic fields. A specific magnetic field correction for the trapped flux in the superconducting coil was made, achieving an accuracy of less than 2 Oe.

X-ray diffraction (XRD) analyses were performed in a conventional Philips PW 1710 (Royal Philips, Amsterdam, The Netherlands) diffractometer, operating with CuK_α radiation, in a Bragg-Brentano configuration.

TEM images were obtained at C.A.C.T.I (Centro de Apoio Científico e Tecnolóxico á Investigación), Vigo (Spain), using a Transmission Electron Microscope JEOL JEM 2010F (JEOL Ltd., Tokyo, Japan) operating at 200 kV. TEM images were processed using ImageJ software, version 1.52p (National Institutes of Health (NIH), Bethesda, MD, USA).

2.3.6. Drug release studies

In total, 0.5 mL of curcumin-loaded magnetoliposomes solution was placed in Amicon® Ultra-0.5 mL centrifugal filters with 0.1 μm pore size (under mild shaking conditions) containing a GUVs solution in the bottom container, with GUVs being used as acceptor membrane models for curcumin. At 30 min intervals (for 4.5 h), 200 μL were collected from the acceptor compartment for assessing curcumin

concentration, and an equal volume of fresh GUVs was added. The fluorescence of the collected solution was measured, and the cumulative release of curcumin was calculated using calibration curves previously obtained. Three independent release assays were performed. Since magnetoliposomes were envisioned as magnetic responsive nanosystems, the release profile of curcumin was also assessed under the actuation of an AMF. The AMF was generated in a custom-designed solenoid device (800 turns per meter, length: 31 cm and internal diameter: 4.8 cm) by applying an alternating electric current. A magnetic field of 2.98 mT at 1000 kHz was used. Release profile assays were performed in triplicate.

2.4. Results and Discussion

2.4.1. Characterization of magnetic nanoparticles

The optical absorption and band gap energy of the prepared nanoparticles were investigated by UV-Vis spectroscopy, which is an indicator of their purity and composition. The prepared nanoparticles showed a broad absorption in the UV-visible wavelength range, between 250–650 nm (**Figure 2.1**). This wide absorption range is a key feature for the objectives of this work, as it reveals that nanoparticles may quench fluorescence emission of curcumin when encapsulated in magnetoliposomes. This effect has already been reported for drug-loaded magnetoliposomes based on magnesium ferrite [76] and calcium ferrite nanoparticles [84].

The UV-Visible absorption spectra of the synthesised $Ca_xMg_{1-x}Fe_2O_4$ nanoparticles allow obtaining the optical band gap values using a Tauc Plot by the **Equation 2.6**.

Equation 2.6

$$(\alpha h\upsilon)^n \propto (h\upsilon - E_g)$$

Where α is the absorption coefficient, n is an exponent that depends on the transition's nature (n=2 for a direct semiconductor and n=1/2 for an indirect one), and E_g is the optical band gap.

The $Ca_{0.25}Mg_{0.75}Fe_2O_4$, $Ca_{0.50}Mg_{0.50}Fe_2O_4$ and $Ca_{0.75}Mg_{0.25}Fe_2O_4$ nanoparticles are direct semiconductors, as a linear relation was only obtained for n=2. From the Tauc plots, the band gaps of the different nanoparticles were estimated (the Tauc plot for $Ca_{0.50}Mg_{0.50}Fe_2O_4$ is shown as an example in the inset of **Figure 2.1**). Band gaps of 1.51 eV, 1.65 eV and 1.91 eV were obtained for

$Ca_{0.25}Mg_{0.75}Fe_2O_4$, $Ca_{0.50}Mg_{0.50}Fe_2O_4$ and $Ca_{0.75}Mg_{0.25}Fe_2O_4$ nanoparticles, respectively. The band gap values tend to increase as the calcium ratio increases in these mixed ferrite nanoparticles. These results agree with the previously reported values of 1.41 eV for $MgFe_2O_4$ [76] and 2.19 eV for $CaFe_2O_4$ [84], being also similar to the value of 1.90 eV reported by Kim *et al.* for calcium ferrite [85].

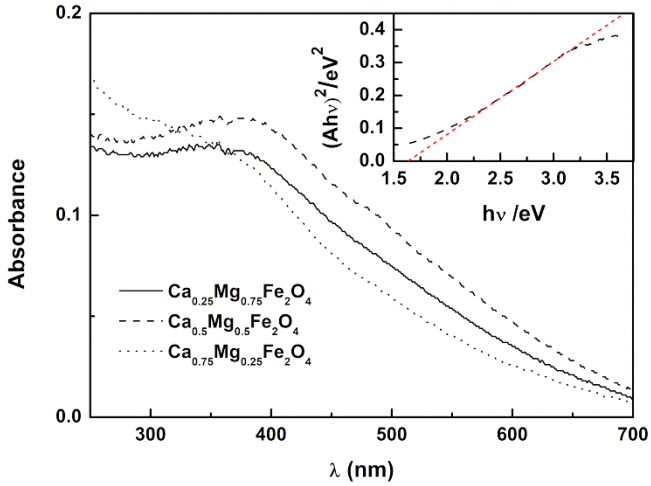


Figure 2.1 Absorption spectra of $Ca_{0.25}Mg_{0.75}Fe_2O_4$, $Ca_{0.50}Mg_{0.50}Fe_2O_4$ and $Ca_{0.75}Mg_{0.25}Fe_2O_4$ magnetic nanoparticles. Inset: Tauc plot for $Ca_{0.50}Mg_{0.50}Fe_2O_4$ nanoparticles, as an example (red line is the linear fitting).

2.4.2. X-Ray Diffraction measurements

XRD measurements confirmed the synthesis of the calcium-substituted magnesium ferrite nanoparticles as, after a calcination process at 600 °C, a pure crystalline ferrite phase corresponds to the observed diffraction peaks (space group $Fd\bar{3}m$, CIF 9000926), marked by their indices (**Figure 2.2**).

For $CaFe_2O_4$ nanoparticles, the inversion degree of i=0.85 [84] was previously used, and for $MgFe_2O_4$, a value of i=0.83 was obtained [76]. Thus, for the ferrites under study, a value of i=0.85 was chosen, and a full Rietveld analysis using the *FullProf* software suite (version 5.8, J. Rodríguez-Carvajal, Lab. Léon Brillouin, Gif sur Yvette, France) [86] was then performed, with the main results indicated in **Table 2.1** and the resulting fits represented in **Figure 2.2.** In a previous study [87], it was found that the use of microabsorption correction is essential [88]. The fits obtained with this correction exhibit the same quality as the ones obtained by optimizing the overall isothermal Debye-Waller factor, B_{over}, that resulted in a negative value, having no physical meaning. Crystallite sizes of 5.8 nm, 6.4 nm, and 7.0 nm were estimated by the Scherrer equation for $Ca_{0.25}Mg_{0.75}Fe_2O_4$, $Ca_{0.50}Mg_{0.50}Fe_2O_4$ and $Ca_{0.75}Mg_{0.25}Fe_2O_4$

nanoparticles, respectively. The lattice parameter increases significantly with Ca content when the Ca percentage is 75% (**Table 2.1** Selected Rietveld analysis parameters.).

Table 2.1 Selected Rietveld analysis parameters.

Sample	$O_{x,y,z}$	Micro absorption correction (#)		Overall temperature factor, B_{over}	Lattice constant (nm)	Size (nm)	R_f	χ^2
$Ca_{0.50}Mg_{0.50}Fe_2O_4$	0.378	No		0 (+)	0.839045	6.3	5.92	1.39
$Ca_{0.50}Mg_{0.50}Fe_2O_4$	0.377	No		-3.67	0.839196	6.4	3.19	1.23
$Ca_{0.50}Mg_{0.50}Fe_2O_4$	0.370	P_0=0.69	τ=0.14	0 (+)	0.839164	6.4	2.64	1.23
$Ca_{0.25}Mg_{0.75}Fe_2O_4$	0.372	P_0=0.71	τ=0.11	0 (+)	0.838978	5.8	3.62	1.26
$Ca_{0.75}Mg_{0.25}Fe_2O_4$	0.384	P_0=0.72	τ=0.09	0 (+)	0.843550	7.0	3.71	1.28

(#) equation (8) in [87] with C=1. (+) fixed values

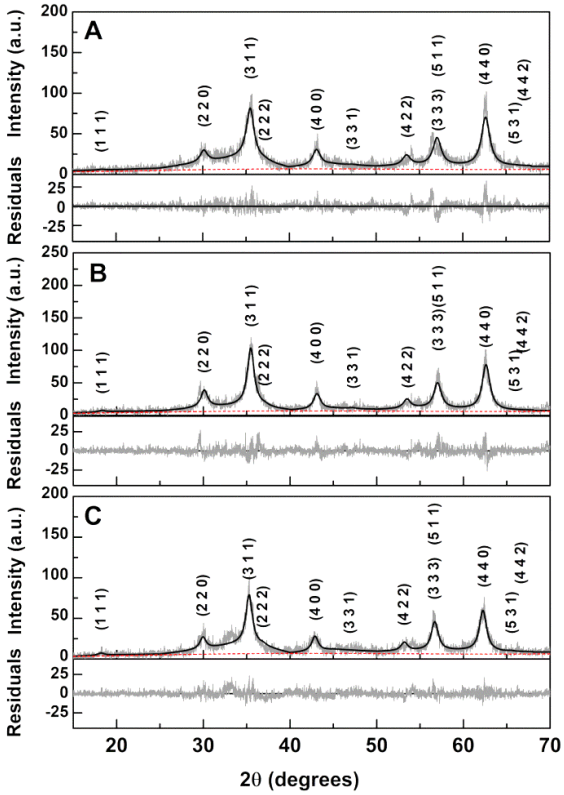


Figure 2.2 XRD patterns with Miller indices of the synthesized calcium-substituted magnesium ferrite nanoparticles. (A) $Ca_{0.25}Mg_{0.75}Fe_2O_4$, (B) $Ca_{0.50}Mg_{0.50}Fe_2O_4$ and (C) $Ca_{0.75}Mg_{0.25}Fe_2O_4$. Grey lines: experimental patterns; black lines: fitted patterns; red dashed lines: background.

2.4.3. Sedimentation kinetics

The sedimentation kinetics of the synthesized calcium-substituted magnesium ferrite nanoparticles was followed by measuring UV-Visible absorption of nanoparticle dispersions in time. For example, the results for $Ca_{0.50}Mg_{0.50}Fe_2O_4$ NPs were obtained as the slopes of the absorption variation function over time for three different NPs concentrations (**Figure 2.3**). Similar behaviour was observed for all NPs, with high stability for NPs concentrations below 1×10^{-4} M and exponential growth for higher concentrations sedimentation. Yet, after 1 h, nanoparticles remain extremely dispersed, in percentages of 85%, 82% and 97% for $Ca_{0.25}Mg_{0.75}Fe_2O_4$, $Ca_{0.50}Mg_{0.50}Fe_2O_4$ and $Ca_{0.75}Mg_{0.25}Fe_2O_4$ nanoparticles, respectively. This is a positive indication of the stability of the nanoparticle's aqueous dispersions, being suitable for biomedical applications.

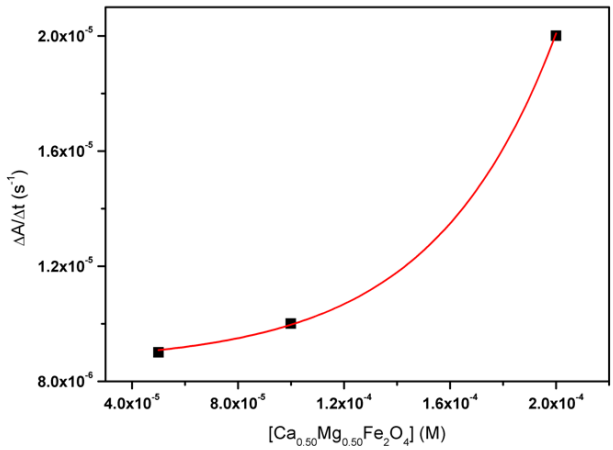


Figure 2.3 Sedimentation kinetics of $Ca_{0.50}Mg_{0.50}Fe_2O_4$ nanoparticles.

2.4.4. Transmission Electron Microscopy

TEM images and small area electron diffraction (SAED) for $Ca_{0.50}Mg_{0.50}Fe_2O_4$ nanoparticles are shown in **Figure 2.4**. Upon manual outline of 193 particles (**Figure 2.4 C**), the size was determined considering an equivalent area circle. The analysis of the corresponding size histogram (**Figure 2.4 D**) resulted in two populations, with sizes 7.0 ± 0.7 nm and 9.9 ± 2.5 nm. The larger population probably corresponds to image projections of nanoparticle aggregates. The deviation from sphericity was analysed by comparing the perimeter of the particle with the one calculated with the equivalent area circle. Most particles have 0.95 sphericity, while a small 5% fraction shows a value of 0.84. SAED results (**Figure 2.4 E**) are compatible with a spinel ferrite crystal structure, as seen from the added semi-circles. These

correspond to spinel structure d-spacings calculated using the same lattice constant obtained from XRD Rietveld analysis (8.3915 Å).

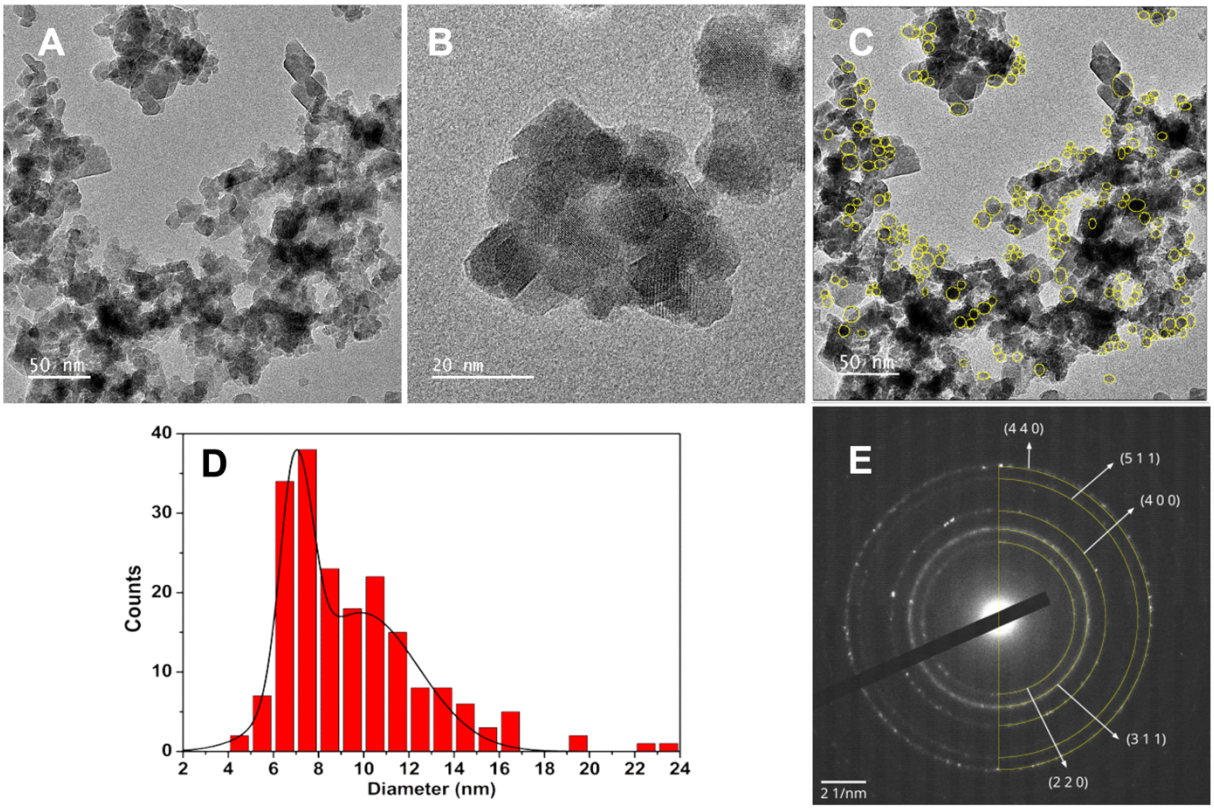


Figure 2.4 (A, B) TEM images of $Ca_{0.50}Mg_{0.50}Fe_2O_4$ nanoparticles with different magnifications. (C) Image A with outlined nanoparticles. (D) Size histogram of image A. (E) SAED image with indexed diffraction planes.

2.4.5. Magnetic Properties

The magnetic properties of calcium-substituted magnesium ferrite nanoparticles ($Ca_xMg_{1-x}Fe_2O_4$) emphasize that the partial substitution of magnesium by calcium in the ferrite structure has nonlinear effects on the maximum magnetization. The overall magnetization is sensitive to the distribution of Fe^{3+} ions in A (tetrahedral) and B (octahedral) sites, as the magnetic moment of Fe^{3+} is 5 μB, while Ca^{2+} and Mg^{2+} are nonmagnetic. Furthermore, the magnetization directly depends on the Ca^{2+} concentration, a large cation whose radius is near the threshold of ~1 Å, with high implications on the distribution of magnetic ions in interstitial sites. At low concentration values, Ca^{2+} ions show a preferred occupancy at A-sites, with $(1-x-y)$ Fe^{3+} ions on the A-site and $(1+x+y)$ Fe^{3+} ions on the B-site, where y and x represent the probability of migration of a small fraction of Mg^{2+} and Ca^{2+} ions to A-sites,

respectively [89]. Thus, the distribution of calcium-substituted magnesium ferrite, for low Ca^{2+} content, takes the form of $(Ca_x^{2+}Mg_y^{2+}Fe_{1-x-y}^{3+})[Ca_x^{2+}Mg_y^{2+}Fe_{1+x+y}^{3+}]O_4^{2-}$, where the curve and square brackets indicate tetrahedral (A-sites) and octahedral (B-sites) sublattice, respectively. Hence, the net magnetisation $|M| = |M_B| - |M_A|$, according to Neel's theorem of sublattice [90], increases with the inclusion of Ca^{2+}, due to the increasing number of Fe^{3+} ions on B-sites and decreasing amount on A-sites. For larger calcium concentration, $x > 0.05$, it is reported that Ca^{2+} ions migrate to B-sites. The distribution then takes the form $(Ca_{x-y}^{2+}Fe_{1+x-y}^{3+})[Mg_{1-x}^{2+}Ca_y^{2+}Fe_{1+x-y}^{3+}]O_4^{2-}$ [91]. Therefore, an increase of Ca^{2+} ions will decrease Fe^{3+} ions on B-sites and increase them on A-sites, weakening the overall magnetization of the whole lattice [89,90].

Figure 2.5 shows the magnetization hysteresis cycles of synthesized calcium-substituted magnesium ferrite nanoparticles, displaying the relationship between the induced magnetic moment and the applied magnetic field (H) at room temperature. The magnetic properties, saturation magnetization (M_s), remnant magnetisation (M_r), and coercive field (H_c) are presented in **Table 2.2**. Higher saturation magnetization values were obtained for $Ca_{0.25}Mg_{0.75}Fe_2O_4$, $Ca_{0.50}Mg_{0.50}Fe_2O_4$ and $Ca_{0.75}Mg_{0.25}Fe_2O_4$ nanoparticles, with 12.98 emu/g and 15.63 emu/g, respectively. A lower value of M_s, 8.83 emu/g, was observed for $Ca_{0.75}Mg_{0.25}Fe_2O_4$, indicating that Ca^{2+} ions migrated to B-sites, leading to a decrease of Fe^{3+} ions in B-sites (and corresponding increase on A-sites), resulting in a lower magnetization.

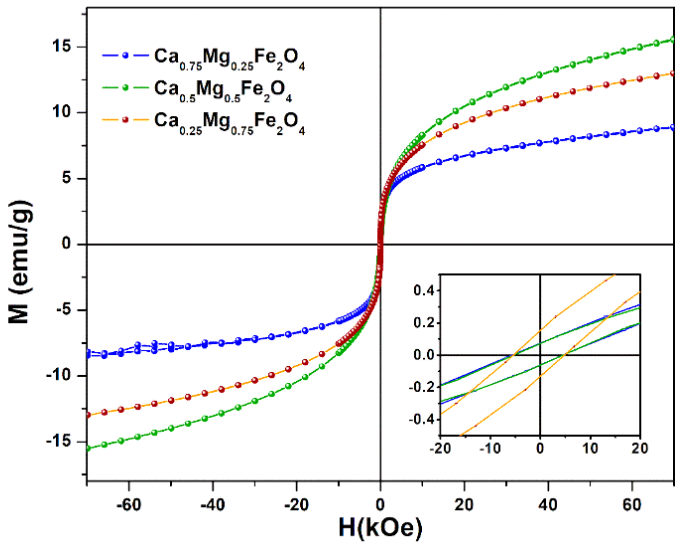


Figure 2.5 Magnetization hysteresis loops of calcium-substituted magnesium ferrite nanoparticles were measured at room temperature. Inset: Enlargement of the loops in the low field region.

Table 2.2 The saturation magnetizations (M_s), remanant magnetisation (M_r), ratio M_r/M_s and coercive field (H_c) of calcium-substituted magnesium ferrite nanoparticles.

Nanoparticles	M_s (emu/g)	M_r (emu/g)	M_r/M_s	H_c (kOe)
$Ca_{0.75}Mg_{0.25}Fe_2O_4$	8.83	0.08	0.009	5.74
$Ca_{0.50}Mg_{0.50}Fe_2O_4$	15.63	0.07	0.004	5.33
$Ca_{0.25}Mg_{0.75}Fe_2O_4$	12.98	0.15	0.011	5.45

In any case, these values compare well with the previously reported maximum magnetization of $MgFe_2O_4$ (16.16 emu/g [76]) and $CaFe_2O_4$ (12.81 emu/g [84]) nanoparticles obtained by the same method of preparation.

The superparamagnetic behaviour of the nanoparticles was investigated considering the magnetic squareness value (ratio between the remnant and saturation magnetisations). If this value is below 0.1, more than 90% of the magnetisations are lost upon removing the applied magnetic field. Here, the calculated magnetic squareness values indicate that the ferrite nanoparticles are superparamagnetic at room temperature, having low coercivity and remnant magnetisations (**Table 2.2**).

The substitution of 50% magnesium by calcium in ferrite structure allows for improved magnetic properties relative to calcium ferrite and enhanced biocompatibility relative to magnesium ferrite, as calcium ferrite is reported as highly biocompatible in studies of cell viability [91]. In addition, all the prepared mixed nanoparticles exhibit superparamagnetic properties and avoid undesirable oxidation and production of ROS in mammalian cells by iron oxide nanoparticles that cause protein and DNA damage and inflammatory responses [60,92-94].

2.4.6. Characterisation of magnetoliposomes

At the date of publication, AMLs and SMLs based on calcium/magnesium mixed ferrite nanoparticles had not been reported. Furthermore, these new nanosystems were tested as magnetic nanocarriers for curcumin.

2.4.6.1. Aqueous magnetoliposomes

AMLs were obtained by entrapping magnetic nanoparticles in liposomes of the natural lipid mixture egg phosphatidylcholine. AMLs can be used as nanocarriers for hydrophilic and hydrophobic drugs. Still, their magnetic properties are poorer than the ones of SMLs (that do not present an aqueous inner volume) due to the diamagnetic contribution of water in AMLs [95,96]. The hydrodynamic size and PDI were measured by DLS (**Table 2.3**), indicating that generally, monodisperse systems (low PDI values) with sizes below 150 nm are suitable for passive targeting through the EPR effect. These sizes are similar to the ones obtained for magnetoliposomes containing calcium ferrite nanoparticles [84].

Table 2.3 Hydrodynamic diameter and PDI of egg-PC AMLs containing calcium-substituted magnesium ferrite nanoparticles.

Nanoparticles	Hydrodynamic diameter ± SD (nm)	PDI
$Ca_{0.75}Mg_{0.25}Fe_2O_4$	147.8 ± 21	0.15 ± 0.018
$Ca_{0.50}Mg_{0.50}Fe_2O_4$	149.2 ± 22	0.20 ± 0.013
$Ca_{0.25}Mg_{0.75}Fe_2O_4$	131.4 ± 19	0.22 ± 0.015

The fluorescence emission investigated the curcumin encapsulation in AMLs based on the three different ferrite nanoparticles (**Figure 2.6**). The fluorescence spectra were compared between liposomes (of the same lipid composition but without magnetic nanoparticles) and AMLs encapsulating curcumin. The emission spectra confirm the incorporation of curcumin in vesicles, exhibiting a quenching effect of drug fluorescence in the presence of magnetic nanoparticles (as expected from the broad wavelength range of nanoparticle absorption). Furthermore, no significant shifts in the band of curcumin were noted between liposomes and AMLs, indicating a similar environment felt by curcumin in the several nanosystems.

To prevent opsonization and allow shielding from proteolytic enzymes, increasing the retention time in the circulation system, PEGylation of Egg-PC AMLs was carried out with 5% DSPE-PEG-2000. While it has been reported that coating with PEG is effective in increasing the circulation time of oleic acid-coated Fe_3O_4 nanoparticles [97] and also of magnetoliposomes [98], it was also recently argued that PEGylation can reduce the interaction of targeted magnetoliposomes with cells, with a decrease in the degree of internalization [99]. Nevertheless, PEGylation remains the primary strategy to improve the circulation time of the lipid nanocarriers (known as stealth liposomes).

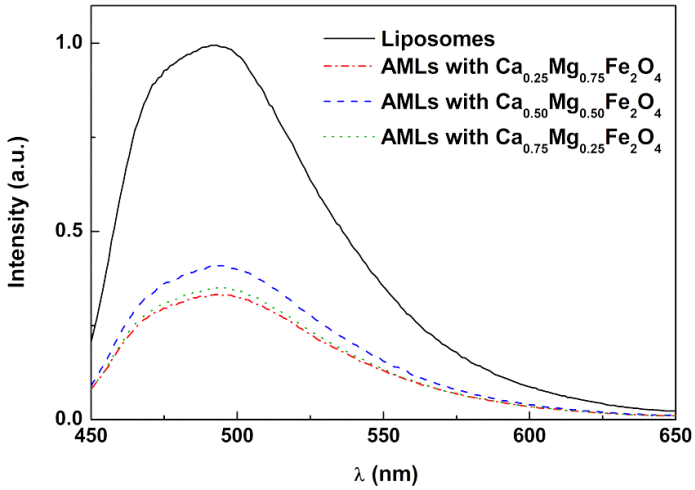


Figure 2.6 Fluorescence spectra of curcumin encapsulated in liposomes and AMLs based on calcium-substituted magnesium ferrite nanoparticles.

Fluorescence anisotropy measurements of curcumin (**Table 2.4**) were determined. The values in Egg-PC liposomes and glycerol are presented for comparison, as in this highly viscous medium (η = 993.4 cP at room temperature [100], curcumin molecules rotate very slowly, and the anisotropy value approaches the fundamental anisotropy of the fluorophore [83]. From the anisotropy values, one can observe that the values in AMLs are similar to liposomes, proving curcumin's location in the lipid membrane, as expected from its hydrophobic character. Egg phosphatidylcholine (PC) bilayer is expected to be more fluid than glycerol, considering its lipid composition (main components are 16:0 PC, 18:0 PC, and 18:1 PC), justifying lower anisotropy values for curcumin (higher degree of rotation). Lipid membranes have microviscosity that depends on their lipid composition but generally lies in the range of 100–200 cP [101,102]. The addition of a superficial PEG layer seems not to influence the degree of rotation of curcumin in AMLs, as inferred from the similar anisotropy value.

Table 2.4 Steady-state fluorescence anisotropy (r) values for curcumin at 25 °C in AMLs containing $Ca_{0.25}Mg_{0.75}Fe_2O_4$. Values for curcumin in liposomes and glycerol are also shown for comparison.

System	Lipid formulation	r
Liposomes	Egg-PC	0.340 [76]
AMLs	Egg-PC	0.320
AMLs	95% Egg-PC / 5% DSPE-PEG2000	0.335
Glycerol	—	0.365 [76]

The hydrophobic nature of curcumin anticipates difficulties in its release from magnetoliposomes. Therefore, it is essential to assess if the developed nanosystems have fusion ability with model membranes, allowing drug release. This capability was investigated by *FRET*, using curcumin as an energy donor and the lipid probe Nile Red as an energy acceptor [76], both included in magnetoliposomes. GUVs [78,79] were used as models of cell membranes. Exciting only the donor curcumin, a strong fluorescence band is observed due to Nile Red emission (maximum emission wavelength at 625 nm). This is a consequence of the non-radiative energy transfer (*FRET*) from curcumin to Nile Red (**Figure 2.7**). After interaction with GUVs, the donor (curcumin) fluorescence increases and the acceptor emission band decreases, proving the decrease of efficiency of the *FRET* process and, consequently, confirming the membrane fusion between AMLs and the model membranes. PEGylated magnetoliposomes (**Figure 2.7 B**) also present fusion capabilities, but to a slightly lower extent, as inferred from the lower increase of donor fluorescence (maximum emission around 500 nm) after interaction with GUVs.

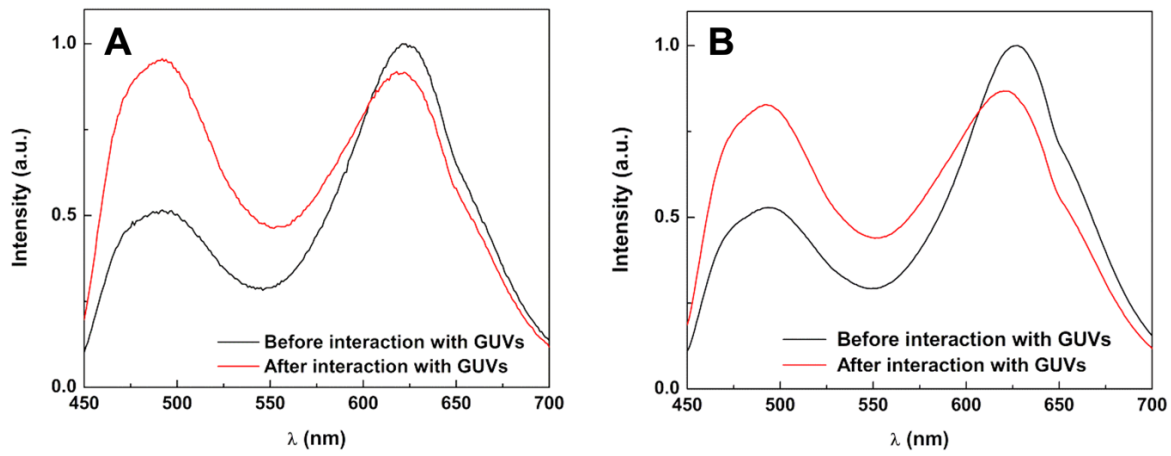


Figure 2.7 Fluorescence spectra (λ_{exc} = 440 nm) of AMLs containing $Ca_{0.25}Mg_{0.75}Fe_2O_4$ nanoparticles (as an example), labelled with both curcumin (2×10^{-6} M) and Nile Red (2×10^{-6} M), before and after interaction with GUVs. (A) AMLs of Egg-PC; (B) AMLs of Egg-PC/DSPE-PEG2000 (0.95:0.05).

2.4.6.2. Solid magnetoliposomes

Regarding SMLs, and taking into account the hydrophobic character of curcumin, a temperature-sensitive lipid, DPPC, with a melting T_m of 41 °C [77], was considered a good choice, as this T_m is near the ones used in mild hyperthermia therapy [103]. Upon melting, the lipid bilayer chains experience an increase

in fluidity (attaining liquid-crystalline phase), with the possibility of enhanced drug release into cell membranes.

To confirm the formation of the lipid bilayer around magnetic nanoparticles clusters, a *FRET* assay was employed, where the labelled lipid NBD-C_{12}-HPC was inserted in the inner lipid layer of SMLs, and the lipid rhodamine B-DOPE (rhodamine B as the acceptor) was incorporated in the outer lipid layer, NBD-C_{12}-HPC being the donor and rhodamine B the acceptor, as described in previous works [76,96]. *FRET* efficiencies were calculated (**Table 2.5**), allowing the determination of donor-acceptor distances (through **Equation 2.2**-**Equation 2.5**, **Table 2.5**). The different Förster radius values obtained reflect differences in the fluorescence quantum yield of the donor because of a distinct quenching effect by the several nanoparticles. The donor-acceptor distances confirm the formation of the double lipid layer in SMLs (cell membranes have a thickness of 7 nm to 9 nm [104]).

Table 2.5 *FRET* efficiencies (Φ_{FRET}), Förster radii (R_0) and donor-acceptor distances (r_{AD}) calculated for the formation of the lipid bilayer in SMLs.

Nanoparticles	Φ_{FRET}	R_0	r_{AD} (nm)
$Ca_{0.25}Mg_{0.75}Fe_2O_4$	0.87	5.31	3.87
$Ca_{0.50}Mg_{0.50}Fe_2O_4$	0.96	5.94	3.42
$Ca_{0.75}Mg_{0.25}Fe_2O_4$	0.68	3.59	3.17

SMLs size and polydispersity were measured by DLS, revealing hydrodynamic diameters around or below 150 nm and low PDI (**Table 2.6**). The size of this type of nanocarrier increase with the calcium content of the nanoparticles. As for AMLs, the values obtained are adequate for passive targeting through the EPR effect.

Table 2.6 Hydrodynamic diameter and polydispersity of DPPC SMLs containing calcium-substituted magnesium ferrite nanoparticles.

Nanoparticles	Hydrodynamic diameter ± SD (nm)	PDI
$Ca_{0.25}Mg_{0.75}Fe_2O_4$	127.3 ± 17	0.213 ± 0.025
$Ca_{0.50}Mg_{0.50}Fe_2O_4$	147.0 ± 15	0.206 ± 0.012
$Ca_{0.75}Mg_{0.25}Fe_2O_4$	155.4 ± 21	0.228 ± 0.021

Fluorescence anisotropy measurements were also performed to confirm curcumins' location in SMLs (**Table 2.7**). The measurements were carried out at room temperature, where DPPC is in the rigid gel phase, and at 55 °C, above the melting T_m of DPPC (liquid-crystalline phase). It can be observed that, above the T_m, curcumin's anisotropy is significantly lower due to the increase in the curcumin microenvironment's fluidity, pointing to a location in the lipid membrane of SMLs with or without a PEG layer. The lower anisotropy values in SMLs at room temperature, relative to AMLs (**Table 2.7**), may reflect a deep penetration of curcumin in the lipid membrane of SMLs, considering that the membrane fluidity decreases from the liposome surface to the interior [105,106]. In PEGylated SMLs, the higher anisotropy at 25 °C may indicate a more exterior location of curcumin.

Table 2.7 Steady-state fluorescence anisotropy (r) values for curcumin at 25 °C and 55 °C in SMLs containing $Ca_{0.25}Mg_{0.75}Fe_2O_4$. Values for curcumin in DPPC liposomes are also shown for comparison.

	Lipid formulation	Temperature (°C)	r
Liposomes	DPPC	25	0.287
		55	0.119
SMLs	DPPC	25	0.156
		55	0.094
SMLs	95% DPPC / 5% DSPE-PEG2000	25	0.209
		55	0.139

To investigate the interaction of SMLs with model membranes (GUVs), FRET assays have not been used. Usually, *FRET* is not observed due to the strong quenching of donor and acceptor emissions by the cluster of magnetic nanoparticles [107], which is very close to the fluorophores (due to the absence of the aqueous pool). Instead, if interaction with GUVs occurs, an unquenching effect should be observed. Therefore, taking advantage of curcumin intrinsic fluorescence, the assay was performed using curcumin-loaded magnetoliposomes. Upon interaction with GUVs, a significant rise in curcumin fluorescence is observed (unquenching effect), proving the increase in distance between the nanoparticles and the fluorescent drug due to membrane fusion (**Figure 2.8 A**). The result is also observed for stealth (PEGylated) SMLs (**Figure 2.8 B**).

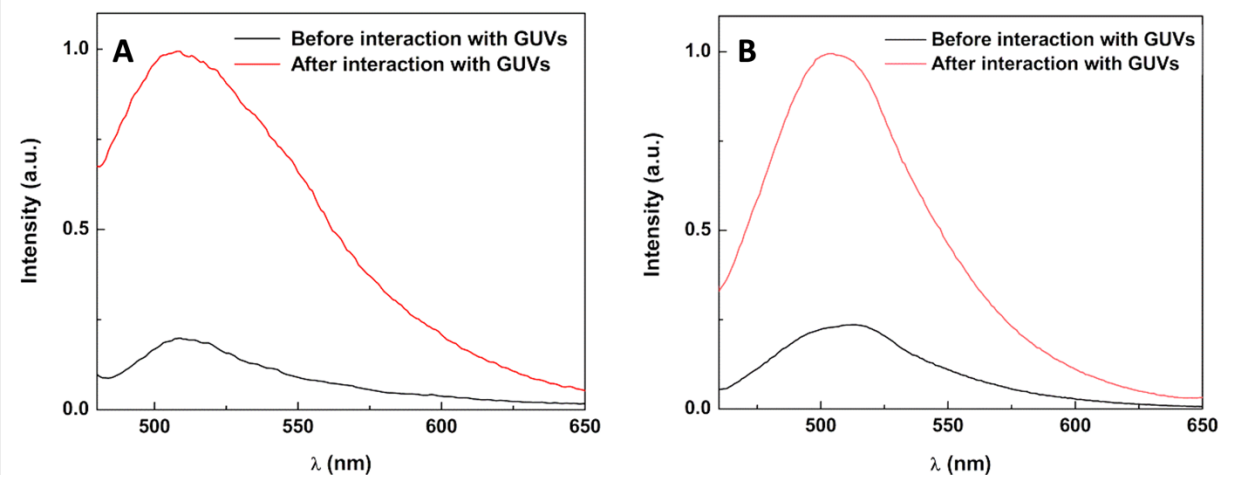


Figure 2.8 Fluorescence spectra (λ_{exc}= 440 nm) of curcumin in SMLs containing $Ca_{0.25}Mg_{0.75}Fe_2O_4$ nanoparticles (as an example), before and after interaction with GUVs. A: SMLs of DPPC; B: SMLs of DPPC/DSPE-PEG.

2.4.6.3. Curcumin release profile

The release behaviour of curcumin from loaded SMLs towards model membranes (GUVs) was studied in the presence and absence of an AMF to evaluate the drug release profile from magnetoliposomes under the magnetic stimulus. The influence of PEGylation was also investigated. The effect of AMF on curcumin release was investigated by exposing curcumin-loaded SMLs based on $Ca_{0.50}Mg_{0.50}Fe_2O_4$ nanoparticles to a magnetic field with an intensity of 2.98 mT and a frequency of 1000 kHz. Limits have been defined that restrict allowable AMF conditions in order to avoid discomfort, pain and damage caused by eddy currents. To be considered for therapy purposes, restriction limits have been set for tolerance and safety of patients. Initially, the Atkinson-Brezovich limit was an asset as a field-frequency product (H×f) of 4.85×10^8 A/(m×s) [108]. However, in practice, a higher limit is used ($H\times f \leq 5\times10^9$ A/(m×s)) as it depends on the area of application in the body [109]. Hence, the field and frequency values used are by the restriction limits, $H\times f = 2.38\times10^9$ A/(m×s). (H = 2.9 mT = 2379.087 A/m and f = 1000 kHz = 10^6/s); so, the field and frequency product are below 5×10^9 A/(m×s).

Three independent experiments were conducted to obtain the average release ratio and correspondent standard deviation. The experimental data were analysed using the nonlinear Korsmeyer-Peppas model (**Table 2.8**) [110-112]. Drug transport constants (K) and transport exponents (n) were determined by fitting to the Korsmeyer-Peppas equation (**Equation 2.7**):

Equation 2.7

$$C_t/C_0 = K \cdot t^n$$

where C_0 and C_t are the concentrations at time 0 and t, respectively, K is the rate constant, and n is the transport exponent. When $n < 0.45$, the release mechanism is diffusion-controlled (Fickian release), $0.45 < n < 0.89$ indicates a combination of diffusion and erosion drug release (non-Fickian release), $0.89 < n < 1$ indicates a relaxation-controlled release, and in the case of $n > 1$, the release is controlled by swelling and chain relaxation [110-112].

Table 2.8 Obtained constant values by fitting the Korsmeyer-Peppas model to the curcumin' kinetic release data from SMLs in the presence and absence of an AMF, and respective coefficient of determination (R^2).

Conditions	Lipid formulation	K (min^{-1})	n	R^2
Without AMF	DPPC	2.98×10^{-3}	0.685	0.9929
	DPPC:DSPE-PEG	2.43×10^{-2}	0.659	0.9927
With AMF	DPPC	3.73×10^{-3}	0.646	0.9900
	DPPC:DSPE-PEG	2.26×10^{-2}	0.663	0.9923

An enhanced release of curcumin from SMLs of DPPC was observed upon the application of an AMF by 1.25 times, $K = 2.98 \times 10^{-3}$ min^{-1} and $K = 3.73 \times 10^{-3}$ min^{-1} in the absence and presence of AMF, respectively (**Figure 2.9**, **Table 2.8**). The local heating promoted by the magnetic nanoparticles makes the liposomes bilayer more fluid, with increased drug release. The estimated n values point to non-Fickian release (combination of diffusion and erosion) [113].

The curcumin release profile from PEGylated SMLs does not show a higher rate constant with AMF application, indicating that the PEG shield may hamper the thermosensitivity of DPPC. Nevertheless, curcumin release is ten times faster in PEGylated systems (with or without AMF). The low maximum magnetization of the calcium-substituted magnesium ferrite nanoparticles is probably the main reason for the small effect of the AMF application on drug release.

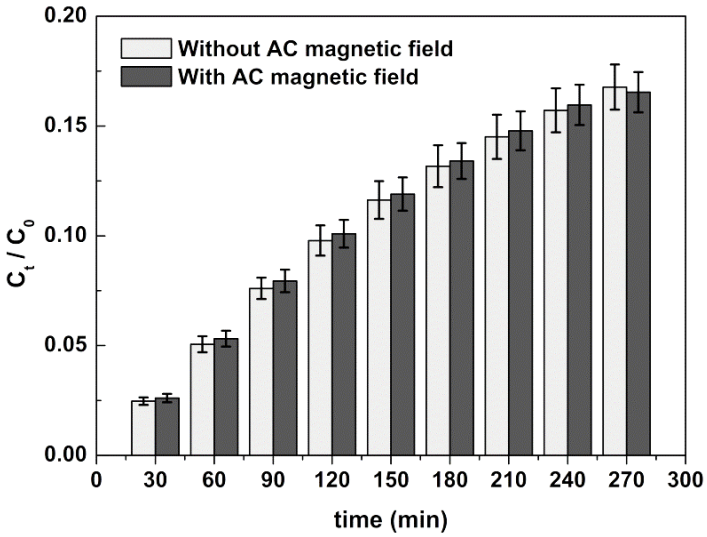


Figure 2.9 The drug release profile of curcumin from DPPC-based SMLs, with and without applying an AMF.

2.5. Conclusions

This section described the preparation, by co-precipitation, of spherical calcium-substituted magnesium ferrite nanoparticles ($Ca_xMg_{1-x}Fe_2O_4$, with x = 0.25, 0.50, 0.75) and the influence that the partial replacement of magnesium by calcium in the ferrite structure has on its properties. From the Tauc plots, it was estimated that $Ca_{0.25}Mg_{0.75}Fe_2O_4$, $Ca_{0.50}Mg_{0.50}Fe_2O_4$, and $Ca_{0.75}Mg_{0.25}Fe_2O_4$ nanoparticles are direct semiconductors, and their band gaps tend to increase as the calcium ratio increases, with band gaps of 1.51 eV, 1.65 eV and 1.91 eV, respectively. In turn, XRD measurements confirmed the synthesis of pure crystalline ferrite and an increased crystallite size with higher calcium content, presenting values of 5.8 nm, 6.4 nm, and 7.0 nm (estimated by the Scherrer equation) for $Ca_{0.25}Mg_{0.75}Fe_2O_4$, $Ca_{0.50}Mg_{0.50}Fe_2O_4$ and $Ca_{0.75}Mg_{0.25}Fe_2O_4$ nanoparticles, respectively. The lower M_s found for $Ca_{0.75}Mg_{0.25}Fe_2O_4$ NPs indicate that, the higher proportion of calcium induces the migration of Ca^{2+} ions to B-sites, leading to a decrease of Fe^{3+} ions in B-sites (and corresponding increase on A-sites), resulting in a lower magnetization. Magnetoliposomes, both aqueous and solid, containing calcium-substituted magnesium ferrite nanoparticles, were developed for the first time. The AMLs of Egg-PC revealed sizes below 150 nm, suitable for passive targeting through the EPR effect. The fluorescence anisotropy of curcumin (r = 0.320) has proven its main location in the lipid membrane, as expected from its hydrophobic character. Regarding SMLs, the hydrodynamic diameter increased with the inclusion of NPs

with higher calcium contents, varying from 127.3±17 nm for $Ca_{0.25}Mg_{0.75}Fe_2O_4$ to 155.4 ± 21 nm for $Ca_{0.75}Mg_{0.25}Fe_2O_4$. Furthermore, the lower anisotropy values found in SMLs than AMLs indicated a deep penetration of curcumin in SMLs. These systems were tested as magnetic responsive carriers for curcumin. Although the anticancer efficacy of curcumin is still to be demonstrated entirely, it has been reported that curcumin-based therapies can be excellent adjuvants of the classic anticancer therapy to improve its effectiveness. In addition, the non-PEGylated nanosystems showed promising magnetic-responsive drug nanocarriers.

In contrast, the PEGylated ones do not respond efficiently to AMF application but exhibit enhanced curcumin release (with and without AMF). The developed magnetoliposomes are promising as carriers for curcumin in future therapeutic applications, making it possible to choose systems with enhanced drug release (PEGylated systems) or systems with increased release by AMF (non-PEGylated systems). Future work will involve the development of calcium/magnesium mixed ferrites with a higher saturation magnetization for an efficient drug release upon application of an AMF.

2.6. References

1. Priyadarsini, K.I. The chemistry of curcumin: from extraction to therapeutic agent. *Molecules* **2014**, *19*, 20091-20112.

2. Catanzaro, M.; Corsini, E.; Rosini, M.; Racchi, M.; Lanni, C. Immunomodulators inspired by nature: a review on curcumin and echinacea. *Molecules* **2018**, *23*, 2778.

3. Murata, M. Inflammation and cancer. *Environmental health and preventive medicine* **2018**, *23*, 1-8.

4. Mohamed, S.I.A.; Jantan, I.; Haque, M.A. Naturally occurring immunomodulators with antitumor activity: an insight on their mechanisms of action. *International Immunopharmacology* **2017**, *50*, 291-304.

5. Kunnumakkara, A.B.; Bordoloi, D.; Padmavathi, G.; Monisha, J.; Roy, N.K.; Prasad, S.; Aggarwal, B.B. Curcumin, the golden nutraceutical: multitargeting for multiple chronic diseases. *British journal of pharmacology* **2017**, *174*, 1325-1348.

6. Srivastava, N.S.; Srivastava, R.A.K. Curcumin and quercetin synergistically inhibit cancer cell proliferation in multiple cancer cells and modulate Wnt/β-catenin signaling and apoptotic pathways in A375 cells. *Phytomedicine* **2019**, *52*, 117-128.

7. Yu, Y.; Shen, Q.; Lai, Y.; Park, S.Y.; Ou, X.; Lin, D.; Jin, M.; Zhang, W. Anti-inflammatory effects of curcumin in microglial cells. *Frontiers in pharmacology* **2018**, *9*, 386.

8. Iqbal, B.; Ghildiyal, A.; Singh, S.; Siddiqui, S.; Kumari, P.; Arshad, M.; Mahdi, A. Combinatorial effect of curcumin and tumor necrosis factor-α-related apoptosis-inducing ligand (TRAIL) in induction of apoptosis via inhibition of nuclear factor kappa activity and enhancement of caspase-3 activity in chronic myeloid cells: An in-vitro study. *Journal of Cancer Research and Therapeutics* **2018**, *14*, 1193.

9. Sethi, G.; Tergaonkar, V. Potential pharmacological control of the NF-κB pathway. *Trends in pharmacological sciences* **2009**, *30*, 313-321.

10. Nakamae, I.; Morimoto, T.; Shima, H.; Shionyu, M.; Fujiki, H.; Yoneda-Kato, N.; Yokoyama, T.; Kanaya, S.; Kakiuchi, K.; Shirai, T. Curcumin derivatives verify the essentiality of ROS upregulation in tumor suppression. *Molecules* **2019**, *24*, 4067.

11. Schieber, M.; Chandel, N.S. ROS function in redox signaling and oxidative stress. *Current biology* **2014**, *24*, R453-R462.

12. Goel, A.; Kunnumakkara, A.B.; Aggarwal, B.B. Curcumin as "Curecumin": From kitchen to clinic. *Biochemical pharmacology* **2008**, *75*, 787-809.

13. Ringman, J.M.; Frautschy, S.A.; Cole, G.M.; Masterman, D.L.; Cummings, J.L. A potential role of the curry spice curcumin in Alzheimer's disease. *Current Alzheimer Research* **2005**, *2*, 131-136.

14. Maheshwari, R.K.; Singh, A.K.; Gaddipati, J.; Srimal, R.C. Multiple biological activities of curcumin: a short review. *Life sciences* **2006**, *78*, 2081-2087.

15. Trujillo, J.; Chirino, Y.I.; Molina-Jijón, E.; Andérica-Romero, A.C.; Tapia, E.; Pedraza-Chaverrí, J. Renoprotective effect of the antioxidant curcumin: Recent findings. *Redox biology* **2013**, *1*, 448-456.

16. FDA, U. GRAS notification for curcumin preparation (Curcumin C3 Complex®). **2013**.

17. Schneider, C.; Gordon, O.N.; Edwards, R.L.; Luis, P.B. Degradation of curcumin: from mechanism to biological implications. *Journal of agricultural and food chemistry* **2015**, *63*, 7606-7614.

18. Heger, M.; van Golen, R.F.; Broekgaarden, M.; Michel, M.C. The molecular basis for the pharmacokinetics and pharmacodynamics of curcumin and its metabolites in relation to cancer. *Pharmacological reviews* **2014**, *66*, 222-307.

19. Kurien, B.T.; Singh, A.; Matsumoto, H.; Scofield, R.H. Improving the solubility and pharmacological efficacy of curcumin by heat treatment. *Assay and drug development technologies* **2007**, *5*, 567-576.

20. Liang, G.; Shao, L.; Wang, Y.; Zhao, C.; Chu, Y.; Xiao, J.; Zhao, Y.; Li, X.; Yang, S. Exploration and synthesis of curcumin analogues with improved structural stability both in vitro and in vivo as cytotoxic agents. *Bioorganic & medicinal chemistry* **2009**, *17*, 2623-2631.

21. Nelson, K.M.; Dahlin, J.L.; Bisson, J.; Graham, J.; Pauli, G.F.; Walters, M.A. The essential medicinal chemistry of curcumin: miniperspective. *Journal of medicinal chemistry* **2017**, *60*, 1620-1637.

22. Anselmo, A.C.; Mitragotri, S. An overview of clinical and commercial impact of drug delivery systems. *Journal of controlled release* **2014**, *190*, 15-28.

23. Dawidczyk, C.M.; Kim, C.; Park, J.H.; Russell, L.M.; Lee, K.H.; Pomper, M.G.; Searson, P.C. State-of-the-art in design rules for drug delivery platforms: lessons learned from FDA-approved nanomedicines. *Journal of controlled release* **2014**, *187*, 133-144.

24. Xu, W.; Ling, P.; Zhang, T. Polymeric micelles, a promising drug delivery system to enhance bioavailability of poorly water-soluble drugs. *Journal of drug delivery* **2013**, *2013*.

25. Kulthe, S.S.; Choudhari, Y.M.; Inamdar, N.N.; Mourya, V. Polymeric micelles: authoritative aspects for drug delivery. *Designed Monomers and Polymers* **2012**, *15*, 465-521.

26. Mandal, A.; Bisht, R.; Rupenthal, I.D.; Mitra, A.K. Polymeric micelles for ocular drug delivery: From structural frameworks to recent preclinical studies. *Journal of controlled release* **2017**, *248*, 96-116.

27. Suhail, N.; Alzahrani, A.K.; Basha, W.J.; Kizilbash, N.; Zaidi, A.; Ambreen, J.; Khachfe, H.M. Microemulsions: Unique Properties, Pharmacological Applications, and Targeted Drug Delivery. *Frontiers in Nanotechnology* **2021**, 69.

28. Üstündağ Okur, N.; Çağlar, E.Ş.; Siafaka, P.I. Novel ocular drug delivery systems: An update on microemulsions. *Journal of Ocular Pharmacology and Therapeutics* **2020**, *36*, 342-354.

29. Benbow, T.; Campbell, J. Microemulsions as transdermal drug delivery systems for nonsteroidal anti-inflammatory drugs (NSAIDs): a literature review. *Drug Development and Industrial Pharmacy* **2019**, *45*, 1849-1855.

30. Podgórna, K.; Szczepanowicz, K.; Piotrowski, M.; Gajdošová, M.; Štěpánek, F.; Warszyński, P. Gadolinium alginate nanogels for theranostic applications. *Colloids and Surfaces B: Biointerfaces* **2017**, *153*, 183-189.

31. Suhail, M.; Rosenholm, J.M.; Minhas, M.U.; Badshah, S.F.; Naeem, A.; Khan, K.U.; Fahad, M. Nanogels as drug-delivery systems: A comprehensive overview. *Therapeutic Delivery* **2019**, *10*, 697-717.

32. Sur, S.; Rathore, A.; Dave, V.; Reddy, K.R.; Chouhan, R.S.; Sadhu, V. Recent developments in functionalized polymer nanoparticles for efficient drug delivery system. *Nano-Structures & Nano-Objects* **2019**, *20*, 100397.

33. Begines, B.; Ortiz, T.; Pérez-Aranda, M.; Martínez, G.; Merinero, M.; Argüelles-Arias, F.; Alcudia, A. Polymeric nanoparticles for drug delivery: Recent developments and future prospects. *Nanomaterials* **2020**, *10*, 1403.

34. Gagliardi, A.; Giuliano, E.; Venkateswararao, E.; Fresta, M.; Bulotta, S.; Awasthi, V.; Cosco, D. Biodegradable polymeric nanoparticles for drug delivery to solid tumors. *Frontiers in pharmacology* **2021**, *12*, 601626.

35. Mahajan, S.; Patharkar, A.; Kuche, K.; Maheshwari, R.; Deb, P.K.; Kalia, K.; Tekade, R.K. Functionalized carbon nanotubes as emerging delivery system for the treatment of cancer. *International journal of pharmaceutics* **2018**, *548*, 540-558.

36. Maleki, R.; Afrouzi, H.H.; Hosseini, M.; Toghraie, D.; Rostami, S. Molecular dynamics simulation of Doxorubicin loading with N-isopropyl acrylamide carbon nanotube in a drug delivery system. *Computer Methods and Programs in Biomedicine* **2020**, *184*, 105303.

37. Yang, H.Y.; Li, Y.; Lee, D.S. Multifunctional and stimuli-responsive magnetic nanoparticle-based delivery systems for biomedical applications. *Advanced Therapeutics* **2018**, *1*, 1800011.

38. Gholami, A.; Mousavi, S.M.; Hashemi, S.A.; Ghasemi, Y.; Chiang, W.-H.; Parvin, N. Current trends in chemical modifications of magnetic nanoparticles for targeted drug delivery in cancer chemotherapy. *Drug metabolism reviews* **2020**, *52*, 205-224.

39. Olusanya, T.O.; Haj Ahmad, R.R.; Ibegbu, D.M.; Smith, J.R.; Elkordy, A.A. Liposomal drug delivery systems and anticancer drugs. *Molecules* **2018**, *23*, 907.

40. Guimarães, D.; Cavaco-Paulo, A.; Nogueira, E. Design of liposomes as drug delivery system for therapeutic applications. *International journal of pharmaceutics* **2021**, *601*, 120571.

41. Akbarzadeh, A.; Rezaei-Sadabady, R.; Davaran, S.; Joo, S.W.; Zarghami, N.; Hanifehpour, Y.; Samiei, M.; Kouhi, M.; Nejati-Koshki, K. Liposome: classification, preparation, and applications. *Nanoscale research letters* **2013**, *8*, 1-9.

42. Maja, L.; Željko, K.; Mateja, P. Sustainable technologies for liposome preparation. *The Journal of Supercritical Fluids* **2020**, *165*, 104984.

43. Stubbs, M.; McSheehy, P.; Griffiths, J.R. Causes and consequences of acidic pH in tumors: a magnetic resonance study. *Advances in enzyme regulation* **1999**, *39*, 13-30.

44. Webb, B.A.; Chimenti, M.; Jacobson, M.P.; Barber, D.L. Dysregulated pH: a perfect storm for cancer progression. *Nature reviews cancer* **2011**, *11*, 671-677.

45. Poon, Z.; Chang, D.; Zhao, X.; Hammond, P.T. Layer-by-layer nanoparticles with a pH-sheddable layer for in vivo targeting of tumor hypoxia. *ACS nano* **2011**, *5*, 4284-4292.

46. Oudin, M.J.; Weaver, V.M. Physical and chemical gradients in the tumor microenvironment regulate tumor cell invasion, migration, and metastasis. In Proceedings of the Cold Spring Harbor symposia on quantitative biology, **2016**; pp. 189-205.

47. Tian, L.; Bae, Y.H. Cancer nanomedicines targeting tumor extracellular pH. *Colloids and Surfaces B: Biointerfaces* **2012**, *99*, 116-126.

48. Haley, B.; Frenkel, E. Nanoparticles for drug delivery in cancer treatment. In Proceedings of the Urologic Oncology: Seminars and original investigations, **2008**; pp. 57-64.

49. Danhier, F.; Feron, O.; Préat, V. To exploit the tumor microenvironment: passive and active tumor targeting of nanocarriers for anti-cancer drug delivery. *Journal of controlled release* **2010**, *148*, 135-146.

50. Sawant, R.R.; Torchilin, V.P. Challenges in development of targeted liposomal therapeutics. *The AAPS journal* **2012**, *14*, 303-315.

51. Maeda, H. SMANCS and polymer-conjugated macromolecular drugs: advantages in cancer chemotherapy. *Advanced drug delivery reviews* **2001**, *46*, 169-185.

52. Matsumura, Y.; Maeda, H. A new concept for macromolecular therapeutics in cancer chemotherapy: mechanism of tumoritropic accumulation of proteins and the antitumor agent smancs. *Cancer research* **1986**, *46*, 6387-6392.

53. Yan, X.; Scherphof, G.L.; Kamps, J.A. Liposome opsonization. *Journal of liposome research* **2005**, *15*, 109-139.

54. Patel, H. Serum opsonins and liposomes: their interaction and opsonophagocytosis. *Critical reviews in therapeutic drug carrier systems* **1992**, *9*, 39-90.

55. Wiederschain, G.Y. The Molecular Probes handbook. A guide to fluorescent probes and labeling technologies. *Biochemistry (Moscow)* **2011**, *76*, 1276-1277.

56. Ulrich, A.S. Biophysical aspects of using liposomes as delivery vehicles. *Bioscience reports* **2002**, *22*, 129-150.

57. Muz, B.; de la Puente, P.; Azab, F.; Azab, A.K. The role of hypoxia in cancer progression, angiogenesis, metastasis, and resistance to therapy. *Hypoxia* **2015**, *3*, 83.

58. Horsman, M.R.; Overgaard, J. The impact of hypoxia and its modification of the outcome of radiotherapy. *Journal of radiation research* **2016**, *57*, i90-i98.

59. Mahmoudi, M.; Sant, S.; Wang, B.; Laurent, S.; Sen, T. Superparamagnetic iron oxide nanoparticles (SPIONs): development, surface modification and applications in chemotherapy. *Advanced drug delivery reviews* **2011**, *63*, 24-46.

60. Gieré, R. Magnetite in the human body: Biogenic vs. anthropogenic. *Proceedings of the National Academy of Sciences* **2016**, *113*, 11986-11987.

61. Phumying, S.; Labuayai, S.; Swatsitang, E.; Amornkitbamrung, V.; Maensiri, S. Nanocrystalline spinel ferrite (MFe2O4, M= Ni, Co, Mn, Mg, Zn) powders prepared by a simple aloe vera plant-extracted solution hydrothermal route. *Materials Research Bulletin* **2013**, *48*, 2060-2065.

62. Dippong, T.; Levei, E.A.; Cadar, O. Recent advances in synthesis and applications of MFe2O4 (M= Co, Cu, Mn, Ni, Zn) nanoparticles. *Nanomaterials* **2021**, *11*, 1560.

63. EW, G. Magnetization in ferrites; saturation magnetization of ferrites with spinal structure. *nature* **1950**, *165*, 798-800.

64. Hussein, S.I.; Elkady, A.S.; Rashad, M.M.; Mostafa, A.; Megahid, R. Structural and magnetic properties of magnesium ferrite nanoparticles prepared via EDTA-based sol–gel reaction. *Journal of Magnetism and Magnetic Materials* **2015**, *379*, 9-15.

65. Carta, D.; Casula, M.F.; Falqui, A.; Loche, D.; Mountjoy, G.; Sangregorio, C.; Corrias, A. A structural and magnetic investigation of the inversion degree in ferrite nanocrystals MFe2O4 (M= Mn, Co, Ni). *The Journal of Physical Chemistry C* **2009**, *113*, 8606-8615.

66. Deatsch, A.E.; Evans, B.A. Heating efficiency in magnetic nanoparticle hyperthermia. *Journal of Magnetism and Magnetic Materials* **2014**, *354*, 163-172.

67. Kawade, V.; Bichile, G.; Jadhav, K. X-ray and infrared studies of chromium substituted magnesium ferrite. *Materials Letters* **2000**, *42*, 33-37.

68. Sharma, R.; Thakur, P.; Sharma, P.; Sharma, V. Mn 2+ doped Mg–Zn ferrite nanoparticles for microwave device applications. *IEEE Electron Device Letters* **2018**, *39*, 901-904.

69. Samariya, A.; Dolia, S.; Prasad, A.S.; Sharma, P.; Pareek, S.; Dhawan, M.; Kumar, S. Size dependent structural and magnetic behaviour of CaFe2O4. *Current Applied Physics* **2013**, *13*, 830-835.

70. Saldívar-Ramírez, M.; Sánchez-Torres, C.; Cortés-Hernández, D.; Escobedo-Bocardo, J.; Almanza-Robles, J.; Larson, A.; Reséndiz-Hernández, P.; Acuña-Gutiérrez, I. Study on the efficiency of nanosized magnetite and mixed ferrites in magnetic hyperthermia. *Journal of Materials Science: Materials in Medicine* **2014**, *25*, 2229-2236.

71. Šepelák, V.; Baabe, D.; Mienert, D.; Litterst, F.; Becker, K. Enhanced magnetisation in nanocrystalline high-energy milled MgFe2O4. *Scripta Materialia* **2003**, *48*, 961-966.

72. Gismelseed, A.M.; Mohammed, K.; Widatallah, H.; Al-Rawas, A.; Elzain, M.; Yousif, A. Structure and magnetic properties of the ZnxMg1-xFe2O4 ferrites. In Proceedings of the Journal of Physics: Conference Series, **2010**; p. 012138.

73. Mazen, S.; Mansour, S.; Zaki, H. Some physical and magnetic properties of Mg-Zn ferrite. *Crystal Research and Technology: Journal of Experimental and Industrial Crystallography* **2003**, *38*, 471-478.

74. Costa, P.; Lobo, J.M.S. Modeling and comparison of dissolution profiles. *European journal of pharmaceutical sciences* **2001**, *13*, 123-133.

75. Batzri, S.; Korn, E.D. Single bilayer liposomes prepared without sonication. *Biochimica et Biophysica Acta (BBA)-Biomembranes* **1973**, *298*, 1015-1019.

76. Cardoso, B.D.; Rio, I.S.; Rodrigues, A.R.O.; Fernandes, F.C.; Almeida, B.; Pires, A.; Pereira, A.; Araújo, J.; Castanheira, E.M.; Coutinho, P.J. Magnetoliposomes containing magnesium ferrite nanoparticles as nanocarriers for the model drug curcumin. *Royal Society open science* **2018**, *5*, 181017.

77. Lentz, B.R. Membrane "fluidity" as detected by diphenylhexatriene probes. *Chemistry and Physics of Lipids* **1989**, *50*, 171-190.

78. Tamba, Y.; Terashima, H.; Yamazaki, M. A membrane filtering method for the purification of giant unilamellar vesicles. *Chemistry and Physics of Lipids* **2011**, *164*, 351-358.

79. Tanaka, T.; Tamba, Y.; Masum, S.M.; Yamashita, Y.; Yamazaki, M. La3+ and Gd3+ induce shape change of giant unilamellar vesicles of phosphatidylcholine. *Biochimica et Biophysica Acta (BBA)-Biomembranes* **2002**, *1564*, 173-182.

80. Kremer, J.; Van der Esker, M.; Pathmamanoharan, C.; Wiersema, P. Vesicles of variable diameter prepared by a modified injection method. *Biochemistry* **1977**, *16*, 3932-3935.

81. Demasa, J.; Crosby, G. The measurement of photoluminescence quantum yields. 1 A Review2. *J. Chem. Phys* **1968**, *48*, 4726.

82. Fery-Forgues, S.; Lavabre, D. Are fluorescence quantum yields so tricky to measure? A demonstration using familiar stationery products. *Journal of chemical education* **1999**, *76*, 1260.

83. Valeur, B.; Berberan-Santos, M.N. *Molecular fluorescence: principles and applications*; John Wiley & Sons: 2012.

84. Pereira, D.S.; Cardoso, B.D.; Rodrigues, A.R.O.; Amorim, C.O.; Amaral, V.S.; Almeida, B.G.; Queiroz, M.-J.R.; Martinho, O.; Baltazar, F.; Calhelha, R.C. Magnetoliposomes containing calcium ferrite nanoparticles for applications in breast cancer therapy. *Pharmaceutics* **2019**, *11*, 477.

85. Kim, H.G.; Borse, P.H.; Jang, J.S.; Jeong, E.D.; Jung, O.-S.; Suh, Y.J.; Lee, J.S. Fabrication of CaFe 2 O 4/MgFe 2 O 4 bulk heterojunction for enhanced visible light photocatalysis. *Chemical Communications* **2009**, 5889-5891.

86. Rodríguez-Carvajal, J. Recent advances in magnetic structure determination by neutron powder diffraction. *Physica B: Condensed Matter* **1993**, *192*, 55-69.

87. Rodrigues, A.R.O.; Matos, J.O.; Nova Dias, A.M.; Almeida, B.G.; Pires, A.; Pereira, A.M.; Araújo, J.P.; Queiroz, M.-J.R.; Castanheira, E.M.; Coutinho, P.J. Development of multifunctional liposomes containing magnetic/plasmonic MnFe2O4/Au core/shell nanoparticles. *Pharmaceutics* **2018**, *11*, 10.

88. Pitschke, W.; Hermann, H.; Mattern, N. The influence of surface roughness on diffracted X-ray intensities in Bragg–Brentano geometry and its effect on the structure determination by means of Rietveld analysis. *Powder Diffraction* **1993**, *8*, 74-83.

89. Bamzai, K.; Kour, G.; Kaur, B.; Kulkarni, S. Preparation, and structural and magnetic properties of Ca substituted magnesium ferrite with composition MgCaxFe2− xO4 (= 0.00, 0.01, 0.03, 0.05, 0.07). *Journal of Materials* **2014**, *2014*.

90. Krishnan, K.M. *Fundamentals and applications of magnetic materials*; Oxford University Press: **2016**.

91. Khanna, L.; Verma, N. Synthesis, characterization and in vitro cytotoxicity study of calcium ferrite nanoparticles. *Materials science in semiconductor processing* **2013**, *16*, 1842-1848.

92. Kawanishi, M.; Ogo, S.; Ikemoto, M.; Totsuka, Y.; Ishino, K.; Wakabayashi, K.; Yagi, T. Genotoxicity and reactive oxygen species production induced by magnetite nanoparticles in mammalian cells. *The Journal of toxicological sciences* **2013**, *38*, 503-511.

93. Liu, G.; Gao, J.; Ai, H.; Chen, X. Applications and potential toxicity of magnetic iron oxide nanoparticles. *Small* **2013**, *9*, 1533-1545.

94. Widdrat, M.; Kumari, M.; Tompa, É.; Pósfai, M.; Hirt, A.M.; Faivre, D. Keeping Nanoparticles Fully Functional: Long-Term Storage and Alteration of Magnetite. *ChemPlusChem* **2014**, *79*, 1225-1233.

95. Zhang, S.; Niu, H.; Zhang, Y.; Liu, J.; Shi, Y.; Zhang, X.; Cai, Y. Biocompatible phosphatidylcholine bilayer coated on magnetic nanoparticles and their application in the extraction of several polycyclic aromatic hydrocarbons from environmental water and milk samples. *Journal of Chromatography A* **2012**, *1238*, 38-45.

96. Rodrigues, A.R.O.; Almeida, B.G.; Rodrigues, J.M.; Queiroz, M.J.R.; Calhelha, R.C.; Ferreira, I.C.; Pires, A.; Pereira, A.M.; Araújo, J.P.; Coutinho, P.J. Magnetoliposomes as carriers for promising antitumor thieno [3, 2-b] pyridin-7-arylamines: photophysical and biological studies. *RSC advances* **2017**, *7*, 15352-15361.

97. Illés, E.; Szekeres, M.; Kupcsik, E.; Tóth, I.Y.; Farkas, K.; Jedlovszky-Hajdú, A.; Tombácz, E. PEGylation of surfacted magnetite core–shell nanoparticles for biomedical application. *Colloids and Surfaces A: Physicochemical and Engineering Aspects* **2014**, *460*, 429-440.

98. Nuytten, N.; Hakimhashemi, M.; Ysenbaert, T.; Defour, L.; Trekker, J.; Soenen, S.; Van der Meeren, P.; De Cuyper, M. PEGylated lipids impede the lateral diffusion of adsorbed proteins at the surface of (magneto) liposomes. *Colloids and Surfaces B: Biointerfaces* **2010**, *80*, 227-231.

99. Estelrich, J.; Busquets, M.A.n.; del Carmen Morán, M. Effect of PEGylation on ligand-targeted magnetoliposomes: a missed goal. *Acs Omega* **2017**, *2*, 6544-6555.

100. Rankin, D.W. CRC handbook of chemistry and physics, edited by David R. Lide. **2009**.

101. Israelachvili, J.; Marčelja, S.; Horn, R.G. Physical principles of membrane organization. *Quarterly reviews of biophysics* **1980**, *13*, 121-200.

102. Kell, D.B.; Harris, C.M. On the dielectrically observable consequences of the diffusional motions of lipids and proteins in membranes. *European Biophysics Journal* **1985**, *12*, 181-197.

103. Hervault, A.; Thanh, N.T.K. Magnetic nanoparticle-based therapeutic agents for thermo-chemotherapy treatment of cancer. *Nanoscale* **2014**, *6*, 11553-11573.

104. Storey, R.D. Textbook errors & misconceptions in biology: Cell physiology. *The American Biology Teacher* **1992**, *54*, 200-203.

105. Tilley, L.; Thulborn, K.R.; Sawyer, W. An assessment of the fluidity gradient of the lipid bilayer as determined by a set of n-(9-anthroyloxy) fatty acids (n= 2, 6, 9, 12, 16). *Journal of Biological Chemistry* **1979**, *254*, 2592-2594.

106. Bahri, M.A.; Heyne, B.J.; Hans, P.; Seret, A.E.; Mouithys-Mickalad, A.A.; Hoebeke, M.D. Quantification of lipid bilayer effective microviscosity and fluidity effect induced by propofol. *Biophysical chemistry* **2005**, *114*, 53-61.

107. Afzalipour, R.; Khoei, S.; Khoee, S.; Shirvalilou, S.; Raoufi, N.J.; Motevalian, M.; Karimi, M.Y. Thermosensitive magnetic nanoparticles exposed to alternating magnetic field and heat-mediated chemotherapy for an effective dual therapy in rat glioma model. *Nanomedicine: Nanotechnology, Biology and Medicine* **2021**, *31*, 102319.

108. Atkinson, W.J.; Brezovich, I.A.; Chakraborty, D.P. Usable frequencies in hyperthermia with thermal seeds. *IEEE Transactions on Biomedical Engineering* **1984**, 70-75.

109. Rainey, N.E.; Moustapha, A.; Saric, A.; Nicolas, G.; Sureau, F.; Petit, P.X. Iron chelation by curcumin suppresses both curcumin-induced autophagy and cell death together with iron overload neoplastic transformation. *Cell death discovery* **2019**, *5*, 1-15.

110. Muela, A.; Muñoz, D.; Martín-Rodríguez, R.; Orue, I.a.; Garaio, E.; Abad Diaz de Cerio, A.; Alonso, J.; García, J.Á.; Fdez-Gubieda, M.L. Optimal parameters for hyperthermia treatment using biomineralized magnetite nanoparticles: theoretical and experimental approach. *The Journal of Physical Chemistry C* **2016**, *120*, 24437-24448.

111. Ghitman, J.; Stan, R.; Ghebaur, A.; Cecoltan, S.; Vasile, E.; Iovu, H. Novel PEG-modified hybrid PLGA-vegetable oils nanostructured carriers for improving performances of indomethacin delivery. *Polymers* **2018**, *10*, 579.

112. Kini, S.; Bahadur, D.; Panda, D. Mechanism of anti-cancer activity of benomyl loaded nanoparticles in multidrug resistant cancer cells. *Journal of biomedical nanotechnology* **2015**, *11*, 877-889.

113. Joy, M.; Iyengar, S.J.; Chakraborty, J.; Ghosh, S. Layered double hydroxide using hydrothermal treatment: morphology evolution, intercalation and release kinetics of diclofenac sodium. *Frontiers of Materials Science* **2017**, *11*, 395-408.

CHAPTER 3

Solid magnetoliposomes based on shape-anisotropic nanoparticles and pre-validation as anticancer drug nanocarriers

This chapter describes the preparation of new shape-anisotropic calcium-substituted magnesium ferrite nanoparticles ($Ca_{0.25}Mg_{0.75}Fe_2O_4$) to improve the magnetic properties over the ones of the spherical counterparts. It also describes the development of a new methodology for synthesising solid magnetoliposomes, composed of a superparamagnetic core based on shape-anisotropic ferrite nanoparticles, as doxorubicin nanocarriers for cancer therapy. The results of this chapter were published in the journal *Pharmaceutics.*

Cardoso, B.D.; Rodrigues, A.R.O.; Bañobre-López, M.; Almeida, B.G.; Amorim, C.O.; Amaral, V.S.; Coutinho, P.J.; Castanheira, E.M. Magnetoliposomes based on shape anisotropic calcium/magnesium ferrite nanoparticles as nanocarriers for doxorubicin. *Pharmaceutics* **2021**, *13*, 1248.

3.1. Overview

The scientific community seeks to make magnetoliposomes a step forward in liposomal drug delivery technology while facing the biological challenges that it still presents. Thus, the development of magnetoliposomes must follow the advances in liposomal and magnetic nanoparticle technology. Combining the widely used liposome structure with magnetic nanoparticles in magnetoliposomes allies the advantages of using liposomes with the possibility to guide, selectively accumulate magnetically, and magnetically control the release of drugs on target. The effectiveness of these nanosystems is intrinsically related to the individual characteristics of the two main components — lipid formulation and magnetic nanoparticles — and their physicochemical combination. The developed new shape-anisotropic calcium-substituted magnesium ferrite nanoparticles ($Ca_{0.25}Mg_{0.75}Fe_2O_4$) revealed a superparamagnetic behaviour, high saturation magnetisation (50.07 emu/g at 300 K), and a large heating capacity. Furthermore, a new method for the synthesis of SMLs was developed to enhance their magnetic response. The manufacturing technicalities were optimised with different lipid compositions (DPPC, DPPC/Ch, and DPPC/DSPE-PEG) originating nanosystems with optimal sizes for biomedical applications (around or below 150 nm) low PDI. The high encapsulation efficiency of DOX in these magnetoliposomes was proven, as well as the ability of the drug-loaded nanosystems to interact with cell membrane models and release DOX by fusion. Furthermore, SMLs were revealed to reduce DOX interaction with HSA, contributing to a prolonged drug bioavailability upon systemic administration. Finally, the drug release kinetic assays revealed a preferable DOX release at hyperthermia temperatures (42 °C) and acidic conditions (pH = 5.5), indicating them as promising controlled release nanocarriers by either internal (pH) and external (AMF) stimuli in cancer therapy.

3.2. Introduction

Realistic advances in liposomal drug delivery technology require the intersection of multidisciplinary approaches that aim to improve systems from their manufacturing process, design process, pharmacokinetics, pharmacodynamics, and pre-clinical and clinical evaluation. The previous chapter explored the basic principles of superparamagnetic nanoparticle synthesis, the influence of different components on their properties, and its inclusion in different types of magnetoliposomes as proof-of-concept. The acquired knowledge was projected for this chapter, which intends the (i) development of a

protocol for the synthesis of nanoparticles with better magnetic properties; and (ii) development of a new methodology for the synthesis of magnetoliposomes with reproducible and improved properties.

The requirement for better magnetic properties is related to the nanoparticle's functional role in magnetoliposomes, which aims to contribute to magnetic guidance, controlled drug release, and magnetic hyperthermia in target sites. The magnetic hyperthermia process can be induced by exposing the NPs to an AMF whose Brownian and Néel relaxations of the rotating magnetic moment induce heat production [1,2]. This effect, named magnetic fluid hyperthermia (MFH), has been investigated to enhance the therapeutic effects of cancer through its direct damage to the cells, while inducing greater perfusion within the tumour, leading to higher internalisation of chemotherapeutic drugs [3-6]. It also promotes higher oxygenation, making the tumour more sensitive to the action of radiotherapy [7]. In turn, the heating power of magnetic NPs highly depends on the application properties of the external magnetic field (such as the frequency, applied field and the combination of both), as well as properties inherent to the NPs themselves, such as the saturation magnetisation and the anisotropy energy of magnetic NPs [8]. The latter is, in turn, dependent on the shape of the NPs, so greater hyperthermia efficiency can be achieved by changing their shape. For instance, cubic-shaped iron oxide magnetic NPs have already shown an improved saturation magnetisation and SAR compared to their spherical counterparts [9]. In addition to directly improving the responsiveness of magnetoliposomes, enhancing the intrinsic properties contributes to reducing the dose of NPs, also reducing the risk of cytotoxicity and undesirable accumulation.

With this in perspective, cubic-shaped calcium-substituted magnesium ferrite NPs (specifically $Ca_{0.25}Mg_{0.75}Fe_2O_4$) can be good candidates to be included on a magnetoliposomes core, enhancing the magnetic response of the previously prepared spherical $Ca_{0.25}Mg_{0.75}Fe_2O_4$-based magnetoliposomes [10]. The development of those magnetoliposomes was focused on the encapsulation of a clinically relevant drug – DOX- rather than a model drug. DOX is an anthracycline antibiotic produced and extracted by Streptomyces peucetius, which has considerable significance in clinics as a chemotherapeutic agent since the 1960s. This drug is used in the treatment of solid tumours, as well as in the treatment of soft tissue and bone sarcomas [11]. It is currently used to treat a wide range of cancers, including breast cancer [12,13], bone cancer [14,15], gastric cancer [16], small cell lung cancer [17], acute lymphoblastic leukaemia [18], liver cancer [19,20] and Hodgkin and non-Hodgkin lymphomas [21-23]. The antineoplastic activity of DOX is indeed effective. However, its conventional use as a free drug is limited by the associated serious adverse effects, pharmacokinetics limitations, irreversible cardiomyopathy (that can occur at any time after treatment), and the associated drug resistance in long-

term anticancer treatments [24-26]. Potential treatment approaches that consider a size increase of the systemically administrated drug (at least 5–10 nm in diameter) [27] and the encapsulation of DOX in multifunctional nanosystems that aims for synergistic therapeutic effects in antitumor activity have been studied [28,29].

The following sections details the development and characterisation process of cubic-shaped $Ca_{0.25}Mg_{0.75}Fe_2O_4$ NPs and a novel method to produce SMLs with a high magnetic content in their inner compartment. Magnetic, hyperthermia, and structural characterisation confirmed the synthesis of shape-anisotropic superparamagnetic NPs with improved saturation magnetisation and heating abilities. Those cubic-shaped $Ca_{0.25}Mg_{0.75}Fe_2O_4$ NPs were included as the solid core of thermosensitive lipid membranes (DPPC, DPPC/Ch and DPPC/DSPE-PEG), aiming the controlled release of DOX under hyperthermia conditions. Furthermore, the interaction of the drug-loaded nanosystem with HSA was investigated to determine the ability of magnetoliposomes to protect the cargo from opsonisation. Finally, the potential of SMLs as a new therapeutic approach for locally controlled release under temperature (42 °C and 37 °C) and pH trigger (pH 5.5 and 7.4) was assessed.

3.3. Materials and Methods

Ultrapure water Milli-Q grade (MilliporeSigma, St. Louis, MO, USA) and spectroscopic grade solvents were used in all the synthesis procedures.

To synthesize magnetic NPs, the following chemicals were used: magnesium acetate tetrahydrate ($(CH_3COO)_2Mg \cdot 4H_2O$, from Sigma-Aldrich, St. Louis, MO, USA); calcium acetate hydrate $(CH_3COO)_2Ca \cdot x\ H_2O$, from Sigma-Aldrich, St. Louis, MO, USA); and iron (III) citrate tribasic monohydrate ($C_6H_5FeO_7 \cdot H_2O$, from Sigma-Aldrich, St. Louis, MO, USA); oleic acid ($CH_3(CH_2)_7CH{=}CH(CH_2)_7COOH$, from Sigma-Aldrich, St. Louis, MO, USA) and octadecylamine ($CH_3(CH_2)_{17}NH_2$, from Sigma-Aldrich, St. Louis, MO, USA).

The following chemicals were used to synthesize SMLs: 1,2-dipalmitoyl-sn-glycero-3-phosphocholine (DPPC, from Sigma-Aldrich, St. Louis, MO, USA); [1,2-distearoyl-sn-glycero-3-phosphoethanolamine-N-methoxy(polyethylene glycol)- 2000] (ammonium salt) (DSPE-PEG2000, from Avanti Polar Lipids, Birmingham, AL, USA); Cholesterol (3β-Hydroxy-5-cholestene, 5-Cholesten-3β-ol, , from Avanti Polar Lipids, Birmingham, AL, USA); doxorubicin hydrochloride ($C_{27}H_{29}NO_{11} \cdot HCl$, from Sigma-Aldrich, St. Louis, MO, USA); and heptane 99% ($CH_3(CH_2)_5CH_3$, from Sigma-Aldrich, water content ≤0.1%).

3.3.1. Synthesis of cubic $Ca_{0.25}Mg_{0.75}Fe_2O_4$ nanoparticles

Shape-anisotropic cubic superparamagnetic NPs of calcium-substituted magnesium ferrite (with 25% calcium), $Ca_{0.25}Mg_{0.75}Fe_2O_4$, were synthesised by a co-precipitation method adapted from [30]. First, 12.6 g of octadecylamine was heated in a heating mantle (Nahita-bleu, series 658) until its melting point was reached (52.9 °C), under continuous magnetic stirring. Next, an aqueous solution containing 0.75 mM of magnesium acetate tetrahydrate, 0.25 mM of calcium acetate hydrate, 2 mM of iron (III) citrate tribasic monohydrate, and 3.1 mM of oleic acid was added to the pre-heated 15 mL of octadecylamine. The mixture was heated at 10 °C/min until reaching 200 °C and then left for 90 min at this temperature. The resulting black precipitated NPs were washed with ethanol by several cycles of centrifugation (Hettich, UNIVERSAL 320). Finally, the NPs were calcined at 600 °C for 30 min (to remove octadecylamine and oleic acid residues) and washed with 10% ethanol in water, resulting in hydrophilic NPs.

3.3.2. Solid magnetoliposomes preparation

A new SMLs preparation method was developed to improve the reproducibility and the magnetic response of the previously used SMLs preparation method [10,31]. For magnetoliposomes preparation, the lipids DPPC and DSPE-PEG2000 were used.

First, SMLs were prepared by encapsulating the synthesised NPs into reverse micelle structures. For the first lipid layer, a thin film of DPPC with a final concentration of 1 mM (above critical concentration) was prepared by solvent evaporation under an ultrapure nitrogen flow. Then, 3 mL of heptane were added to the thin film and ultrasonicated (Misonix, Touch-screen S-4000) at a power of 190 W for a time interval of 15 min to form reverse micelles with uniform size. After that, 1 μM of the previously synthesised dried NPs was added to the ultrasonicated lipid formulation and subjected to 20 min of ultrasonication at 190 W to enforce the entrance of hydrophilic NPs into the reverse micelles and form a magnetic cluster core. Finally, magnetic decantation was used to purify the reverse micelles with a magnetic core. For that, a NdFeB N48 block magnet (Eclipse Magnetics Ltd., Sheffield, UK) with nickel-plated (Ni-Cu-Ni) coating was applied to the sample for 1 h. After that time, the non-magnetic supernatant was discarded, and the remaining solvent was evaporated under an ultrapure nitrogen flow. Then, the magnetic pellet was resuspended in ultrapure water.

Then, a total lipid concentration of 1 mM was added to the pre-heated (>41 °C) reverse micelle solution to form the second lipid layer. Then, centrifugation washed the resulting SMLs and purified them with

ultrapure water. In this step, magnetoliposomes containing Ch in the lipid bilayer added a lipid formulation that includes Ch in a DPPC:Ch molar ratio of 7:3, respectively. To synthesise PEGylated magnetoliposomes, a lipid formulation of DPPC:DSPE-PEG in a molar ratio of 95:5 was employed. Finally, DOX was encapsulated in SMLs by co-injecting a DOX ethanolic solution (final concentration 2×10^{-6} M) with the addition of the second lipid layer under vortexing (LBX, V05 series) (**Figure 3.1**).

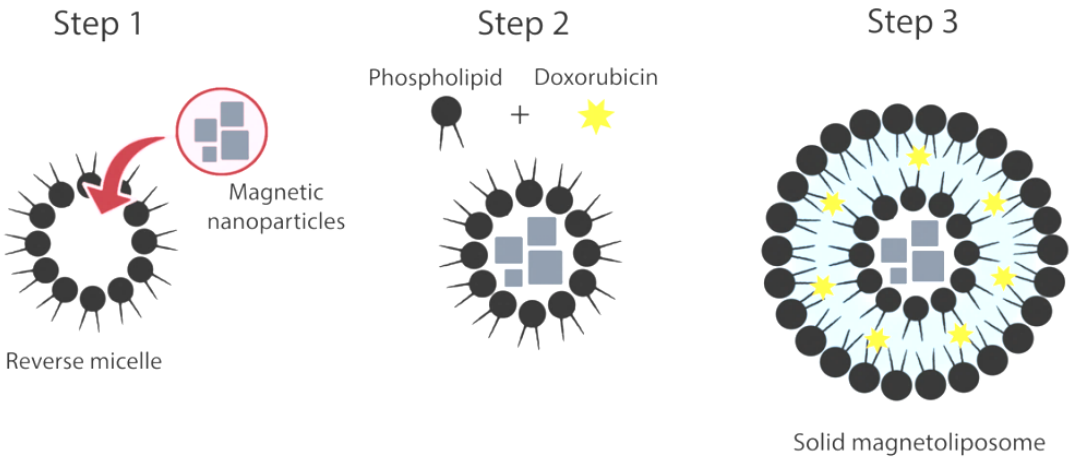


Figure 3.1 Schematic representation of the synthesis methodology of DOX-loaded SMLs.

3.3.3. Magnetic measurements and structural characterization

Magnetic properties of $Ca_{0.25}Mg_{0.75}Fe_2O_4$ NPs were investigated at room temperature in a superconducting quantum interference device (SQUID) magnetometer Quantum Design MPMS5XL (Quantum Design Inc., San Diego, CA, USA), using applied magnetic fields up to 5.5 T. The magnetisation hysteresis loop measurements were made by fixing the temperature and measuring the magnetisation at various applied magnetic fields.

The crystallographic state of the synthesised NPs was investigated by XRD following the detailed information in **section 2.3.5**.

HR-TEM images of magnetic NPs were recorded using a Transmission Electron Microscope JEOL JEM 2010F (JEOL Ltd., Tokyo, Japan) operating at 200 kV coupled to an Electron-Dispersive Spectroscopic analyser (EDS). The processing of TEM images was performed using ImageJ software (version 1.52 p, National Institutes of Health (NIH), Bethesda, MD, USA).

The average hydrodynamic diameter and size distributions of the liposomal formulations were measured after preparation using DLS equipment NANO ZS Malvern Zetasizer (Malvern Panalytical Ltd., Malvern,

UK), using a He-Ne laser of λ = 633 nm, a detector angle of 173°, and a controlled temperature of 25 °C. The SMLs solutions (at a lipid concentration of 1 mM) were prepared in filtered ultrapure water and measured in polystyrene cells, with a solvent refractive index of 1.33, a material refractive index of 1.4, and an absorption coefficient of 0.001 L/m. Five independent measurements were taken for each sample, and the data were processed using Malvern Zetasizer software (VERSION 7.13).

DLS measurements also assessed the colloidal stability of SMLs. 3 mL of DPPC-based SMLs aqueous solutions (at a lipid concentration of 1 mM) were stored at 4 °C for 30 days. Changes in hydrodynamic size and PDI of the samples were monitored during that time under the same conditions mentioned above.

3.3.4. Magnetic hyperthermia measurements

The heating efficiencies of $Ca_{0.25}Mg_{0.75}Fe_2O_4$ NPs were evaluated in a hyperthermia equipment DM 100 system, nB nanoscale Biomagnetics (Zaragoza, Spain) under an oscillating magnetic field at two different combinations of field strengths and frequencies: (a) H = 250 Gauss and f = 869 kHz and (b) H = 200 Gauss and f = 688 kHz, for a time range of 1 h. An optical fibre sensor was placed in the mid-point of a glass container containing an aqueous solution of 1 mg of NPs dispersed in 1 mL of water for temperature monitoring during the experiment. The container, in its turn, was placed in the mid-point of a copper coil. The temperature increase was logged as a function of time. Since magnetic hyperthermia is strongly dependent on NPs' power absorption from the applied magnetic field, the SAR can be calculated per unit mass of the NPs used and is given by the **Equation 3.1**,

Equation 3.1

$$\mathrm{SAR} = C \times \frac{\Delta T}{\Delta t} \times \frac{m_s}{m_m}$$

where C is the specific heat capacity of suspension in J/(kg °C), $\frac{\Delta T}{\Delta t}$ is the initial slope of the curve, and m_s and m_m express the mass (in kg) of suspension and magnetic material content in suspension, respectively. Even though the SAR is the most used way to characterise the heat capability generation, it does not allow comparing different experimental set-ups because the SAR value strongly depends on the strength and frequency of the applied field. To normalise SAR values, the intrinsic loss power (ILP, nH m^2/kg) has been suggested and is given by **Equation 3.2**,

Equation 3.2

$$ILP = \frac{SAR}{H^2 f}$$

where H is the field strength in kA/m, f is the frequency in kHz, and SAR should be introduced in W/kg [32].

3.3.5. Spectroscopic measurements

The absorption and fluorescence spectra were acquired with the equipment described in **section 2.3.1**. Doxorubicin hydrochloride was used to prepare solutions in several solvents (water, methanol, acetonitrile, ethanol, ethyl acetate, and chloroform) at 1×10^{-5} M, and the spectra were recorded in the 300–600 nm wavelength range. The spectrofluorometer has a temperature-controlled cuvette holder (with continuous stirring), being adjusted to 25 °C, 42 °C, or 55 °C for the different performed experiments. Fluorescence spectra were corrected for the instrumental response of the system. The fluorescence quantum yields (Φ_F) for DOX in several solvents are the average of 3 independent measurements (**Equation 2.2**). *FRET* assays were performed to confirm the formation of the lipid bilayer in the new method of SMLs preparation. The steady-state fluorescence anisotropy measurements were to study DOX incorporation in SMLs. Several assays were performed for the different lipid formulations and temperatures.

3.3.6. Drug Encapsulation efficiency and drug-loading capacity

DOX encapsulation efficiency (EE%) in magnetoliposomes was estimated by absorbance measurements. After magnetoliposomes loading with DOX, the aqueous solution of magnetoliposomes was magnetically decanted. The supernatant containing the non-encapsulated drug was used to determine the drug concentration by monitoring the absorbance at 480 nm (characteristic of DOX). Three independent measurements were performed for each system, and standard deviations (SD) were calculated. The drug encapsulation efficiencies of different lipid nanosystems were determined using **Equation 3.3**.

Equation 3.3

$$EE\ (\%) = \frac{Initial\ drug\ concentration\ (M) - drug\ concentration\ in\ the\ supernatant(M)}{Initial\ drug\ concentration\ (M)} \times 100$$

3.3.7. Interaction with human serum albumin

The binding to HSA was studied by the titration of a fixed concentration of 0.2 mM of HSA aqueous solution (equivalent to HSA blood plasma concentration) with a freshly prepared aqueous solution containing the ligand (free DOX, DPPC liposomes loaded with DOX, and DPPC/DSPE-PEG liposomes loaded with DOX). The experiment was carried out with liposomes instead of magnetoliposomes since the presence of magnetic NPs has a quenching effect on HSA fluorescence emission and thus strongly influences the results. In each increment (1 μL of ligand solution), the sample was left stabilizing at room temperature for 30 min. Each assay consisted of selectively measuring the fluorescent emission of tryptophan residues (excitation wavelength at 280 nm). The calculations were based on the changes in maximum fluorescence emission intensity found at 344 nm. The results were expressed by plotting fluorescence quenching of HSA emission as a function of ligands concentration. The emission spectra were recorded in the range of 290–700 nm, with an integration time of 1 s and the width of the slits set to 2 nm. The relative efficiency of HSA quenching can be described by **Equation 3.4** [33],

Equation 3.4

$$\%\ quenching = \frac{{y_{max}}^{n}}{1 + \frac{k_d}{[ligand]}}$$

where y_{max} is the maximum fluorescence quenching registered, n is the number of binding sites, and k_d is the dissociation constant. The affinity between the protein and the ligand (k_b) is inversely proportional to k_d and can be expressed by $1/k_d$.

3.3.8. Drug release kinetics and mathematical modelling of release profile

DOX release from SMLs was assessed in phosphate buffer at pH = 5.5 and 7.4 to simulate the drug release profile in the acidic tumour extracellular microenvironment and physiological fluids, respectively. The release studies were carried out at 37 °C and 42 °C (the latter representing hyperthermia treatments). All measurements were done in triplicate. For this purpose, a reusable 96-well Micro Equilibrium Dialysis Device HTD 96b from HTDialysis, LLC (Gales Ferry, CT, US) was used with regenerated cellulose dialysis membranes. The DOX release was followed for 30 h. The samples were collected from the acceptor compartments at different time points and measured by fluorescence

spectroscopy (λ_{exc} = 480 nm, in the range of 550–650 nm). The experimental DOX release profiles were fitted to different kinetics models (Weibull, first-order and Korsmeyer–Peppas — see Appendix A, **section A.3**) using Prism 8 software (GraphPad Software, La Jolla, CA, USA).

3.4. Results and Discussion

3.4.1. X-Ray diffraction analysis

A new preparation method for superparamagnetic shape anisotropic $Ca_{0.25}Mg_{0.75}Fe_2O_4$ ferrite NPs was developed. The corresponding XRD diffractogram is shown in **Figure 3.2** and was analyzed using Profex software based on BGMN Rietveld calculations [34]. The Ca/Mg mixed ferrite was defined by the magnesioferrite CIF file nr adaptation. 1011245 (space group Fd-3m:1), considering the distribution of cations across the tetrahedral and octahedral sites according to stoichiometry. The inversion degree was fixed to 0.825, as obtained previously for magnesioferrite [34]. A reasonable fit was obtained, with χ^2 = 2.06 and R_P = 10.3. The lattice parameter obtained was 8.350 Å, near the value reported in the magnesioferrite CIF file (8.360 Å). The influence of preferred orientation on the relative intensity of the diffraction peaks was modelled by taking into account the symmetry of the ferrite space group through spherical harmonics, as is implemented in BGMN [34]. Still, the fit is not perfect, indicating the influence of the anisotropic structure of the prepared NPs. Medium size of 20.9 ± 0.5 nm is estimated using the implementation of size broadening effects on BGMN [34].

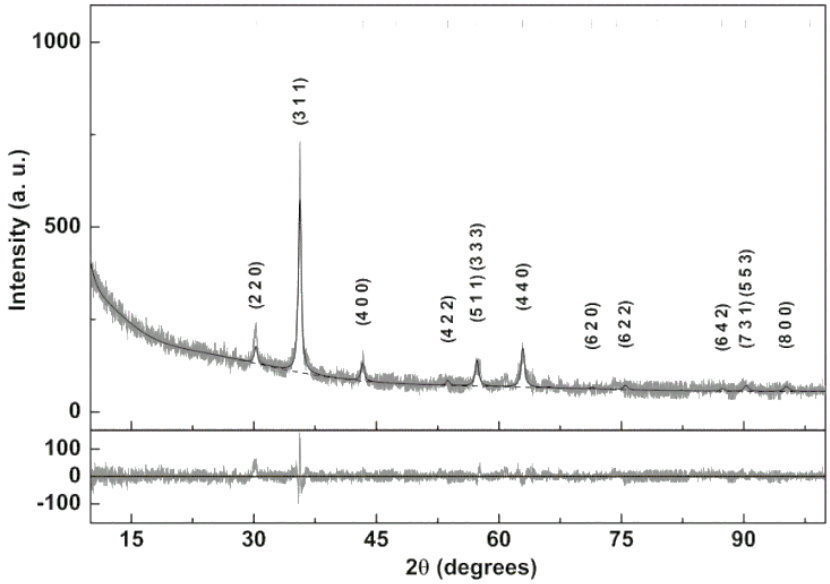


Figure 3.2 XRD pattern of the $Ca_{0.25}Mg_{0.75}Fe_2O_4$ NPs and corresponding Rietveld analysis.

3.4.2. Transmission electron microscopy

TEM analysis and small area electron diffraction (SAED) were carried out to determine the NPs' morphology, crystal structure, and size distribution (**Figure 3.3**). From the statistical analysis of 106 outlined NPs in **Figure 3.3 A**, it was possible to extrapolate the mean length of the major and minor axes of the particles and calculate the mean corresponding aspect ratio (height/width). In **Figure 3.3 B** and **C**, it is possible to distinguish well-elongated NPs, which belong to a population with an aspect ratio slightly higher than 1. The aspect ratio distribution histogram is displayed in **Figure 3.3 D** and reveals that NPs generally present a cubic, slightly rectangular shape, resulting in a population with a mean aspect ratio of 1.04±0.01. In addition, the size histogram was estimated considering the NPs' height (nm) and fitted to a Gaussian distribution, resulting in a population with a mean size of 20.8±5.3 nm (**Figure 3.3 E**), which is the size estimated by XRD. The SAED ring pattern (**Figure 3.3 F**) was indexed to a body centred cubic (BCC) structure, indexing (1 1 0), (2 0 0), (2 1 1), (2 2 0), and (3 1 0) from inside to outside.

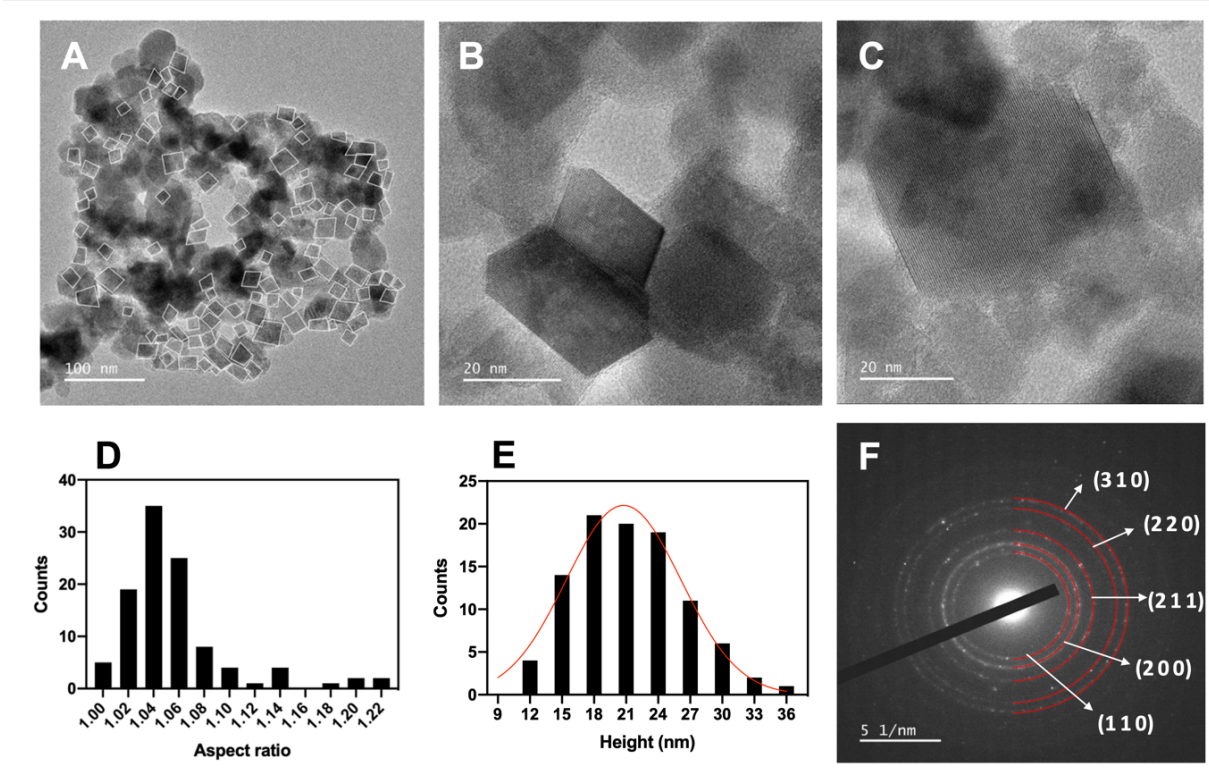


Figure 3.3 (A–C) HR-TEM images of $Ca_{0.25}Mg_{0.75}Fe_2O_4$ ferrite NPs at different magnifications. (D) Aspect ratio distribution histogram. (E) Size histogram and distribution fit ($R^2 = 0.96$) and (F) SAED image with indexed diffraction planes.

3.4.3. UV-Visible absorption

The optical properties of $Ca_{0.25}Mg_{0.75}Fe_2O_4$ ferrite NPs were determined using the Tauc model for energy band gap estimation. The UV-visible absorption (or transmission) spectrum of the synthesized NPs allows obtaining its optical band gap using a Tauc plot, which is given by **Equation 3.5**.

Equation 3.5

$$(\alpha h\nu)^n \sim (h\nu - E_g)$$

where α is the absorption coefficient (proportional to the absorbance), n is an exponent that depends on the nature of the transition (being $n = 2$ for a direct semiconductor and $n = 1/2$ for an indirect semiconductor), and E_g is the optical band gap. A linear relation was only obtained for $n = 2$, indicating that shape anisotropic $Ca_{0.25}Mg_{0.75}Fe_2O_4$ NPs behave as a direct semiconductor. The NPs' band gap was estimated from the intercept of $(\alpha h\nu)^2$ linear extrapolation with the Y-axis (**Figure 3.4**), resulting in a value of 1.29 eV. This band gap value is slightly lower than the previously obtained for spherical $Ca_{0.25}Mg_{0.75}Fe_2O_4$ ferrite (1.51 eV) [35], resulting from structural changes. In the same previous work [35], there was a demonstrated increase in band gap values with increased calcium ratio in mixed ferrite NPs.

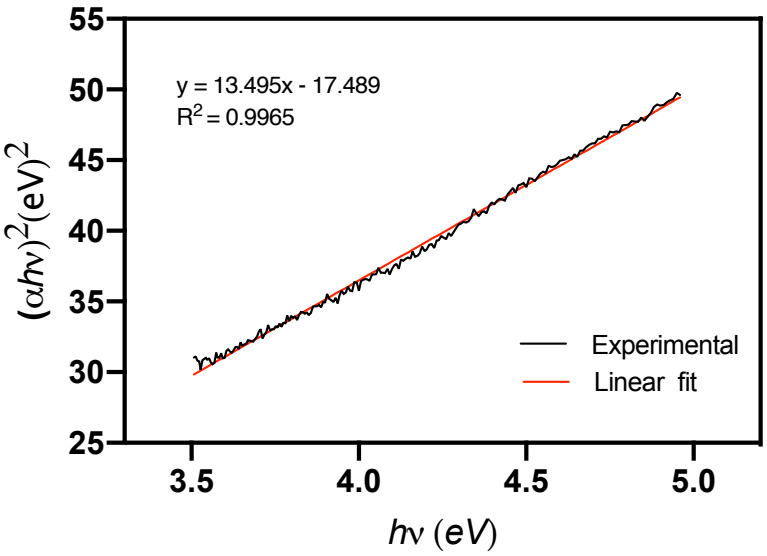


Figure 3.4 Tauc plot for shape-anisotropic $Ca_{0.25}Mg_{0.75}Fe_2O_4$ ferrite NPs (the red line corresponds to the linear fit).

3.4.4. Magnetic properties

Since magnetic hyperthermia is one of the aims of using SMLs in cancer therapy, it is fundamental to ensure that the magnetic NPs (which constitute the SMLs' core) present ideal features for biological application effectiveness.

In the previous work [35], the magnetic properties of spherical calcium-substituted magnesium ferrite NPs ($Ca_xMg_{1-x}Fe_2O_4$; x = 0.25, 0.50, 0.75) were studied, and a nonlinear effect on maximum magnetisation, as a result of calcium substitution, was noticed. Although Ca^{2+} is a non-magnetic ion, its concentration highly influences the distribution of Fe^{3+} ions (which have a magnetic moment of $5\mu_B$) between A (tetrahedral) and B (octahedral) sites. When calcium proportion in a ferrite structure assumes values of $x > 0.05$, Ca^{2+} migrates to B sites, and the distribution of calcium-substituted magnesium ferrite takes the form $\left(Ca^{2+}_{x-y}Fe^{3+}_{1+x-y}\right)\left[Mg^{2+}_{1-x}Ca^{2+}_{y}Fe^{3+}_{1+x-y}\right]O^{2-}_{4}$ (where the curve and square brackets indicate tetrahedral (A-sites) and octahedral (B-sites) sublattice, respectively), x and y represent the probability of migration of a small fraction of Mg^{2+} and Ca^{2+} ions to A-sites, respectively. The results revealed that adding a small proportion of calcium, and consequent substitution of magnesium in ferrite structure, leads to improved magnetic properties when compared to calcium ferrite and magnesium ferrite synthesised by the same preparation method. However, ion distribution, size, and shape anisotropy can influence NPs' overall magnetisation. The shape of NPs influences the anisotropy in magnetic nanomaterials, and the acicular shape is reported to have a favourable effect on the magnetic properties [36].

The magnetisation measurements of shape-anisotropic $Ca_{0.25}Mg_{0.75}Fe_2O_4$ ferrite NPs, upon calcination, were made at 5 K and 300 K. **Figure 3.5** presents their magnetisation hysteresis cycle. The image inset magnifies the low field region to make the coercivity more noticeable. The magnetic properties, including saturation magnetisation (M_s), coercive field (H_c), and remnant magnetisation (M_r), are displayed in **Table 3.1**.

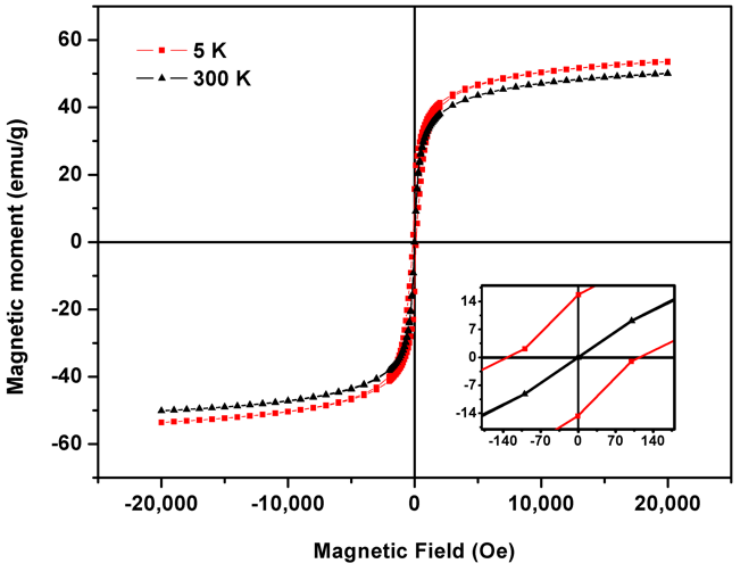


Figure 3.5 Magnetisation hysteresis cycle of $Ca_{0.25}Mg_{0.75}Fe_2O_4$ ferrite NPs at 5 K and 300 K. Inset: enlargement of the hysteresis loop in the low field region.

Table 3.1 H_C, M_s, M_r, and ratio M_r/M_s for cubic $Ca_{0.25}Mg_{0.75}Fe_2O_4$ ferrite NPs.

	T (K)	**H_C (Oe)**	**M_s (emu/g)**	**M_r (emu/g)**	**M_r/M_s**
M (H)	300	19.93	50.07	1.41	0.03
	5	128.64	53.65	15.66	0.29

At room temperature, the hysteresis loop is almost closed, and the low coercivity and remnant magnetisation values are compatible with superparamagnetic behaviour at high temperatures. The magnetic squareness value of the hysteresis cycle, which corresponds to the ratio between the remnant and saturation magnetisation (M_r/M_s), allows us to infer the presence of a superparamagnetic behaviour. The magnetic squareness values here obtained are below 0.1 at 300 K, indicating that more than 90% of the magnetisation was lost upon removing the magnetic field, corroborating the superparamagnetic behaviour. The low values of M_r/M_s (below 0.5) indicate a uniaxial anisotropy. Even though TEM images revealed NPs with larger dimensions than previously obtained, it is worth noting that the superparamagnetic behaviour is maintained. This happens since the critical grain size depends on the

shape of the NPs, and nanoarchitectures with shape anisotropy can remain in the single domain in larger dimensions than spherical NPs [36].

As expected, the saturation magnetisation values at T = 5 K are higher than those measured at T = 300 K due to the reduced thermal fluctuations at low temperatures. In addition, the coercivity value is higher for T = 5 K due to the disappearance of the superparamagnetic behaviour below the temperature at which the spins are blocked, that is, the blocking temperature. This noteworthy increase in coercivity is observed for all samples at 5 K and is attributed to the more significant magnetic anisotropy at low temperatures. Here, the effect of thermal fluctuations of blocked moments across the anisotropy barrier is responsible for enhancing the NPs' coercivity values. Therefore, the absence of thermal fluctuations tends to make the magnetic moments isotropic for low temperatures, resulting in a coercivity increase [37].

The saturation magnetisation of mixed ferrite NPs strongly depends on the shape of the NPs. Comparing the previously obtained spherical mixed ferrite NPs of calcium and magnesium with the shape-anisotropic ones here synthesised (for the same proportion of calcium and magnesium ions) [35], a noticeable improvement in the magnetic properties was observed for the shape-anisotropic ones. Noh *et al.* [38] also compared the saturation magnetisation between cubic and spherical $Zn_{0.4}Fe_{2.6}O_4$ NPs, the cubic ones reporting a higher saturation magnetisation (M_s = 165 emu/g) than spherical particles (M_s = 145 emu/g), corresponding to 1.14 times improvement. In this work, a higher enhancement of 3.86 times in M_s was achieved, from a saturation magnetisation of 12.98 emu/g (for the spherical NPs [35]) to 50.07 emu/g (for shape-anisotropic NPs with the same proportion of calcium and magnesium ions) (**Figure 3.5**). This enhancement comes from the effect of shape anisotropy on the ordering of surface atomic spins. Cubic NPs have lower energy surface facets of the family (1 0 0), and the spherical present different parts, resulting in a more significant surface spin disorder broadly distributed in the sphere surface. In contrast, in the cubic, the disorder is dominant only at the corners.

The obtained results point to a new and improved synthesis method for calcium-substituted magnesium ferrite NPs, in which the given shape anisotropy does not compromise their superparamagnetic behaviour. Furthermore, their magnetic features indicate their suitability for SMLs magnetic guidance and effectiveness as magnetic mediators for magnetic hyperthermia in cancer therapy.

3.4.5. Magnetic hyperthermia

To assess the hyperthermia potential of the synthesised cubic $Ca_{0.25}Mg_{0.75}Fe_2O_4$ ferrite NPs and SMLs based on those NPs, their heating efficiencies were evaluated under an oscillating magnetic field at two

different combinations of field strengths and frequencies: (a) H=250 Gauss and f=869 kHz and (b) H=200 Gauss and f=688 kHz. 1 mg of $Ca_{0.25}Mg_{0.75}Fe_2O_4$ ferrite NPs were dispersed in 1 mL of water. **Figure 3.6** shows a time-dependent temperature of the aqueous suspension under an AMF application. The synthesised NPs demonstrated a heating profile compatible with mild hyperthermia. The NPs revealed a large temperature variation over 30 min, with a ΔT=25.5 °C and ΔT=19.4 °C for H=250 Gauss and f = 869 kHz and H = 200 Gauss and f=688 kHz, respectively. The corresponding SMLs showed lower temperature variations, with a ΔT=19.4 °C and ΔT=16.4 °C for the same combinations of field strengths and frequencies. Hertg and Dutz [39] have estimated that the product of the applied magnetic field and oscillating frequency, when exposed to small body regions, should be $H \cdot f \leq 5 \times 10^9$ $A \cdot m^{-1} \cdot s^{-1}$. Thus, the experiments performed here are slightly above this criterion limit.

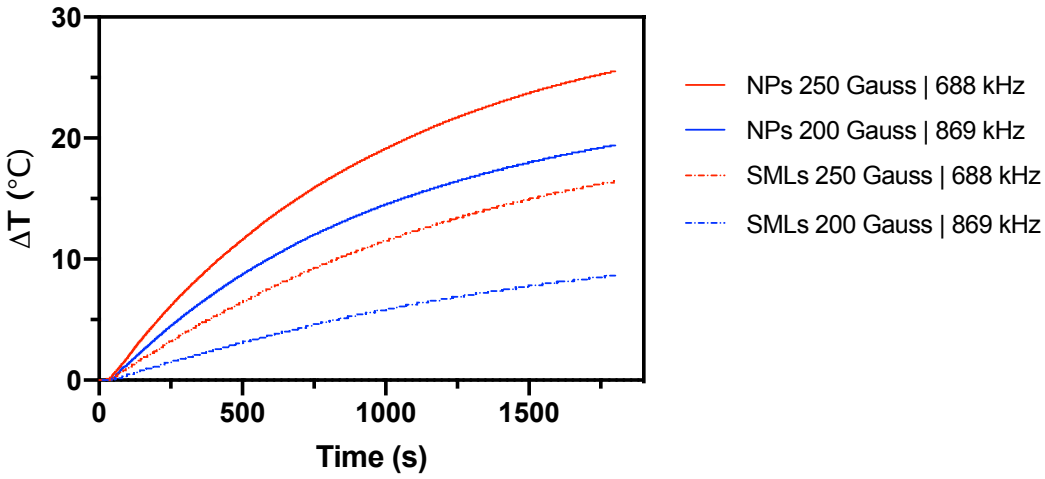


Figure 3.6 Magnetically-induced thermal response curve (temperature variation vs time) of $Ca_{0.25}Mg_{0.75}Fe_2O_4$ NPs and SMLs for magnetic hyperthermia. 1 mg of NPs were dispersed in 1 mL of water and subjected to an AMF with different field frequencies and strengths over 30 min (1800 s).

As so, the NPs must be further investigated to determine the conditions at which the reached temperatures are maintained at a mild hyperthermia threshold temperatures range, at the defined restriction limits for the safety and tolerance of patients. SAR and ILP were estimated from the initial slope of the heating curve, following **Equation 2.6** and **Equation 2.7**, respectively. For NPs, a SAR value of 34.66 W/g_{Fe} was estimated for an applied field of 200 G; in contrast, a SAR of 46.85 W/g_{Fe} was determined using an applied field of 250 G. The ILP estimated values were 15.69 $nH.m^2/kg$ and 17.13 $nH \cdot m^2/kg$, respectively. For SMLs, a SAR value of 12.26 W/g_{Fe} was assessed for an applied field of 200 G and 25.32 W/g_{Fe} for an applied field of 250 G; the calculated ILP values were 5.55 $nH \cdot m^2/kg$ and 9.25 $nH \cdot m^2/kg$, respectively. This reduction of the heating performance of SMLs relatively to the NPs in

the same conditions can be explained by dipole interactions related to the NPs cluster size. It was reported that at increased cluster sizes, the inherent NPs shape anisotropy is gradually lost, and consequently, the heating capabilities are reduced [40]. Furthermore, Haase and Nowak [41] have demonstrated that an optimal particle concentration exists to achieve the highest heating power per sample.

3.4.6. Photophysical properties of doxorubicin in solution

DOX, as an anthracycline, is an amphiphilic molecule that possesses a fluorescent hydroxy-substituted anthraquinone chromophore and a hydrophilic aminoglycosidic side chain (**Figure 3.7 A**) [42]. Considering those solute-solvent interactions can modify the intensity, position, and shape of absorption and emission bands, they can provide information about the structural changes of a molecule. Therefore, the effect of several solvents on DOX photophysical behaviour was studied by its absorption and fluorescence profiles, with the determination of maximum absorption wavelengths (λ_{abs}), maximum emission wavelengths (λ_{em}) molar absorption coefficients (ε), and fluorescence quantum yields (Φ_F), all summarised in **Table 3.2**. The UV-VIS absorption spectra of DOX and normalised steady-state fluorescence in different solvents are shown in **Figure 3.7 B**, and **C**, respectively.

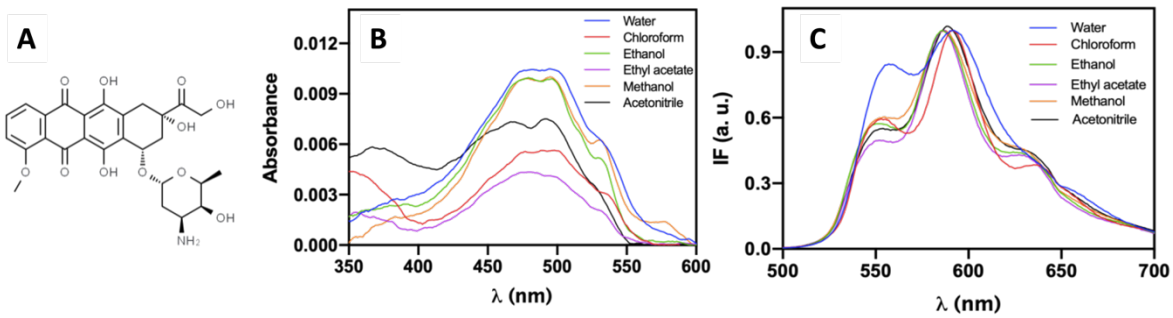


Figure 3.7 (A) Molecular structure of DOX ($C_{27}H_{29}NO_{11}$). (B) Absorption spectra of DOX solutions, at 1×10^{-5} M, in several solvents. (C) Normalized fluorescence (at the peak of maximum emission) spectra of DOX (1×10^{-6} M, λ_{exc} = 480 nm) in several solvents.

Fiallo *et al.* [43] reported that the leading band in the absorption spectra, around 480 nm, is associated with the π ⟶ π * transition polarised along the long (*y*) axis. In contrast, the band around 360 nm is associated with a partially forbidden *n* ⟶ π * transition (involving the three C=O groups). Therefore, the maximum at 480 nm is given for the transition of a quinonoid structure [44]. These allowed transitions

are responsible for the high molar absorption coefficients (in the range 10^3 – 10^4 $M^{-1}.cm^{-1}$) of DOX in all the studied solvents.

Regarding the fluorescence spectra, two prominent peaks and a shoulder are distinguished around 560 nm, 590 nm, and 633 nm [45]. The DOX fluorescence quantum yield (**Table 3.2**) demonstrated a higher value in water, $\Phi_F \approx 20\%$, while in other solvents, it varies in the range of 4% (methanol, acetonitrile, and chloroform) to 6% (ethanol). These low fluorescence quantum yields can result from DOX aggregation, forming non-fluorescent dimers [46,47]. In addition, an evident change in spectral shape in water is observed, with loss of vibrational structure [48], the relative increase in first peak intensity, and band enlargement. This broadening suggests a weak charge-transfer character for the lowest electronic excitation in the ground-state geometry. A slight red shift is observed with increasing medium polarity, this bathochromic shift indicating a π → π * transition.

Table 3.2 Maximum absorption (λ_{abs}) and emission wavelengths (λ_{em}), molar absorption coefficients (ε), and fluorescence quantum yields (Φ_F) for DOX in several solvents. [a] Relative to fluorescein in 0.1 M NaOH aqueous solution.

Solvent	**λ_{abs}/nm ($\varepsilon/10^4$ M^{-1} cm^{-1})**	**λ_{em}/nm**	**Φ_F [a]**
Water	487 (0.50)	591	0.20 ± 0.02
Methanol	488 (0.49)	586	0.04 ± 0.01
Acetonitrile	480 (0.38)	588	0.04 ± 0.01
Ethanol	489 (0.49)	587	0.06 ± 0.01
Ethyl acetate	484 (0.21)	587	0.05 ± 0.01
Chloroform	488 (0.28)	592	0.04 ± 0.01

[a] Relative to fluorescein in 0.1 M NaOH aqueous solution.

The intermolecular solute-solvent interactions can induce changes in the profile of a spectrally active molecule [49]. The solvent contributions can be classified as (i) specific interactions, which include localised donor-acceptor interactions with specific orbitals and acid-base interactions involving hydrogen bonding, and (ii) non-specific interactions resulting from solvent acting as a dielectric continuum. Here, four physicochemical parameters were studied: λ_{em}, λ_{abs}, the Stokes' shift ($\Delta\tilde{\nu}$), and fluorescence Φ_F.

These results demonstrate that solvent dipolarity can be neglected for slight variations in emission maxima, but solvent acidity, basicity, and polarizability play an active role in DOX emission maxima shift. In addition, solvent dipolarity is not a critical parameter in describing absorption maxima and Stokes' shifts. Finally, fluorescence quantum yield values are not primarily influenced by the solvents' basicity and dipolarity. Detailed analysis and information are presented in the Appendix A in **section A.1**. The knowledge of fluorescence emission properties of DOX will be used in the following sections to monitor drug location and release from the developed nanosystems.

3.4.7. Characterisation of Magnetoliposomes

3.4.7.1. Synthesis of solid magnetoliposomes

Herein, a new preparation method for SMLs was developed. This new approach begins with the preparation of DPPC reverse micelles, in which, by ultrasonication, the previously synthesised magnetic NPs are forced to enter. After magnetic decantation, a second DPPC layer is injected, resulting in a lipid bilayer vesicle with a magnetic core in a solid magnetoliposome architecture. Since the new methodology involves the independent addition of DPPC layers, the lipid bilayer formation was confirmed by *FRET*, following the previously reported procedure [35]. The first lipid layer was labelled with rhodamine B-DOPE (rhodamine B as the energy acceptor), and the second lipid layer was labelled with NBD-C_{12}-HPC (NBD as the energy donor). Once the second layer was added, the two fluorophores became close, and the conditions for *FRET* occurrence were satisfied. **Figure 3.8** shows the emission spectra of SMLs labelled with the energy donor NBD and the energy acceptor rhodamine B, separately and together in a single system, which are all measured upon excitation of the donor (λ_{exc}= 470 nm). The pronounced decrease in the NBD emission, accompanied by an increase in rhodamine B emission, evidences the energy transfer from excited NBD to rhodamine.

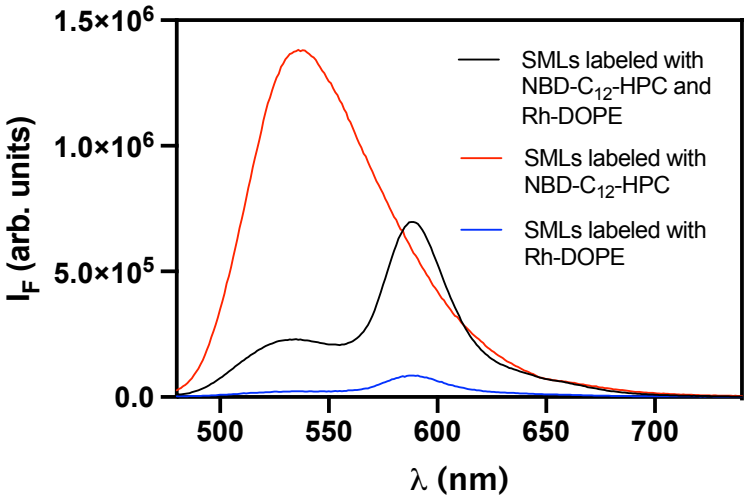


Figure 3.8 Fluorescence spectra (λ_{exc}=470 nm) of SMLs with a DPPC bilayer labelled with only NBD-C_{12}-HPC, with only Rh-DOPE, and labelled with both NBD-C_{12}-HPC and Rh-DOPE.

The calculated FRET efficiency (**Equation 2.2**) of 89.6% proves the probes' proximity, as a strong energy transfer is observed from donor to acceptor. The lipid bilayer formation was corroborated by a donor-acceptor distance of 3.5 nm (from **Equation 2.3** and **Equation 2.4**) since a lipid bilayer has a typical thickness between 7 and 9 nm [50]. *FRET* efficiency value is very similar to the previously obtained magnetoliposomes containing spherical $Ca_{0.25}Mg_{0.75}Fe_2O_4$ NPs [35], which reported a *FRET* efficiency of 87%. One of the main differences between the new synthesis method herein described and the previously reported [31,35] is that the magnetoliposomes prepared by this new method do not present any water in the inner compartment. As a result, the solid core makes the nanosystem less flexible (more rigid), which is translated into a decrease in lateral and rotational motion of lipids, improving the energy transfer between the probes.

3.4.7.2. Dynamic light scattering and transmission electron microscopy

Considering the crucial role that the nanosystems' inherent parameters (as size, PDI and shape) play on biological administration suitability and behaviour, DLS and TEM measurements were performed. DLS experiments allowed obtaining the size distribution of DPPC-based SMLs (**Table 3.3**), exhibiting an average hydrodynamic size of 117.5±0.5 nm and a generally small PDI. Correlation curves are presented in **Figure A.2** (see Appendix A in **section A.2**). The obtained average hydrodynamic size is slightly smaller than the previously obtained 127.3±17 nm for SMLs containing spherical $Ca_{0.25}Mg_{0.75}Fe_2O_4$ NPs [35], PDI values also being marginally lower. The stability of DPPC-based SMLs in storage at 4 °C was

also monitored for 30 days. **Figure 3.9** exhibits the size and PDI evolution of an aqueous solution of DPPC-based SMLs. This formulation is stable until day 15, with a slight increase in size between days 15 and 20, to around 240 nm. Similar behaviour was observed for PDI values, which increased to 0.25 on day 30 after storage. These results show that the nanosystems are utterly stable for 15 days.

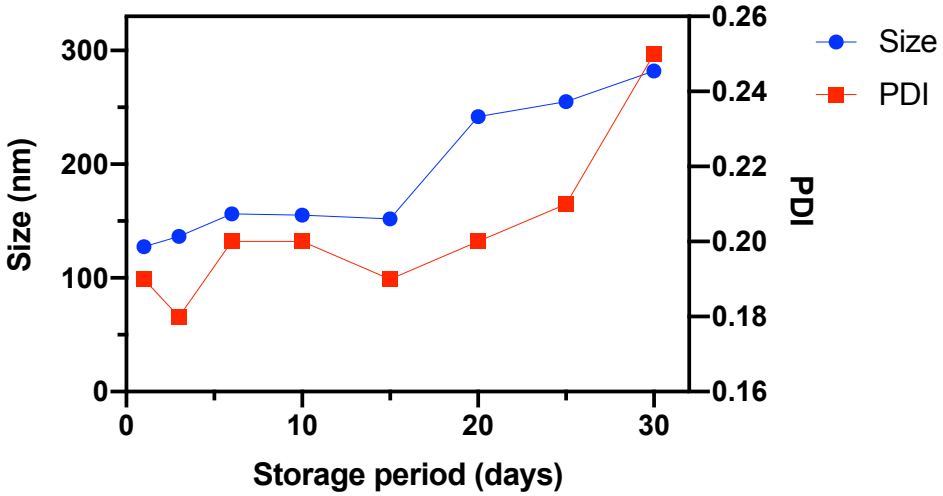


Figure 3.9 Hydrodynamic diameter and PDI evolution of an aqueous solution of DPPC-based SMLs during storage at 4 °C for 30 days.

The encapsulation of low molecular weight molecules (as DOX in lipid vesicles increases the size of the administrated anticancer agent above the renal clearance threshold (≈40 000 Da), resulting in a reduction in kidney excretion and, consequently, blood half-life increase. It is reported that the encapsulation of DOX in liposomes can improve its plasma half-life from 5–10 min (as a free drug) to 2–3 days (in liposomes) [51]. This increase in circulation times takes better advantage of the EPR effect, resulting in a more efficient and selective accumulation in the tumour [52]. As mentioned before, the extravasation of liposomes to tumours is more effective at sizes below 200 nm [53]. DLS measurements confirm that SMLs' hydrodynamic size conforms to the preferable size range (**Table 3.3**). Considering that modifications in liposomal and micellar formulations have shown promising results in preventing the aggregation and opsonisation of plasma proteins, PEGylated magnetoliposomes were also studied, exhibiting an average hydrodynamic diameter of 153.8±0.8 nm and a low PDI. The average size and PDI of PEGylated formulations were slightly higher than those of non-PEGylated ones (prepared by the same method). These results were not expected since a general size reduction trend in PEGylated liposomal formulations was reported. This size reduction is usually explained by an increased lateral repulsion

caused by PEG molecules, which induces curvature in the lipid bilayer and a consequent decrease in the vesicle size [54]. The difference in size can be partially explained by a structural variation between liposomes and these magnetoliposomes since the latter, instead of an aqueous inner volume, have a solid compartment constituted by a cluster of magnetic NPs. The hydrodynamic diameter of SMLs with Ch is similar to the values for PEGylated SMLs (151.4±0.60 nm), however, with a lower PDI value (0.20±0.01).

Table 3.3 Hydrodynamic diameter and PDI of several SMLs lipid formulations at 25 °C. Results as mean ± SD.

SMLs Lipid Formulation	D_H (nm)	PDI
DPPC	117.5±0.5	0.17±0.01
DPPC/DSPE-PEG	153.8±0.8	0.27±0.01
DPPC/Ch	151.4±0.6	0.20±0.01

TEM characterises the size and shape of SMLs. **Figure 3.10 A** exhibits a representative SML, characterised by the presence of a NPs cluster, highly contrasting with the bright, thin DPPC lipid bilayer. Using ImageJ software for image processing, several different segmented lines along the SML image were taken into account to measure the nanosystem mean diameter, resulting in a mean diameter of 116.5±5.5 nm. The same procedure was carried out to estimate the lipid bilayer's length, resulting in mean size of 8.3±1 nm, complying with those reported in the literature and obtained from FRET measurements. A schematic representation of SMLs was drawn from the clear TEM image and is presented in **Figure 3.10 B**.

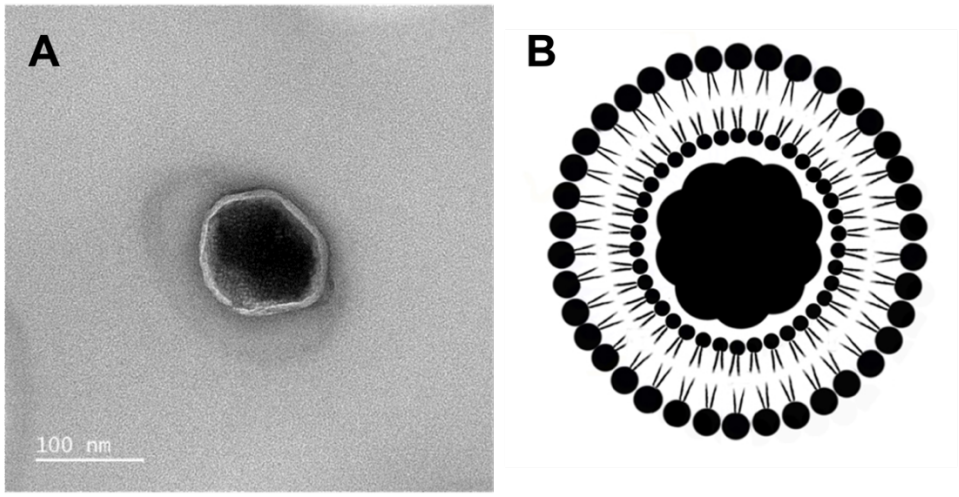


Figure 3.10 (A) HR-TEM image of a SML containing $Ca_{0.25}Mg_{0.75}Fe_2O_4$ ferrite NPs. (B) Schematic representation of a SML, characterised by the presence of a core (cluster of magnetic NPs) covered with a lipid bilayer.

3.4.7.3. Doxorubicin encapsulation in solid magnetoliposomes

The photophysical properties of DOX were exploited to study its encapsulation in SMLs and its location in the nanosystems. **Figure 3.11** shows the emission spectra of DOX, at the same concentration, in $Ca_{0.25}Mg_{0.75}Fe_2O_4$-based SMLs and liposomes of the same lipid composition (without magnetic NPs).

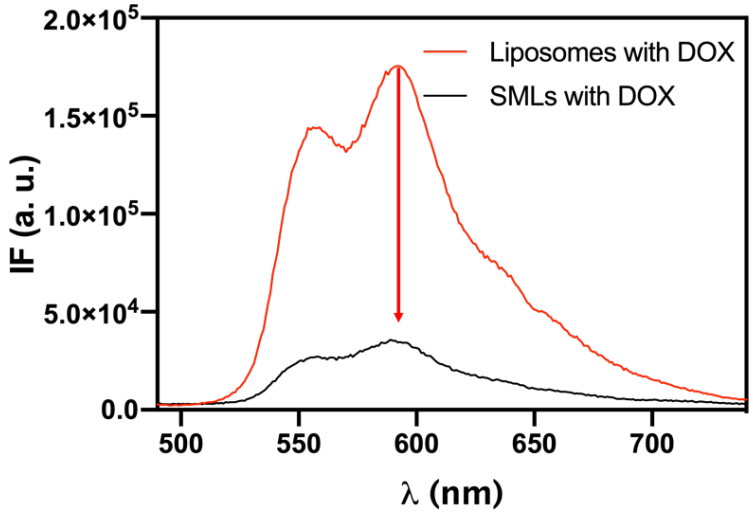


Figure 3.11 Fluorescence spectra (λ_{exc} = 480 nm) of DOX (2×10^{-6} M) in liposomes (without magnetic NPs) and in SMLs containing $Ca_{0.25}Mg_{0.75}Fe_2O_4$ magnetic NPs.

Compared to liposomes, the pronounced decrease in DOX's fluorescence emission in SMLs is due to a quenching effect by the NPs and confirms the incorporation of DOX in the nanocarriers. The incorporation of DOX in SMLs was further confirmed by fluorescence anisotropy measurements (**Equation 2.1**) related to the rotational mobility of the fluorescent molecule. The results are shown in **Table 3.4**.

Table 3.4 Steady-state fluorescence anisotropy values for DOX in SMLs with different lipid formulations, in SMLs upon interaction with GUVs and in GUVs (for comparison). Total lipid concentration: 1×10^{-3} M; DOX: 2×10^{-6} M.

Nanosystem	Lipid Formulation	Temperature (°C)	r
SMLs	DPPC	25	0.137
	DPPC:DSPE-PEG (95:5)		0.206
	DPPC:Ch (7:3)		0.075
	DPPC	55	0.100
	DPPC:DSPE-PEG (95:5)		0.133
	DPPC:Ch (7:3)		0.043
GUVs	Soybean lecithin	25	0.116
		55	0.058
SMLs + GUVs	DPPC	25	0.166
	DPPC:DSPE-PEG (95:5)		0.187
	DPPC:Ch (7:3)		0.139
	DPPC	55	0.081
	DPPC:DSPE-PEG (95:5)		0.121
	DPPC:Ch (7:3)		0.098

The fundamental fluorophore anisotropy (r_0) corresponds to the maximum fluorescence anisotropy, and a value of 0.33 was reported for DOX [55]. As expected, upon the encapsulation of DOX in SMLs (DPPC), room temperature anisotropy measurements registered values below r_0 (r = 0.137), but typical of a fluorophore in a lipid bilayer, which confirms the DOX encapsulation in SMLs. Since the melting transition temperature of DPPC occurs at 41 °C, an increase in membrane fluidity is expected when the liquid-

crystalline phase is attained. A lower fluorescence anisotropy value was observed at 55 °C, since the temperature increase implies increased mobility of DOX aglycone in the bilayer, providing evidence of DPPC phase transition from the gel to the liquid-crystalline phase.

Considering that the incorporation of Ch (present in most liposomal formulations used as drug carriers) and PEGylated lipids can significantly change the structural properties of a lipid bilayer, the anisotropy values of DOX were measured for SMLs containing these modifiers. A considerable increase in anisotropy value, at 25 °C, in DPPC/DPSE-PEG SMLs was observed, indicating that DOX can be reliably retained in the membrane of PEGylated magnetoliposomes. PEGylated SMLs showed higher anisotropy values at each condition than the other lipid formulations (**Table 3.4**), indicating a DOX location in a more exterior environment. The lipid bilayer fluidity varies with depth due to changes in membrane-free volume, showing a tendency to decrease from the liposome surface to the interior [56,57]. So, the higher *r* values may indicate that DOX is superficially near PEG. Additionally, the significant decrease in anisotropy from 25 to 55 °C indicates that hyperthermia can enhance PEGylated SMLs' ability to interact and release drugs in the target (due to the increase in membrane fluidity).

In the case of systems containing Ch, a general decrease in anisotropy was registered compared to non-modified vesicles. It is reported [58] that the addition of Ch in bilayers increases the apparent microviscosity of phosphatidylcholine (PC) membranes (up to 1.4 times) as a result of membrane-induced ordering of the PC acyl chains in the liquid phase. However, this effect is only verified in concentrations up to 20 mol% Ch. At higher content, its admixture decreases the microviscosity in the polar region of liposomes. Above 20 mol%, the area where Ch OH groups are located has a larger free volume available than in Ch-free membranes, resulting in a decreased fluorophore anisotropy [58]. This explains the smaller anisotropy values obtained for Ch-modified membranes.

The percentage of incorporated drug determined DOX encapsulation efficiencies (EE%) into SMLs relative to the initial amount of drug added (**Equation 3.3**). Different lipid formulations with two different initial DOX concentrations were studied. As shown in **Table 3.5**, EE% decreased with increasing drug/lipid ratio. The EE% of non-modified DPPC-based SMLs varied between 72±3% (for the initial concentration of 1×10^{-4} M) and 65±8 % (for the initial concentration of 2×10^{-4} M). Under the same conditions, a slight decrease was evidenced from non-modified SMLs to PEGylated SMLs. These results suggest that PEGylation has a negligible effect on drug EE%. The lowest EE% was found in DPPC:Ch-based SMLs, which varied between 50±2% and 48±8%. The general high encapsulation efficiencies observed in all systems evidence the suitability of the new method herein presented for DOX encapsulation and the use of these nanocarriers for dual cancer therapy (by combining magnetic hyperthermia and chemotherapy).

Table 3.5 EE% and corresponding encapsulated DOX concentration (M) in SMLs containing $Ca_{0.25}Mg_{0.75}Fe_2O_4$ at different concentrations of DOX. The standard deviation is from triplicate drug encapsulation assays.

	Initial DOX Concentration	
Lipid Formulation	**1×10^{-4} M**	**2×10^{-4} M**
DPPC	72%±3% (7.23×10^{-5} M)	65%±8% (1.31×10^{-4} M)
DPPC/DSPE-PEG (95:5)	70%±22% (7.04×10^{-5} M)	52%±19% (1.05×10^{-4}M)
DPPC/Ch (7:3)	50%±2% (5.05×10^{-5} M)	48%±8% (9.75×10^{-5} M)

Non-specific interaction between drug-loaded magnetoliposomes and GUVs, used as membrane models, was investigated to assess the ability of magnetoliposomes to release the content by fusion. Since DOX fluorescence emission suffers a quenching effect from the magnetic NPs that compose the SMLs core, this assay was performed by analysing DOX fluorescence variations before and after interaction with GUVs. Upon interaction, if fusion between the systems occurs, the DOX emission spectrum will reveal an unquenching effect due to forming a larger membrane and a corresponding increase in distance between the magnetic NPs and DOX. The interest in DPPC-based SMLs is due to DPPC melting T_m, closely similar to the temperatures used in mild hyperthermia therapy. Therefore, the assays were also conducted at 55 °C to conclude the potential of magnetic hyperthermia to enhance fusion with cell membranes and the release capability of the SMLs. In all spectra of DPPC-based SMLs, DPPC/DSPE-PEG-based SMLs, and DPPC/Ch-based SMLs, an unquenching effect of DOX fluorescence is noticed upon SMLs' interaction with GUVs (**Figure 3.12**). However, when the exchange occurs at 55 °C, the spectra reveal a more pronounced unquenching effect. These results prove that membrane fusion occurs and that the fusogenic capability is enhanced with an increase in temperature.

To corroborate the results, DOX anisotropy was also measured upon SML interaction with GUVs (**Table 3.4**). It is essential to notice that before interaction, DOX presented a lower anisotropy value in DPPC and DPPC/Ch lipid formulations than in DPPC/DSPE-PEG. Upon interaction with GUVs, DOX shows a slightly higher anisotropy in DPPC and DPPC/Ch-based SMLs than before. In the DPPC/DSPE-PEG, a decrease in anisotropy is noticed. Since DOX is located more superficially in PEGylated SMLs, anisotropy has an intermediate value between soy lecithin GUVs and DPPC/DSPE-PEG, proving interaction and fusion. These results can also explain the more pronounced unquenching effect in DPPC/DSPE-PEG

spectra upon interaction with GUVs at 25 °C. In addition, above the DPPC phase T_m, an enhanced fusion between all systems occurs. The anisotropy values registered at 55 °C are relatively low (around 0.07), which is the anisotropy value of DOX in a saline PBS buffer [59]. These values point to a possible DOX release to the aqueous medium.

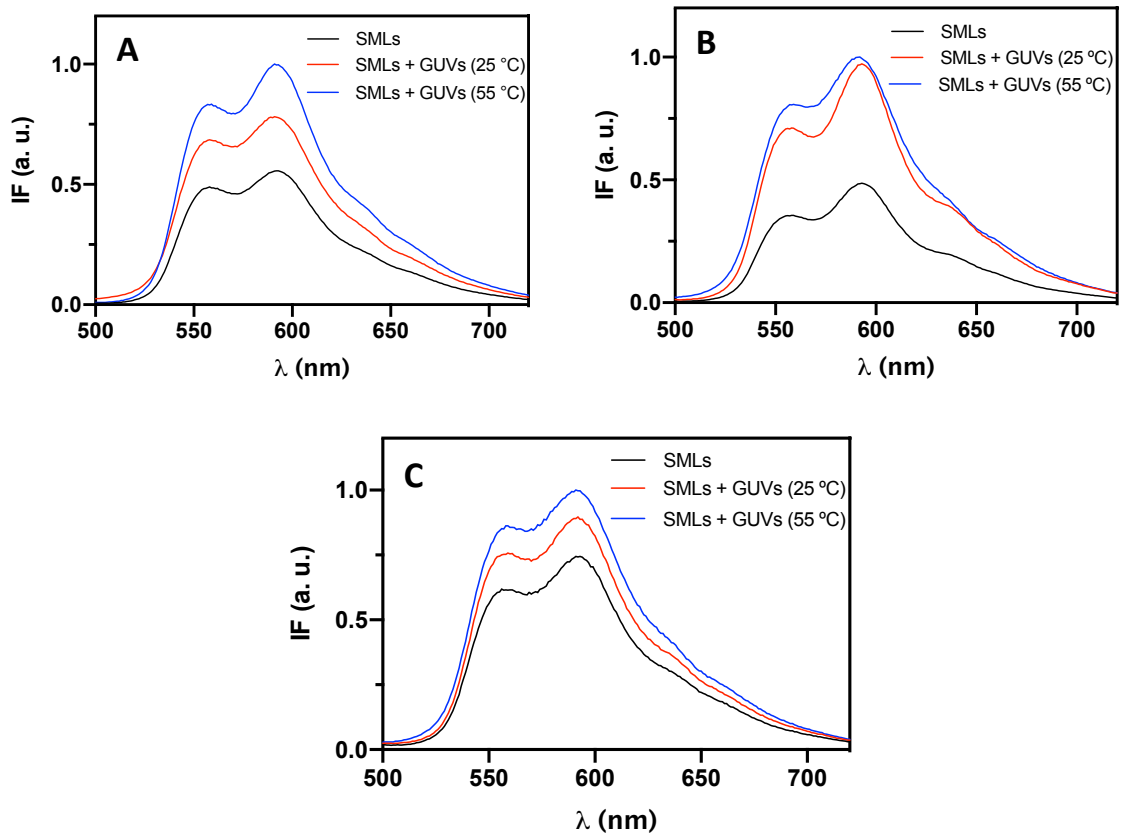


Figure 3.12 Fluorescence spectra (λ_{exc}= 480 nm) of DOX in SMLs containing $Ca_{0.25}Mg_{0.75}Fe_2O_4$, before and after interaction with GUVs at 25 °C and 55 °C, for the different lipid formulations. A: DPPC; B: DPPC:DSPE-PEG; C: DPPC:Ch.

3.4.7.4. Interaction with human serum albumin

The interaction between nanocarriers and HSA has significance in investigating and designing new nanocarriers *in vitro*. HSA intrinsic fluorescence comes from the emission of tryptophan, tyrosine, and phenylalanine residues. However, HSA emission arises mainly from the Trp214 residue in the hydrophobic cavity. The interaction between HSA and lipid vesicles induces protein conformation changes, resulting in a quenching effect of Trp214 fluorescence. Therefore, fluorescence quenching

assays can give an insight into the interactions of DOX and DOX-loaded liposomes with plasma proteins that affect the stability of the different lipid formulations under physiological conditions.

The titration of an HSA aqueous solution (0.2 mM) with 1 μL of the different freshly prepared solutions (free DOX, DOX-loaded DPPC liposomes, and DOX-loaded DPPC/DSPE-PEG liposomes) revealed a gradual HSA fluorescence drop, implying an interaction between the protein and DOX or drug-loaded liposomes. The variation of HSA fluorescence quenching (%) with ligand concentration is shown in **Figure 3.13**, evidencing an apparent reduction of interaction between DOX and HSA when the drug is encapsulated in PEGylated nanocarriers.

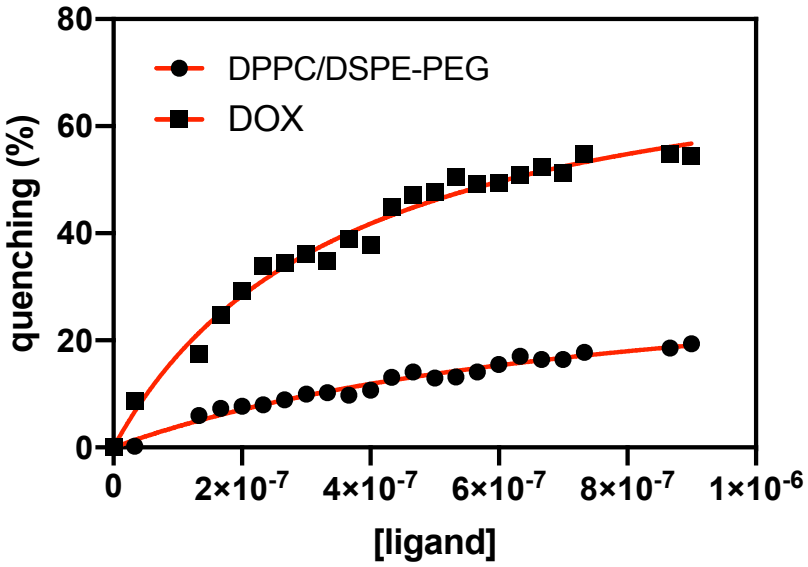


Figure 3.13 HSA fluorescence quenching (%) as a function of increasing DOX concentration in free form and loaded in DPPC/DSPE-PEG-based liposomes. According to **Equation 3.4**, a nonlinear fit is presented (red lines).

Fitting the results according to the nonlinear regression given by **Equation 3.4**, it was possible to calculate the dissociation constant (K_d) and the number of specific binding sites and then estimate the binding constant (K_b) (**Table 3.6**). The results revealed a sizeable binding constant between DOX and HSA and 1.20 binding sites, indicating a significant binding of free DOX to the blood plasma protein. A significant decrease in binding constant is observed upon the encapsulation of DOX in DPPC-based and DPPC/DSPE-PEG-based liposomes. The results suggest that DPPC and DPPC/DSPE-PEG nanosystems protect DOX from interacting with plasma proteins. Even though the binding constant presents a higher value in PEGylated liposomes when compared to non-PEGylated ones, the number of available binding

locations decreases. Thakur *et al.* [60] demonstrated that HSA penetrates DPPC liposomes, inducing an alteration in their packing order. This penetration is caused by hydrophobic interactions, which lead to the release of encapsulated payload. Thus, PEGylated vesicles can better protect the payloads, enhancing their bioavailability for longer time intervals, which is especially relevant for the effectiveness of the EPR effect in tumours.

Table 3.6 The dissociation constant (k_d), binding constant ($k_b = 1/k_d$), and the number of binding locations (n) of DOX, DPPC liposomes, and DPPC:DSPE-PEG liposomes to HSA.

	k_d (M)	k_b (M^{-1})	n	R^2
Free DOX	3.69×10^{-9}	27.1×10^{7}	1.20	0.99
DPPC	2.54×10^{-6}	3.93×10^{5}	2.27	0.97
DPPC/DSPE-PEG	14.47×10^{-7}	1.18×10^{6}	1.78	0.97

3.4.7.5. Drug release kinetics and mathematical modelling of release profile

Considering the complexity of cancer cells' biology and the difficulties found along the treatments, it is essential to integrate combined and synergistic approaches to ensure a more effective, localised, and controlled therapy. The DOX release profiles from DPPC-based and DPPC/DSPE-PEG-based SMLs at different pH values (5.5 and 7.4) and temperatures (37 °C and 42 °C) are presented in **Figure 3.14**. The results of DPPC SMLs show that the drug release rate is highly dependent on pH and temperature. The release profile at 42 °C and pH = 5.5 stands out compared to the other combinations, exhibiting a burst release of 21.0±0.4% in the initial 6 h. The burst release is followed by a linear release phase, presenting a slow and controlled release profile that achieved the maximum release of 25±2% at 28 h. Considering that 42 °C is above the DPPC T_m, there was an expected higher release rate at this temperature, considering the increase in permeability of magnetoliposomes membrane, which was verified at pH = 5.5. However, at pH = 7.4, the maximum release percentage is only 6.5±0.2%, which is 3.5 times lower than the values obtained at pH = 5.5. These results provide evidence that acidic pH increases the hydrophilicity of DOX, contributing to an accelerated drug release that is also verified at 37 °C. At physiological temperature, both pH conditions present slow-release kinetics, achieving a maximum release of 9±1% at pH = 5.5 and 4±1% at pH = 7.4. At physiological pH, DOX is protected by

magnetoliposomes, and its release is delayed. In therapeutic conditions, the cardiotoxicity of the anthracyclines is dose-limiting, often leading to heart failure due to dilated cardiomyopathy years after exposure [61]. Willis *et al.* [62] demonstrated dose-dependent cardiac atrophy in mice at relatively low doses. By delaying DOX release at physiological conditions, magnetoliposomes offer a protective effect over DOX-associated cardiomyopathy and other systemic adverse side effects. Liposomal DOX was associated with a cardiac and gastrointestinal toxicity reduction while maintaining a similar antitumor efficacy [63]. Recently, Swietch *et al.* [64] demonstrated that the medium pH impacts the affinity of DOX toward the carrier, and the anthracycline's protonation at acidic pH facilitates drug release. In addition, Chai *et al.* [65] observed an increased release rate of DOX at a decreased medium pH in DOX-loaded poly(lactic-*co*-glycolic acid) (PLGA) NPs. The authors attributed the results to a strongly pH-dependent solubility, facilitating DOX release at low pH values.

A similar release kinetics behaviour was found for DPPC/DSPE-PEG-based SMLs (**Figure 3.14 B**), with a notable delayed release rate at 42 °C. PEGylated SMLs did not exhibit a burst release in the early hours, only achieving a maximum DOX release of 13±1% at 28 h. These results indicate that the PEG matrix on SMLs' surfaces acts as a barrier by reducing the diffusion of DOX into the surroundings. The increased sustained DOX release in PEGylated SMLs indicates a prolonged drug delivery period.

The results indicate a preferable DOX release at hyperthermia and acidic conditions, meaning that drug release may occur more readily in tumours. These are preliminary results of the behaviour of the novel nanocarriers with a temperature and pH trigger, not considering the mechanical effect that superparamagnetic NPs (subjected to an AMF) would have on the active drug release. Considering that the purpose of controlled release systems is to maintain drugs in target sites at the desired concentration and control the drug release rate and duration, the sustained release ability of SMLs suggests a novel controlled release nanosystem.

The DOX release profile was fitted to three kinetic models: Weibull, first-order, and Korsmeyer-Peppas (see Appendix A in **section A.3**, **Table A.3** and **Table A.4**). The coefficients of determination (R^2) indicate that Weibull is the best-fitting model to describe the overall release of DOX from both formulations. Since the Weibull model is empirical, it lacks kinetic basis information, and its parameters do not present a physical meaning. Papadopoulou *et al.* [66] studied a link between the values of b and the diffusional mechanisms of the release, proposing that for $b > 1$, the drug transport follows a complex release mechanism; $b \leq 0.75$ indicates Fickian diffusion (in either fractal or Euclidian spaces); $0.75 < b < 1$ indicates a combined mechanism (Fickian diffusion and Case II transport). **Table A.3** (DPPC SMLs) shows that at 42 °C, both pH conditions present a b value higher than 1, evidencing a complex

mechanism for DOX release. At 37 °C, it is verified that $0.75 < b < 1$, evidencing a Fickian diffusion. **Table A.4** (DPPC/DSPE-PEG SMLs) indicates that $b < 0.75$ in all the conditions, pointing to a Fickian diffusion. The results indicate a change in the mechanism of DOX release when functionalising DPPC SMLs with DSPE-PEG.

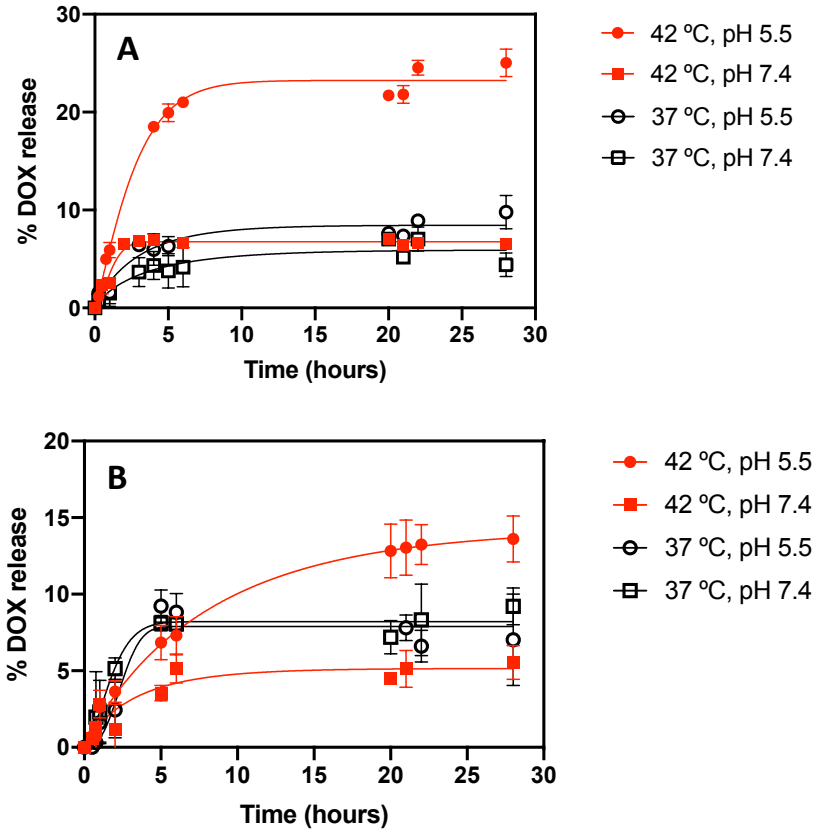


Figure 3.14 *In vitro* kinetic release profile of DOX encapsulated in SMLs at different conditions of temperatures and pH, with the triplicate mean fitted to the Weibull kinetic model. (A) DPPC-based SMLs. (B) DPPC/DSPE-PEG-based SMLs.

Similarly to the Weibull model, the first-order model revealed a higher R^2 for the assays performed at 42 °C and pH = 5.5 in both formulations, suggesting that the amount of released DOX is proportional to the remaining drug in the nanocarrier. The Korsmeyer-Peppas model presents the worst coefficient of determination values. The n values are under the threshold of 0.43 unless in the PEGylated SMLs at 42 °C and pH = 5.5. However, $n < 0.5$, indicating a diffusion-controlled release mechanism [67]. Since DOX is encapsulated in nearly spherical-shaped nanosystems, values of $n \leq 0.45$ represent a Fickian diffusion mechanism [68]. The large variations of R^2 found at 42 °C in DPPC SMLs (compared to the

ones obtained by the Weibull model) indicate a complex drug release mechanism instead of only a diffusion-controlled release.

The morphology evolution of DOX-loaded DPPC and DPPC/DSPE-PEG SMLs as a function of temperature at both pH values were studied by DLS measurements (**Figure 3.15**). Overall, it was noticed that the SMLs size tends to gradually decrease at pH = 7.4 with increasing temperature. At pH = 5.5, both formulations revealed an opposite variation in increasing temperature. At pH = 5.5, both formulations revealed an opposite variation in size, with a tendency to increase with rising temperature. These results show that SMLs size tend to increase with rising temperature. These results show that SMLs become more unstable at acidic conditions and above the DPPC T_m, become more unstable at acidic conditions and above the DPPC T_m, corroborating the DOX release profiles presented above.

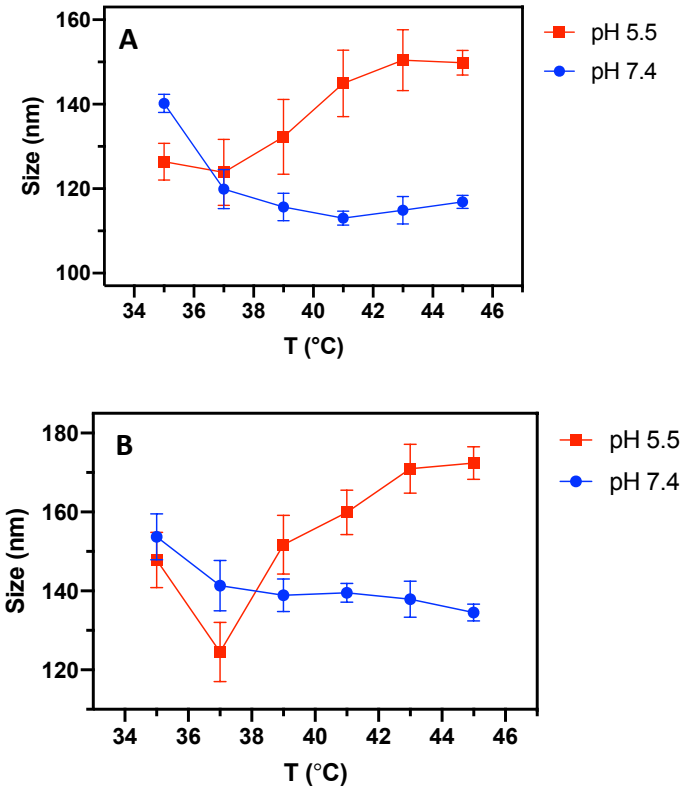


Figure 3.15 Size variation of DOX-loaded SMLs with increasing temperature at different pH values. (A) DPPC-based SMLs. (B) DPPC/DSPE-PEG-based SMLs. Mean size values and standard deviation are from triplicate assays.

3.5. Conclusions

In this work, cubic-shaped $Ca_{0.25}Mg_{0.75}Fe_2O_4$ NPs, with an average size of approximately 20 nm, were successfully synthesised by a co-precipitation method, their saturation magnetisation being considerably higher than that of the spherical counterparts. These NPs were incorporated in SMLs prepared by a new method. The technique produced SMLs with different lipid formulations and sizes suitable for biomedical applications, encapsulating the chemotherapeutic drug DOX. DOX-loaded SMLs revealed the ability to fuse with model membranes (GUVs), with enhanced fusogenic capabilities at higher temperatures. The interaction of DOX with HSA protein is strongly reduced when the drug is loaded in the liposomal nanocarriers, indicating a protective effect that improves drug bioavailability. DOX release profiles revealed an enhanced release under acidic conditions and mild hyperthermia temperature. A more sustained release was obtained for PEGylated SMLs, pointing to a prolonged delivery from PEGylated nanocarriers.

Overall, the results indicate that combining shape-anisotropic magnetic NPs and thermosensitive lipid bilayers is a promising approach for dual cancer therapy, combining chemotherapy and magnetic hyperthermia. In addition, to the best of our knowledge, it is the first time that SMLs were prepared using cubic calcium-substituted magnesium ferrite NPs.

Future work will focus on magnetically controlled drug release, determining the strength, frequency and AMF application time for optimal DOX release. In addition, the synergistic effect between chemotherapy and magnetic hyperthermia will be investigated in human tumour cell lines.

3.6. References

1. Fortin, J.-P.; Gazeau, F.; Wilhelm, C. Intracellular heating of living cells through Néel relaxation of magnetic nanoparticles. *European Biophysics Journal* **2008**, *37*, 223-228.

2. Makridis, A.; Topouridou, K.; Tziomaki, M.; Sakellari, D.; Simeonidis, K.; Angelakeris, M.; Yavropoulou, M.P.; Yovos, J.G.; Kalogirou, O. In vitro application of Mn-ferrite nanoparticles as novel magnetic hyperthermia agents. *Journal of Materials Chemistry B* **2014**, *2*, 8390-8398.

3. Gieré, R. Magnetite in the human body: Biogenic vs. anthropogenic. *Proceedings of the National Academy of Sciences* **2016**, *113*, 11986-11987.

4. Kolen'ko, Y.V.; Bañobre-López, M.; Rodríguez-Abreu, C.; Carbó-Argibay, E.; Sailsman, A.; Piñeiro-Redondo, Y.; Cerqueira, M.F.; Petrovykh, D.Y.; Kovnir, K.; Lebedev, O.I. Large-scale synthesis of colloidal Fe3O4 nanoparticles exhibiting high heating efficiency in magnetic hyperthermia. *The Journal of Physical Chemistry C* **2014**, *118*, 8691-8701.

5. Auffan, M.; Achouak, W.; Rose, J.; Roncato, M.-A.; Chanéac, C.; Waite, D.T.; Masion, A.; Woicik, J.C.; Wiesner, M.R.; Bottero, J.-Y. Relation between the redox state of iron-based nanoparticles and their cytotoxicity toward Escherichia coli. *Environmental science & technology* **2008**, *42*, 6730-6735.

6. Afzalipour, R.; Khoei, S.; Khoee, S.; Shirvalilou, S.; Raoufi, N.J.; Motevalian, M.; Karimi, M.Y. Thermosensitive magnetic nanoparticles exposed to alternating magnetic field and heat-mediated chemotherapy for an effective dual therapy in rat glioma model. *Nanomedicine: Nanotechnology, Biology and Medicine* **2021**, *31*, 102319.

7. Rau, B.; Wust, P.; Hohenberger, P.; Löffel, J.; Hünerbein, M.; Below, C.; Gellermann, J.; Speidel, A.; Vogl, T.; Riess, H. Preoperative hyperthermia combined with radiochemotherapy in locally advanced rectal cancer: a phase II clinical trial. *Annals of surgery* **1998**, *227*, 380.

8. Cotin, G.; Perton, F.; Blanco-Andujar, C.; Pichon, B.; Mertz, D.; Bégin-Colin, S. Design of anisotropic iron-oxide-based nanoparticles for magnetic hyperthermia. In *Nanomaterials for Magnetic and Optical Hyperthermia Applications*; Elsevier: **2019**; pp. 41-60.

9. Khurshid, H.; Alonso, J.; Nemati, Z.; Phan, M.; Mukherjee, P.; Fdez-Gubieda, M.; Barandiarán, J.; Srikanth, H. Anisotropy effects in magnetic hyperthermia: A comparison between spherical and cubic exchange-coupled FeO/Fe3O4 nanoparticles. *Journal of Applied Physics* **2015**, *117*, 17A337.

10. Cardoso, B.D.; Rodrigues, A.R.O.; Almeida, B.G.; Amorim, C.O.; Amaral, V.S.; Castanheira, E.M.; Coutinho, P.J. Stealth magnetoliposomes based on calcium-substituted magnesium ferrite nanoparticles for curcumin transport and release. *International journal of molecular sciences* **2020**, *21*, 3641.

11. Johnson-Arbor, K.; Dubey, R. Doxorubicin. **2017**.

12. Lao, J.; Madani, J.; Puértolas, T.; Álvarez, M.; Hernández, A.; Pazo-Cid, R.; Artal, Á.; Antón Torres, A. Liposomal doxorubicin in the treatment of breast cancer patients: a review. *Journal of drug delivery* **2013**, *2013*.

13. Lankelma, J.; Dekker, H.; Fernández Luque, R.; Luykx, S.; Hoekman, K.; Valk, P.v.d.; Van Diest, P.J.; Pinedo, H.M. Doxorubicin gradients in human breast cancer. *Clinical cancer research* **1999**, *5*, 1703-1707.

14. Kamba, S.A.; Ismail, M.; Hussein-Al-Ali, S.H.; Ibrahim, T.A.T.; Zakaria, Z.A.B. In vitro delivery and controlled release of doxorubicin for targeting osteosarcoma bone cancer. *Molecules* **2013**, *18*, 10580-10598.

15. Mateu-Sanz, M.; Ginebra, M.-P.; Tornín, J.; Canal, C. Cold atmospheric plasma enhances doxorubicin selectivity in metastasic bone cancer. *Free Radical Biology and Medicine* **2022**, *189*, 32-41.

16. Wils, J.; Klein, H.O.; Wagener, D.; Bleiberg, H.; Reis, H.; Korsten, F.; Conroy, T.; Fickers, M.; Leyvraz, S.; Buyse, M. Sequential high-dose methotrexate and fluorouracil combined with doxorubicin—a step ahead in the treatment of advanced gastric cancer: a trial of the European Organization for Research and Treatment of Cancer Gastrointestinal Tract Cooperative Group. *J Clin Oncol* **1991**, *9*, 827-831.

17. Piscitelli, S.C.; Rodvold, K.A.; Rushing, D.A.; Tewksbury, D.A. Pharmacokinetics and pharmacodynamics of doxorubicin in patients with small cell lung cancer. *Clinical Pharmacology & Therapeutics* **1993**, *53*, 555-561.

18. Frost, B.M.; Eksborg, S.; Björk, O.; Abrahamsson, J.; Behrendtz, M.; Castor, A.; Forestier, E.; Lönnerholm, G. Pharmacokinetics of doxorubicin in children with acute lymphoblastic leukemia: Multi-institutional collaborative study. *Medical and Pediatric Oncology: The Official Journal of SIOP—International Society of Pediatric Oncology (Societé Internationale d'Oncologie Pédiatrique* **2002**, *38*, 329-337.

19. Tam, K. The roles of doxorubicin in hepatocellular carcinoma. *ADMET and DMPK* **2013**, *1*, 29-44.

20. Lee, W.Y.; Cheung, C.C.; Liu, K.W.; Fung, K.; Wong, J.; Lai, P.B.; Yeung, J.H. Cytotoxic effects of tanshinones from Salvia miltiorrhiza on doxorubicin-resistant human liver cancer cells. *Journal of natural products* **2010**, *73*, 854-859.

21. Waldner, R.; Laschan, C.; Lohninger, A.; Gessner, M.; Tüchler, H.; Huemer, M.; Spiegel, W.; Karlic, H. Effects of doxorubicin-containing chemotherapy and a combination with L-carnitine on oxidative

metabolism in patients with non-Hodgkin lymphoma. *Journal of cancer research and clinical oncology* **2006**, *132*, 121-128.

22. Cunningham, D.; Hawkes, E.A.; Jack, A.; Qian, W.; Smith, P.; Mouncey, P.; Pocock, C.; Ardeshna, K.M.; Radford, J.A.; McMillan, A. Rituximab plus cyclophosphamide, doxorubicin, vincristine, and prednisolone in patients with newly diagnosed diffuse large B-cell non-Hodgkin lymphoma: a phase 3 comparison of dose intensification with 14-day versus 21-day cycles. *The Lancet* **2013**, *381*, 1817-1826.

23. Ogura, M. Adriamycin (doxorubicin). *Gan to kagaku ryoho. Cancer & chemotherapy* **2001**, *28*, 1331-1338.

24. Ferreira, A.; Cunha-Oliveira, T.; Simões, R.F.; Carvalho, F.S.; Burgeiro, A.; Nordgren, K.; Wallace, K.B.; Oliveira, P.J. Altered mitochondrial epigenetics associated with subchronic doxorubicin cardiotoxicity. *Toxicology* **2017**, *390*, 63-73.

25. Olson, R.D.; Mushlin, P.S. Doxorubicin cardiotoxicity: analysis of prevailing hypotheses. *The FASEB Journal* **1990**, *4*, 3076-3086.

26. Chen, C.; Lu, L.; Yan, S.; Yi, H.; Yao, H.; Wu, D.; He, G.; Tao, X.; Deng, X. Autophagy and doxorubicin resistance in cancer. *Anti-cancer drugs* **2018**, *29*, 1-9.

27. Slingerland, M.; Guchelaar, H.-J.; Gelderblom, H. Liposomal drug formulations in cancer therapy: 15 years along the road. *Drug discovery today* **2012**, *17*, 160-166.

28. Babincová, N.; Sourivong, P.; Babinec, P.; Bergemann, C.; Babincová, M.; Durdík, Š. Applications of magnetoliposomes with encapsulated doxorubicin for integrated chemotherapy and hyperthermia of rat C6 glioma. *Zeitschrift für Naturforschung C* **2018**, *73*, 265-271.

29. Khaledian, M.; Nourbakhsh, M.S.; Saber, R.; Hashemzadeh, H.; Darvishi, M.H. Preparation and evaluation of doxorubicin-loaded pla–peg–fa copolymer containing superparamagnetic iron oxide nanoparticles (Spions) for cancer treatment: Combination therapy with hyperthermia and chemotherapy. *International Journal of Nanomedicine* **2020**, *15*, 6167.

30. Cotin, G.; Kiefer, C.; Perton, F.; Boero, M.; Ozdamar, B.; Bouzid, A.; Ori, G.; Massobrio, C.; Begin, D.; Pichon, B. Evaluating the critical roles of precursor nature and water content when tailoring magnetic nanoparticles for specific applications. *ACS Applied Nano Materials* **2018**, *1*, 4306-4316.

31. Cardoso, B.D.; Rio, I.S.; Rodrigues, A.R.O.; Fernandes, F.C.; Almeida, B.; Pires, A.; Pereira, A.; Araújo, J.; Castanheira, E.M.; Coutinho, P.J. Magnetoliposomes containing magnesium ferrite nanoparticles as nanocarriers for the model drug curcumin. *Royal Society open science* **2018**, *5*, 181017.

32. Kallumadil, M.; Tada, M.; Nakagawa, T.; Abe, M.; Southern, P.; Pankhurst, Q.A. Suitability of commercial colloids for magnetic hyperthermia. *Journal of Magnetism and Magnetic Materials* **2009**, *321*, 1509-1513.

33. Azevedo, A.M.; Ribeiro, D.M.; Pinto, P.C.; Lúcio, M.; Reis, S.; Saraiva, M.L.M. Imidazolium ionic liquids as solvents of pharmaceuticals: Influence on HSA binding and partition coefficient of nimesulide. *International journal of pharmaceutics* **2013**, *443*, 273-278.

34. Doebelin, N.; Kleeberg, R. Profex: a graphical user interface for the Rietveld refinement program BGMN. *Journal of applied crystallography* **2015**, *48*, 1573-1580.

35. Pereira, D.S.; Cardoso, B.D.; Rodrigues, A.R.O.; Amorim, C.O.; Amaral, V.S.; Almeida, B.G.; Queiroz, M.-J.R.; Martinho, O.; Baltazar, F.; Calhelha, R.C. Magnetoliposomes containing calcium ferrite nanoparticles for applications in breast cancer therapy. *Pharmaceutics* **2019**, *11*, 477.

36. Sau, T.K.; Rogach, A.L. *Complex-shaped metal nanoparticles: bottom-up syntheses and applications*; John Wiley & Sons: **2012**.

37. Köseoğlu, Y.; Baykal, A.; Gözüak, F.; Kavas, H. Structural and magnetic properties of CoxZn1−xFe2O4 nanocrystals synthesized by microwave method. *Polyhedron* **2009**, *28*, 2887-2892.

38. Noh, S.-h.; Na, W.; Jang, J.-t.; Lee, J.-H.; Lee, E.J.; Moon, S.H.; Lim, Y.; Shin, J.-S.; Cheon, J. Nanoscale magnetism control via surface and exchange anisotropy for optimized ferrimagnetic hysteresis. *Nano letters* **2012**, *12*, 3716-3721.

39. Hergt, R.; Dutz, S. Magnetic particle hyperthermia—biophysical limitations of a visionary tumour therapy. *Journal of Magnetism and Magnetic Materials* **2007**, *311*, 187-192.

40. Fu, R.; Yan, Y.; Roberts, C.; Liu, Z.; Chen, Y. The role of dipole interactions in hyperthermia heating colloidal clusters of densely-packed superparamagnetic nanoparticles. *Scientific reports* **2018**, *8*, 1-10.

41. Haase, C.; Nowak, U. Role of dipole-dipole interactions for hyperthermia heating of magnetic nanoparticle ensembles. *Physical Review B* **2012**, *85*, 045435.

42. Karukstis, K.K.; Thompson, E.H.; Whiles, J.A.; Rosenfeld, R.J. Deciphering the fluorescence signature of daunomycin and doxorubicin. *Biophysical chemistry* **1998**, *73*, 249-263.

43. Fiallo, M.M.; Tayeb, H.; Suarato, A.; Garnier-Suillerot, A. Circular dichroism studies on anthracycline antitumor compounds. Relationship between the molecular structure and the spectroscopic data. *Journal of pharmaceutical sciences* **1998**, *87*, 967-975.

44. Manfait, M.; Bernard, L.; Theophanides, T. Resonance and pre-resonance Raman spectra of the antitumor drugs adriamycin and daunomycin. *Journal of Raman Spectroscopy* **1981**, *11*, 68-74.

45. Changenet-Barret, P.; Gustavsson, T.; Markovitsi, D.; Manet, I.; Monti, S. Unravelling molecular mechanisms in the fluorescence spectra of doxorubicin in aqueous solution by femtosecond fluorescence spectroscopy. *Physical Chemistry Chemical Physics* **2013**, *15*, 2937-2944.

46. Agrawal, P.; Barthwal, S.K.; Barthwal, R. Studies on self-aggregation of anthracycline drugs by restrained molecular dynamics approach using nuclear magnetic resonance spectroscopy supported by absorption, fluorescence, diffusion ordered spectroscopy and mass spectrometry. *European journal of medicinal chemistry* **2009**, *44*, 1437-1451.

47. Lakowicz, J.R. *Principles of fluorescence spectroscopy*, Springer: **2006**.

48. Bakhshiev, N. Universal Intermolecular Interactions and Their Effect on the Position of the Electronic Spectra of Molecules in Two-Component Solutions. V. Dependence of the Spectra on the Electrical Properties, Dimensions, and Structure of the Molecules Under Stud. *Optics and Spectroscopy* **1962**, *13*, 24.

49. Baur, M.E.; Nicol, M. Solvent stark effect and spectral shifts. *The Journal of Chemical Physics* **1966**, *44*, 3337-3343.

50. Curtis, H.; Barnes, N.S. *Invitation to biology*, Macmillan: **1994**.

51. Gabizon, A.; Catane, R.; Uziely, B.; Kaufman, B.; Safra, T.; Cohen, R.; Martin, F.; Huang, A.; Barenholz, Y. Prolonged circulation time and enhanced accumulation in malignant exudates of doxorubicin encapsulated in polyethylene-glycol coated liposomes. *Cancer research* **1994**, *54*, 987-992.

52. Maeda, H.; Nakamura, H.; Fang, J. The EPR effect for macromolecular drug delivery to solid tumors: Improvement of tumor uptake, lowering of systemic toxicity, and distinct tumor imaging in vivo. *Advanced drug delivery reviews* **2013**, *65*, 71-79.

53. Deshpande, P.P.; Biswas, S.; Torchilin, V.P. Current trends in the use of liposomes for tumor targeting. *Nanomedicine* **2013**, *8*, 1509-1528.

54. Sriwongsitanont, S.; Ueno, M. Effect of a PEG lipid (DSPE-PEG2000) and freeze-thawing process on phospholipid vesicle size and lamellarity. *Colloid and Polymer Science* **2004**, *282*, 753-760.

55. Saldívar-Ramírez, M.; Sánchez-Torres, C.; Cortés-Hernández, D.; Escobedo-Bocardo, J.; Almanza-Robles, J.; Larson, A.; Reséndiz-Hernández, P.; Acuña-Gutiérrez, I. Study on the efficiency of nanosized magnetite and mixed ferrites in magnetic hyperthermia. *Journal of Materials Science: Materials in Medicine* **2014**, *25*, 2229-2236.

56. Tilley, L.; Thulborn, K.R.; Sawyer, W. An assessment of the fluidity gradient of the lipid bilayer as determined by a set of n-(9-anthroyloxy) fatty acids (n= 2, 6, 9, 12, 16). *Journal of Biological Chemistry* **1979**, *254*, 2592-2594.

57. Bahri, M.A.; Heyne, B.J.; Hans, P.; Seret, A.E.; Mouithys-Mickalad, A.A.; Hoebeke, M.D. Quantification of lipid bilayer effective microviscosity and fluidity effect induced by propofol. *Biophysical chemistry* **2005**, *114*, 53-61.

58. Kępczyński, M.; Nawalany, K.; Kumorek, M.; Kobierska, A.; Jachimska, B.; Nowakowska, M. Which physical and structural factors of liposome carriers control their drug-loading efficiency? *Chemistry and Physics of Lipids* **2008**, *155*, 7-15.

59. Shah, S.; Chandra, A.; Kaur, A.; Sabnis, N.; Lacko, A.; Gryczynski, Z.; Fudala, R.; Gryczynski, I. Fluorescence properties of doxorubicin in PBS buffer and PVA films. *Journal of Photochemistry and Photobiology B: Biology* **2017**, *170*, 65-69.

60. Thakur, R.; Das, A.; Chakraborty, A. Interaction of human serum albumin with liposomes of saturated and unsaturated lipids with different phase transition temperatures: a spectroscopic investigation by membrane probe PRODAN. *RSC advances* **2014**, *4*, 14335-14347.

61. Cardinale, D.; Sandri, M.T.; Martinoni, A.; Tricca LabTech, A.; Civelli, M.; Lamantia, G.; Cinieri, S.; Martinelli, G.; Cipolla, C.M.; Fiorentini, C. Left ventricular dysfunction predicted by early troponin I release after high-dose chemotherapy. *Journal of the American College of Cardiology* **2000**, *36*, 517-522.

62. Willis, M.S.; Parry, T.L.; Brown, D.I.; Mota, R.I.; Huang, W.; Beak, J.Y.; Sola, M.; Zhou, C.; Hicks, S.T.; Caughey, M.C. Doxorubicin exposure causes subacute cardiac atrophy dependent on the striated muscle–specific ubiquitin ligase MuRF1. *Circulation: Heart Failure* **2019**, *12*, e005234.

63. Šimůnek, T.; Štěrba, M.; Popelová, O.; Adamcová, M.; Hrdina, R.; Geršl, V. Anthracycline-induced cardiotoxicity: overview of studies examining the roles of oxidative stress and free cellular iron. *Pharmacological reports* **2009**, *61*, 154-171.

64. Swiech, O.; Majdecki, M.; Opuchlik, L.J.; Bilewicz, R. Impact of pH and cell medium on the interaction of doxorubicin with lipoic acid cyclodextrin conjugate as the drug carrier. *Journal of Inclusion Phenomena and Macrocyclic Chemistry* **2020**, *97*, 129-136.

65. Chai, F.; Sun, L.; He, X.; Li, J.; Liu, Y.; Xiong, F.; Ge, L.; Webster, T.J.; Zheng, C. Doxorubicin-loaded poly (lactic-co-glycolic acid) nanoparticles coated with chitosan/alginate by layer by layer technology for antitumor applications. *International Journal of Nanomedicine* **2017**, *12*, 1791.

66. Papadopoulou, V.; Kosmidis, K.; Vlachou, M.; Macheras, P. On the use of the Weibull function for the discernment of drug release mechanisms. *International journal of pharmaceutics* **2006**, *309*, 44-50.

67. Singh, M.; Kaskhedikar, S.; Singhvi, G.; Soni, L. HPLC estimation of perindopril erbumine in tablet dosage form. *Asian Journal of Chemistry* **2011**, *23*, 3909.

68. Supramaniam, J.; Adnan, R.; Kaus, N.H.M.; Bushra, R. Magnetic nanocellulose alginate hydrogel beads as potential drug delivery system. *International journal of biological macromolecules* **2018**, *118*, 640-648.

CHAPTER 4

Advances towards an optimized multi-stimuli-responsive nanosystem for cancer therapy

This chapter is divided into two sub-chapters, which address advances in the optimization of lipid formulations and heat generation with $Ca_{0.25}Mg_{0.75}Fe_2O_4$ superparamagnetic nanoparticles to obtain a multi-stimuli-responsive nanosystem.

4.1. Lipid formulation evaluation and optimization of magnetoliposomes as multi-stimuli-responsive vesicles for controlled doxorubicin release

This subchapter is focused on the investigation of nine different lipid combinations used in the design and validation of solid magnetoliposomes as multi-stimuli-responsive vesicles for doxorubicin-controlled release in cancer therapy. It was intended to optimise a previously developed new methodology for synthesising magnetoliposomes based on shape-anisotropic calcium/magnesium ferrite nanoparticles, with the choice of the best liposomal formulations for the envisioned purpose. The results of this chapter were published in the journal *Biomedicines.*

Cardoso, B.D.; Cardoso, V.F.; Lanceros-Méndez, S.; Castanheira, E.M. Solid magnetoliposomes as multi-stimuli-responsive systems for controlled release of doxorubicin: assessment of lipid formulations. *Biomedicines* **2022**, *10*, 1207.

4.1.1. Overview

Stimuli-responsive liposomes are a class of nanocarriers whose drug release occurs preferentially when exposed to a specific biological environment, to an external stimulus, or both. This chapter is focused on the design of SMLs as lipid-based nanosystems aiming to obtain multi-stimuli responsive vesicles for DOX controlled release in pathological areas, under the action of thermal, magnetic, and pH stimuli. The effect of lipid combinations on structural, colloidal stability, and thermodynamic parameters were evaluated. The results confirmed the reproducibility of SMLs' synthesis based on nine lipid formulations (combining DPPC, DSPC, CHEMS, DOPE and DSPE-PEG), with structural and colloidal properties suitable for biological applications. A loss of stability and thermosensitivity was observed for formulations containing DOPE lipid. SMLs PEGylation is an essential step to enhance both their long-term storage stability and stealth properties. DOX encapsulation (efficiency ranging between 87% and 96%) in the bilayers lowered its pK_a, favouring the displacement of DOX from the acyl chains to the surface when changing from alkaline to acidic pH. The release profiles demonstrated a preferential release at acidic pH, more pronounced under mimetic mild-hyperthermia conditions (42 °C). Release kinetics varied with the lipid formulation, generally displaying hyperthermia temperatures and acidic pH as determining factors in DOX release; PEGylation was shown to act as a diffusion barrier on the SMLs surface. The integrated assessment and characterisation of SMLs allow tuning lipid formulations that best respond to the needs for specific controlled release profiles of stimuli-responsive nanosystems as a multi-functional approach to cancer targeting and therapy.

4.1.2. Introduction

Despite all the research and progress in cancer, this disease remains a significant social burden, being the first leading cause of death in people under 70 years in 112 of 183 countries [1]. The clinical failure of chemotherapy, one of the first-line cancer treatment approaches, is mainly associated with the free chemotherapeutic drugs systemic administration and the nonselective nature of the agents, leading to reduced bioavailability at the target site [2-4]. Following the advances in the development of DOX-loaded SMLs presented in the previous chapter, this one focuses on the optimization process that sought to obtain multi-stimuli responsive vesicles for DOX controlled release in pathological areas. Thus, it aimed to understand the effect of lipid formulations on the parameters of drug-loaded magnetoliposomes and to assess the mechanisms of drug-controlled release induction under multi-stimulus.

Screening lipid combinations is essential to promote the functionality of lipid-based approaches as they have already shown to play an active role in improving drug delivery to the tumour site while decreasing the systemic toxicity of free drugs [5-7]. The selectivity of these products results from the EPR effect (for detailed information, see **section 2.2**) [8] that provides a means to increase tumour specificity by 20-30% [9]. However, it is highly dependent not only on intrinsic tumour biology (as the degree of angiogenesis and intratumour pressure), but also on the physicochemical properties of the nanocarrier (particle size, surface charge and circulation time). Thus, adding other targeting methods to the nanocarriers is essential to overcome the variable effect of passive targeting, improve the drug delivery to the target site, and ultimately create a synergy between different therapies.

One of the strategies used to target tumours is using thermosensitive liposomes that allow controlled release of the payload when subjected to tolerable and clinically relevant local–regional mild-hyperthermia (39–43 °C) [10-12]. Hyperthermia, characterized by increased body temperature above mean values [13], is a technique that is beneficial in cancer treatment when combined with radiotherapy and chemotherapy [14,15]. In addition to causing tumour cells a complex apoptotic induction [16], hyperthermia allows for a 1.5 to 5 fold improvement in the radiotherapy efficiency due, among others, to the increase in oxygenation and perfusion of cancer cells [14]. Combined with chemotherapy, it can induce an anti-cancer drug sensitization, allowing resistant cells to respond again to those drugs [17,18]. The heat leads to greater tissue perfusion and chemical reaction acceleration, enhancing chemotherapy's therapeutic effectiveness [14,19]. Clinically, hyperthermia can be applied locally, regionally, or to the entire body. Hot water blankets, thermal chambers, perfusion with heated fluids, ultrasound, and electromagnetic energy are used for that purpose [20]. However, these techniques do not allow specificity for tumour cells, so they sensitize both tumour and healthy cells to the enhanced toxic effects of radio- and chemotherapy. One of the most promising alternatives to ensure preferential heating of malignant cells is to use magnetic nanoparticles as mediators of magnetic hyperthermia, producing heat under the action of AMF [20-23]. When combined with, for instance, thermosensitive liposomes – forming magnetoliposomes – they offer a multifunctional approach to targeting and therapy. Another strategy concerns the synthesis of pH-sensitive liposomes whose drug release is induced by the destabilization under acidic conditions [24-26]. This trigger is particularly interesting in tumour targeting as a potentiator of cellular uptake in response to enhanced acidification (in the pH range of 6.5-6.8) found in the extracellular tumour microenvironment, resulting from the oncogenic metabolisms [27]. Furthermore, endo/lysosomal pH (5.0-6.5) induces preferential cargo release in these target cells [24,27].

In this context, the present work is focused on designing DOX-loaded SMLs based on different lipid compositions and evaluating combinations that validate the physicochemical, structural, and stability features for biological application in targeted cancer therapy. The main objective of studying different lipid combinations is to obtain a multi stimuli-responsive nanosystem to enhance DOX controlled release under tumour microenvironment and hyperthermia conditions based on (1) thermal, (2) magnetic, and (3) pH- responsiveness.

In the present work: (1) thermal responsiveness is achieved by combining different lipids with dipalmitoylphosphatidylcholine (DPPC), which has the reversible thermotropic gel-to-liquid crystalline phase transition (T_m=41.4 °C) near the temperatures used in mild hyperthermia. This feature aims to the thermal-specific drug release; (2) the magnetic responsiveness is achieved by a superparamagnetic magnetic core composed of shape-anisotropic cubic superparamagnetic NPs of calcium-substituted magnesium ferrite ($Ca_{0.25}Mg_{0.75}Fe_2O_4$). This feature aims to (i) accumulate the DOX-loaded SMLs in tumours via a permanent magnetic field locally applied; (ii) induce magnetic hyperthermia under an AMF for bilayer destabilization, increase endothelial permeability to liposomes, cause direct damage to cells, enhance the fusion or endocytosis effect of cancer cells and to reduce the local pH of the target site [28]; (3) the pH-responsiveness is achieved by the incorporation of titrable and polymorphic phase lipids within the lipid bilayer, aiming a site-specific drug release in cancer tissues which, in turn, is synergistically stimulated by the warming effect caused by hyperthermia.

4.1.3. Materials and Methods

pH buffer stock solutions in the pH range between 2 and 11 were prepared from a sodium phosphate (Na_3PO_4, from Sigma-Aldrich, St. Louis, MO, USA) 0.1 M solution, adjusting the pH by mixing properly a solution containing citric acid ($HOC(COOH)(CH_2COOH)_2$, from Sigma-Aldrich, St. Louis, MO, USA) at 0.05 M and boric acid (H_3BO_3, from Sigma-Aldrich, St. Louis, MO, USA) at 0.2 M in ultrapure water, following [29]. The pH values were measured with a mini-pH meter NiCd-1 (ORION, SA250 PH Meter Digital), and each solution's pH was correctly adjusted using a solution of HCl and NaOH (1 M).

For magnetoliposomes preparation, the lipids dipalmitoylphosphatidylcholine (DPPC) (from Sigma-Aldrich, St. Louis, MO, USA), distearoylphosphatidylcholine (DSPC) (from Sigma-Aldrich, St. Louis, MO, USA), dioleoylphosphatidylethanolamine (DOPE) (from Sigma-Aldrich, St. Louis, MO, USA), cholesteryl hemisuccinate (CHEMS) (from Sigma-Aldrich, St. Louis, MO, USA) and 1,2-distearoyl-*sn*-glycero-3-

phosphoethanolamine-*N*-[methoxy(polyethylene glycol)-2000] (ammonium salt) (DSPE-PEG2000, from Avanti Polar Lipids, Birmingham, AL, USA) were used.

4.1.3.1. Solid magnetoliposomes preparation

DPPC was selected as the primary lipid for every lipid formulation due to its drug encapsulation capacity and thermosensitivity and because it had already been validated as suitable for biomedical applications and controlled release [30]. However, it is reported that drug release occurs slightly before the main T_m peak [31] and that the rate and amount of drug release are relatively low. As DSPC has a higher T_m (T_m ≈55 °C), the binary formulation of DPPC/DSPC mixtures results in more rigid vesicles associated with a reduction in their clearance by the MPS [32,33], while enhancing the amount of drug release [33,34]. Furthermore, it is reported that the number of induced nanoscale gaps in liposome membranes can be adjusted by changing the ratio between DPPC and DSPC to enhance the release kinetics [35]. The neutral cone-shaped lipid DOPE was used to synthesise pH-sensitive SMLs. Due to its conical shape and packing parameter higher than 1, this lipid forms non-bilayer structures at physiological pH. CHEMS, a weakly acidic amphiphile, is commonly used as a complementary molecule to stabilise DOPE bilayers at physiological pH by filling the space between the head groups of DOPE. The pH-induced cargo release mechanism relies on destabilisation caused by the transition from a bilayer structure (L_α phase) at neutral pH to the inverted hexagonal phase II (H_{II} phase) at an acidic pH [36]. CHEMS can reduce acyl chain mobility of DPPC above the phase transition [37]; its protonated form mimics some of the membrane properties of the Ch [38], while acting as a DPPC membrane stabiliser [37]. Furthermore, the incorporation of CHEMS in lipid formulations based on DPPC and DSPC has already proven to increase the interaction of liposomes with target cells (with negative surface charge) and, in addition, make the vesicles more fusogenic when exposed to acidic pH (as in endosomes and lysosomes) [39]. PEG, which steric hindrance prevents aggregation and reduces the absorption of plasma proteins, was added to the lipid formulations because of the reduced stability and half-life in the bloodstream of conventional liposomes [40].

Figure 4.1 presents a schematic representation that summarises the process for lipid combinations to synthesise DOX-loaded SMLs. First, the lipid DSPC and DOPE were combined to form DPPC binary formulations, branching the varieties into three groups: (A) DPPC, (B) DPPC/DSPC, and (C) DPPC/DOPE. Then, CHEMS and DSPE-PEG were sequentially added to each group resulting in nine formulations.

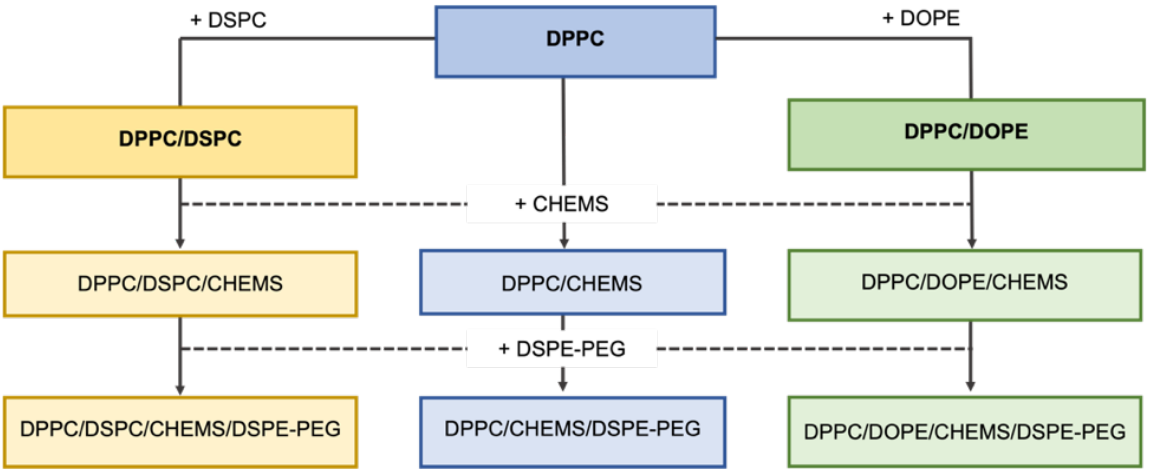


Figure 4.1 Schematic representation of the lipid combinations used to prepare DOX-loaded SMLs.

The SMLs here synthesised were prepared following a procedure described in [30]. All SMLs were synthesised at a total lipid concentration of 1 mM. The lipid formulations, the respective molar ratios and the expected type of behaviour of the SMLs are described in **Table 4.1**. First, reverse micelles were synthesised. 3 mL of heptane 99% (from Sigma-Aldrich, St. Louis, US, with water content ≤ 0.1%) was added to a thin film based on the corresponding lipid formulation and ultrasonicated at a power of 190 W for a time interval of 15 min. To form a magnetic core, 1 μM of shape-anisotropic cubic superparamagnetic NPs of calcium-substituted magnesium ferrite ($Ca_{0.25}Mg_{0.75}Fe_2O_4$, synthesised according to [30]) were added to micelles solution and subjected to 20 min of ultrasonication at the same conditions. Afterwards, a NdFeB N48 block magnet (Eclipse Magnetics Ltd., Sheffield, UK) with nickel-plated (Ni-Cu-Ni) coating was applied to the sample to separate the reverse micelles with a magnetic core. The non-magnetic supernatant was discarded, and the remaining solvent was evaporated under an ultrapure nitrogen flow. The magnetic micelles were re-suspended in ultrapure water, and the aqueous solution was heated at 50 °C. To form the second lipid layer, resulting in SMLs, an ethanolic solution containing the lipid formulation at the corresponding molar ratio (**Table 4.1**) was added, under vortexing, to the pre-heated reverse micelle solution. Also, a DOX ethanolic solution with a final concentration of 2×10^{-6} M was co-injected in this step.

Table 4.1 Lipid composition and the molar ratio of the lipids to synthesise SMLs with different types of action.

Group	Lipid composition	Molar ratio	Type
A	DPPC	1	Non-long-circulating and thermosensitive
	DPPC/CHEMS	9:1	Non-long-circulating, fusogenic, thermo- and pH-sensitive
	DPPC/CHEMS/DSPE-PEG	80:15:5	Long-circulating, fusogenic, thermo- and pH-sensitive
B	DPPC/DSPC	3:1	Non-long-circulating and thermo-sensitive
	DPPC/DSPC/CHEMS	7:2:1	Mid-long-circulating, fusogenic thermo- and pH-sensitive
	DPPC/DSPC/CHEMS/DSPE-PEG	60:20:15:5	Long-circulating, fusogenic, thermo- and pH-sensitive
C	DPPC/DOPE	7:3	Non-long-circulating, fusogenic, pH-sensitive
	DPPC/DOPE/CHEMS	6:3:1	Non-long-circulating, fusogenic, pH-sensitive
	DPPC/DOPE/CHEMS/DSPE-PEG	50:30:15:5	Long-circulating, fusogenic, pH-sensitive

4.1.3.2. Dynamic Light Scattering measurements

The determination of the average D_H, PDI, colloidal stability, and ζ-potential dependence on the pH of SMLs based on the different lipid combinations was the first approach used for the validation of nanosystems and the method to produce them for biological applications. The measurements were carried out by DLS using a Litesizer 500 DLS equipment, possessing three detection angles (15°, 90°, 175°) from Anton Paar (Anton Paar GmbH, Graz, Austria), using a semiconductor laser diode of λ = 658 nm and 40 mW. Polystyrene cells were used to hold the samples, and a solvent refractive index

of 1.33, a material refractive index of 1.4, and an absorption coefficient of 0.001 L/m were used as acquisition parameters.

The polystyrene cells were washed with ethanol and then in deionised water before and after the measurements. Three independent measurements were taken for each lipid formulation, and experimental data were processed using Kalliope software (Anton Paar GmbH, Graz, Austria).

For D_H and PDI determination, SMLs were prepared at the corresponding molar ratio and synthesis procedure described in **section 2.1**. Each SMLs sample was designed with a final lipid concentration of 1 mM and filtered five times through a 0.2 μm filter before the measurements. The results are presented as mean and corresponding standard deviation from triplicate assays.

To assess the colloidal stability, SMLs were prepared at the corresponding molar ratio and synthesis procedure described in **section 3.3.1**. For that, 3 mL of SMLs aqueous solutions based on the nine different lipid formulations were stored at 4 °C for 30 days at a lipid concentration of 1 mM. Changes in the D_H and PDI were monitored under the same acquisition and procedure conditions mentioned above.

To obtain ζ-potential dependence on the pH value and the corresponding isoelectric point, ζ-potential was measured for each lipid formulation in a pH range between 2 and 11. SMLs were prepared at the corresponding molar ratio and synthesis procedure described in **section 2.1** and re-suspended in the buffer stock solution at the related pH. The solutions were filtered five times through a 0.2 μm filter, and the final pH value was measured and adjusted using a mini-pH meter NiCd-1. The results are presented as mean and corresponding standard deviation from triplicate assays.

4.1.3.3. Fluorescence spectroscopy measurements

The intrinsic fluorescence of DOX [41] can be used as a facilitating tool to characterise the properties of DOX-loaded SMLs. Thus, the fluorescence spectroscopy technique was used to study the systems, following the described methodology in **section 2.1.3.1**. The excitation of the DOX-loaded SMLs was set at a λ_{exc}= 480 nm, and the emission spectrum was collected between 490 nm and 650 nm with a slit of 4 nm in both excitation and emission. Based on the different lipid formulations, fluorescence emission measurements were performed to quantify DOX's EE% in SMLs. After preparation, drug-loaded SMLs were placed in Amicon® Ultra-0.5 mL centrifugal filters with 0.1 μm pore size and centrifuged at 3000 rpm for 10 min. The supernatant was pipetted out, and its fluorescence was measured, allowing it to determine the drug concentration using a calibration curve previously obtained. Three independent measurements were performed for each system, and standard deviations (s.d.) were calculated. The EE (%) was determined using **Equation 3.3**.

Steady-state anisotropy fluorescence values, r, are dependent on the fluorophore rotational diffusion (and thus dependent on viscosity, temperature, and molecular size of the fluorophore) [42] that can be used to study drug-lipid vesicle interactions. r was measured in the latter equipment, using Glan-Thompson polarisers, and an average value in an appropriate spectral range was calculated by [43]. Several assays were performed for the different lipid formulations over a pH range from 2 to 11 to associate DOX rotational mobility with pH variation.

HSA is the most abundant protein in human plasma that interacts with drugs and influence their pharmacokinetics and pharmacodynamics [44]. The intrinsic fluorescence of HSA allows the drug/protein interaction study by fluorescence spectroscopy through the analysis of the fluorescence quenching that results from that interaction [44,45]. The interaction of DOX-loaded SMLs with HSA was studied following the same procedure described in **section 2.2.3.7**. An aqueous solution of HSA of a fixed concentration of 0.2 mM (mimicking the HSA blood plasma concentration) was titrated with DOX-loaded liposomes. For that, 1 μL of liposomes were added between each increment, and the sample was left stabilising at room temperature for 20 min. The excitation of tryptophan residues was set at a λ_{exc}= 280 nm, and the emission spectra were recorded in the range of 290–700 nm, with an integration time of 1 s and the width of the slits set to 2 nm. The changes in the maximum fluorescence emission intensity found at 344 nm were analysed, and the relative efficiency of HSA quenching can be described by **Equation 3.4** [45].

The effect of different lipid combinations on DOX release kinetics was quantified for different environments and conditions to evaluate the effect of thermo/pH-sensitive lipids combination in multi-stimuli responsive SMLs. The tests were carried out following the methodology and equipment described in **section 2.2.3.8**. They were performed at pH 5.5 and 7.4 to simulate the drug release profile in the acidic tumour microenvironment and physiological fluids [26,27]. They were also carried out at 37 °C and 42 °C, representing physiological temperature and hyperthermia conditions [10,12]. The DOX release was followed for 30 h by collecting the samples from the acceptor compartments at different time points and measured by fluorescence spectroscopy (λ_{exc} = 480 nm, in the range of 550–650 nm). The experimental DOX release profiles were fitted to different kinetics models (Weibull [46], first-order [47] and Korsmeyer-Peppas [48] – see Appendix B in **section B.2**) using Prism 8 software (GraphPad Software, La Jolla, CA, USA).

4.1.3.4. Differential Scanning Calorimetry

DSC measurements were performed to determine the temperature transition from gel to liquid-crystalline (T_m) phase of DOX-loaded SMLs and, thus, evaluate their potential as thermosensitive nanocarriers. The measurements were performed in a Mettler-Toledo DSC822e apparatus with Sample Robot TS 0801 RO (Mettler-Toledo, Columbus, Ohio, United States). 30 µL of the prepared SMLs samples (1 mM) were placed into the corresponding 40 µL aluminium pans, accurately weighed on an analytical balance, and sealed. Each sample was placed in the calorimeter and isothermally held at 25 °C for 5 min before heating to 60 °C, with a scanning rate of 2 °C/min. Three independent measurements were performed for each system, and all experiments were carried out under a nitrogen atmosphere at a temperature between 25 and 60 °C. The peak temperature (T_m) and the width of the main peak were determined from the DSC curve.

4.1.4. Results and discussion

4.1.4.1. Influence of formulation on structural, colloidal and thermodynamic parameters of doxorubin-loaded solid magnetoliposomes

Evaluating the average size, PDI, and stability of nanosystems is typically the first and most relevant step in validating a lipid-based nanocarrier as a drug delivery system and the method to produce it. The vesicle size significantly influences, for example, pharmacokinetics, tissue diffusion, and kidney excretion, so its determination makes it possible to predict some of the system's behaviour [49]. It is generally accepted that the desirable size of drug delivery systems should be between 50 and 200 nm [50]. In addition, PDI values allow relating the degree of heterogeneity of size distributions, and it is recognised that, for this type of application, the PDI valuesmust be equal to or below 0.3, indicating a homogeneous population of the systems [49]. The combined analysis of these parameters is one of the criteria used to assess the stability of the systems, either in the short, medium or long term. The results of DLS measurements are summarised in **Table 4.2**. All the studied lipid formulations revealed a hydrodynamic diameter below 200 nm. In every group, it was noticed a negligible effect in the size by CHEMS addition and a more significant increase when DSPE-PEG was added. In addition, the lipid formulations revealed a size narrowly distributed, with a PDI below the 0.3 limit. Thus, all lipid formulations resulted in DOX-loaded SMLs with adequate sizes and PDI to act as drug delivery systems.

Table 4.2 Hydrodynamic diameter, PDI, EE%, pI and T_m of DOX-loaded SMLs based on different lipid formulations at 25 °C.

Group	Lipid composition	D_H (nm)	PDI	EE (%)	pI	T_m (°C)
A	DPPC	116±3	0.18±0.02	96.9±0.5	7.80	41.40±0.02
	DPPC/CHEMS	149±7	0.21±0.01	95±1	5.61	38.2±0.2
	DPPC/CHEMS/DSPE-PEG	156±18	0.20±0.02	94±3	6.22	41.34±0.02
B	DPPC/DSPC	157±1	0.22±0.03	88±2	5.95	42.4±0.2
	DPPC/DSPC/CHEMS	160±1	0.20±0.01	92±2	5.37	39.7±0.1
	DPPC/DSPC/CHEMS/DSPE-PEG	187±4	0.22±0.02	92±5	5.61	41.4±0.2
C	DPPC/DOPE	111±17	0.24±0.07	96.7±0.5	8.00	*
	DPPC/DOPE/CHEMS	118±4	0.20±0.04	87±12	5.49	*
	DPPC/DOPE/CHEMS/DSPE-PEG	117.39±0.03	0.23±0.06	93±4	5.13	*

* T_m peak not found.

The drug encapsulation in lipid vesicles can be associated with the synthesis method for production, the lipid composition, and the drug itself [51]. DOX encapsulation efficiencies (EE%) were determined by the percentage of incorporated drug into SMLs relative to the initial amount of drug added, and the results are also summarised in **Table 4.2**. All formulations demonstrated a high drug encapsulation efficiency, ranging between 87% and 96%, allowing to conclude that the different lipid formulations do not significantly influence encapsulation at this drug/lipid ratio. Furthermore, it proves the reproducibility of the methodology previously developed for other lipid formulations [30].

The ζ-potential dependence on pH of DOX-loaded SMLs was measured at pH values ranging from 2 to 11 (**Figure 4.2**). The ζ-potential of SMLs changed from negative to positive with decreasing pH values. This behaviour is beneficial to potentiate the electrostatic interaction between magnetoliposomes and tumour tissues [52]; the latter has acid-outside plasma pH gradients, while normal tissues have an neutral one (between 7.35 and 7.45) [52]. However, significant variations of ζ-potential values were not observed in any of the binary formulations of each group (DPPC, DPPC/DSPC, and DPPC/DOPE) in the pH window of therapeutic interest (± between 5 and 8), the formulations showing a near-neutral ζ-potential, as commonly observed for formulations based on zwitterionic lipids. It is noted that adding CHEMS to the formulations alters their ζ-potential, which is more relevant in Group A and C. In these groups, the absolute values of ζ-potential increased compared to the base formulation, being more

significant for pH higher than 7. The estimated pH at the isoelectric point was calculated and is presented in **Table 4.2Error! Reference source not found.**. In all groups, the pH of the isoelectric point was reduced with the addition of CHEMS; this behaviour was maintained, although for slightly higher values, with the subsequent addition of DSPE-PEG.

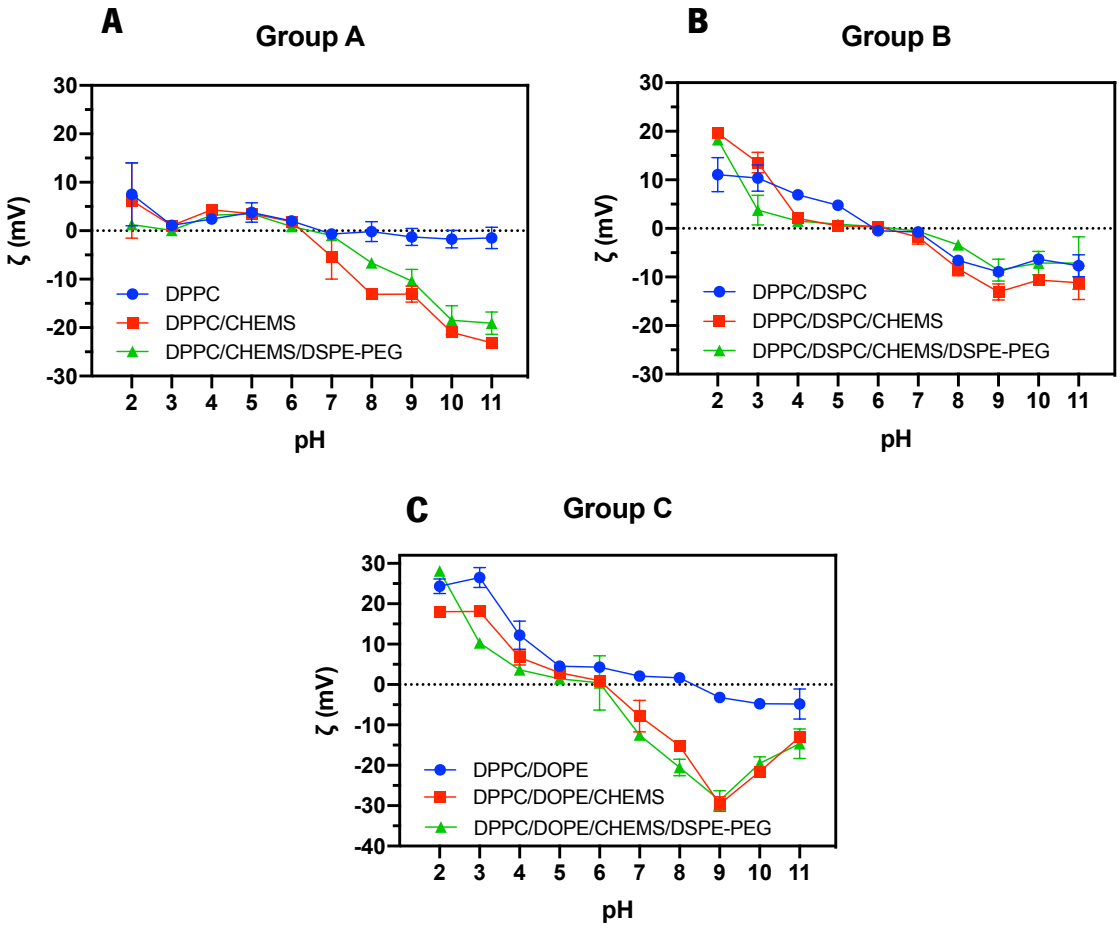


Figure 4.2 ζ-potential-pH profiles of DOX-loaded SMLs based on: (A) Group A, (B) Group B and (C) Group C lipid formulations.

Due to its protonable amino group, DOX is positively charged at pH 7. However, it was found that most formulations showed negative ζ-potential values at pH 7, except for DPPC/DOPE formulations whose estimated ζ-potential was slightly positive (+ 2.07 mV). Furthermore, by masking the positive charge of DOX, these systems are a vehicle to avoid multi-drug resistance (MDR) that limits the clinical success of chemotherapy [52]. The overexpression of some plasma proteins on the surface of tumour cells – such as membrane P-glycoproteins that can extrude positively charged compounds – prevents the intracellular accumulation of drugs and their therapeutic action [52,53].

DSC measurements assessed their potential as nanocarriers for controlled drug release under hyperthermia conditions by determining the temperature transition from gel to liquid-crystalline phase (T_m). **Figure 4.3** summarises the average DSC scans of the three independent measurements performed for each system. Initially, the DSC curve for pure DPPC-based liposomes was obtained to study the influence of magnetic NPs on DSC curves. A decrease in the intensity of the T_m peak and the appearance of a double transition peak was noticed in SMLs compared to the liposomes' counterparts. Drazenovic *et al.* [54] described similar results as a direct effect of lamellarity and size. The authors found that when subjecting large unilamellar DPPC vesicles (LUVs) to the extrusion process through sequentially lower polycarbonate filters (400 nm, 200 nm, 100 nm, and 50 nm), the intensity and definition of the peak gradually decreased, and a second peak appeared and broadened with reducing vesicle sizes. Our DSC results may have influence of size and of the presence of magnetic NPs. The remaining lipid combinations demonstrate a similar peak broadening pattern, which is justified, not only by those effects mentioned above, but also because they are lipid mixtures rather than single-component lipid systems. Furthermore, this peak broadening is associated with an ideal mixing of lipids acyl chains [55], as well as the lowering of cooperativity of the phase transition [56].

The thermograms corresponding to Group C are not shown in **Figure 4.3**, since it was not possible to record any phase transition in these formulations. These results are due to the presence of DOPE ($T_m \approx$ -16 °C), which results in lipid combinations with a T_m lower than the detection limits programmed in the experiment (limits of interest in hyperthermia conditions).

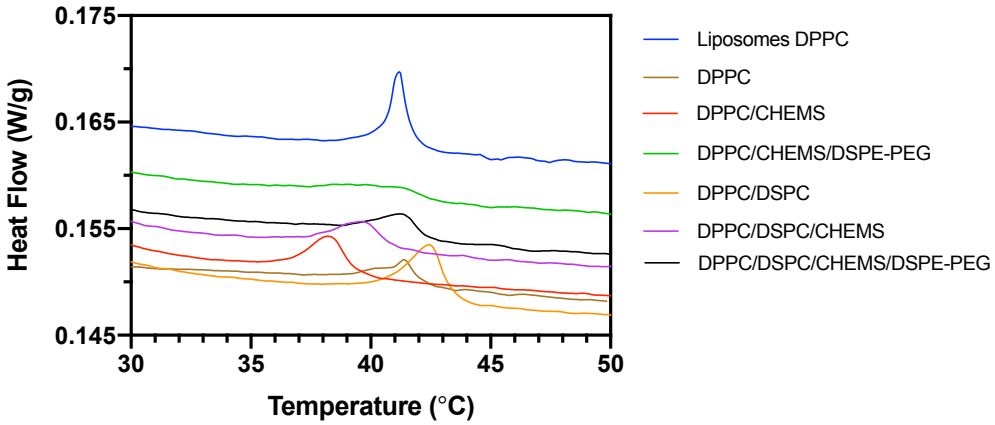


Figure 4.3 DSC heating thermograms of DOX-loaded SMLs based on different lipid formulations.

The calculated T_m for each formulation is also shown in **Table 4.2**. DPPC-based SMLs show a similar T_m (T_m=41.40±0.02 °C), to that obtained for the liposomes (T_m=41.12±0.15 °C). The addition of

CHEMS to those SMLs resulted in a decrease of T_m to 38.21±0.20 °C. The subsequent addition of DSPE-PEG raised the T_m to 41.34±0.02 °C, which is a similar value to that of the base formulation.

Concerning Group B, the addition of DSPC to the lipid base of DPPC raised the T_m to 42.4±0.2 °C, which was expected since DSPC has a T_m of ≈55 °C. This result indicates that the binary DPPC/DSPC mixture allows obtaining systems with a tuneable T_m (varying the ratio of both lipids), offering the system the practical advantages of both lipids. Similarly to Group A, the addition of CHEMS to the DPPC/DSPC base formulation resulted in a decrease of T_m to 39.7±0.1 °C. This deviation was mitigated by adding DSPE-PEG to the latter, slightly increasing T_m to 41.4±0.2 °C. This effect, resulting from the increasing inclusion mol% of DS chains of DSPE-PEG, has been previously described by Needham *et al.* [57].

The thermosensitivity of the formulations in Groups A and B was confirmed. Further, the most complex lipid formulations (the PEGylated ones) assume an optimal thermosensitivity for controlled drug release under hyperthermia conditions. Therefore, even though the structural characterisation techniques validated the primary requirements of the nine lipid combinations for the proposed application, the thermodynamic parameters only allow the validation of the formulations of groups A and B as thermosensitive formulations.

4.1.4.2. Stability of liposomal aqueous suspensions upon storage at 4 °C

The stability of magnetoliposomes was monitored for 30 days by DLS, measuring the variation of system size and size distribution compared to day 1 values (**Figure 4.4**). The storage method at 4 °C is the most common for lipid vesicles in aqueous media [58]. Groups A and B (DPPC and DPPC/DSPC as the base formulation, respectively) show minor variations in size and PDI after 30 days of storage. It has been described that spherical particles with sizes between 50 and 200 nm can more easily avoid uptake by the liver and spleen and avoid kidney clearance exhibiting a greater tendency for long circulation [59]. Therefore, the 200 nm size is used in this analysis as the stability limit of the systems.

In Group A, it was found that adding CHEMS to DPPC caused the SMLs to exceed the 200 nm limit on day 6, whereas in the pure DPPC formulation, this mark was only exceeded on the 10th day. These results may be related to the decrease in the T_m observed in these systems. The stability of lipid systems depends, for instance, on the effects of lipids' chain length and the T_m associated with lipid vesicles [60]. Longer acyl chains result in stronger van der Waals interactions, increasing the T_m. Prislan *et al.* [61] demonstrated that longer acyl chains increase the stability of lipid bilayers. Likewise, the rate of hydrolysis tends to increase with decreasing chain length of phospholipids [62]. The DPPC/CHEMS/DSPE-PEG

formulation has the slightest variation over time and, therefore, the greatest stability. The 200 nm limit was only exceeded on day 20, while the PDI values remained reduced, not exceeding the 0.3 threshold. The behaviour of the systems in Group B remains, in general, very similar among all the formulations. The formulations recorded a peak size increase around day 5, less pronounced in the DPPC/DSPC/CHEMS/DSPE-PEG formulation, followed by a period of stabilisation. The PDI of these formulations showed similar behaviour, always maintaining adequate values for the application.

Regarding Group C, only the PEGylated formulation demonstrated stability. In contrast, the DPPC/DOPE formulation duplicates the size at day 3, with the appearance of multiple-sized populations and, as such, a significant increase in PDI. The measurements in this formulation were interrupted on day 8, due to the formation of polydisperse aggregates, with size values larger than 600 nm. Adding CHEMS to the DPPC/DSPC formulation helped stabilise the membranes; however, from day 5 onwards, the sizes were not adequate, and from day 10 forward, the samples presented multiple population sizes (which made it impossible to continue the measurements). The PEGylated formulation was the only one that could be measured up to day 30. It highlighted the effect of adding a small amount of DSPE-PEG as a long-term stabiliser of all lipid formulations when stored at 4 °C.

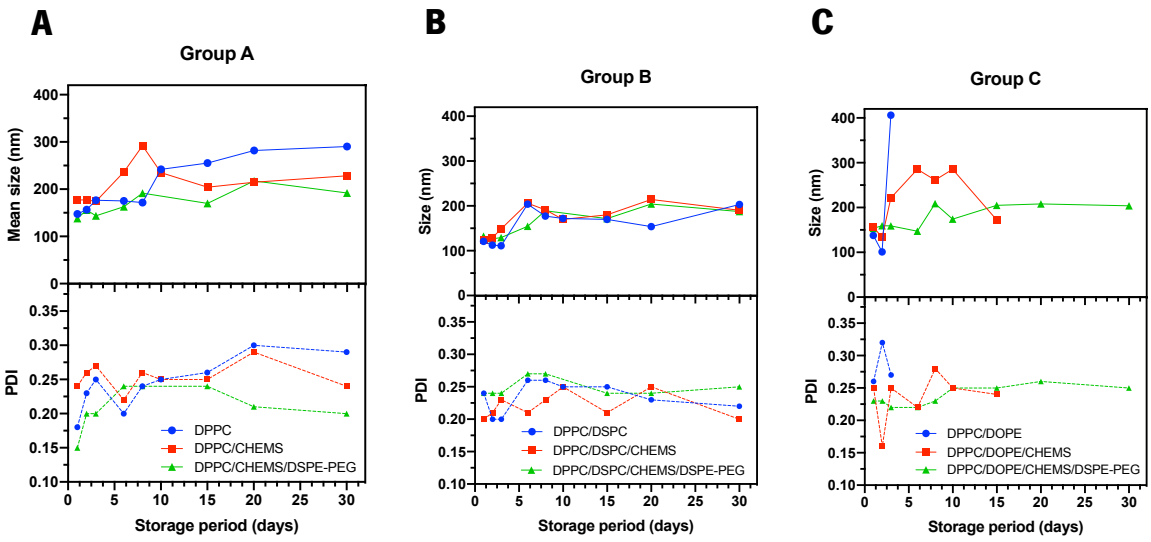


Figure 4.4 Stability data of DOX-loaded SMLs aqueous suspensions, based on (A) Group A, (B) Group B and (C) Group C lipid formulations, upon storage at 4 °C. The stability of the formulations is expressed as the mean size and PDI variations compared to the original values (measured on day 1).

4.1.4.3. Interaction with human serum albumin

It is also essential to gain insight into the stability of formulations under physiological conditions, which will significantly determine the bioavailability of drugs on the target site. The interaction of nanosystems with plasma proteins, such as HSA, is one of the indirect techniques studied for this purpose. These assays are based on the fluorescence quenching effect associated with the Trp214 residue (located in the hydrophobic cavity of the HSA) that results from changes in the conformation of HSA when binding to lipid vesicles [45]. In practical terms, the lower the interaction between the lipid vesicles and HSA, the smaller the associated fluorescence quenching effect. **Figure 4.5** summarises the results obtained for each group of formulations, presented as HSA fluorescence quenching (%) as a function of DOX-loaded SMLs increasing concentration. The non-linear fit, following **Equation 3.4**, is also shown, and the calculated variables (dissociation constant, binding constant, and the number of binding locations) are presented in **Table B.1**(see Appendix B in **section B.1**).

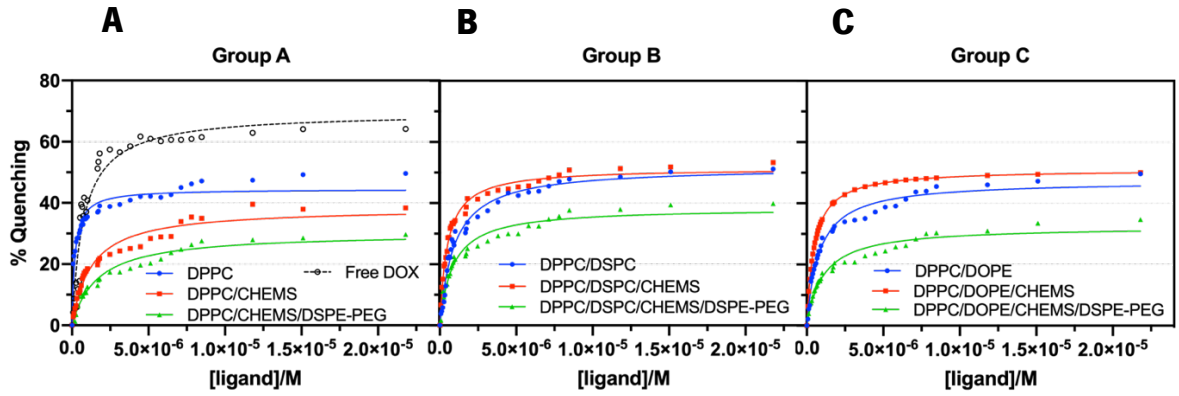


Figure 4.5 HSA fluorescence quenching (%) as a function of increasing free DOX concentration (as a reference in Group A) and loaded in (A) Group A, (B) Group B and (C) Group C lipid formulations. A non-linear fit, according to **Equation 3.4**, is presented (corresponding lines).

The considerably higher binding constant for free DOX compared to that obtained after its encapsulation in lipid systems reveals the capacity of the latter to provide adequate drug protection against interaction with HSA, preventing opsonisation and increasing its bioavailability. Group A (DPPC-based) revealed a decrease in affinity for HSA when CHEMS was added to the formulation (**Figure 4.5 A**). Group B (DPPC/DSPC) shows, in general, a slightly higher binding affinity to HSA compared to Group A (**Figure 4.5 B**). Following our results, Semple *et al.* [63] reported that DSPC liposomes bind more to serum proteins than DPPC liposomes. Therefore, including CHEMS in the lipid formulation induces a slightly

higher binding affinity to HSA than for systems without CHEMS. DPPC/DSPC/CHEMS systems revealed twice the binding constant value (k_d=2.12×10^6 M^{-1}) compared to the DPPC/DSPC formulation (k_d=1.01×10^6 M^{-1}), with a very similar number of binding locations (1.66 and 1.67, respectively). Since CHEMS is a Ch mimicking molecule, and following Semple *et al.* [63], a decrease in protein binding ability was expected. The authors demonstrated that an increase in Ch content (up to 30 mol% Ch) caused a significant reduction in protein binding to the vesicles. This effect comes from the ability of Ch to alleviate packing defects (angular fracture planes) characteristic of DSPC-based large unilamellar vesicles (LUVs) and to which serum proteins are more easily adsorbed. However, these results may be merely size related, as these defect regions are common in LUVs, which are considerably larger than the SMLs studied here. A similar behaviour was also found in Group C (DPPC/DOPE-based systems) (**Figure 4.5-C**).

All the PEGylated nanosystems revealed enhanced stealth properties within the corresponding group. Following those obtained in the previous section, these results allow us to conclude that including a small amount of DSPE-PEG provides greater long-term storage stability and cargo protection under physiological conditions. The binding of HSA results from the electrostatic interaction between the anionic residues of HSA and the cationic choline lipid head groups. Lee and Larson [64] reported that the degree of binding of HSA to PEGylated bilayers depends on PEG size and grafting density. Furthermore, the conformation of the PEG layer in the vesicles is also determinant: when PEG has a mushroom conformation, the HSA can penetrate the PEG layer and bind to the bilayer, which does not happen in a brush state [64].

4.1.4.4. Implications of lipid formulation and pH on the location of doxorubicin

Fluorescence spectroscopy and steady-state fluorescence anisotropy measurements of DOX-loaded SMLs were performed in a pH range between 2 and 11. This assay had as main objectives: (i) to associate fluorescence intensity with the distance of DOX from the magnetic core with pH variation; (ii) to connect DOX fluorescence anisotropy to its rotational mobility; and (iii) to relate the combined effect of pH and lipid composition to the location of DOX in the lipid systems and predict the ease of DOX release in the studied pH range.

The analysis of fluorescence intensity changes is based on the distance-dependent quenching effect exerted by magnetic NPs in DOX fluorescence; however, it must also be considered that the fluorescence

emission of DOX presents a mild pH-sensitivity (< 5% per pH unit) [41]. The steady-state fluorescence anisotropy values (obtained at 25 °C using

Equation 2.1) reflect DOX location, considering the fluidity decrease from the bilayer surface to the interior, where the acyl chain end **A** rs increased disorder [65]. Therefore, the fluore **B** ce intensity (I_F) variations must be analysed or supported by the anisotropy results at the corresponding pH. **Figure 4.6 A** shows a decrease in I_F with increasing pH, which can be explained by DOX pH sensitivity and its distance to the magnetic core (that acts as a quencher). The abrupt drop recorded in all formulations and increased anisotropy prove the formation of magnetoliposomes and the DOX incorporation into the nanosystems.

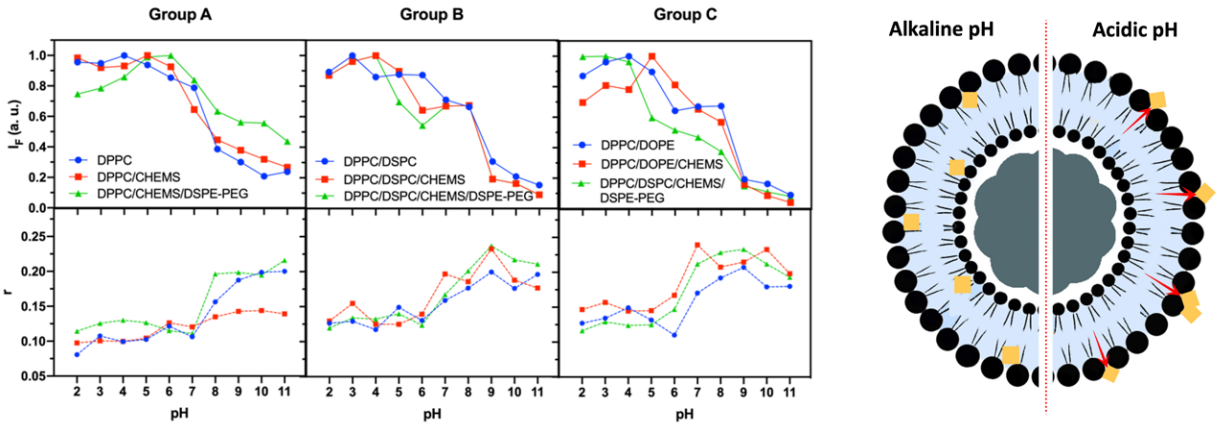


Figure 4.6 (A) Fluorescence intensity and steady-state fluorescence anisotropy (r) variation with pH (from 2 to 11) of DOX-loaded SMLs based on different lipid formulations. Total lipid concentration: 1 mM; DOX: 2 μM. (B) Schematic representation of DOX molecules localisation in the lipid bilayer at different pH (predictive).

Considering that DOX has pK_a≈9.93, the pronounced variation of I_F and anisotropy for pH between 5 and 7 again proves the incorporation of DOX into the lipid bilayer, as its neutral form is favoured. In the case of basic groups (like DOX), it is reported a tendency to shift pK_a to values below the typical values in water [66,67], which is verified for DOX in a hydrophobic environment (such as lipid bilayers). The obtained anisotropy values are consistent with the typical fluorophore values in bilayers and lower than the fundamental anisotropy reported for DOX (r_0=0.33) [43].

Similar I_F and anisotropy variation profiles were found in all lipid formulations. Those profiles are characterised by a general decreasing trend in I_F with increasing pH and an inverse effect in anisotropy

values. **Figure 4.6 B** shows a schematic representation (predicted by the obtained results) of DOX position in the lipid bilayer when subjected to different pH conditions. At alkaline pH, DOX is near acyl chains (higher anisotropy and lower I_F values), and, in acidic media, it moves to the membrane surface, even being adsorbed on the surface of SMLs. These results predict higher ease of DOX release at lower pH, namely at pH 7 for Group A formulations and pH 6 for Groups B and C. Furthermore, it is also verified that the functionalisation with DSPE-PEG also allows the protonation of DOX and, as such, its location on the surface of the SMLs. However, less release is expected since PEG is a barrier to drug diffusion.

4.1.4.5. Effect of lipid formulations on doxorubicin release kinetics and profile

DOX release assays from the nine SMLs formulations were carried out in different environments and conditions. A lipid formulation suitable for controlled release in cancer therapy should potentiate DOX release at therapeutic conditions (42 °C and/or acidic pH), while reducing non-specific release under physiological conditions. Also, it should not present a very pronounced release over the first 24 h. These assays measured DOX release using as triggers the separate and combined effect of temperature and pH (

Figure 4.7Error! Reference source not found.). These screenings intend to pre-select the lipid formulations that best fit controlled release patterns for a future exploration using an AMF and/or photothermia as a trigger.

Table 4.3 shows the ratio between the maximum release value for each formulation and the one obtained under physiological conditions (37 °C, pH 7.4). It is intended to compare the interplay of thermosensitivity with pH sensitivity. The slope (*m*) of the release plotted in the first 5 h was calculated to better interpret the short-term response upon stimuli application. Therefore, multi-stimuli responsive formulations for DOX controlled release should present: (i) a release ratio > 1 at acidic pH, related to the ability to release DOX locally in tumours; and (ii) a higher release rate at 42 °C, pH 5.5 than that obtained at 37 °C, to ensure a local temperature-triggered controlled release.

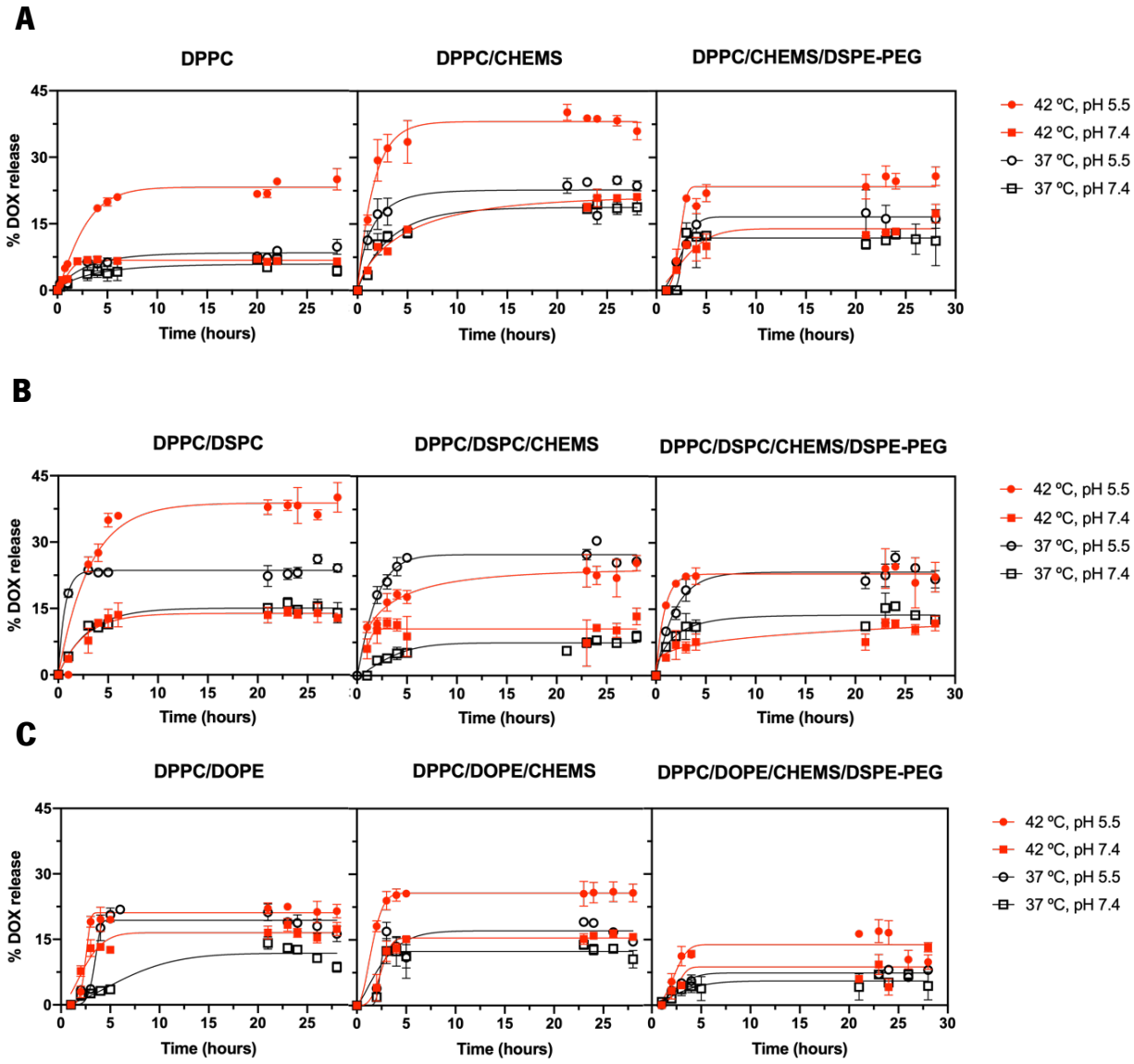


Figure 4.7 *In vitro* kinetic release profile of DOX encapsulated in SMLs is based on (a) Group A, (b) Group B, and (c) Group C lipid formulations at different conditions of temperature and pH. Triplicate mean fitted to the Weibull kinetic model.

Table 4.3 Summary of release slope (*m*) values of DOX plotted in the first 5 h and ratio between the saturation release under 37 °C, pH 7.4 and the corresponding release conditions.

Group	Lipid composition	42 °C, pH 5.5		42 °C, pH 7.4		37 °C, pH 5.5		37 °C, pH 7.4	
		m	ratio	*m*	ratio	*m*	ratio	*m*	ratio
A	DPPC	4.04	5.67	1.77	1.47	1.30	2.21	0.68	1
	DPPC/CHEMS	6.39	1.91	2.58	1.12	5.92	1.25	2.70	1
	DPPC/CHEMS/DSPE-PEG	4.71	2.30	2.39	1.54	3.53	1.74	2.52	1
B	DPPC/DSPC	6.39	1.86	2.32	0.59	5.89	1.12	2.7	1
	DPPC/DSPC/CHEMS	4.23	2.88	1.77	1.51	5.25	2.92	0.98	1
	DPPC/DSPC/CHEMS/DSPE-PEG	7.21	1.75	1.74	0.93	6.19	1.71	2.11	1
C	DPPC/DOPE	4.04	2.48	2.70	2.01	4.20	1.88	0.79	1
	DPPC/DOPE/CHEMS	5.83	2.42	3.26	1.48	3.15	1.37	2.67	1
	DPPC/DOPE/CHEMS/DSPE-PEG	3.42	1.66	1.69	0.93	1.83	1.82	1.03	1

Concerning Group A, there was a general increase in DOX release with the addition of CHEMS to the DPPC formulation. Besides the evident rise in maximum release at 42 °C and pH 5.5 (ideal therapeutic conditions), there is an accentuation of the release at 37 °C and pH 5.5 in the first hours. There was not a significant variation in the release profiles at pH 7.4. These results point to a synergy between pH and temperature stimuli, which are determining factors in the release of DOX and reflect the pH-dependent solubility of DOX, due to the protonation of anthracycline moiety at acidic pH. A similar profile was found upon the addition of DSPE-PEG to the latter formulation (DPPC/CHEMS/DSPE-PEG). However, the obtained maximum release of DOX was lower than for the formulation without DSPE-PEG. The same behaviour was reported previously [30] and may be associated with a diffusion barrier action of PEG on the surface of SMLs.

The addition of DSPC to the DPPC formulation (Group B) generally potentiated DOX release. The DPPC/DSPC binary formulation allowed a 1.6× increase in the total DOX released and a higher release rate in the first 5 h. Once again, an acidic pH-determining action is noted, even under physiological temperature conditions, resulting from drug protonation. At pH 7.4, the release profile is very similar. However, unlike the Group A counterpart, adding CHEMS reduced the maximum DOX release, except at 37 °C and pH 5.5. This may result from a prevalence of pH sensitivity over thermosensitivity, as adding CHEMS reduced T_m from 42.4 °C to 39.7 °C. The addition of DSPE-PEG (DPPC/DSPC/CHEMS/DSPE-

PEG formulation) increased T_m to 41.4 °C and resulted in a slight decrease in the maximum release at 37 °C and pH 5.5.

It should be noted that the SMLs based on DPPC/DSPC/CHEMS/DSPE-PEG were the ones that showed not only a higher release rate in the first 5 h at 42 °C and pH 5.5, but also a higher release rate difference between the corresponding condition and the non-therapeutic one. Furthermore, the incorporation of CHEMS also makes these nanosystems fusogenic in the presence of acidic pH of the tumour microenvironment and the endosomes and lysosomes of tumour cells [39]. These results indicate a lipid combination with excellent potential for targeted and controlled therapeutic action in tumour environments.

Concerning group C, the DPPC/DOPE formulation showed an irregular behaviour from 21 h onwards, when the calculated % DOX release started to decrease. The results suggest that the DOX is taken up again by lipid structures that result from the inherent instability of these nanosystems. This is consistent with the stability assays of this formulation, which demonstrated the appearance of multiple-sized populations and a significant increase in PDI in the days after preparation. This instability is caused by adopting a non-bilayer structure by DOPE (hexagonal, H_{II}) in an aqueous medium at neutral pH [68] and can be counteracted by adding CHEMS to the formulation, which helps the assembly. This is verified in the DOX release profile from DPPC/DOPE/CHEMS formulation, in which a regular release profile was verified. The addition of DSPE-PEG resulted in a substantial decrease in DOX release under all conditions. As the addition of DOPE resulted in the loss of thermosensitivity, the controlled release is ensured by the pH-dependent solubility of DOX and by the pH-induced destabilisation of DOPE. PEG as a diffusion barrier protects the formulation from this pH sensitivity, which was also found in the previous formulations.

The DOX release kinetics of all the formulations and release conditions were fitted to three kinetic models: Weibull [46], first-order [47], and Korsmeyer-Peppas [48] (see Appendix B in **section B.2**, **Table B.2**, **Table B.3**, **Table B.4**, for Group A, B, and C, respectively). The formal parameter b of the Weibull model, besides characterising the release kinetics curve type, it is also associated with three different release diffusional mechanisms: (i) combined mechanism of Fickian diffusion and Case II transport when $0.75 < b < 1$; (ii) Fickian diffusion (in either fractal or Euclidian spaces) when $b \leq 0.75$; and (iii) complex release mechanism when $b > 1$. Likewise, the transport exponent (n) of the Korsmeyer-Peppas model also gives access to the type of release mechanism. When $n < 0.45$, the release mechanism is diffusion-controlled (Fickian release), $0.45 < n < 0.89$ indicates a combination of diffusion and erosion drug release (non-Fickian release), $0.89 < n < 1$ means a relaxation-controlled release, and in the case of $n > 1$, the release is controlled by swelling and chain relaxation.

In Group A, adding CHEMS to DPPC changed the mechanism of DOX release. In DPPC, there was a complex release mechanism at 42 °C, in both pH conditions, and a Fickian diffusion at 37 °C. However, the fit of release from DPPC/CHEMS to the Weibull model revealed, in all applied conditions, $0.75 < b < 1$, which corresponds to diffusion in a normal Euclidian space with the contribution of another release mechanism [46]. The fit to the Korsmeyer-Peppas model, although with lower R^2 values, revealed $n < 0.45$, characteristic of a diffusion-controlled release mechanism (Fickian release). The release mechanism was changed again with the addition of DSPE-PEG. The DPPC/CHEMS/DSPE-PEG formulation only assumed good R^2 values when using the Weibull model, with $b > 1$ in all conditions studied, revealing a complex release mechanism.

In Group B, the fit of release from DPPC/DSPC to the Weibull model revealed a transversally $b > 1$, whose sigmoid curve indicates the action of a complex release mechanism. The DPPC/DSPC/CHEMS formulation demonstrated different release types associated with each applied experimental condition. For pH 5.5 and 42 °C, an b value of 0.59 was estimated, corresponding to diffusion in fractal or disordered substrate different from the percolation cluster [46], while at 37 °C, the b value is 1.1, corresponding to a complex mechanism. At pH 7.4 and 42 °C, a good R^2 value was not found ($R^2<0.74$) for any of the models, while at 37 °C, a b value of 0.38 reveals a diffusion mechanism in fractal substrate morphologically similar to the percolation cluster [69]. Like Group A, the addition of DSPE-PEG showed a $b>1$ in all conditions studied, indicating a complex release mechanism. Considering Group C, good R^2 values were only obtained by fitting data with the Weibull model. All formulations in this group showed $b > 1$ under all conditions, indicating that a complex mechanism governs the release of DOX in these formulations. This means a non-linear release rate increase in the initial phase up to the inflexion point [46].

4.1.5. Conclusions

Liposomes are the colloidal nanocarriers with the highest potential as mediators for targeted and combined cancer therapy. Besides increasing the stability and bioavailability of drugs, the versatility in production with multiple lipid combinations and conjugating them with magnetic NPs – forming magnetoliposomes – allows for enlarging the range of their applicability, targeting and combined therapies.

This work confirmed the reproducibility of the previously developed synthesis method for SMLs of different lipid combinations. Furthermore, all the synthesised SMLs exhibited hydrodynamic sizes and polydispersity indices required for biomedical applications. The high values of encapsulation efficiency

(87% < EE% < 96%) point to these systems as advantageous DOX nanocarriers. SMLs' ability to mask the positive charge of DOX was proven, giving them the potential to avoid multi-drug resistance. The thermodynamic parameters of DOX-loaded SMLs revealed thermosensitivity for the DPPC- and DPPC/DSPC-based formulations (Groups A and B), with T_m of 41.34±0.02 °C for DPPC/CHEMS/DSPE-PEG and T_m of 41.4±0.2 °C for DPPC/DSPC/CHEMS/DSPE-PEG.

In contrast, all formulations containing DOPE demonstrated a loss of thermosensitivity. The role of DSPE-PEG in lipid formulations should be highlighted. In addition, to allow obtaining SMLs with optimal thermosensitivity for controlled release under mild-hyperthermia conditions, PEGylation proved to be fundamental as a long-term storage stabiliser, providing stealth properties under physiologically relevant conditions, which is a determining factor for the bioavailability of drugs at the target site.

Release profiles revealed a synergistic effect of a temperature rise (42 °C) with acidic pH (5.5), which is crucial for the controlled release of DOX. These profiles result from an interplay of the formulations' thermosensitivity, the protonation of DOX at acidic pH, and its displacement to SMLs' surface. Once again, formulations based on DPPC and DPPC/DSPC (Groups A and B, respectively) stand out as multi-stimuli-responsive systems (thermo/pH sensitivity) under therapeutic conditions (42 °C and acidic pH). Although DSPE-PEG acts as a DOX diffusion barrier, PEGylated formulations, particularly the DPPC/DSPC/CHEMS/DSPE-PEG, demonstrate an overall potential for a targeted and controlled therapeutic action in tumour environments.

4.1.6. References

1. Mathers, C.D. History of global burden of disease assessment at the World Health Organization. *Archives of Public Health* **2020**, *78*, 1-13.

2. Olusanya, T.O.; Haj Ahmad, R.R.; Ibegbu, D.M.; Smith, J.R.; Elkordy, A.A. Liposomal drug delivery systems and anticancer drugs. *Molecules* **2018**, *23*, 907.

3. Vyas, D.; Laput, G.; Vyas, A.K. Chemotherapy-enhanced inflammation may lead to the failure of therapy and metastasis. *OncoTargets and therapy* **2014**, *7*, 1015.

4. Yao, X.; Panichpisal, K.; Kurtzman, N.; Nugent, K. Cisplatin nephrotoxicity: a review. *The American journal of the medical sciences* **2007**, *334*, 115-124.

5. Von Hoff, D.D.; Mita, M.M.; Ramanathan, R.K.; Weiss, G.J.; Mita, A.C.; LoRusso, P.M.; Burris, H.A.; Hart, L.L.; Low, S.C.; Parsons, D.M. Phase I study of PSMA-targeted docetaxel-containing nanoparticle BIND-014 in patients with advanced solid tumors. *Clinical Cancer Research* **2016**, *22*, 3157-3163.

6. Barenholz, Y.C. Doxil®—the first FDA-approved nano-drug: lessons learned. *Journal of controlled release* **2012**, *160*, 117-134.

7. Mross, K.; Niemann, B.; Massing, U.; Drevs, J.; Unger, C.; Bhamra, R.; Swenson, C.E. Pharmacokinetics of liposomal doxorubicin (TLC-D99; Myocet) in patients with solid tumors: an open-label, single-dose study. *Cancer chemotherapy and pharmacology* **2004**, *54*, 514-524.

8. Maeda, H.; Wu, J.; Sawa, T.; Matsumura, Y.; Hori, K. Tumor vascular permeability and the EPR effect in macromolecular therapeutics: a review. *Journal of controlled release* **2000**, *65*, 271-284.

9. Arap, W.; Pasqualini, R.; Ruoslahti, E. Cancer treatment by targeted drug delivery to tumor vasculature in a mouse model. *science* **1998**, *279*, 377-380.

10. Motamarry, A.; Asemani, D.; Haemmerich, D. Thermosensitive liposomes. *Liposome. Rijeka InTech* **2017**, 187-212.

11. Yatvin, M.B.; Weinstein, J.N.; Dennis, W.H.; Blumenthal, R. Design of liposomes for enhanced local release of drugs by hyperthermia. *Science* **1978**, *202*, 1290-1293.

12. Oude Blenke, E.; Mastrobattista, E.; Schiffelers, R.M. Strategies for triggered drug release from tumor targeted liposomes. *Expert opinion on drug delivery* **2013**, *10*, 1399-1410.

13. DeVita, V.T.; Lawrence, T.S.; Rosenberg, S.A. *DeVita, Hellman, and Rosenberg's cancer: principles & practice of oncology*; Lippincott Williams & Wilkins: **2008**; Volume 2.

14. Jha, S.; Sharma, P.K.; Malviya, R. Hyperthermia: role and risk factor for cancer treatment. *Achievements in the life sciences* **2016**, *10*, 161-167.

15. Datta, N.; Ordóñez, S.G.; Gaipl, U.; Paulides, M.; Crezee, H.; Gellermann, J.; Marder, D.; Puric, E.; Bodis, S. Local hyperthermia combined with radiotherapy and-/or chemotherapy: Recent advances and promises for the future. *Cancer treatment reviews* **2015**, *41*, 742-753.

16. Mantso, T.; Vasileiadis, S.; Anestopoulos, I.; Voulgaridou, G.-P.; Lampri, E.; Botaitis, S.; Kontomanolis, E.; Simopoulos, C.; Goussetis, G.; Franco, R. Hyperthermia induces therapeutic effectiveness and potentiates adjuvant therapy with non-targeted and targeted drugs in an in vitro model of human malignant melanoma. *Scientific reports* **2018**, *8*, 1-16.

17. van der Heijden, A.G.; Dewhirst, M.W. Effects of hyperthermia in neutralising mechanisms of drug resistance in non-muscle-invasive bladder cancer. *International journal of hyperthermia* **2016**, *32*, 434-445.

18. Kampinga, H.H. Cell biological effects of hyperthermia alone or combined with radiation or drugs: a short introduction to newcomers in the field. *International journal of hyperthermia* **2006**, *22*, 191-196.

19. Song, C.W. Effect of local hyperthermia on blood flow and microenvironment: a review. *Cancer research* **1984**, *44*, 4721s-4730s.

20. Chang, D.; Lim, M.; Goos, J.A.; Qiao, R.; Ng, Y.Y.; Mansfeld, F.M.; Jackson, M.; Davis, T.P.; Kavallaris, M. Biologically targeted magnetic hyperthermia: Potential and limitations. *Frontiers in pharmacology* **2018**, *9*, 831.

21. Gavilán, H.; Avugadda, S.K.; Fernández-Cabada, T.; Soni, N.; Cassani, M.; Mai, B.T.; Chantrell, R.; Pellegrino, T. Magnetic nanoparticles and clusters for magnetic hyperthermia: optimizing their heat performance and developing combinatorial therapies to tackle cancer. *Chemical Society Reviews* **2021**.

22. Dutz, S.; Hergt, R. Magnetic nanoparticle heating and heat transfer on a microscale: Basic principles, realities and physical limitations of hyperthermia for tumour therapy. *International journal of hyperthermia* **2013**, *29*, 790-800.

23. Xie, J.; Yan, C.; Yan, Y.; Chen, L.; Song, L.; Zang, F.; An, Y.; Teng, G.; Gu, N.; Zhang, Y. Multi-modal Mn–Zn ferrite nanocrystals for magnetically-induced cancer targeted hyperthermia: a comparison of passive and active targeting effects. *Nanoscale* **2016**, *8*, 16902-16915.

24. Yatvin, M.; Kreutz, W.; Horwitz, B.; Shinitzky, M. p H-Sensitive Liposomes: Possible Clinical Implications. *Science* **1980**, *210*, 1253-1255.

25. Franco, M.S.; Gomes, E.R.; Roque, M.C.; Oliveira, M.C. Triggered drug release from liposomes: Exploiting the outer and inner tumor environment. *Frontiers in Oncology* **2021**, *11*, 470.

26. Karanth, H.; Murthy, R. pH-Sensitive liposomes-principle and application in cancer therapy. *Journal of pharmacy and pharmacology* **2007**, *59*, 469-483.

27. Feng, L.; Dong, Z.; Tao, D.; Zhang, Y.; Liu, Z. The acidic tumor microenvironment: a target for smart cancer nano-theranostics. *National Science Review* **2018**, *5*, 269-286.

28. Weinstein, J.N.; Magin, R.; Yatvin, M.; Zaharko, D. Liposomes and local hyperthermia: selective delivery of methotrexate to heated tumors. *science* **1979**, *204*, 188-191.

29. Perrin, D. *Buffers for pH and metal ion control*; Springer Science & Business Media: 2012.

30. Cardoso, B.D.; Rodrigues, A.R.O.; Bañobre-López, M.; Almeida, B.G.; Amorim, C.O.; Amaral, V.S.; Coutinho, P.J.; Castanheira, E. Magnetoliposomes based on shape anisotropic calcium/magnesium ferrite nanoparticles as nanocarriers for doxorubicin. *Pharmaceutics* **2021**, *13*, 1248.

31. Needham, D.; Dewhirst, M.W. The development and testing of a new temperature-sensitive drug delivery system for the treatment of solid tumors. *Advanced drug delivery reviews* **2001**, *53*, 285-305.

32. Allen, T.M.; Hansen, C.; Rutledge, J. Liposomes with prolonged circulation times: factors affecting uptake by reticuloendothelial and other tissues. *Biochimica et Biophysica Acta (BBA)-Biomembranes* **1989**, *981*, 27-35.

33. Gaber, M.H.; Hong, K.; Huang, S.K.; Papahadjopoulos, D. Thermosensitive sterically stabilized liposomes: formulation and in vitro studies on mechanism of doxorubicin release by bovine serum and human plasma. *Pharmaceutical research* **1995**, *12*, 1407-1416.

34. Maruyama, K.; Unezaki, S.; Takahashi, N.; Iwatsuru, M. Enhanced delivery of doxorubicin to tumor by long-circulating thermosensitive liposomes and local hyperthermia. *Biochimica et Biophysica Acta (BBA)-Biomembranes* **1993**, *1149*, 209-216.

35. Lu, T.; Ten Hagen, T.L. Inhomogeneous crystal grain formation in DPPC-DSPC based thermosensitive liposomes determines content release kinetics. *Journal of controlled release* **2017**, *247*, 64-72.

36. Soares, D.C.F.; de Oliveira, M.C.; de Barros, A.L.B.; Cardoso, V.N.; Ramaldes, G.A. Liposomes radiolabeled with 159Gd: In vitro antitumoral activity, biodistribution study and scintigraphic image in Ehrlich tumor bearing mice. *european journal of pharmaceutical sciences* **2011**, *43*, 290-296.

37. Zhang, G.-J.; Liu, H.-W.; Yang, L.; Zhong, Y.-G.; Zheng, Y.-Z. Influence of membrane physical state on the lysosomal proton permeability. *The Journal of membrane biology* **2000**, *175*, 53-62.

38. Kulig, W.; Tynkkynen, J.; Javanainen, M.; Manna, M.; Rog, T.; Vattulainen, I.; Jungwirth, P. How well does cholesteryl hemisuccinate mimic cholesterol in saturated phospholipid bilayers? *Journal of molecular modeling* **2014**, *20*, 1-9.

39. Shabbits, J.A.; Mayer, L.D. Intracellular delivery of ceramide lipids via liposomes enhances apoptosis in vitro. *Biochimica et Biophysica Acta (BBA)-Biomembranes* **2003**, *1612*, 98-106.

40. Gubernator, J. Active methods of drug loading into liposomes: recent strategies for stable drug entrapment and increased in vivo activity. *Expert opinion on drug delivery* **2011**, *8*, 565-580.

41. Karukstis, K.K.; Thompson, E.H.; Whiles, J.A.; Rosenfeld, R.J. Deciphering the fluorescence signature of daunomycin and doxorubicin. *Biophysical chemistry* **1998**, *73*, 249-263.

42. Gijsbers, A.; Nishigaki, T.; Sánchez-Puig, N. Fluorescence anisotropy as a tool to study protein-protein interactions. *JoVE (Journal of Visualized Experiments)* **2016**, e54640.

43. Valeur, B.; Berberan-Santos, M.N. *Molecular fluorescence: principles and applications*; John Wiley & Sons: 2012.

44. Chuang, V.T.G.; Maruyama, T.; Otagiri, M. Updates on contemporary protein binding techniques. *Drug metabolism and pharmacokinetics* **2009**, *24*, 358-364.

45. Azevedo, A.M.; Ribeiro, D.M.; Pinto, P.C.; Lúcio, M.; Reis, S.; Saraiva, M.L.M. Imidazolium ionic liquids as solvents of pharmaceuticals: influence on HSA binding and partition coefficient of nimesulide. *International Journal of Pharmaceutics* **2013**, *443*, 273-278.

46. Papadopoulou, V.; Kosmidis, K.; Vlachou, M.; Macheras, P. On the use of the Weibull function for the discernment of drug release mechanisms. *International Journal of Pharmaceutics* **2006**, *309*, 44-50.

47. Noyes, A.A.; Whitney, W.R. The rate of solution of solid substances in their own solutions. *Journal of the American Chemical Society* **1897**, *19*, 930-934.

48. Korsmeyer, R.W.; Gurny, R.; Doelker, E.; Buri, P.; Peppas, N.A. Mechanisms of solute release from porous hydrophilic polymers. *International Journal of Pharmaceutics* **1983**, *15*, 25-35.

49. Danaei, M.; Dehghankhold, M.; Ataei, S.; Hasanzadeh Davarani, F.; Javanmard, R.; Dokhani, A.; Khorasani, S.; Mozafari, M. Impact of particle size and polydispersity index on the clinical applications of lipidic nanocarrier systems. *Pharmaceutics* **2018**, *10*, 57.

50. Guimarães, D.; Cavaco-Paulo, A.; Nogueira, E. Design of liposomes as drug delivery system for therapeutic applications. *International Journal of Pharmaceutics* **2021**, 120571.

51. Pattni, B.S.; Chupin, V.V.; Torchilin, V.P. New developments in liposomal drug delivery. *Chemical reviews* **2015**, *115*, 10938-10966.

52. Honary, S.; Zahir, F. Effect of zeta potential on the properties of nano-drug delivery systems-a review (Part 1). *Tropical Journal of Pharmaceutical Research* **2013**, *12*, 255-264.

53. Brigger, I.; Dubernet, C.; Couvreur, P. Nanoparticles in cancer therapy and diagnosis. *Advanced drug delivery reviews* **2012**, *64*, 24-36.

54. Drazenovic, J.; Wang, H.; Roth, K.; Zhang, J.; Ahmed, S.; Chen, Y.; Bothun, G.; Wunder, S.L. Effect of lamellarity and size on calorimetric phase transitions in single component phosphatidylcholine vesicles. *Biochimica et Biophysica Acta (BBA)-Biomembranes* **2015**, *1848*, 532-543.

55. Marsh, D.; Bartucci, R.; Sportelli, L. Lipid membranes with grafted polymers: physicochemical aspects. *Biochimica et Biophysica Acta (BBA)-Biomembranes* **2003**, *1615*, 33-59.

56. Neunert, G.; Tomaszewska-Gras, J.; Baj, A.; Gauza-Włodarczyk, M.; Witkowski, S.; Polewski, K. Phase Transitions and Structural Changes in DPPC Liposomes Induced by a 1-Carba-Alpha-Tocopherol Analogue. *Molecules* **2021**, *26*, 2851.

57. Needham, D.; Park, J.-Y.; Wright, A.M.; Tong, J. Materials characterization of the low temperature sensitive liposome (LTSL): effects of the lipid composition (lysolipid and DSPE–PEG2000) on the thermal transition and release of doxorubicin. *Faraday discussions* **2013**, *161*, 515-534.

58. Crommelin, D.; Van Bommel, E. Stability of liposomes on storage: freeze dried, frozen or as an aqueous dispersion. *Pharmaceutical research* **1984**, *1*, 159-163.

59. Subhan, M.A.; Yalamarty, S.S.K.; Filipczak, N.; Parveen, F.; Torchilin, V.P. Recent Advances in Tumor Targeting via EPR Effect for Cancer Treatment. *Journal of Personalized Medicine* **2021**, *11*, 571.

60. O'Driscoll, K.; Sanayei, R.A. Chain-length dependence of the glass transition temperature. *Macromolecules* **1991**, *24*, 4479-4480.

61. Alhakamy, N.A.; Elandaloussi, I.; Ghazvini, S.; Berkland, C.J.; Dhar, P. Effect of lipid headgroup charge and pH on the stability and membrane insertion potential of calcium condensed gene complexes. *Langmuir* **2015**, *31*, 4232-4245.

62. Grit, M.; Crommelin, D.J. Chemical stability of liposomes: implications for their physical stability. *Chemistry and physics of lipids* **1993**, *64*, 3-18.

63. Semple, S.C.; Chonn, A.; Cullis, P.R. Influence of cholesterol on the association of plasma proteins with liposomes. *Biochemistry* **1996**, *35*, 2521-2525.

64. Lee, H.; Larson, R.G. Adsorption of plasma proteins onto PEGylated lipid bilayers: the effect of PEG size and grafting density. *Biomacromolecules* **2016**, *17*, 1757-1765.

65. Alves, A.C.; Magarkar, A.; Horta, M.; Lima, J.L.; Bunker, A.; Nunes, C.; Reis, S. Influence of doxorubicin on model cell membrane properties: insights from in vitro and in silico studies. *Scientific reports* **2017**, *7*, 1-11.

66. Isom, D.G.; Castañeda, C.A.; Cannon, B.R. Large shifts in pKa values of lysine residues buried inside a protein. *Proceedings of the National Academy of Sciences* **2011**, *108*, 5260-5265.

67. Fitch, C.A.; Karp, D.A.; Lee, K.K.; Stites, W.E.; Lattman, E.E.; García-Moreno, E.B. Experimental pKa values of buried residues: analysis with continuum methods and role of water penetration. *Biophysical journal* **2002**, *82*, 3289-3304.

68. Ellens, H.; Bentz, J.; Szoka, F.C. pH-induced destabilization of phosphatidylethanolamine-containing liposomes: role of bilayer contact. *Biochemistry* **1984**, *23*, 1532-1538.

69. Kosmidis, K.; Argyrakis, P.; Macheras, P. Fractal kinetics in drug release from finite fractal matrices. *The Journal of chemical physics* **2003**, *119*, 6373-6377.

4.2. Investigation of superparamagnetic nanoparticles' potential for near infrared-derived hyperthermia

This sub-chapter aimed to insight into the potential of $Ca_{0.25}Mg_{0.75}Fe_2O_4$ superparamagnetic nanoparticles to photothermal therapy and their effects upon inclusion in lipid vesicles.

4.2.1. Overview

Magnetoliposomes are hybrid lipid-nanoparticle complexes. Thus, its optimization towards a stimuli-responsive system capable of delivering drugs in a controlled and effective way is a tricky process. Following the advances of lipid formulations' effect on the mechanisms that govern the drug-controlled release induction under multi-stimuli in the previous sub-chapter, this one focuses on the ability of $Ca_{0.25}Mg_{0.75}Fe_2O_4$ magnetic NPs to mediate these stimuli, namely magnetic and thermal-responsiveness. This work studied the heating abilities of those NPs under NIR laser irradiation. As a result, the potential for NIR-induced photothermal measurements using an 808 nm laser recorded the maximum temperature variations of 9.6±0.4 °C, 11.34±0.6 °C and 16.5±0.4 °C for aqueous suspensions with 1, 2 and 4 mg/mL of NPs, respectively.

Similarly, SMLs samples based on a fixed concentration of lipid formulation (1 mM of DPPC/DSPC/CHEMS/DSPE-PEG) for a varying initial weight of magnetic NPs (1, 2 and 4 mg) were studied. All the magnetization hysteresis loops of dried SML samples revealed a superparamagnetic behaviour with a reduction of M_s compared to the raw NPs. In turn, a gradual decrease in the average size of SMLs was found with increased encapsulated NPs. Finally, the encapsulation efficiency was determined for the several initial iron/phospholipid ratios, and the values ranged between 0.87 and 3.24 mg of NPs per mM of phospholipids.

4.2.2. Introduction

The use of heat for therapeutic effects has been described for centuries, mainly in ablating cancer cells [1,2]. It is called mild hyperthermia when these effects result from a mild temperature increase (41-50 °C) which can induce therapeutic effects without promoting the uncontrolled death of normal tissues [3,4]. The limitations of conventional cancer therapies require, in fact, the development of complementary, alternative and adjuvant approaches. For instance, the treatment of pancreatic cancer usually fails due to chemotherapy resistance, and hyperthermia asserts itself as a very attractive approach to second-line therapy [5,6]. Furthermore, this technique has been improved to make the heat distribution selectively directed to the tumour sites, allowing a more effective, controlled, and uniform overheating of the tumours, deep-seated access tumour and specifically targeting tumour vasculature/hypoxic tumour cells [7]. Thus, hyperthermia therapy crossed paths with nanotechnology,

more specifically with NPs, which was in line with the forecast by Freeman *et al.* [8] who, in 1962, discussed the potential of "the marriage of magnetism and medicine".

NPs can generate heat when subjected to external energy sources. The most common is the conversion of AMF and light into thermal energy. Under high-frequency magnetic fields, heating dissipation happens when NPs are resonantly excited. That depends on the type of magnetic nanoparticle and may be induced by four mechanisms [9]: (i) Eddy currents, (ii) hysteresis loss, (iii) Brownian relaxation and (iv) Néel relaxation. Superparamagnetic NPs are typically less than 20 nm in size and resonate in magnetic fields ranging from 10 kHz to 10 MHz, allowing it to penetrate soft tissues and bones [10]. Another approach to inducing hyperthermia is photothermal therapy (PTT) with NIR laser light irradiation, in which the nanomaterials can convert light into heat energy [11]. The most currently studied NIR-absorbing nanomaterials are gold nanostructures due to the surface plasmon phenomenon. Those include gold nanorods [12-15], gold nanoshells [16-18], gold nanocages [19,20], and gold nanostars [21-23], among others [24-27]. However, gold nanostructures demonstrate mechanical weakness in the photothermal process and are associated with reduced biodegradability and toxicity [28]. In this sense, the potential of magnetic NPs in PTT has been investigated [29,30]. In this process, vibration energy is released through the photothermal properties of magnetic NPs and converted into thermal energy. This feature is especially advantageous if it is possible to accommodate in a single type of nanoparticle the ability to generate heat under different external energy sources and thus develop an "all-in-one" nanoparticle.

Furthermore, near infrared-induced photothermal hyperthermia is minimally invasive, allows remote controllability and presents higher tissue penetrating capabilities [31,32]. Thus, PTT may address some limitations in using AMF, whose need for high currents and voltages has limits of tolerance in the human body [33]. These are related to boundary effects between tissues of different dielectric constants, and conductivity AMF treatments are impossible in patients with metal implants less than 30 cm from the treatment site [34]. Furthermore, unlike photothermal approaches, AMF fields are generally targeted toward the whole body [35].

Thus, this sub-chapter aimed to insight into the potential of the previously developed shape-anisotropic $Ca_{0.25}Mg_{0.75}Fe_2O_4$ NPs and their effects upon inclusion in lipid vesicles. Initially, it is dedicated to the potential of these NPs for hyperthermia, both under the influence of a NIR laser and under the action of an AMF. Next, and following the advances achieved in the previous sub-chapter, only the most promising lipid formulation for targeted and controlled therapeutic action in tumour environments was selected. The chosen lipid formulation was DPPC/DSPC/CHEMS/DSPE-PEG (60:20:15:5), corresponding to long-circulating, fusogenic, thermo- and pH-sensitive SMLs. Emphasis is given to the encapsulation efficiency

of different concentrations of these magnetic NPs in a fixed concentration of the lipid formulation and their effect on the properties and functionality of SMLs.

4.2.3. Materials and Methods

For magnetoliposomes preparation, the lipids dipalmitoylphosphatidylcholine (DPPC) (from Sigma-Aldrich, St. Louis, MO, USA), distearoylphosphatidylcholine (DSPC) (from Sigma-Aldrich, St. Louis, MO, USA), cholesteryl hemisuccinate (CHEMS) (from Sigma-Aldrich, St. Louis, MO, USA) and 1,2-distearoyl-*sn*-glycero-3-phosphoethanolamine-*N*-[methoxy(polyethylene glycol)-2000] (ammonium salt) (DSPE-PEG2000, from Avanti Polar Lipids, Birmingham, AL, USA) were used.

For lipid quantification ferric chloride hexahydrate ($FeCl_3 \cdot 6H_2O$, from Sigma-Aldrich, St. Louis, MO, USA), ammonium thiocyanate (NH_4SCN, from Sigma-Aldrich, St. Louis, MO, USA) and pure chloroform ($CHCl_3$, from Sigma-Aldrich, St. Louis, MO, USA) were used. For the quantification of iron(iii) chloride complexes, hydrochloric acid (HCl, from Sigma-Aldrich, St. Louis, MO, USA) was used.

4.2.3.1. Near infrared-induced photothermal hyperthermia

The photothermal capacity of NPs was assessed in a home-made experimental setup, **Figure 4.8**, consisting of a sample holder, a laser light source with a wavelength of 808 nm and 1.6 W of power, an optical density filter, and a T-type thermocouple connected to a digital multimeter (Agilent U1242A) for temperature measurement. For that, aqueous suspensions with different Ca0.25Mg0.75Fe2O4 concentrations (1, 2 and 4 mg/mL) were placed in transparent glass tubes. The open end of the glass tubes was covered with parafilm, which was poked with a small orifice for inserting the thermocouple. Each trial consisted of 30 minutes of heating (laser on), followed by 30 minutes of cooling (laser off), with the temperature recorded over time at fixed time points (heating: every 20 seconds up to minute 3, and every 1 minute up to minute 30; colling: every 20 seconds up to 3 minutes, and every 1 minute up to 30 minutes). As controls, the temperature variation of distilled water under the same irradiation conditions was also carried out. All experiments were conducted in triplicate.

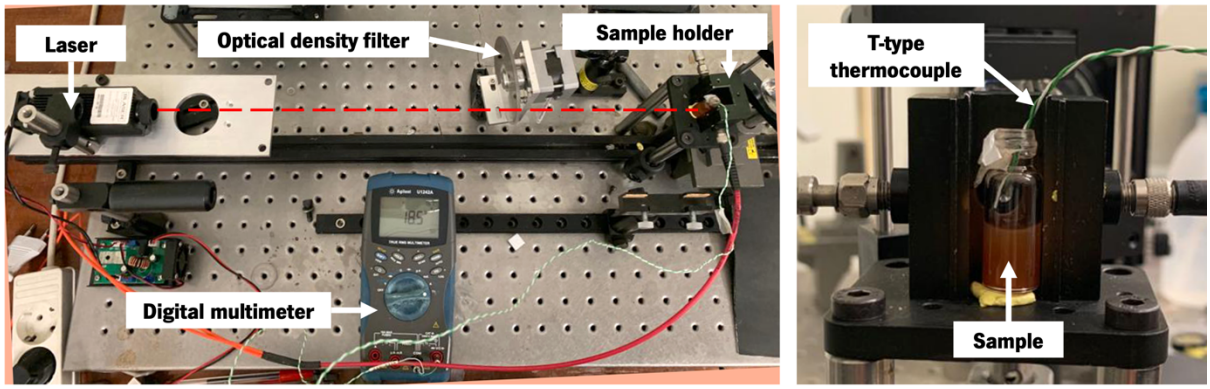


Figure 4.8 Experimental setup for near infrared-induced photothermal hyperthermia measurements.

4.2.3.2. Solid magnetoliposomes preparation

DPPC/DSPC/CHEMS/DSPE-PEG (60:20:15:5) based SMLs were prepared following the methodology presented in **section 4.1.3.1**, with slight modifications in the magnetic nanoparticle insertion and magnetoliposomes separation steps. The SMLs studied here aimed to encapsulate 1 mg, 2 mg and 4 mg of magnetic NPs to 1 mM of total lipid. For this, in forming a magnetic core within reverse micelles, the corresponding masses of dry NPs were added and followed by 20 min of ultrasonication (Misonix, Touch-screen S-4000) at a power of 190 W for a time interval of 15 min. Then, the procedure followed the one previously described, except that at the end, the sample of magnetoliposomes was left to sonicate for 1 additional hour. After that, to separate the magnetoliposomes from other components, two subsequent magnetic decanting processes were performed. The first aimed to remove non-encapsulated magnetic NPs and is based on the fact that free NPs respond quickly to the presence of a magnet. For this, a NdFeB N48 block magnet (Eclipse Magnetics Ltd., Sheffield, UK) with nickel-plated (Ni-Cu-Ni) coating was applied to the sample for 5 minutes, and the separated NPs were stored. The second process aimed to separate magnetoliposomes from empty lipid vesicles. Thus, the sample of magnetoliposomes was left to decant magnetically, following the previous procedure, for 24 h. Finally, pellets containing the SMLs were resuspended in 1 mL of ultrapure water and stored for later characterization.

4.2.3.3. Vibrating-sample magnetometer measurements

Magnetic properties of magnetoliposomes were measured at room temperature by magnetic hysteresis loops using a MicroSense EZ7 vibrating sample magnetometer (VSM) from 1.8 to 1.8 T.

Assays were conducted using SMLs synthesized using 1 mg, 2 mg and 4 mg of magnetic nanoparticle in their synthesis. Cut Eppendorf tubes (1.5 mL) tips were used as sample holders, as they are water

and temperature resistant. First, each Eppendorf tip was accurately weighed on a precision analytical balance. Then, the solutions of each magnetoliposome condition were slowly dried, drop by drop, on the corresponding Eppendorf tip to ensure the formation of a thin lipid film. After the drying process, each Eppendorf tip was weighted again to determine the mass of magnetoliposomes in each sample. In the end, each Eppendorf tip was mounted to the sample holder of VSM, the measurements were made, and the data was recorded.

4.2.3.4. Lipid quantification in solid magnetoliposomes samples

The Stewart assay for lipid concentration was used to determine the percentage of lipids capable of encapsulating magnetic NPs and forming SMLs. This method, recognised as Stewart assay [36], is based on the ability of phospholipids to form a complex with ammonium ferrothiocyanate, with absorbance values reflecting the amount of phospholipids present in the samples. The process was initiated by preparing a solution of ammonium ferrothiocyanate (AF). For this, 27.03 g of ferric chloride hexahydrate and 30.4 g of ammonium thiocyanate were dissolved in 1 L of deionized water. Next, the SMLs solution was evaporated until a lipid film was formed. To this lipid film, 2 mL of chloroform and 2 mL of AF solution were added. The solution was vortexed for 1 minute and let to sit for 30 minutes in the dark. After this period, the lower chloroform phase was removed for analysis by UV-Vis absorption spectroscopy with a blank in a pure chloroform. The calibration curve was obtained using the lipid formulation used in the synthesis of magnetoliposomes, following the same procedure described above, and plotting the absorbance *vs.* concentration at 490 nm.

4.2.3.5. Encapsulation efficiency of nanoparticles in solid magnetoliposomes

The encapsulation efficiency of NPs in SMLs was determined indirectly by quantifying iron(III) chloride complexes in the samples. This assay was based on the fact that the addition of concentrated hydrochloric acid (HCl) to the magnetic NPs promotes the formation of iron(III) chloride complexes with a strong signal in the UV-Vis range [37]. After magnetoliposome synthesis and purification, the SMLs solution was evaporated until a lipid film was formed. Then, 1.2 mL of HCl solution (37%) was added and sonicated for 5 minutes and left to digest for 1 h to promote the digestion of the NPs. Then, 1.8 mL of Milli-Q grade water was added to dilute the acid concentration to 4 M. The calibration curve was obtained by digesting known masses of the same NPs following a linear fitting of at least seven points.

Three independent measurements were performed for each system, and standard deviations (SD) were calculated.

4.2.4. Results and Discussion

4.2.4.1. Near infrared-derived heating performance of $Ca_{0.25}Mg_{0.75}Fe_2O_4$ nanoparticles

The NIR-induced hyperthermia performance of magnetic NPs was investigated using aqueous suspensions with different $Ca_{0.25}Mg_{0.75}Fe_2O_4$ concentrations, including 1, 2 and 4 mg/mL. In **Figure 4.9 A** a representative sample of each of the conditions is presented. The pronounced colour indicates an increased concentration of NPs in solution and, also, a good dispersion in water. Photothermal therapy most commonly uses lasers with a wavelength of 808 nm because biological tissues have a window of high transmission in the 650-900 nm range (first biological window, NIR-I) and due to better knowledge of photon propagation through deep living tissue in this range [38]. The photothermal conversion efficiency of the NPs is related to their optical absorption coefficient; a high NIR (700–1000 nm) optical absorption coefficient is associated with a high photothermal conversion efficiency at the NIR wavelength. Thus, for a better understanding of the concentration effect on the absorption behaviour of solutions, absorption spectra were obtained in a Shimadzu UV-3101PC UV-Vis-NIR (Shimadzu Corporation, Kyoto, Japan) spectrophotometer at 300 to 900 nm wavelength range (**Figure 4.9 B**). In general, all concentrations of $Ca_{0.25}Mg_{0.75}Fe_2O_4$ aqueous solutions revealed a broad absorption spectrum from ultraviolet to the NIR band. Furthermore, the NPs show increased NIR absorption intensity with increased concentrations, particularly at 808 nm.

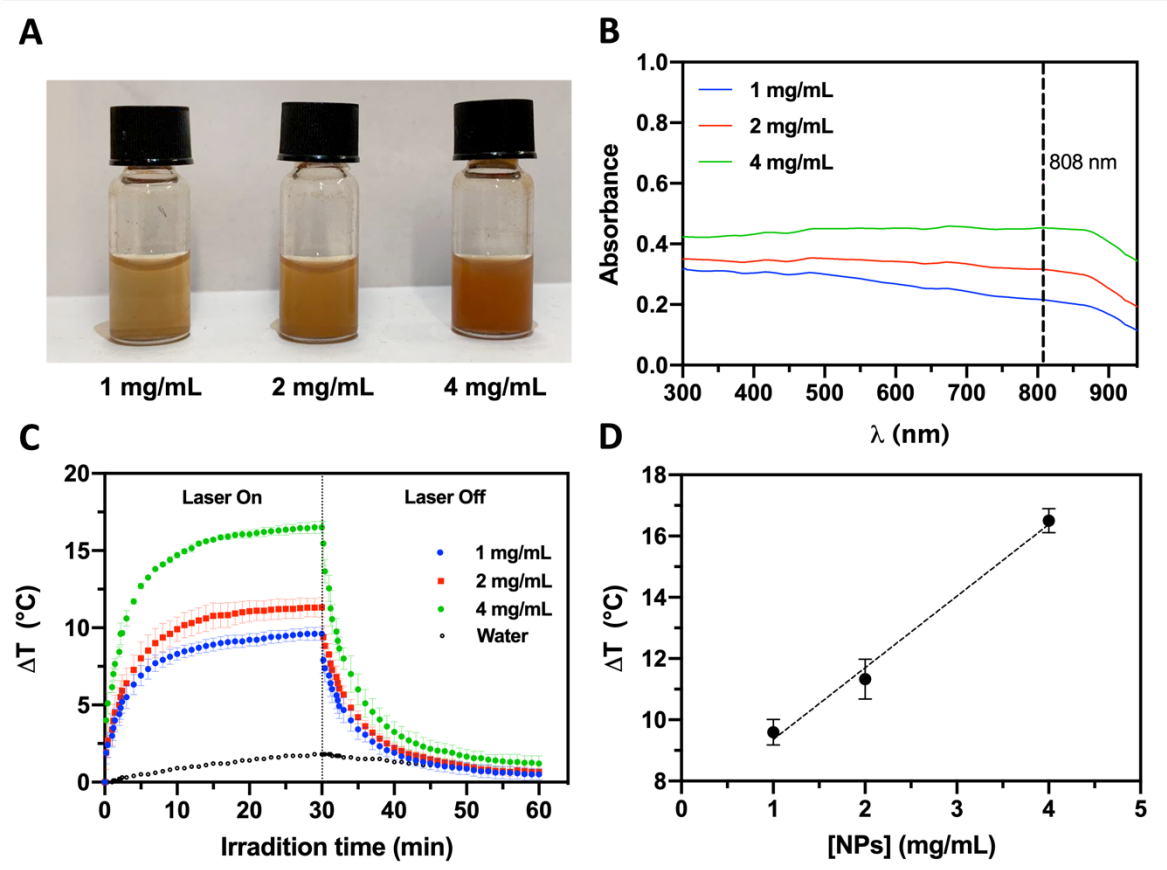


Figure 4.9 (A) Representative image of aqueous suspensions of the different $Ca_{0.25}Mg_{0.75}Fe_2O_4$ concentrations and (B) their corresponding UV/Visible absorption spectra. (C) Heating and cooling profiles of the tested samples during laser irradiation (808 nm, 1 W/cm^2). (D) Correlation between the photothermal capacity and NPs concentration.

A simple home-made setup (detailed information is presented in **section 4.2.3.1**) was used for the photothermal conversion measurements. Each sample was irradiated for 30 minutes with an 808 nm-diode laser (laser On) followed by 30 minutes of cooling (laser Off), and the temperature was monitored. The heating abilities of different $Ca_{0.25}Mg_{0.75}Fe_2O_4$ concentrations and water under NIR irradiation is summarized in **Figure 4.9 C**. All the investigated suspensions registered a temperature increase until reaching a plateau at, approximately, 10 min. The maximum temperature variation was more significant for higher concentrations of magnetic NPs, with increases of 9.6±0.4 °C (1 mg/mL), 11.34±0.6 °C (2 mg/mL) and 16.5±0.4 °C (4 mg/mL) being recorded, while the temperature of the deionized water only increased by 1.8 °C at the same conditions. The NPs can still convert light into heat at a concentration of 4 mg/mL. It is concluded that, at this concentration, the phenomenon of temperature saturation, which has been reported for high concentrations, is not yet verified. The cooling

curves revealed, in turn, an abrupt drop in temperature that stabilized at temperatures close to the initial temperature after 10 min of turning off the laser. Furthermore, **Figure 4.9 D** shows a roughly linear dependency on concentration of the photothermal capacity in the used range of concentrations. Future assays should include measuring heat generation with different applied laser power at the concentrations studied here and their photothermal stability for at least five on/off cycles.

4.2.4.2. Effects of increased magnetic nanoparticles inclusion on the properties of magnetoliposomes

The functionality of lipid vesicles is highly dependent on the lipid formulation, which, in turn, influences the magnetoliposomes physicochemical, structural, and stability properties in physiologically and therapeutically relevant environments [39-42]. On the other hand, magnetic NPs are the centrepiece of magnetoliposomes, whose increased functionality depends not only on their performance but also on the effect of their distribution within magnetoliposomes, their interactions with membranes, and changes in their response resulting from those interactions [43-45]. Therefore, it is crucial to evaluate and optimize the properties of magnetic NPs and their inclusion in magnetoliposomes to obtain better functionalities. This section assesses the improvement of increased NPs concentration encapsulation in magnetoliposomes to establish the optimal NPs/lipid ratio.

First, the inclusion of NPs was optimized to the previously proposed method, following the described in **section 4.2.3.3**. **Figure 4.10 A** presents a representative image of SMLs' samples based on a fixed concentration of lipid formulation (1 mM of DPPC/DSPC/CHEMS/DSPE-PEG (60:20:15:5)) for a varying initial weight of magnetic NPs (1, 2 and 4 mg). Compared to aqueous suspensions of $Ca_{0.25}Mg_{0.75}Fe_2O_4$ NPs, the SMLs had a milky appearance due to the presence of the lipid. In addition, their magnetic behaviour was evaluated by the VSM technique, and **Figure 4.10 B** represents the average field-dependent magnetization per mass of each condition. In chapter 3, **section 3.4.4**, the magnetic properties of these magnetic NPs were detailed; these revealed good magnetic properties with a saturation magnetization of 50.07 emu/g. The magnetization hysteresis loop of the dried SML samples indicates a superparamagnetic nature. However, as expected, there was a significant reduction in the M_s of the samples (summarized in **Table 4.4**) when incorporating the NPs into the core of the SMLs. For instance, García-Jimeno *et al.* [46] reported Fe_3O_4 NPs with a M_s of 96.43 emu/g, which, after encapsulation in liposomes, was reduced to 0.025 emu/g. Similar behaviour was reported by Guo *et al.* [47] for methotrexate (MTX) modified thermo-sensitive magnetoliposomes (MTX-MagTSLs).

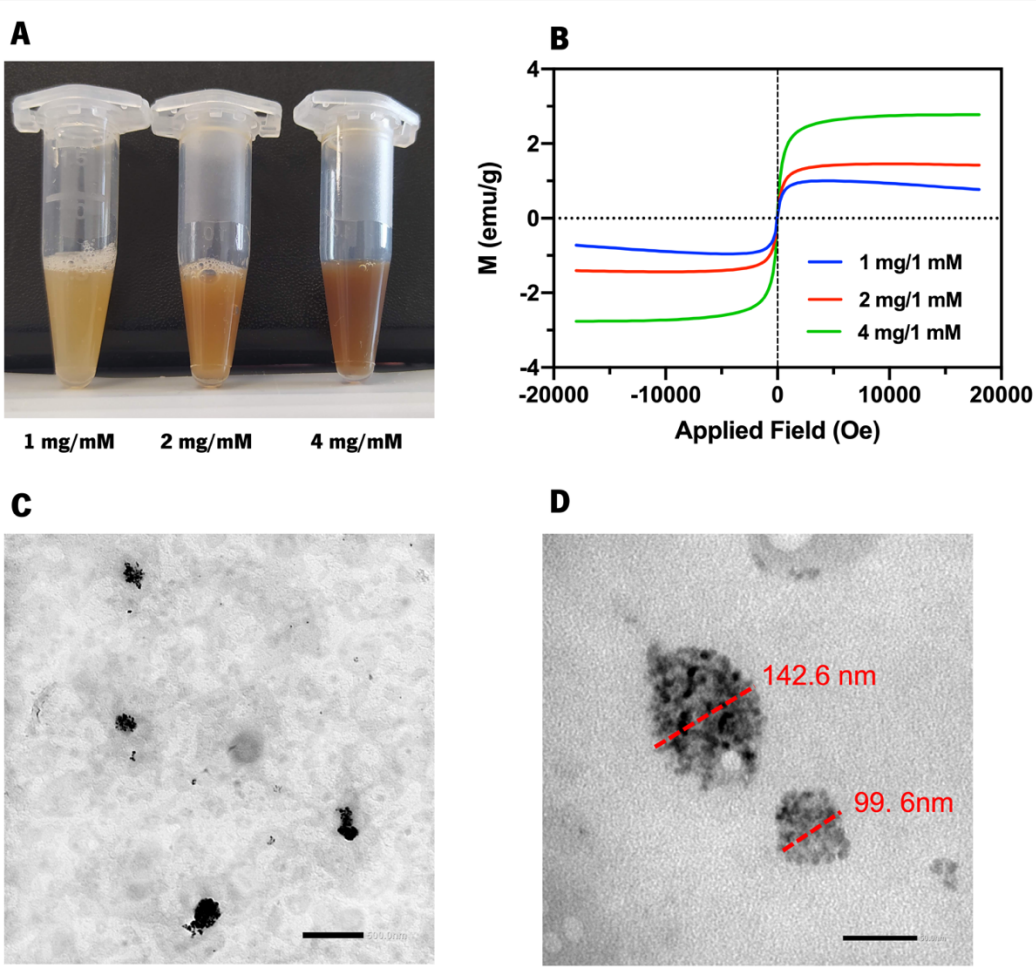


Figure 4.10 (A) Representative image of aqueous dispersions of SMLs based on DPPC/DSPC/CHEMS/DSPE-PEG (1 mM) containing 1, 2 and 4 mg of magnetic NPs and (B) VSM measurements for dried samples of corresponding SMLs. (C) TEM image of several SMLs with the initial NPs/lipid formulation ratio of 2 mg/1 mM (scale bar: 500 nm; mean diameter of 146.07 ± 10 nm) and (D) TEM image of SMLs with the initial NPs/lipid formulation ratio of 2 mg/1 mM (scale bar: 100 nm).

Figure 4.10 C exhibits the TEM image of several SMLs with the initial NPs/lipid formulation ratio of 2 mg/1 mM. Even though the SMLs have not been stained, there is a high contrast corresponding to the presence of NPs, that allowed to estimate the mean diameter of the nanosystems. ImageJ software for image processing was used for that, which determined an average size of 146.07±10 nm. The same procedure was performed for **Figure 4.10 D**. The image shows an SML with a similar size to those in **Figure 4.10 C**, revealing a size of 142.6 nm, and a slightly smaller one with diameter of 99.6 nm. These assays were complemented with the DLS studies of mean size and PDI variations accordingly to the several initial NPs/lipid formulation ratios. **Table 4.4** summarizes the obtained results. A gradual

decrease in the SMLs' average size was found with increased initial inserted NPs. It should be noted that the average size values estimated by TEM images (for SMLs with the initial NPs/lipid formulation ratio of 2 mg/1 mM) are in line with those obtained by DLS. The magnetoliposomes with lower initial NPs/lipid ratio (1 mg/1 mM) demonstrated a higher PDI of 0.23. Although, all samples revealed PDI values lower than 0.3, as required in the biomedical application of drug delivery systems. To relate the obtained VSM data with the ratio of encapsulated magnetic NPs, the masses of both the lipid formulation and the encapsulated magnetic NPs were quantified (following **section 4.2.3.5** and **4.2.3.6)** are summarized in **Table 4.4**. It should be noted that the given values were quantified with the samples used in the VSM measurements.

Table 4.4 M_s, D_H, PDI, encapsulated NPs (with the corresponding percentage of NPs encapsulation efficiency below), lipid with encapsulated NPs (with the corresponding percentage of lipids encapsulation efficiency below) and the final obtained NPs/lipid formulation ratio of SMLs samples starting from different initial NPs/lipid ratios.

Initial NPs/lipid	M_s (emu/g)	D_H (nm)	PDI	Encapsulated NPs (mg)	Lipid w/ NPs (mM)	Final NP/lipid ratio
1 mg/1 mM	0.9±0.0(2)	159±3	0.23±0.0(1)	0.41±0.0(7) (43.5±7%)	0.47±0.0(5) (47.1±5%)	≈ 0.87
2 mg/1 mM	1.4±0.(1)	143±4	0.17±0.0(3)	1.23±0.(1) (61.4±1%)	0.52±0.0(5) (51.8±5%)	≈ 2.36
4 mg/1 mM	2.7±0.(3)	135±1	0.20±0.0(2)	1.75±0.(1) (71.5±1%)	0.54±0.0(1) (54.0±1%)	≈ 3.24

It is found that the amount of encapsulated NPs increased with increasing initial NPs/lipid formulation ratio. However, a linear relationship was not found between the increase of lipids and the increase of encapsulated NPs. In fact, the percentage of lipids with encapsulated NPs increased from 47% to 54%, while the rate of encapsulation of NPs augmented from 43.5% to 71.5%. These results seem to point out that the degree of encapsulation of NPs is more dependent on the conditions of the NPs, which although having reduced size (20.8±5.3 nm), tend to form larger clusters that inhibit the entry in the core of liposomes. These clusters of NPs, in turn, are lost in the two steps stipulated for the removal of by-products of the synthesis of SMLs. In conclusion, the sample that appears to present more NPs per core

of SMLs is the formulation that starts from the initial encapsulation of 2 mg of NPs in 1 mM of lipid formulation.

4.2.5. Conclusions

This sub-chapter evaluated the ability of $Ca_{0.25}Mg_{0.75}Fe_2O_4$ NPs to mediate the magnetic and thermal-responsiveness stimuli for which the SMLs were optimized. Although it is focused on the conversion of light into thermal energy, in the future, the conversion of AMF into thermal heat will be comprehensively studied. Thus, it is intended to highlight the ability of these NPs to combine magnetic hyperthermia and photothermal therapy in an "all-in-one" nanoparticle, which may be an asset as a dual therapy in the treatment of cancer.

The NIR-derived heating performance of aqueous suspensions with 1, 2 and 4 mg/mL of NPs registered maximum temperature variations of 9.6±0.4 °C, 11.34±0.6 °C and 16.5±0.4 °C, respectively, after approximately 10 minutes of irradiation with an 808 nm laser diode. It was also concluded that at a concentration of 4 mg/mL, the suspensions have not yet reached the phenomenon of temperature saturation. Including these concentration of NPs in a fixed concentration of 1 mM DPPC/DSPC/CHEMS/DSPE-PEG resulted in the synthesis of SMLs with a superparamagnetic behaviour, however, with a significant reduction in the M_s of the samples. In addition, a gradual decrease in the SMLs' average size was found with increased initial inserted NPs. The NPs and lipids quantification revealed that the amount of encapsulated NPs increased non-linearly with the increase in the initial NPs/lipid ratio. This points to a dependence on the aggregation conditions of NPs when synthesizing SMLs. Furthermore, the 2 mg/1 mM (NPs/lipid) sample was the one that revealed more NPs per SMLs, with a final NP/lipid ratio of 2.36, indicating more significant potential for the work to progress. In turn, the TEM images of this type of system (2 mg/1 mM) revealed an average size of 146.07±10 nm, which was in line with the value of 143±4 obtained by DLS.

Concluding, the comprehensive evaluation of this work with the previous one allowed taking a significant step in the development and optimization of SMLs. Future work should follow to increase the stability of NPs and evaluate the effect of the degree of stability on the percentage of encapsulated NPs. The magnetoliposome synthesis protocol could also be modified so that the research and development of SMLs are based on a principle of continuous improvements.

4.2.6. References

1. Brace, C. Thermal tumor ablation in clinical use. *IEEE pulse* **2011**, *2*, 28-38.
2. McDaniel, J.R.; Dewhirst, M.W.; Chilkoti, A. Actively targeting solid tumours with thermoresponsive drug delivery systems that respond to mild hyperthermia. *International Journal of Hyperthermia* **2013**, *29*, 501-510.
3. Harmon, B.; Takano, Y.; Winterford, C.; Gobe, G. The role of apoptosis in the response of cells and tumours to mild hyperthermia. *International journal of radiation biology* **1991**, *59*, 489-501.
4. Armour, E.P.; McEachern, D.; Wang, Z.; Corry, P.M.; Martinez, A. Sensitivity of human cells to mild hyperthermia. *Cancer research* **1993**, *53*, 2740-2744.
5. Stathis, A.; Moore, M.J. Advanced pancreatic carcinoma: current treatment and future challenges. *Nature reviews Clinical oncology* **2010**, *7*, 163-172.
6. Brus, C.; Saif, M.W. Second line therapy for advanced pancreatic adenocarcinoma: where are we and where are we going? *JOP. Journal of the Pancreas* **2010**, *11*, 321-323.
7. Shetake, N.G.; Balla, M.M.; Kumar, A.; Pandey, B.N. Magnetic hyperthermia therapy: An emerging modality of cancer treatment in combination with radiotherapy. *Journal of Radiation and Cancer Research* **2016**, *7*, 13.
8. Freeman, M.; Arrott, A.; Watson, J. Magnetism in medicine. *Journal of Applied Physics* **1960**, *31*, S404-S405.
9. Deatsch, A.E.; Evans, B.A. Heating efficiency in magnetic nanoparticle hyperthermia. *Journal of Magnetism and Magnetic Materials* **2014**, *354*, 163-172.
10. Kaur, P.; Aliru, M.L.; Chadha, A.S.; Asea, A.; Krishnan, S. Hyperthermia using nanoparticles–promises and pitfalls. *International Journal of Hyperthermia* **2016**, *32*, 76-88.
11. Enwemeka, C.S. Intricacies of dose in laser phototherapy for tissue repair and pain relief. *Photomedicine and Laser Surgery* **2009**, *27*, 387-393.
12. Pérez-Juste, J.; Pastoriza-Santos, I.; Liz-Marzán, L.M.; Mulvaney, P. Gold nanorods: synthesis, characterization and applications. *Coordination chemistry reviews* **2005**, *249*, 1870-1901.
13. Chen, H.; Shao, L.; Li, Q.; Wang, J. Gold nanorods and their plasmonic properties. *Chemical Society Reviews* **2013**, *42*, 2679-2724.
14. Yu, Y.-Y.; Chang, S.-S.; Lee, C.-L.; Wang, C.C. Gold nanorods: electrochemical synthesis and optical properties. *The Journal of Physical Chemistry B* **1997**, *101*, 6661-6664.
15. Ye, J.; Wen, Q.; Wu, Y.; Fu, Q.; Zhang, X.; Wang, J.; Gao, S.; Song, J. Plasmonic anisotropic gold nanorods: Preparation and biomedical applications. *Nano Research* **2022**, 1-28.

16. Averitt, R.D.; Westcott, S.L.; Halas, N.J. Linear optical properties of gold nanoshells. *JOSA B* **1999**, *16*, 1824-1832.

17. Huang, X.; Jain, P.K.; El-Sayed, I.H.; El-Sayed, M.A. Plasmonic photothermal therapy (PPTT) using gold nanoparticles. *Lasers in medical science* **2008**, *23*, 217-228.

18. Kim, J.; Park, S.; Lee, J.E.; Jin, S.M.; Lee, J.H.; Lee, I.S.; Yang, I.; Kim, J.S.; Kim, S.K.; Cho, M.H. Designed fabrication of multifunctional magnetic gold nanoshells and their application to magnetic resonance imaging and photothermal therapy. *Angewandte Chemie* **2006**, *118*, 7918-7922.

19. Chen, J.; Glaus, C.; Laforest, R.; Zhang, Q.; Yang, M.; Gidding, M.; Welch, M.J.; Xia, Y. Gold nanocages as photothermal transducers for cancer treatment. *Small* **2010**, *6*, 811-817.

20. Skrabalak, S.E.; Chen, J.; Au, L.; Lu, X.; Li, X.; Xia, Y. Gold nanocages for biomedical applications. *Advanced Materials* **2007**, *19*, 3177-3184.

21. Song, C.; Li, F.; Guo, X.; Chen, W.; Dong, C.; Zhang, J.; Zhang, J.; Wang, L. Gold nanostars for cancer cell-targeted SERS-imaging and NIR light-triggered plasmonic photothermal therapy (PPTT) in the first and second biological windows. *Journal of Materials Chemistry B* **2019**, *7*, 2001-2008.

22. Liu, Y.; Ashton, J.R.; Moding, E.J.; Yuan, H.; Register, J.K.; Fales, A.M.; Choi, J.; Whitley, M.J.; Zhao, X.; Qi, Y. A plasmonic gold nanostar theranostic probe for in vivo tumor imaging and photothermal therapy. *Theranostics* **2015**, *5*, 946.

23. Arami, H.; Kananian, S.; Khalifehzadeh, L.; Patel, C.B.; Chang, E.; Tanabe, Y.; Zeng, Y.; Madsen, S.J.; Mandella, M.J.; Natarajan, A. Remotely controlled near-infrared-triggered photothermal treatment of brain tumours in freely behaving mice using gold nanostar s. *Nature nanotechnology* **2022**, *17*, 1015-1022.

24. Zhu, Y.; Sun, Q.; Liu, Y.; Ma, T.; Su, L.; Liu, S.; Shi, X.; Han, D.; Liang, F. Decorating gold nanostars with multiwalled carbon nanotubes for photothermal therapy. *Royal Society open science* **2018**, *5*, 180159.

25. Liu, Y.; Zhang, X.; Luo, L.; Li, L.; Zhu, R.Y.; Li, A.; He, Y.; Cao, W.; Niu, K.; Liu, H. Gold-nanobranched-shell based drug vehicles with ultrahigh photothermal efficiency for chemo-photothermal therapy. *Nanomedicine: Nanotechnology, Biology and Medicine* **2019**, *18*, 303-314.

26. Huang, P.; Rong, P.; Lin, J.; Li, W.; Yan, X.; Zhang, M.G.; Nie, L.; Niu, G.; Lu, J.; Wang, W. Triphase interface synthesis of plasmonic gold bellflowers as near-infrared light mediated acoustic and thermal theranostics. *Journal of the American Chemical Society* **2014**, *136*, 8307-8313.

27. Chen, M.; Tang, S.; Guo, Z.; Wang, X.; Mo, S.; Huang, X.; Liu, G.; Zheng, N. Core–Shell Pd@ Au nanoplates as theranostic agents for in-vivo photoacoustic imaging, CT imaging, and photothermal therapy. *Advanced Materials* **2014**, *26*, 8210-8216.

28. Koo, C.; Hong, H.; Im, P.W.; Kim, H.; Lee, C.; Jin, X.; Yan, B.; Lee, W.; Im, H.-J.; Paek, S.H. Magnetic and near-infrared derived heating characteristics of dimercaptosuccinic acid coated uniform Fe@ Fe3O4 core–shell nanoparticles. *Nano convergence* **2020**, *7*, 1-9.

29. Wang, S.; Hou, Y. Photothermal therapy based on magnetic nanoparticles in cancer. *Journal of Applied Physics* **2021**, *130*, 070902.

30. Shivanna, A.T.; Dash, B.S.; Chen, J.-P. Functionalized Magnetic Nanoparticles for Alternating Magnetic Field-or Near Infrared Light-Induced Cancer Therapies. *Micromachines* **2022**, *13*, 1279.

31. Liu, Y.; Bhattarai, P.; Dai, Z.; Chen, X. Photothermal therapy and photoacoustic imaging via nanotheranostics in fighting cancer. *Chemical Society Reviews* **2019**, *48*, 2053-2108.

32. Xu, C.; Pu, K. Second near-infrared photothermal materials for combinational nanotheranostics. *Chemical Society Reviews* **2021**, *50*, 1111-1137.

33. Jordan, A.; Scholz, R.; Maier-Hauff, K.; Johannsen, M.; Wust, P.; Nadobny, J.; Schirra, H.; Schmidt, H.; Deger, S.; Loening, S. Presentation of a new magnetic field therapy system for the treatment of human solid tumors with magnetic fluid hyperthermia. *Journal of Magnetism and Magnetic Materials* **2001**, *225*, 118-126.

34. Thiesen, B.; Jordan, A. Clinical applications of magnetic nanoparticles for hyperthermia. *International Journal of Hyperthermia* **2008**, *24*, 467-474.

35. Dennis, C.; Jackson, A.; Borchers, J.; Ivkov, R.; Foreman, A.; Hoopes, P.; Strawbridge, R.; Pierce, Z.; Goerntiz, E.; Lau, J. The influence of magnetic and physiological behaviour on the effectiveness of iron oxide nanoparticles for hyperthermia. *Journal of Physics D: Applied Physics* **2008**, *41*, 134020.

36. Stewart, J.C.M. Colorimetric determination of phospholipids with ammonium ferrothiocyanate. *Analytical biochemistry* **1980**, *104*, 10-14.

37. Torras, M.; Moya, C.; Pasquevich, G.A.; Roig, A. Accurate iron quantification in colloids and nanocomposites by a simple UV-Vis protocol. *Microchimica Acta* **2020**, *187*, 1-10.

38. Weissleder, R. A clearer vision for in vivo imaging. *Nature biotechnology* **2001**, *19*, 316-317.

39. Dos Santos, S.C.; Silva, N.O.; Junior, J.B.d.S.E.; Marinho, M.A.G.; Borges, Z.V.; Branco, N.B.C.; Faita, F.L.; Soares, B.M.; Horn, A.P.; Parize, A.L. Molecular interactions and physico-chemical characterization of quercetin-loaded magnetoliposomes. *Chemistry and Physics of Lipids* **2019**, *218*, 22-33.

40. Skouras, A.; Papadia, K.; Mourtas, S.; Klepetsanis, P.; Antimisiaris, S.G. Multifunctional doxorubicin-loaded magnetoliposomes with active and magnetic targeting properties. *European journal of pharmaceutical sciences* **2018**, *123*, 162-172.

41. Skouras, A.; Mourtas, S.; Markoutsa, E.; De Goltstein, M.-C.; Wallon, C.; Catoen, S.; Antimisiaris, S.G. Magnetoliposomes with high USPIO entrapping efficiency, stability and magnetic properties. *Nanomedicine: Nanotechnology, Biology and Medicine* **2011**, *7*, 572-579.

42. Lopes, F.A.; Fernandes, A.V.; Rodrigues, J.M.; Queiroz, M.-J.R.; Almeida, B.G.; Pires, A.; Pereira, A.M.; Araújo, J.P.; Castanheira, E.M.; Rodrigues, A.R.O. Magnetoliposomes containing multicore nanoparticles and a new antitumor thienopyridine compound with potential application in chemo/thermotherapy. *Biomedicines* **2022**, *10*, 1547.

43. Nuñez-Magos, L.; Lira-Escobedo, J.; Rodríguez-López, R.; Muñoz-Navia, M.; Castillo-Rivera, F.; Viveros-Méndez, P.X.; Araujo, E.; Encinas, A.; Saucedo-Anaya, S.A.; Aranda-Espinoza, S. Effects of DC Magnetic Fields on Magnetoliposomes. *Frontiers in molecular biosciences* **2021**, *8*.

44. Fortes Brollo, M.E.; Patricia, H.-F.; Gutiérrez, L.; Johansson, C.; Barber, D.F.; Morales, M. Effect of magnetic nanoparticles aggregation and spatial distribution on the magnetic behaviour of liposomes and cells. **2019**.

45. Shaghasemi, B.S.; Virk, M.M.; Reimhult, E. Optimization of Magneto-thermally Controlled Release Kinetics by Tuning of Magnetoliposome Composition and Structure (vol 7, 2017). *Scientific reports* **2018**, *8*.

46. García-Jimeno, S.; Escribano, E.; Queralt, J.; Estelrich, J. Magnetoliposomes prepared by reverse-phase followed by sequential extrusion: Characterization and possibilities in the treatment of inflammation. *International journal of pharmaceutics* **2011**, *405*, 181-187.

47. Guo, Y.; Zhang, Y.; Ma, J.; Li, Q.; Li, Y.; Zhou, X.; Zhao, D.; Song, H.; Chen, Q.; Zhu, X. Light/magnetic hyperthermia triggered drug released from multi-functional thermo-sensitive magnetoliposomes for precise cancer synergetic theranostics. *Journal of controlled release* **2018**, *272*, 145-158.

CHAPTER 5

In vitro evaluation of doxorubicin-loaded magnetoliposomes efficacy on breast cancer therapeutics

This chapter describes the preliminary evaluation of doxorubicin-loaded solid magnetoliposomes' action on breast cancer therapeutics and the variable effects according to the cellular organisation of the cancer cells. Furthermore, it explores the design, fabrication and optimisation of microfluidic platforms for breast cancer spheroids inclusion and retention in a microfluidic cell culture chamber.

5.1. Overview

Breast cancer comprises a set of diseases with high genetic and epigenetic heterogeneity [1]. However, the activity of new anticancer drugs or delivery strategies is generally evaluated in 2D cultured cell lines that present limitations in the representation of structural properties, drug transport and heterogeneity. Thus, the potential of 3D cultured cell lines has been pointed out to best mimic the *in vivo* tumour microenvironment and its limited nutrients and drug penetration availability. However, these structures also do not allow evaluation of the multiple transport processes of *in vivo* intravenously injected chemotherapeutic drugs, from drug transport in the circulation to temporal and spatial intratumorally transport. Thus, this work begins by evaluating the differential effects of DOX and DOX-loaded SMLs between *in vitro* 2D and 3D cultures. For that, Sk-br-3 breast cancer cell culture was established in 4 different cell organisational levels: (i) conventional 2D adherent cell culture; (ii) 1-week dense spheroids plated on conventional adherent cell culture plates (pseudo-3D); (iii) newly formed spheroids plated on non-adherent cell culture plates and (iv) 1-week dense spheroids plated on non-adherent cell culture plates. The assays revealed significantly different structural organisations and treatment responses. Nevertheless, the overall results indicate a greater ability of SMLs to incorporate and release DOX into cells. Finally, microfluidic platforms were designed and fabricated based on the microenvironment gradient as a proof-of-concept. These platforms allow the control of the fluid flow direction and real-time visualisation of the processes inside it. Thus, they allow monitoring and directing Sk-br-3 breast cancer spheroids from a microfluidic channel towards a microfluidic cell culture chamber (perpendicular to the microfluidic channel) and their retention in the latter by pillars with appropriate shape, arrangement and dimensions. This proof-of-concept is the beginning of establishing microfluidic platform designs for drug screening to comprehensively study drug diffusion, binding, and apoptotic effects in a more biomimetic context.

5.2. Introduction

According to the American Cancer Society, breast cancer represents 1 in 3 of all new female cancers each year, and the incidence rate has been growing by 0.5% per year in recent years [2]. Although breast cancer is the second leading cause of cancer death in women, the death rate dropped by 43% between 1989 and 2020 [2]. The 5-year survival rate of breast cancer is high (90.3%) in all subtypes and stages; however, in metastatic breast cancer, this value drops to 29%, reaching 12% in metastatic triple-negative breast cancer [3]. Chemotherapy is routinely used in treating all breast cancer subtypes, both early-stage

breast cancer and metastatic or advanced breast cancer. Nevertheless, this type of treatment is associated with the acquisition of chemoresistance, which is the primary cause of tumour recurrence and, consequently, the death of patients [4]. Furthermore, much of the knowledge generated on breast cancer results from *in vitro* models using 2D conventional methods. In addition, breast cancer cell lines represent limited breast cancer heterogeneity and molecular features [5]. These challenges encourage the development of new therapeutic strategies as well as the development of new models for accurate and effective drug screening.

Tumour growth happens exponentially; since cancer cells lose their "contact inhibition" property, they continue to grow beyond the blood vessels [6-10]. However, this distancing of the vessels induces the formation of nutrients and oxygen gradients in the tumour, where the deficient cells enter a quiescence state to survive in this environment of deprivation [11,12]. Thus, proliferating cells are located closer to blood vessels while, when gradually moving away from them, cells become quiescent, apoptotic, and, at last, necrotic (**Figure 5.1**) [13]. Furthermore, the presence of heterogeneous subpopulations of cells with distinct molecular signatures implies erratic behaviours and sensitivities among the cancer cells [14]. For instance, since quiescent cells are nonproliferating and chemotherapy drugs act preferentially on proliferating cells, treatments assume reduced efficacy [15-17]. For these reasons, the vasculature of tumours is essential for tumour development, which is why tumours with diameters greater than 1-2 mm become angiogenic [18]. Those new blood vessels in solid tumours are a disorganised mixture of vessels with a structure, organisation, and function differently from the vasculature of normal tissues. It features a serpentine and broader supply structure, which alters its surface area to volume ratio, impairing tissue nutrition [19,20]. Likewise, this effect extends to the limited effectiveness of chemotherapy since the vasculature comprises the delivery and accumulation of chemotherapeutic drugs in solid tumours [21,22].

The effectiveness of intravenously injected chemotherapeutic drugs is dependent on multiple processes: (A) drug transport in the circulation, which includes distribution in the vasculature and effects of tumour microvascular structure and functions; (B) drug transport into tissues, which includes transport through microvessels walls and transport through extravascular space; and (C) mass transport-related mechanisms, which include convection and diffusion, transport across vessels walls and penetration of solutes into tissues (for detailed information see [23]). The complexity of drug delivery mechanisms and their dependent action on cell subpopulations hinder cancer therapy and an eventual cure. It also widens the differential gap of biochemical assays, animal models testing and *in vivo* responses. Furthermore,

the conventional monolayer cell culture approaches (the most well-established and commonly used method for cell culture) do not reflect any of those mechanisms nor the heterogeneity of tumours.

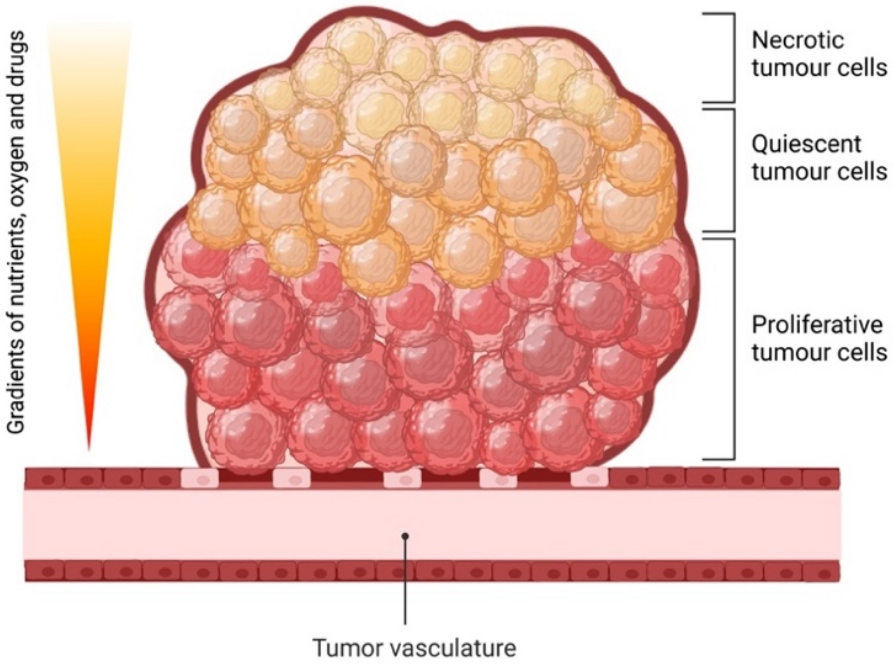


Figure 5.1 Schematic representation of the heterogeneity in solid tumours. The continuous outgrowth of cells leads to the formation of gradients (such as nutrients and oxygen) that induce the generation of tumour microenvironments. Proliferative tumour cells, which define the area closest to the tumour vasculature, receive the oxygen and nutrients needed to proliferate. Quiescent tumour cells represent a median region with viable but nonproliferating cells. In the area of greatest oxygen, nutrient deprivation and accumulation of toxic waste products, necrotic tumour cells are found.

This systematically distances drug research and development processes from products with a societal impact (for detailed information about the advantages and challenges of 2D cell culture methods, see **section 1.3.1.1**). 3D cell culture methods create an artificial environment in the three dimensions, which allows cells to grow and interact with each other and the surrounding space and, therefore, more accurately reproduce the *in vivo* spatiotemporal conditions [24,25]. Spheroids, 3D architectures of cancer cells, represent a better model for drug screening than monolayer culture counterparts (for detailed information about the advantages and challenges of 3D cell culture methods, see **section**

1.3.1.2) [26,27]. Furthermore, similar to *in vivo* tumours, they have limited nutrients and drug penetration availability, which is limited to diffusion through concentric cell layers [28].

Thus, this work used the Sk-br-3 breast cancer cell line as a model for breast cancer. To evaluate the preliminary effects of DOX-loaded SMLs on this cell line, as well as the variability of the cell response according to cell organisation, this cell line was cultured by 2D and 3D (spheroids) methods. These assays not only revealed variations in the cellular organisation of Sk-br-3 cancer cells, but also evidenced therapeutic effects (free DOX and DOX-loaded SMLs) that vary according to the complexity of the cellular architectures. Despite all the advantages of the spheroids model, its dense structure makes it challenging to observe the interior of spheroids, preventing real-time quantification of drug diffusion and binding processes to different layers of tumour tissue. Therefore, Walsh and colleagues [29] introduced the concept of microenvironment gradient, where a variable chemical environment is created according to the position of cells in the cell mass. The authors constrained cells in a microfluidic square chamber to force the formation of a perpendicular linear-gradient, allowing the exchange of nutrients, growth factors and wastes by diffusion.

Considering the advantages and limitations of the 2D and 3D cell culture methods and the concept of microenvironment gradient, this work designed microfluidic platforms for spheroids' inclusion and cell culture. These platforms were designed to physically, chemically and molecularly approximate the drug screening system to the physiological process of drug delivery of intravenously injected chemotherapeutic drugs (**Figure 5.2 A**). The structure of these platforms allows directing spheroids to a microfluidic cell culture chamber whose function is to enable the development of spheroids until the formation of a heterogeneous tumour tissue confined in defined borders. The heterogeneous tumour recreates a mimetic tumour environment and, due to the transparency and gas permeability of the PDMS material, allows the monitorisation of the mechanisms involved in drug delivery in real-time (**Figure 5.2 B**). The future optimisation of these microfluidic platforms will allow the establishment of the spheroids cell culture miniaturisation and its supplementation processes (both nutrition and the treatments to be studied). By bringing the screening assays of DOX-loaded SMLs closer to mimetic conditions, it will allow the reproduction of the mechanisms that reduce drug efficacy with greater accuracy and, if needed, go back into the magnetoliposomes development process to potentiate their therapeutic action.

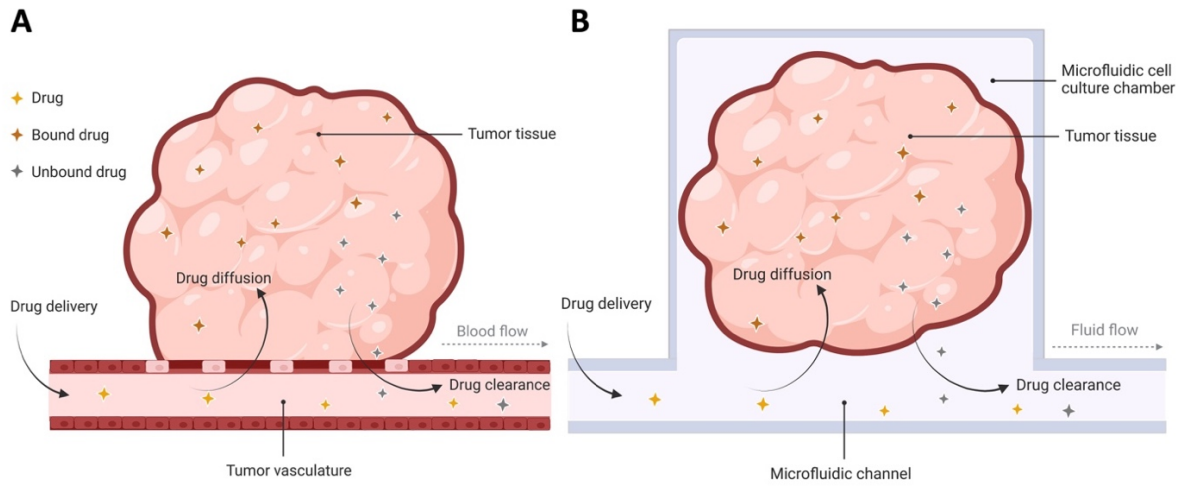


Figure 5.2 Schematic representation of (A) Drug delivery of intravenously injected chemotherapeutic drugs into a tumour tissue by diffusion, binding and drug clearance from tumour tissue; and (B) Simulation of the tumour environment and the respective mechanisms involved in drug delivery on a microfluidic platform, where the microfluidic channel represents the tumour vasculature, and the microfluidic chamber allows the development of mimetic tumour tissue.

5.3. *In vitro* preliminary evaluation of doxorubicin-loaded solid magnetoliposomes on different cell organisational levels

This subsection reports on the preliminary evaluation of DOX-loaded SMLs' action on breast cancer therapeutics and the variable effects according to the cellular organization of the cancer cells. As previously mentioned, it uses the Sk-br-3 cancer cell line, cultivated in different cell culture methods, to obtain four cell organizational levels. These include establishing Sk-br-3 breast cancer cell culture in conventional 2D adherent cell culture, 1-week dense spheroids plated on conventional adherent cell culture plates (pseudo-3D), newly formed spheroids plated on non-adherent cell culture plates and 1-week dense spheroids plated on non-adherent cell culture plates.

To better understand the action of DOX-loaded SMLs, their effects are compared to two controls (culture medium and DMSO), SMLs without DOX and free DOX (at the same concentration).

5.3.1. Materials and methods

5.3.1.1. Cell culture and spheroids formation

A human breast cancer cell line (Sk-br-3, ATCC) was cultivated in Dulbecco's Modified Eagle's Medium (DMEM, PAN Biotech) with 4.5 g/L containing 10% of fetal bovine serum (FBS, Biochrom) and 1% of penicillin/streptomycin (P/S, Biochrom). The cells were grown at 37 °C in humidified air containing 5% CO_2 atmosphere. When they reached approximately 80% confluence, the cells were trypsinised with Trypsin-EDTA (PAN Biotech). For the formation of Sk-br-3 breast cancer spheroids, Sk-br-3 cells were seeded at a density of 2.5×10^4 cells/mL per 25 cm^2 cell culture flasks with ultra-low attachment (Corning) and allowed to grow for 1 week.

5.3.1.2. 2D, pseudo-3D and 3D cell culture assays

Four different levels of the cellular organisations of Sk-br-3 breast cancer cell culture were established, namely: (i) conventional 2D adherent cell culture; (ii) 1-week dense spheroids plated on conventional adherent cell culture plates (pseudo-3D); (iii) newly formed spheroids plated on non-adherent cell culture plates and (iv) 1-week dense spheroids plated on non-adherent cell culture plates. To establish conventional 2D Sk-br-3 cell culture, cells were seeded at a density of 2.5×10^4 cells/mL in 12-well adherent cell culture plates. For pseudo-3D assays, 200 μL of the previously formed 1-week Sk-br-3 breast cancer spheroids were added to 300 μL of cell culture medium (same process as in the 2D cell culture, however it is not possible to precisely know the corresponding cell density) and seeded in 12-well adherent cell culture plates. The newly formed spheroids were prepared by seeding a density of 2.5×10^4 cells/mL in 12-well cell non-adherent cell culture plates. For the assays with 1-week spheroids, 200 μL of the previously formed 1-week Sk-br-3 breast cancer spheroids were added to 300 μL of cell culture medium and seeded in non-adherent cell culture plates. For each type of cell organisation, 5 treatment conditions were studied: control, DMSO (20%), SMLs (without DOX), 5 μM of DOX, and 5 μM DOX-loaded SMLs. SMLs and DOX-loaded SMLs were prepared as described in sections 4.1.3.1 and 4.2.3.2. However, for the SMLs, DOX was not added in their preparation, while for the DOX-loaded SMLs, a 5 μM ethanolic DOX solution was co-injected with the second lipid layer under vortexing.

5.3.1.3. Image acquisition, processing and analysis

Bright-field and fluorescence images were acquired in an inverted fluorescence microscope (Leica dmi 3000b). The fluorescence images were based on the intrinsic red fluorescence of DOX when excited with green light (λ_{exc} = 480 nm; λ_{em} = 590 nm). After incubation with the corresponding treatment condition (control, DMSO, SMLs, DOX and DOX-loaded SMLs), the images of all conditions were captured at 1h, 4h, 6h, 24h and 48h after the beginning of each treatment.

The acquired images of Sk-br-3 cells seeded on adherent plates (2D) were subjected to quantitative analysis. Only the cells that could be unequivocally identified with visible borders were manually circumvented and counted. For that, ImageJ software (http://imagej.nih.gov/ij/; provided in the public domain by the National Institutes of Health, Bethesda, MD, USA) was used. Several morphological parameters of the selected cells were collected, and the roundness parameter was chosen as a representative parameter for further statistical analysis. In turn, the images of the 3D cell cultured spheroids were converted into spatially related images through the interactive "3D Surface Plot" plug-in (Internationale Medieninformatik, Berlin, Germany) of ImageJ.

5.3.2. Statistical analysis

The statistical significance of treatment groups over time was tested by applying a two-way ANOVA. In addition, multiple pairwise comparisons with the control were performed using the Dunnett post-test (GraphPad Prism V 8.0; San Diego, CA, USA) to isolate significant differences between the control and different treatments. *p* values <0.05 were considered statistically significant. Values are reported as the mean ± standard deviation.

5.3.3. Results and discussion

5.3.3.1. Establishment of Sk-br-3 breast cancer cell culture on conventional adherent plates

To obtain two distinct levels of cellular organisation, cell culture of Sk-br-3 cancer cells on adherent plates was established starting from cells and 1-week dense Sk-br-3 spheroids. **Table 5.1** summarises the representative images of Sk-br-3 cancer cells seeded on conventional 2D cell culture plates.

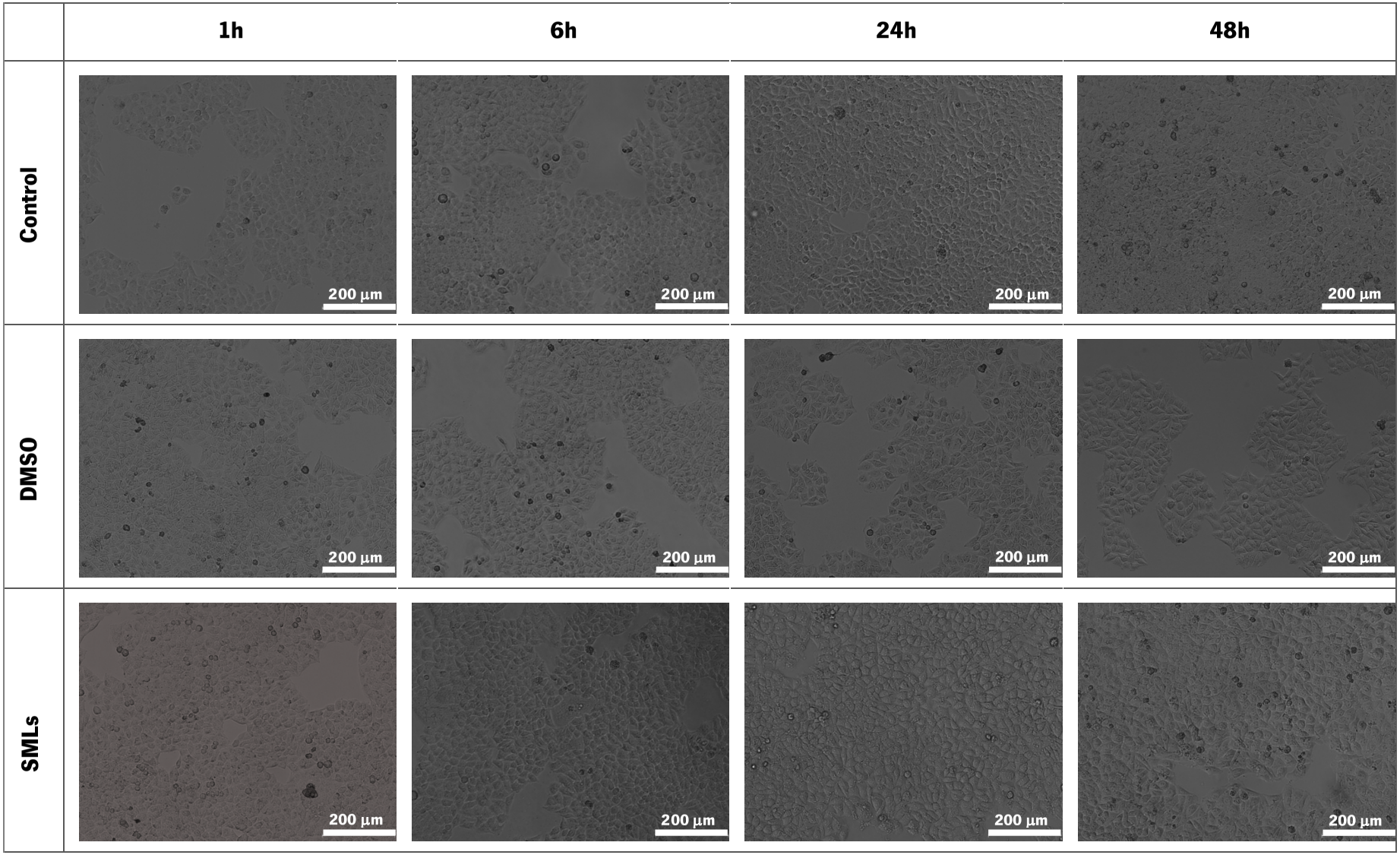
The control condition exhibits an increasing cell confluence over time, as expected. In turn, it was verified that SMLs (without DOX encapsulation) present a cell growth pattern analogous to the control condition,

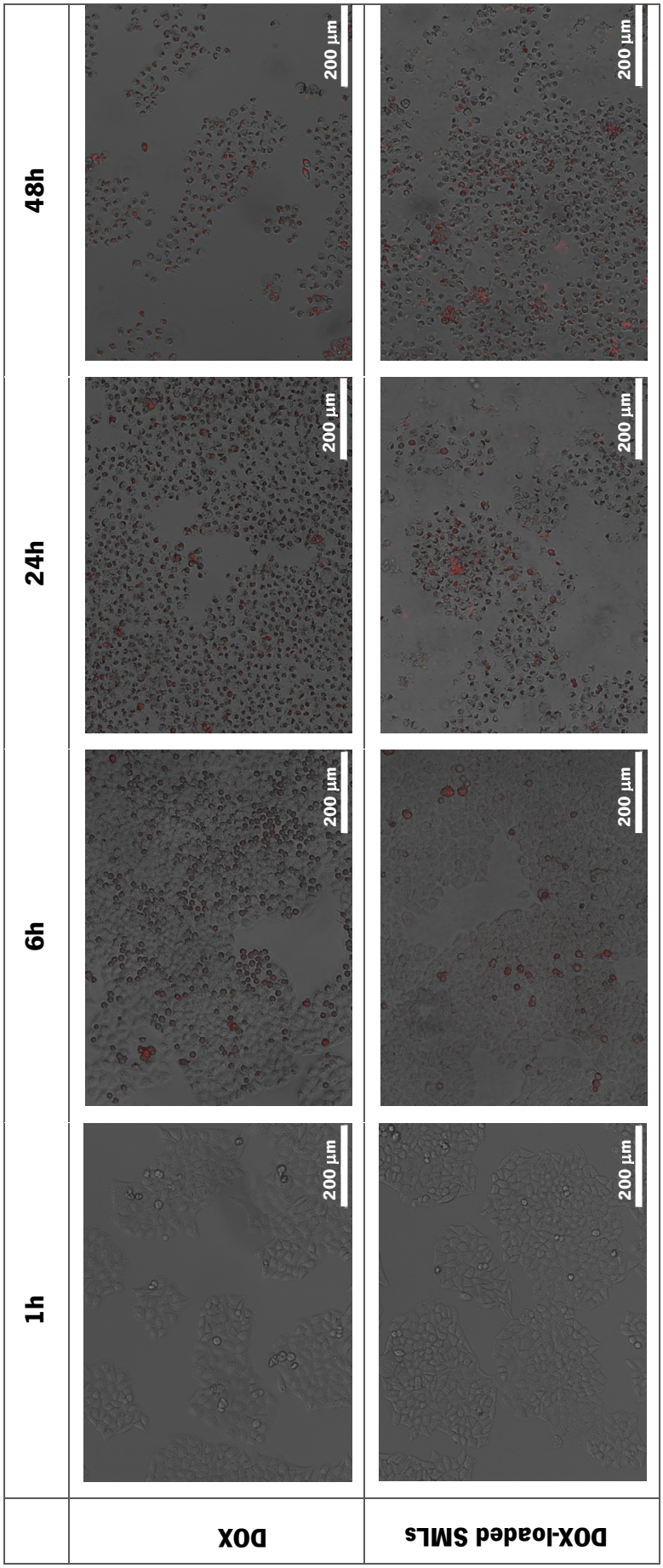
with an increased ratio of cells covering the adhesion surface over time. Although the DMSO control has not been shown to kill the cells, the gap between them and the lack of confluence evidence its effect in inhibiting cell replication. The merge of bright-field and fluorescence images is presented in the conditions of DOX and DOX-loaded SMLs treatments to access the DOX preferential accumulation. DOX fluorescence inside the cells only becomes evident from 6 h onwards. At 24 h, both drug treatment conditions showed pronounced cell death, which was maintained at 48 h. These assays are intended to evaluate the therapeutic kinetics and the morphological variation between the two organisational levels. However, they did not include cell staining or biochemical determination of apoptosis in real-time. Since cell size and shape indicate cell death [30-32], the cell roundness parameter was analanalysed2D cell culture microscopy images to correlate these variations.

Dunnett's multiple comparison tests (see Appedix C in **section C.1**, **Table C.1**) of cell roundness variation (relative to the control) showed that at 1 h, only the DOX-loaded SMLs condition was statistically significant, with a slight reduction in the roundness parameter (**Figure 5.3**). Similar behaviour is found at 6 h in the SMLs (without drug). These preliminary results indicate a possible internalisation or fusion of SMLs with cells. The difference between the control and the SMLs becomes more pronounced at 48 h, since the control condition significantly loses roundness, and the SMLs condition keeps roundness values similar to the initial ones. This may indicate that the internalisation of SMLs inhibits cell replication, although it does not induce cell death. At 6 h, there is a significant increase in roundness in the condition of free DOX. The corresponding image (**Table 5.1**) exhibits several prominent round cells. However, these cells may represent cell replication instead of cell death.

Although the roundness variation is not as significant in DOX-loaded SMLs (at 6 h), the corresponding image does not present as many round cells. This agrees with the results obtained for SMLs, reinforcing that the internalisation of SMLs (with or without DOX) negatively influences cell replication. At 24 h, both DOX and DOX-loaded SMLs reveal a roundness close to 1, demonstrating the detachment of cells from the surface and, therefore, their death. Finally, at 48 h, the slight decrease in roundness reveals the deformation of dead cells.

Table 5.1 Representative bright-field and fluorescence microscopy images (merged) of free DOX, SMLs and DOX-loaded SMLs on Sk-br-3 breast cancer cells cultured in adherent conventional 2D cell plates over 48h.




1h
6h
24h
48h
DOX
DOX-loaded SMLs
200 µm

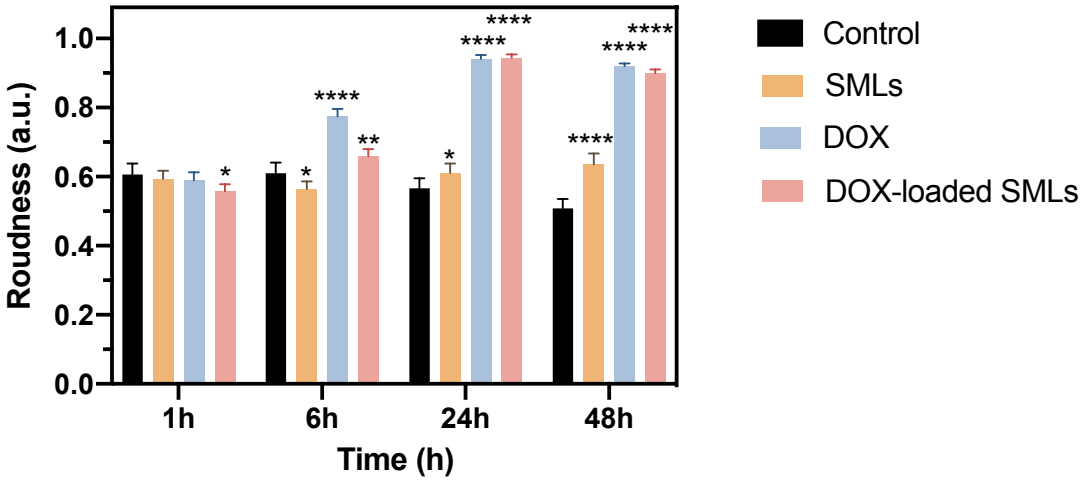


Figure 5.3 Roundness parameter variation of Sk-br-3 cells over 48 h when exposed to different treatment conditions. The histogram shows roundness mean values ± SD and the multiple comparisons with Dunnett's test. *$p < 0.05$; **$p < 0.01$; ***$p < 0.001$; ****$p < 0.0001$; by ANOVA followed by Dunnett's post-test.

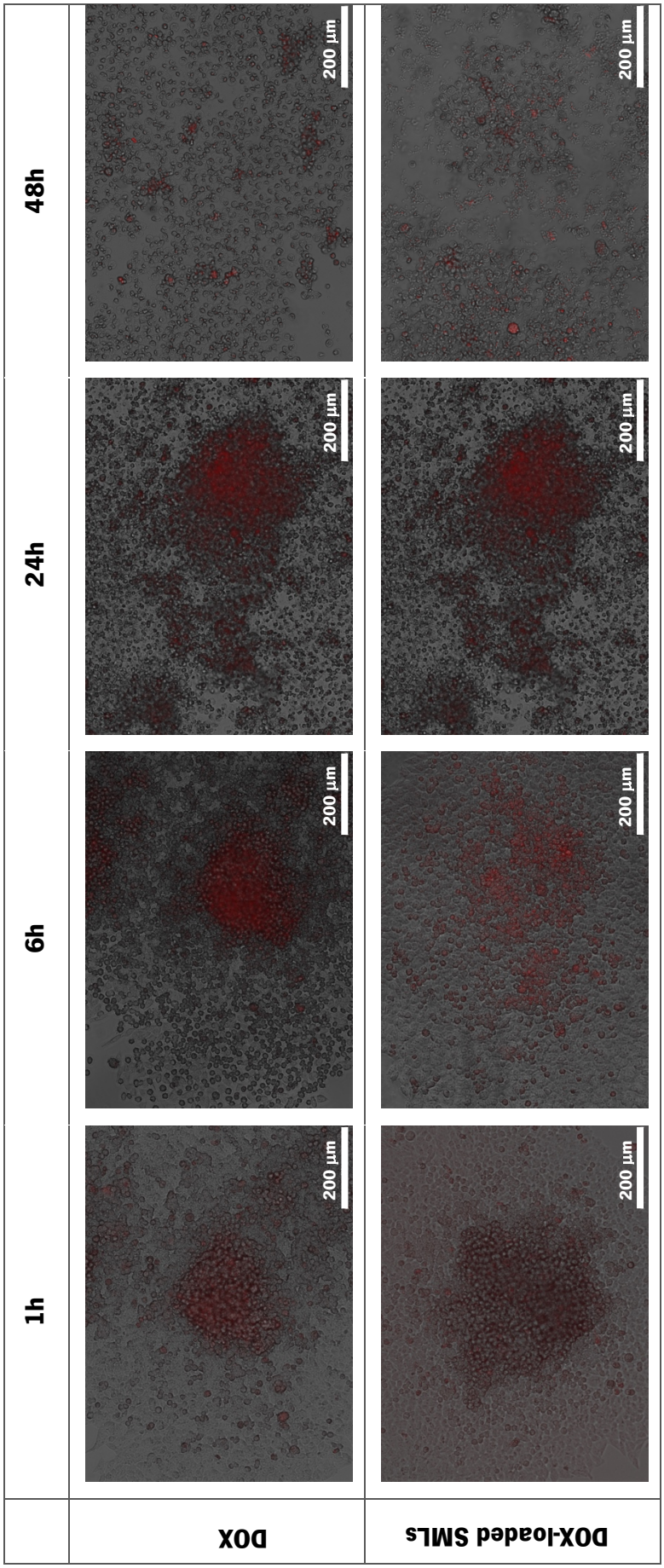
The 1-week dense spheroids seeded on conventional adherent cell culture plates is considered pseudo-3D, since this structure comprises two dimensions of cellular organisation. **Table 5.2** summarises the representative images of this condition under different treatments over time. When plating the spheroids in adherent cell culture plates, they spread their more superficial layer cells on the plate, forming a monolayer. The remaining spheroid, positioned above the monolayer, maintained its 3D structure during the 48 h of the assay, as shown in the control condition image. Furthermore, an increase in cell density over time is verified in monolayer cells and spheroids counterparts. Although dense spheroids provide relevant information in the representation of solid tumours, this technique is disadvantageous since it is impossible to control the size, density and number of formed spheroids. Thus, the density of the spheroids in each of the conditions is very variable; therefore, the comparison between the conditions must be careful. Contrary to the cell's monolayer, fluorescence was noted at 1 h with free DOX and DOX-loaded SMLs. These results may arise from the drug's greater ease of penetrating three-dimensionally organised cells, due to its larger available contact area or a higher cell density effect on these structures that amplifies the fluorescence signal.

Contrary to the previously described assay, at 24 h, it is still possible to distinguish some live cells in both treatment conditions. However, it is not possible to ensure whether these results are related to

differences in cell organisation or if they are cell number dependent. Nevertheless, the treatment with DOX-loaded SMLs shows a more significant number of dead cells at this point, which may indicate the earlier therapeutic activity of DOX when encapsulated in lipid systems. In turn, at 48 h, both treatments showed total cell death.

Overall, the results indicate a greater ability of SMLs to incorporate and release DOX into cells. This agrees with the functionality of the lipid formulation, based on DPPC/DSPC/CHEMS/DSPE-PEG (60:20:15:5), which gives SMLs fusogenic- and pH-sensitive capabilities.

Table 5.2 Representative bright-field and fluorescence microscopy images (merged) of free DOX, SMLs and DOX-loaded SMLs on 1-week dense Sk-br-3 breast cancer spheroids cultured on conventional adherent cell culture (pseudo-3D) plates over 48h.


DOX-loaded SMLs
DOX
1h
6h
24h
48h
200 µm

5.3.3.2. Establishment of Sk-br-3 breast cancer cell culture on non-adherent plates

The area and cell density of the formed spheroids are highly dependent on the time after cells seed on the non-adherent plates [33-35]. Thus, spheroids with different formation times were tested to assess the time influence on spheroids' behaviour, properties and therapeutic response.

The assays were performed with newly formed Sk-br-3 breast cancer spheroids (by seeding cells on non-adherent test plates) and 1-week dense Sk-br-3 breast cancer spheroids. Representative images of the treatment evolution are summarised in **Table 5.3** and **Table 5.4**.

One of the advantages of using newly formed spheroids is that, unlike 1-week dense spheroids, they allow starting from the same number of cells as the assays with cells seeded on conventional 2D cell culture plates. Although it is impossible to quantify the spheroids' cell density over time, it allows a qualitative approximation between both assays. Both spheroid types demonstrated similar behaviours between the corresponding treatment conditions (**Table 5.3**). Regarding the control, at 1 h, both show several small spheroids that, over time, tend to agglomerate (see 6 h and 24 h images) until forming a dense and large mass (48 h). As expected, in the assays with newly formed spheroids, all treatment conditions started with a lower number and cell density of spheroids compared to the assays with 1-week dense spheroids (**Table 5.4**). In the latter, the formation of a giant spheroid with high cellular density is distinguished at 6 h, to which more spheroids are continuously added until 48 h.

Very similar behaviour was found for treatment with SMLs (without drug), where a gradual aggregation between spheroids is identified until the formation of a dense mass. Unlike cell monolayer assays, these do not allow identifying slight variations in cell roundness between conditions. The DMSO control also did not completely kill cells in both systems. However, DMSO affects the spheroids' aggregation state over time. Furthermore, the cell density in this condition is lower than in control, whereby DMSO inhibits cell replication.

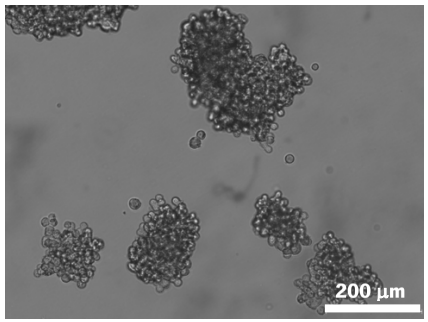
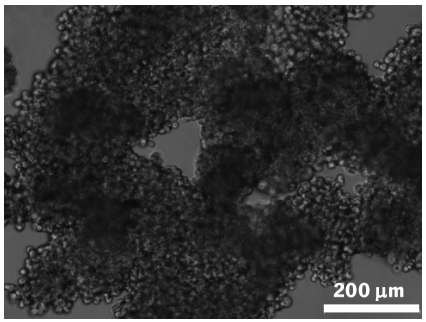
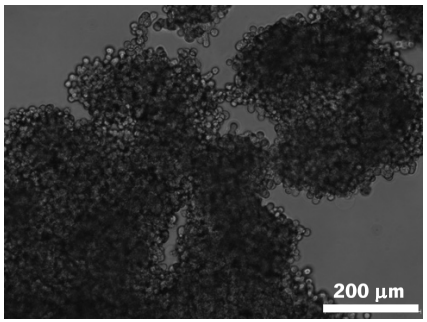
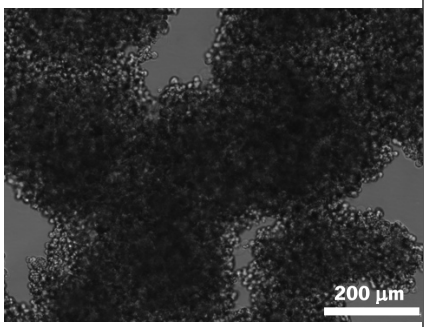
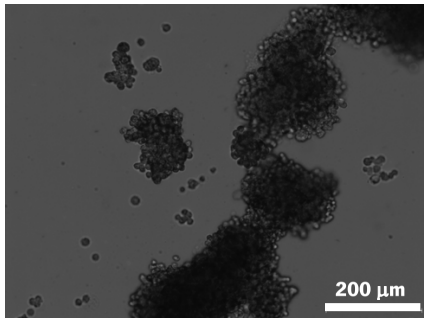
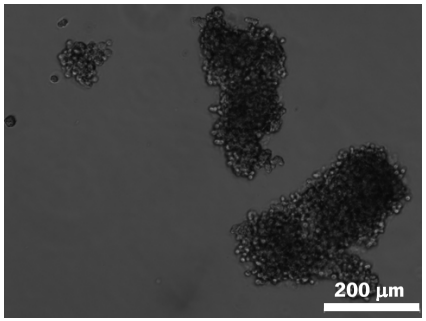
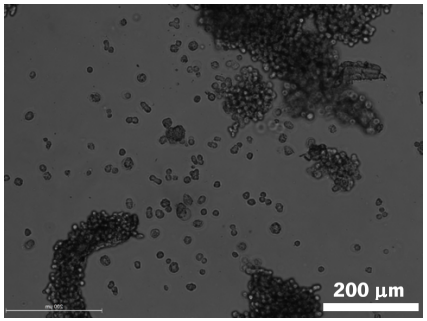
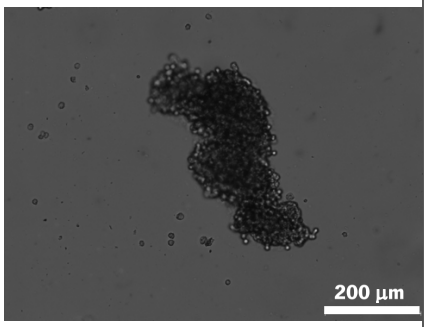
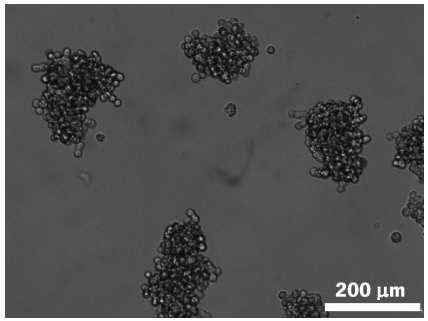
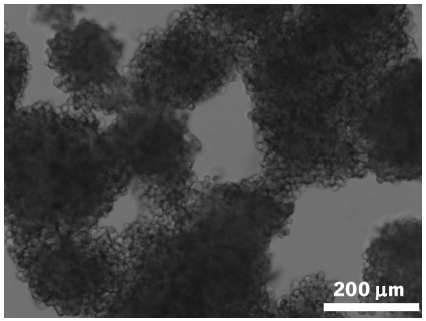
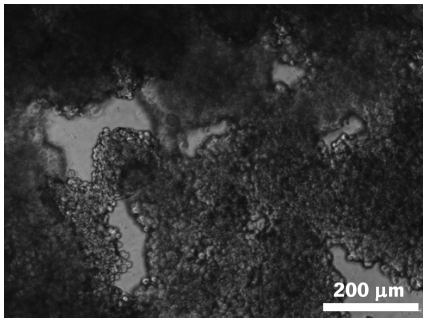
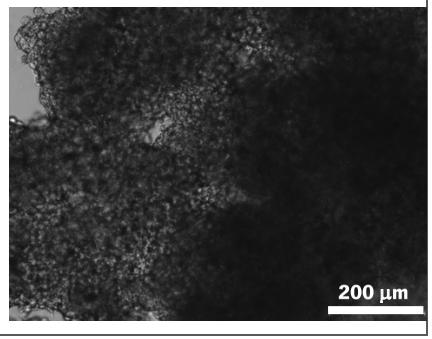
Regarding drug treatments, the DOX fluorescence becomes evident at 1 h, becoming more pronounced at 6 h, indicating a gradual accumulation of DOX within cells. The conditions with DOX-loaded SMLs seem to have an earlier therapeutic effect than free DOX. Similar to what was detailed in the pseudo-3D organisation analysis, these results point to a greater facility for SMLs to incorporate and release the drug into cells due to the fusogenic and pH-sensitive properties of the lipid formulation. Comparing these effects on the newly formed Sk-br-3 breast cancer spheroids, it was found that at 6 h, the treatment with DOX-loaded SMLs showed greater disintegration of spheroids compared to the treatment with free DOX. In fact, at 6 h, it was no longer possible to find spheroids with the high cell density found at 4 h (see Appendix C in **section C.2**, **Figure C.1**). This disintegration and cell death effect becomes more evident

at 24 h and lasts until 48 h, so no spheroids were found at the end of the treatment. In turn, in the treatment with free DOX, the disintegration of the spheroids is more evident after 24 h. Although the cell density is significantly lower than the control, free DOX presents small spheroids still disintegrating at 48 h, which points to a slower therapeutic effect.

The assays on 1-week dense Sk-br-3 breast cancer spheroids demonstrated very similar behaviour to newly formed spheroids (**Table 5.4**). Although this type of spheroids has many more cells than newly formed spheroids, DOX-loaded SMLs appear to have an earlier and more effective therapeutic effect than free-DOX. This effect is pronounced comparing the two therapeutic conditions at 24 h and 48 h. In addition to the disintegration of the spheroid, two populations of cells with rounded and misshapen morphologies, both indicators of cell death, are distinguished. Furthermore, the images corresponding to the treatment with DOX-loaded SMLs show residues in the image's background that correspond to cell death waste. The 1-week spheroids show more residues than the newly formed counterparts, which may indicate the proportional death of a more significant number of cells in the former.

Interactive 3D surface plots of DOX-loaded SMLs treatments (on both types of spheroids) were projected to give a visually quantitative perspective to this analysis. The used plug-in in images post-treatment is based on the luminance of each pixel in the picture, which is interpreted as the plot's height. **Table 5.5** and **Table 5.6** present two perspectives (front view and top view) of the height variation of the spheroids throughout the treatment of newly formed and 1-week spheroids, respectively. The surface plot of the newly formed spheroids at 1 h demonstrates the differences in height and cell density compared to the 1-week spheroid counterparts unequivocally. Between 1 h and 6 h, an increase in height and the number of spheroids is demonstrated, more significant in 1-week spheroids. At 24 h after treatment, both types of spheroids undergo significant disintegration that ends, at 48 h, in the presence of residual cells.

Table 5.3 Representative bright-field and fluorescence microscopy images (merged) of free DOX, SMLs and DOX-loaded SMLs on Sk-br-3 breast cancer cells cultured on non-adherent cell culture plates (newly formed spheroids) over 48h.

	1h	6h	24h	48h
Control				
DMSO				
SMLs				

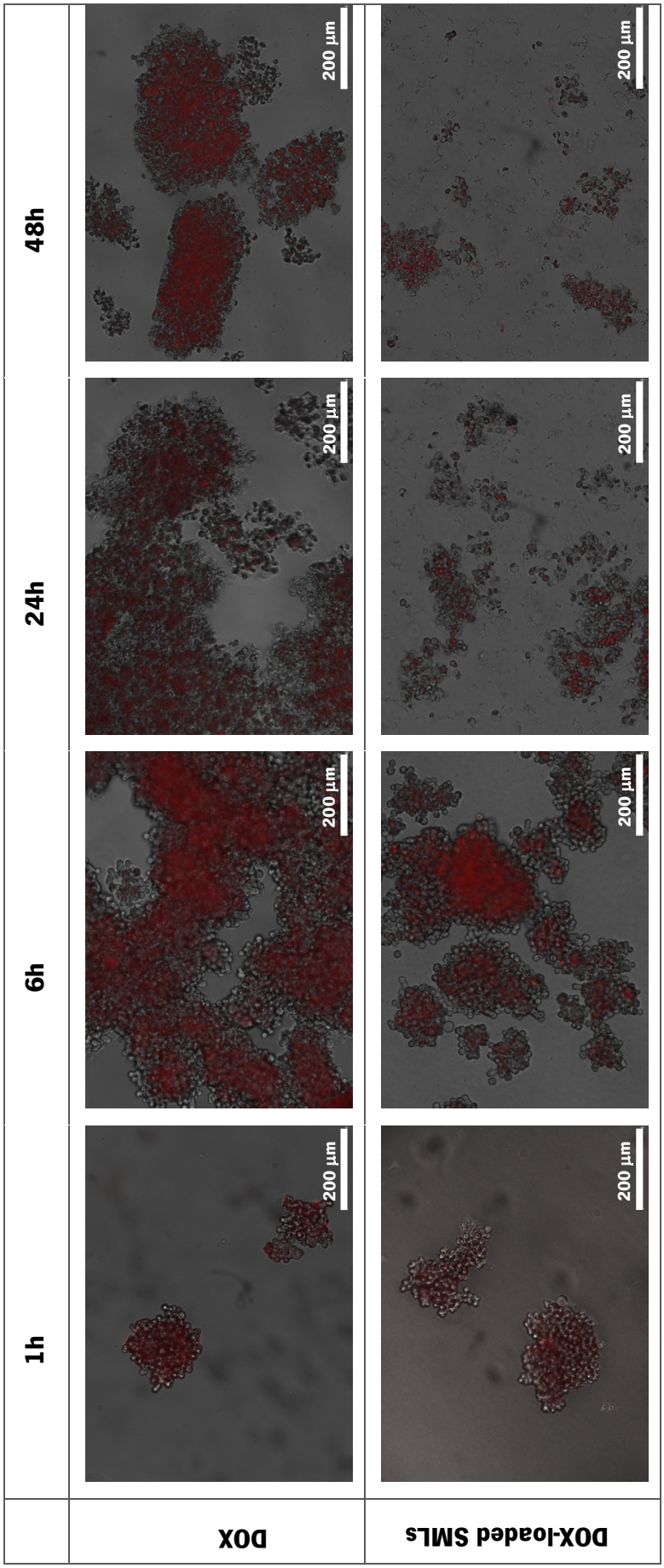
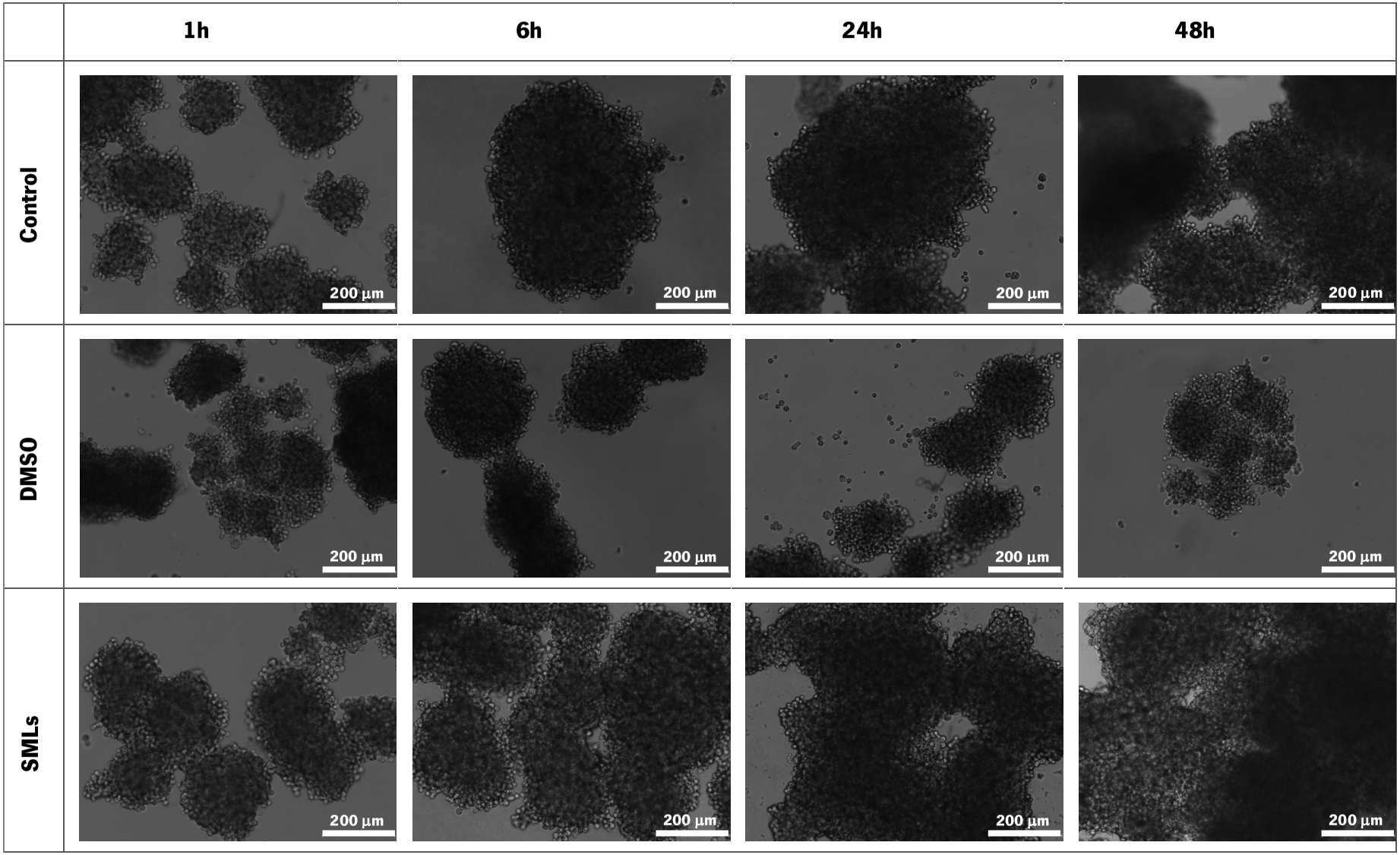

1h
6h
24h
48h
DOX
DOX-loaded SMLs
200 µm

Table 5.4 Representative bright-field and fluorescence microscopy images (merged) of free DOX, SMLs and DOX-loaded SMLs on one-week dense Sk-br-3 breast cancer spheroids cultured on non-adherent cell culture plates over 48h.



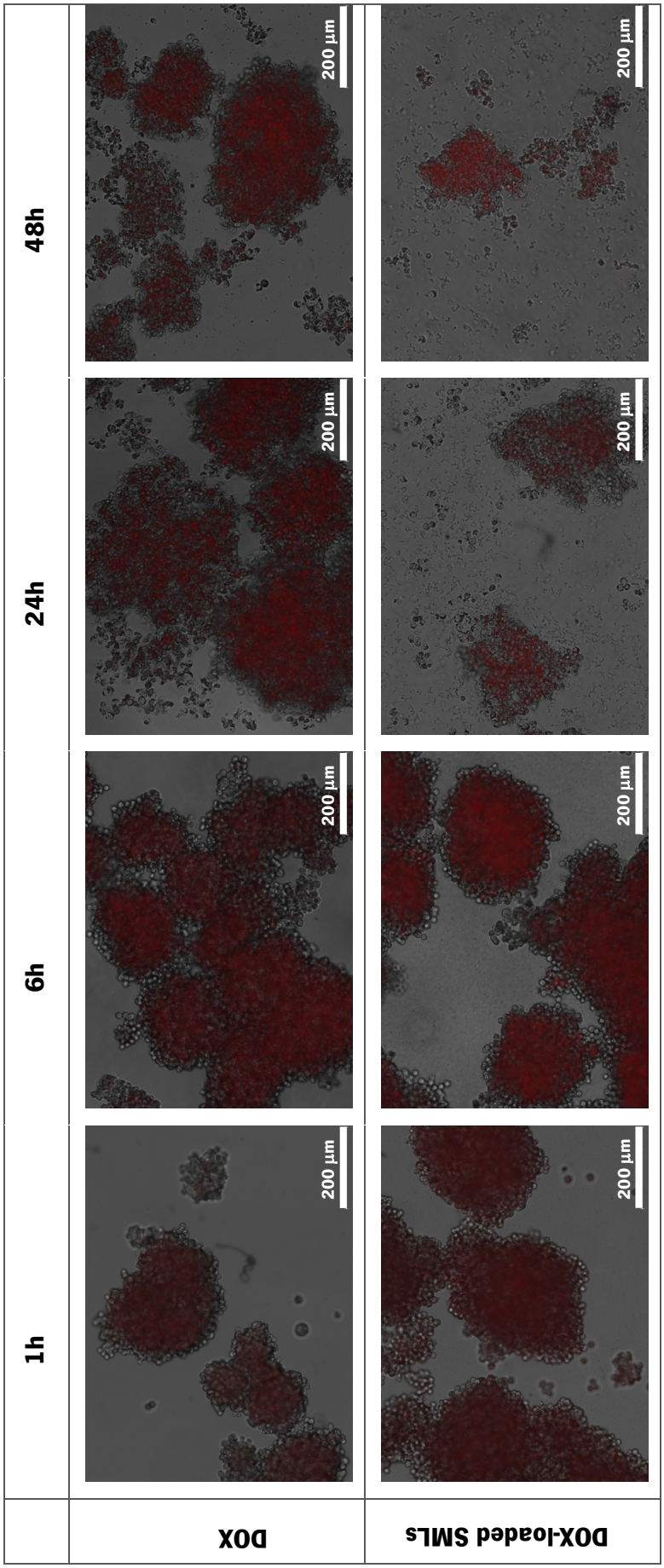

1h
6h
24h
48h
DOX
DOX-loaded SMLs
200 µm

Table 5.5 Interactive 3D surface plots (front view and top view) of DOX-loaded SMLs effects on Sk-br-3 breast cancer cells seeded on non-adherent cell culture plates (newly formed spheroids) over 48 h.

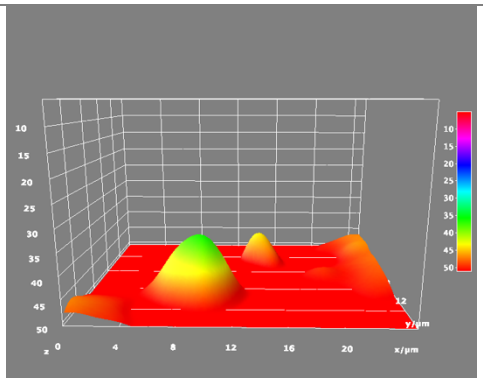
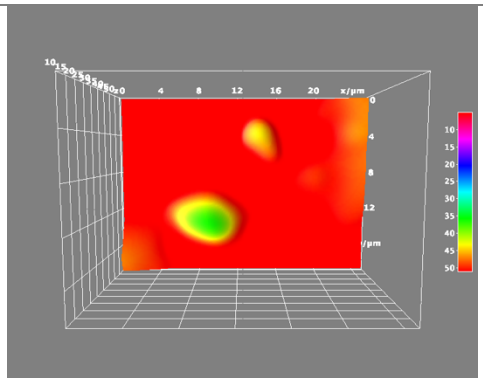
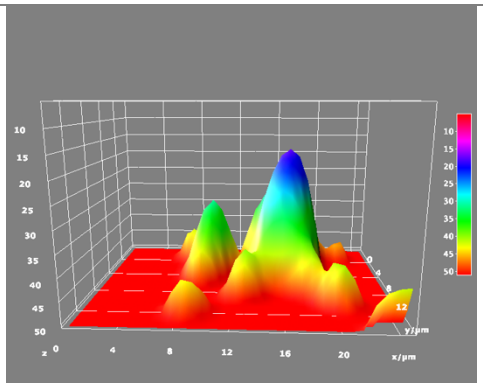
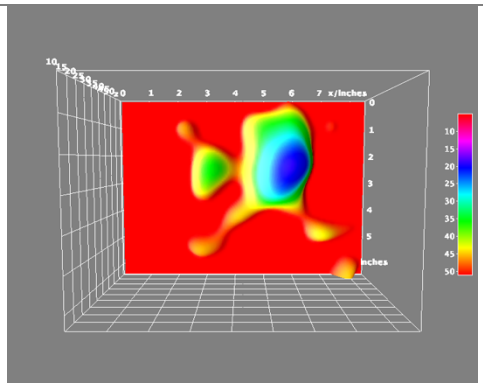
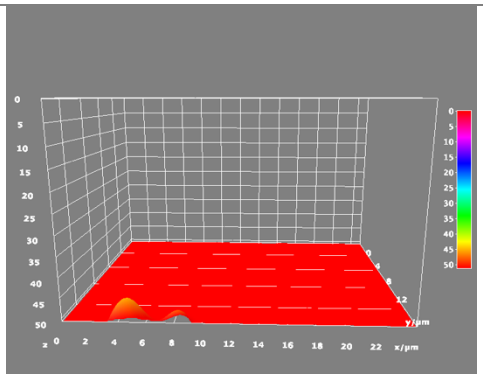
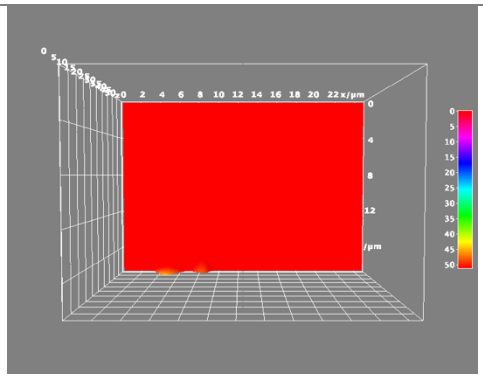
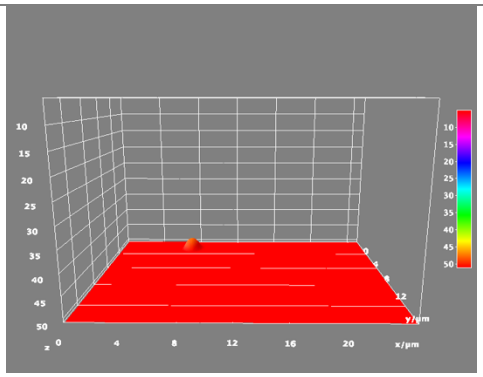
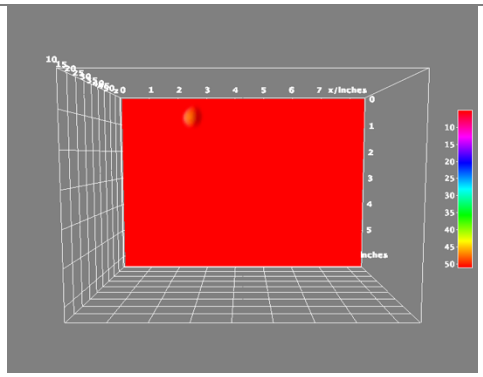
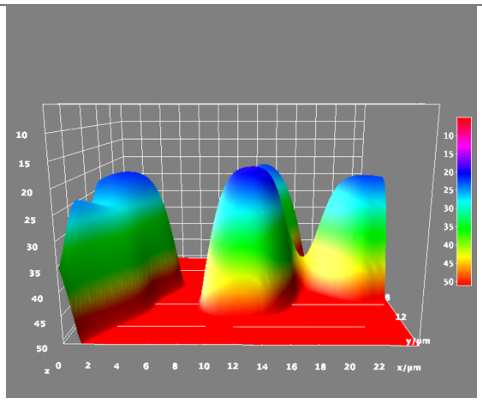
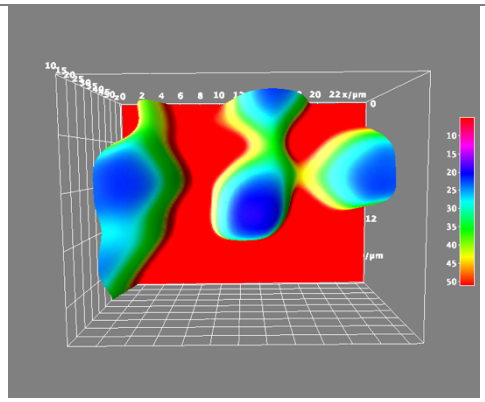
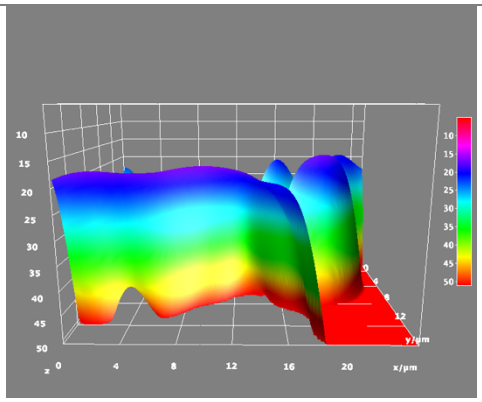
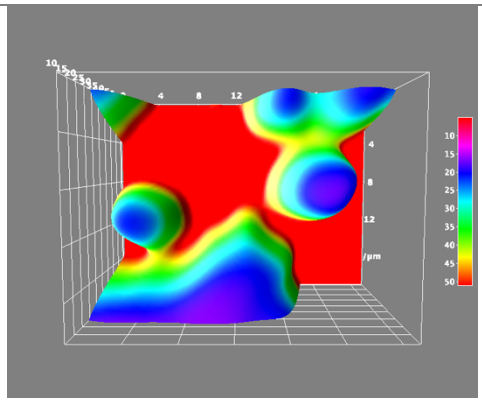
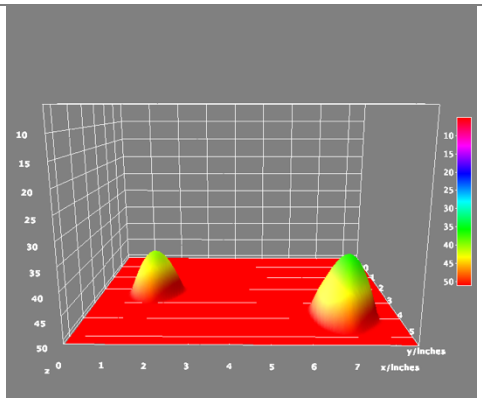
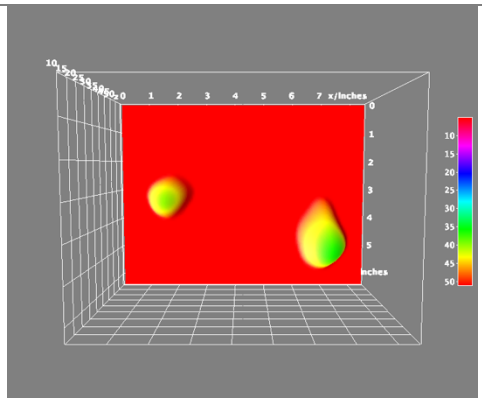
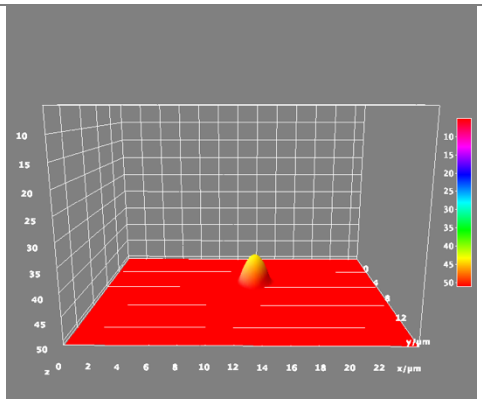
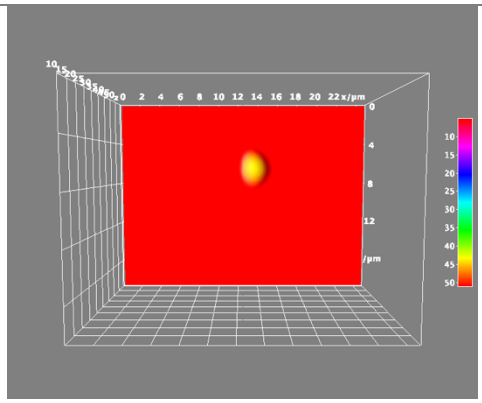
	Front view	Top view
1h		
6h		
24h		
48h		

Table 5.6 Interactive 3D surface plots (front view and top view) of DOX-loaded SMLs effects on 1-week dense Sk-br-3 breast cancer spheroids seeded on non-adherent cell culture plates over 48 h.

	Front view	Top view
1h		
6h		
24h		
48h		

5.4. Design and fabrication of biomimetic microfluidic platforms for spheroids culture

Following the advances described in the previous subsection and the concepts explored in the introductory section, this subsection describes the design and fabrication of a more biomimetic cell culture platforms based on microfluidic technology. First, it describes the optimization process of its design conformation. Finally, the proof of its ability to direct and include 1-week Sk-br-3 breast cancer spheroids in the microfluidic cell culture chambers is presented.

5.4.1. Materials and Methods

5.4.1.1. Microfluidic platform design and fabrication

PDMS microfluidic platforms were fabricated by replica moulding by means of prefabricated SU-8 moulds obtained by photolithography. Two different designs were envisaged according to the dimensions described in **Figure 5.4**. The pillars hold the spheroids into the channel perpendicular to the main channel next to Outlet 2, thus allowing the growth of a 3D tumour tissue. The inlet will allow the introduction of continuous culture medium, spheroids, as well as any compounds under study (such as DOX, SMLs, and DOX-loaded SMLs, among others) using a flow pump. Moreover, the platforms are composed of two outlets. Outlet 1 has the dual function of allowing the passage of the spheroids into the perpendicular channel when a valve attached to the tubing of the outlet channel is closed, as well as allowing the flow of fluids during the assays after the proper growth of tumour tissue/spheroids (valve open). Outlet 2 allows a constant fluid flow when retaining the spheroids next to the pillars and during the assays. It is intended that the SU-8 moulds have a thickness of ~150 μm, which will then be replicated on the PDMS platforms.

The SU-8 fabrication process took place at CMEMS research unit facilities located at Didáxis - Vale S. Cosme, Vila Nova de Famalicão, Braga, Portugal.

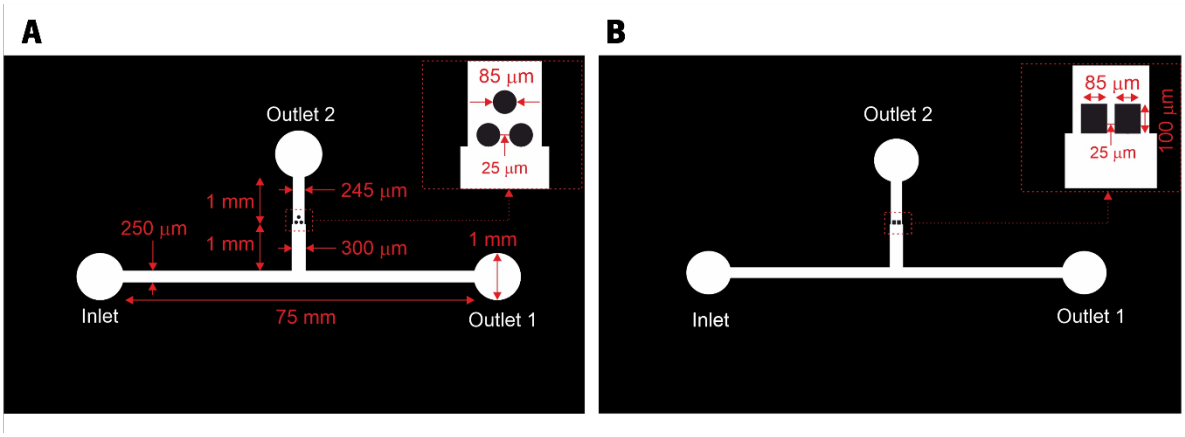


Figure 5.4 Representation of the geometry and dimensions used to fabricate the two SU-8 master moulds using: (A) 3 round pillars with a diameter of ~85 µm; (B) 2 rectangles with a width and length of ~85 and ~100 µm, respectively, in order to trap the spheroids.

Materials

SU-8 100 (epoxy-based negative photoresist) and Sylgard® 184 Silicone Elastomer (PDMS) were acquired from *Microchem* and *Dow Corning*, respectively. Standard microscope glass slides (76×26 mm^2) were purchased from Labbox, and aluminium adhesive tape (cat. no. 56223) from Tesa. Isopropyl alcohol (IPA) was provided by Sigma-Aldrich.

For the PDMS devices, 1.6 mm polytetrafluorethylene-based microfluidic tubing and 1/4-28 Shut-Off Valves were obtained from Bola, Germany and Darwin Microfluidics, Paris, France, respectively. Fluid flows were controlled by a NE-1600 Six Channel Programmable Syringe Pump (purchased by KF TECHNOLOGY SRL, Roma, Italy).

Methods

SU-8 processing conditions are summarised in **Table 5.7** and were defined according to the thickness and pre-optimisation process described in detail in [36].

Table 5.7 Processing conditions used to obtain the SU-8 moulds [36].

Conditions/SU-8 thickness (µm)		150
Room temperature (°C)		~ 22
Substrate (mm)		Glass slides (26×76)
Rotational speed (rpm)		2900
Pre-bake time (min)	at 65 °C	50
	at 95 °C	80
UV exposure time (min)		8
Post-bake time (min)	at 65 °C	30
	at 95 °C	32
Development time (min)		12

Briefly, 1 g of SU-8 100 was deposited on cleaned glass slides (76×26 mm^2) using a spin-coater (Polos 2000) at a rotational speed of 500 rpm, acceleration of 300 $rpm.s^{-1}$ for 7 s, followed by a rotational speed of 2900 rpm, acceleration of 300 $rpm.s^{-1}$ for 30 s, to achieve a thickness of ~150 µm at the end of the fabrication process. The samples were then pre-baked at 65 and 95 °C using a hot plate (Prazitherm type PZ23-2, 1400W) at a heating rate of 20 Watt%. After 8 min of UV exposure at 350 nm, (Photomeca-type IPP 45) with previously impressed patterned photolithos (**Figure 5.4**), the samples were post-bake and immersed in SU-8 developer for 12 min to remove the non-exposed epoxy. To obtain the final SU-8 mould, the sample was cleaned with IPA and gently dried with compressed air.

The PDMS microfluidic system was prepared using a PDMS solution with a base:curing agent ratio of 10:1 %wt that was previously placed in a homemade vacuum system to remove air bubbles. The solution was slowly deposited on the SU-8 mould, surrounded by aluminium adhesive tape. Simultaneously, another PDMS solution was prepared, placed in the vacuum system, and spin-coated in a cleaned glass slide (76×26 mm^2) at a rotational speed of 3000 rpm and acceleration of 300 $rpm.s^{-1}$ for 50 s. The PDMS microchannel and PDMS glass slide were partially cured at 80 °C for 20 min. After opening the inlet and outlets with a PDMS biopsy punch (1.25 mm from Elveflow), the PDMS platform was bonded irreversibly to the PDMS glass slide by curing completely at 80 °C for 2 h.

Finally, the topography of the PDMS microfluidic device (unsealed) was assessed with a NanoSEM - FEI Nova 200 (FEG/SEM) scanning electron microscope at 10 kV. Before SEM, samples were gold coated by magnetron sputtering using a Polaron SC502 sputter coater.

5.4.1.2. Spheroids inclusion on microfluidic platforms

First, the microfluidic platform was sterilised with 70% ethanol and then flushed with PBS in the device to remove residual ethanol and air. Next, the spheroids were introduced into the microfluidic chamber using a sterilised syringe and microfluidic tubing. A flow rate of 3 μL/min was established to simulate the velocity of blood in tumours (1.7 mm/sec) [29]. For this, 1 mL of the culture medium containing the previously formed 1-week Sk-br-3 breast cancer spheroids (see **section 1.3.1.1**) was diluted in 2 mL of new culture medium through inlet 1, keeping the outlet 1 valve closed and the outlet 2 valve open (**Figure 5.4**) until a spheroid entered and retained in the chamber. After that, the outlet 3 valve was closed, and the outlet 2 valve was opened. The spheroids entry was accompanied in real-time by an inverted fluorescence microscope (Olympus, LX71). Then, the syringe containing the spheroids was removed and replaced by a syringe containing 7 mL of culture medium, which, in turn, was connected to the syringe pump.

5.4.2. Results and discussion

5.4.2.1. Microfluidic platform design and fabrication validation

Microfluidic platforms were designed with the aim of (1) simulating the tumour vasculature distance-dependent gradients that are formed with the continuous outgrowth of cells, (2) inducing the formation of a perfused heterogeneous tumour microenvironment that ensures the presence of distinct molecular signatures and drug sensitivities; (3) develop a model to predict the free drugs and encapsulated drugs transport in the circulation, transport into tissues, intratumoral transport, mass transport-related mechanisms and clearance; and (4) quantify the apoptotic effects of DOX and DOX-loaded magnetoliposomes on breast cancer tissues. The final objective is to bring drug screening systems closer to the physiological environment and to the mechanisms that govern and regulate the effectiveness of drugs. As mentioned in **section 1.3.4**, two designs were fabricated according to **Figure 5.4 A** and **B** schematic representations. The geometry of the devices is distinguished by the shape, arrangement and dimensions of the pillars created between the microchamber and outlet 2. One of the geometries includes three round pillars with a diameter of ~85 μm, and the other contains two rectangular pillars with a width and length of ~85 and 100 μm, respectively, all of them with a height of ~150 μm. These geometries were designed to reinforce spheroid retention and support the maintenance of tumour tissue without being washed out. Representative SEM images of the microfluidic platforms are represented in **Figure**

5.5, demonstrating well-defined topographies. In **Figure 5.5 A**, the microfluidic device with 3 pillars is represented, revealing pillars with a pyramidal shape instead of a round one. These results show limitations of the fabrication process in manufacturing the structures according to this designed conformation. Relevant processing parameters, e.g. UV exposure time, were varied in an attempt to overcome this limitation without success. Using chromium masks instead of photolithos and mask-aligner can be an option to achieve better results. In turn, the rectangular pillars (**Figure 5.5 B**) showed a better ability to keep the form intact, revealing taller pillars. Thus, the latter offers better structural properties to retain the Sk-br-3 breast cancer spheroids for the later formation of the tumour tissue, as verified experimentally and explained in the next section.

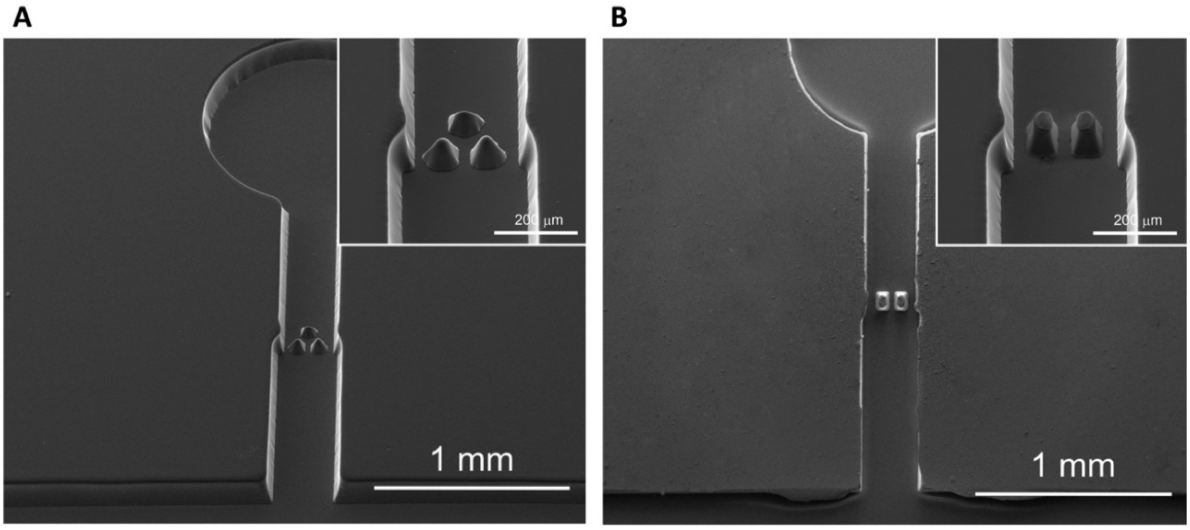


Figure 5.5 Representative SEM images of the microfluidic platforms designed with (A) 3 round pillars and (B) 2 rectangular pillars. The inset shows a zoom of the pillars.

Figure 5.6 shows a representative photograph of a PDMS microfluidic device containing an inlet and 2 outlets whose function is described in **section 1.3.4**. Each microfluidic platform had three replicas of the cell culture system shown in the above SEM images.

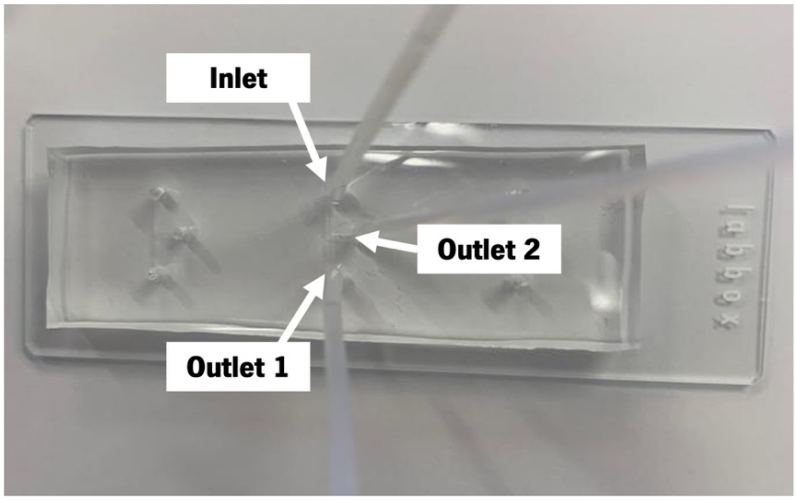


Figure 5.6 Photograph of a PDMS microfluidic device composed of 3 replicas of the cell culture system.

5.4.2.2. Evaluation of the microfluidic platform for spheroids inclusion and retention

This subsection details the laboratory assembly process of the microfluidic platform to its functional components and the inclusion of spheroids in the cell culture microchamber. These assays also used the 1-week Sk-br-3 breast cancer spheroids as a proof-of-concept. Thus, the first step concerned the preparation of spheroids from Sk-br-3 breast cancer cells, according to **section 1.3.1**. In addition to being models that best represent the *in vivo* spatiotemporal conditions, the spheroids also facilitate their inclusion in the device. This happens because, on the one hand, the structure in PDMS was sealed to a glass slide, forming a closed system. Another advantage of a closed microfluidic system is the reduced risk of contamination, as it ensures a sterilised environment for the cells.

Afterwards, several 1-week dense Sk-br-3 spheroids were placed in a syringe coupled to a flow pump, connected to microfluidic tubing with the corresponding valves. The flow pump, set to a flow rate of 3 μL/min, slowly injects the Sk-br-3 spheroids solution from the microfluidic tubing inlet to the cell culture chamber. Excess medium and lose cells are expelled through outlet 2. This process is monitored in real-time using an inverted optical microscope, following the assembly scheme shown in **Figure 5.7**.

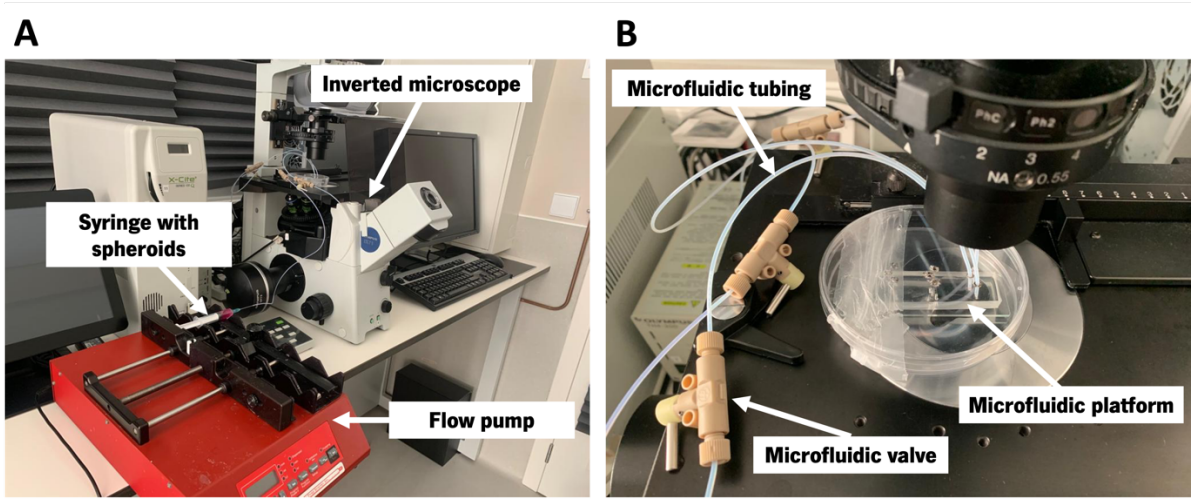


Figure 5.7 Assembly scheme overview of (A) microfluidic platform connected to the flow pumping and image acquisition systems and (B) working device with microfluidic inlet and outlets tubbing and the corresponding valves coupled.

Hereupon, the ability of the microfluidic platforms (with pyramidal and rectangular pillars) to include and retain Sk-br-3 spheroids was evaluated. However, the pyramidal PDMS structures failed to maintain the spheroids. Even though the spheroids correctly flowed from the inlet to the cell culture chamber, they escaped between the pyramidal pillars, resulting in their washout through outlet 2. On the other hand, the rectangular pillars retained several Sk-br-3 spheroids and their accumulation in the cell culture chamber.

Figure 5.8 shows the sequential process of inclusion and retention of spheroids by a fabricated microfluidic platform with rectangular pillars (even though one of the pillars is not perfectly rectangular). The first image shows the microfluidic platform before inserting the spheroids. Closing outlet 1 valve and opening outlet 2 valve induced fluid flow in the schematic direction (red arrows). The second image shows a spheroid retained on the pillars and an intact spheroid (pointed) flowing through the microfluidic channel towards the microfluidic cell culture chamber (third image), which ends up being kept together with the other spheroid (fourth image). It should be noted that the spheroids' structure is slightly fluid, which is why they manage to meld themselves around the pillars. After the accumulation of these spheroids in the microfluidic cell culture chamber, outlet 2 and inlet valves were closed to retain the cells.

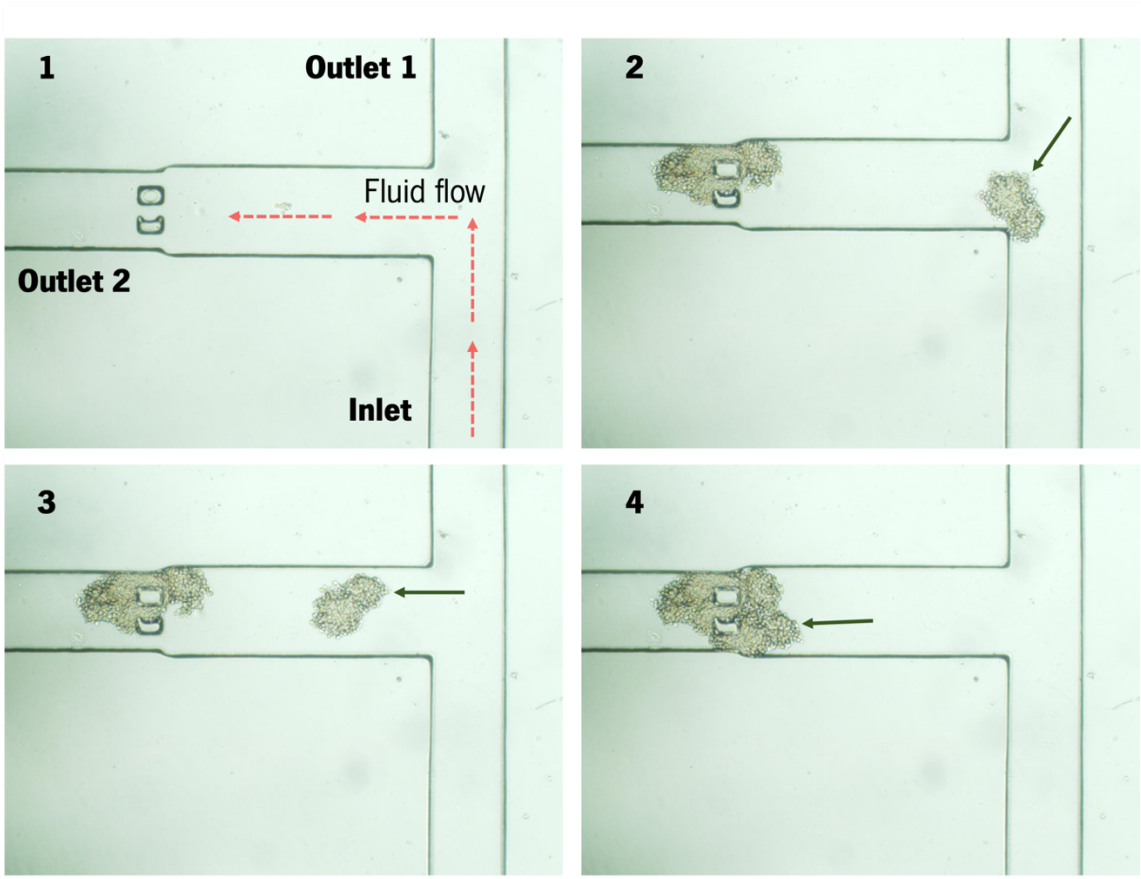


Figure 5.8 Sequential microscopy images of Sk-br-3 spheroids inclusion and retention on a microfluidic platform with rectangular pillars.

These assays validated the operating concept of this microfluidic platform in retaining spheroids for the subsequent formation of tumour tissue. Future work should explore its potential in assessing the therapeutic effects of DOX and DOX-loaded magnetoliposomes and compare/associate the results with those obtained by the 2D and 3D methods. In addition, it is intended to make this platform a model for drug screening that allows the comprehensive study of several therapeutic approaches in a mimetic context.

5.4.3. Conclusions

In conclusion, this work may contribute towards a better understanding about different cellular organisational levels' influence on the screening of new therapeutic strategies. It allowed to made several generalisations about the effect of free DOX and DOX encapsulated in SMLs on the Sk-br-3 breast cancer cell line grown in 2D, pseudo-3D and 3D cell culture methods (spheroids).

The 2D Sk-br-3 cancer cell culture was the one that revealed fewer variability effects between free DOX and DOX-loaded SMLs. It was found that both treatments showed total cell death at 24 h. However, live cells were found in the pseudo-3D assays at 24 h after the treatments. The results reveal different cell sensibility profiles according to their organisation. Moreover, the results point to an earlier therapeutic activity of DOX when encapsulated in SMLs which could be explained by the greater ability of SMLs to incorporate and release DOX into cells. The Sk-br-3 spheroids assays with different cell densities revealed very similar behaviours. However, the greater cell size and density in the 1-week spheroids stand out. These systems show gradual aggregation among themselves until the formation of a dense mass. Similarly to pseudo-3D systems, an early therapeutic effect of DOX-loaded SMLs stands out compared to free DOX. In fact, at the end of the assays, only the DOX-loaded SMLs conditions resulted in the almost total disintegration of the spheroids.

Finally, a proof-of-concept of a microfluidic platform for Sk-br-3 spheroids retention was carried out. This platform can control the flow and Sk-br-3 spheroids' direction to the cell culture chamber. Furthermore, Sk-br-3 spheroids are effectively retained on the rectangular support pillars for further cell replication and formation of heterogeneous tumour tissue. Although it is at an early stage of development, future work will ensure the microfluidic platform optimisation to a functional system that brings screening assays closer to mimetic conditions by reproducing the mechanisms that govern and limit drug efficacy with greater accuracy.

5.5. References

1. Riaz, M.; van Jaarsveld, M.; Hollestelle, A.; Prager-van der Smissen, W.J.; Heine, A.A.; Boersma, A.W.; Liu, J.; Helmijr, J.; Ozturk, B.; Smid, M. miRNA expression profiling of 51 human breast cancer cell lines reveals subtype and driver mutation-specific miRNAs. *Breast cancer research* **2013**, *15*, 1-17.
2. Siegel, R.; Miller, K.; Jemal, A. Cancer statistics, 2020 CA Cancer J Clin. *American Cancer Society* **2020**, *70*, 7-30.
3. Burguin, A.; Diorio, C.; Durocher, F. Breast cancer treatments: updates and new challenges. *Journal of Personalized Medicine* **2021**, *11*, 808.
4. Coley, H.M. Mechanisms and strategies to overcome chemotherapy resistance in metastatic breast cancer. *Cancer treatment reviews* **2008**, *34*, 378-390.
5. Cope, L.M.; Fackler, M.J.; Lopez-Bujanda, Z.; Wolff, A.C.; Visvanathan, K.; Gray, J.W.; Sukumar, S.; Umbricht, C.B. Do breast cancer cell lines provide a relevant model of the patient tumor methylome? *PloS one* **2014**, *9*, e105545.
6. Trosko, J.E.; Ruch, R.J. Cell-cell communication in carcinogenesis. *Frontiers in Bioscience-Landmark* **1998**, *3*, 208-236.
7. Pernot, S.; Evrard, S.; Khatib, A.-M. The Give-and-Take Interaction Between the Tumor Microenvironment and Immune Cells Regulating Tumor Progression and Repression. *Frontiers in Immunology* **2022**, *13*, 850856-850856.
8. Kamińska, K.; Szczylik, C.; Bielecka, Z.F.; Bartnik, E.; Porta, C.; Lian, F.; Czarnecka, A.M. The role of the cell–cell interactions in cancer progression. *Journal of cellular and molecular medicine* **2015**, *19*, 283-296.
9. Pietras, K.; Östman, A. Hallmarks of cancer: interactions with the tumor stroma. *Experimental cell research* **2010**, *316*, 1324-1331.
10. Seguin, L.; Desgrosellier, J.S.; Weis, S.M.; Cheresh, D.A. Integrins and cancer: regulators of cancer stemness, metastasis, and drug resistance. *Trends in cell biology* **2015**, *25*, 234-240.
11. Zhang, X.; De Milito, A.; Olofsson, M.H.; Gullbo, J.; D'Arcy, P.; Linder, S. Targeting mitochondrial function to treat quiescent tumor cells in solid tumors. *International journal of molecular sciences* **2015**, *16*, 27313-27326.
12. Nik Nabil, W.N.; Xi, Z.; Song, Z.; Jin, L.; Zhang, X.D.; Zhou, H.; De Souza, P.; Dong, Q.; Xu, H. Towards a framework for better understanding of quiescent cancer cells. *Cells* **2021**, *10*, 562.
13. Sutherland, R.M. Cell and environment interactions in tumor microregions: the multicell spheroid model. *Science* **1988**, *240*, 177-184.

14. Dagogo-Jack, I.; Shaw, A.T. Tumour heterogeneity and resistance to cancer therapies. *Nature reviews Clinical oncology* **2018**, *15*, 81-94.

15. Oudin, M.J.; Weaver, V.M. Physical and chemical gradients in the tumor microenvironment regulate tumor cell invasion, migration, and metastasis. In Proceedings of the Cold Spring Harbor symposia on quantitative biology, 2016; pp. 189-205.

16. Tannock, I.F. Tumor physiology and drug resistance. *Cancer and Metastasis Reviews* **2001**, *20*, 123-132.

17. Justice, B.A.; Badr, N.A.; Felder, R.A. 3D cell culture opens new dimensions in cell-based assays. *Drug discovery today* **2009**, *14*, 102-107.

18. Gimbrone Jr, M.A.; Leapman, S.B.; Cotran, R.S.; Folkman, J. Tumor dormancy in vivo by prevention of neovascularization. *The Journal of experimental medicine* **1972**, *136*, 261-276.

19. Warren, B.A. The vascular morphology of tumors. In *Tumor blood circulation: Angiogenesis, vascular morphology and blood flow of experimental and human tumors*; CRC press: **2020**; pp. 1-47.

20. Nagy, J.A.; Chang, S.-H.; Shih, S.-C.; Dvorak, A.M.; Dvorak, H.F. Heterogeneity of the tumor vasculature. In Proceedings of the Seminars in thrombosis and hemostasis, 2010; pp. 321-331.

21. Kim, B.j.; Forbes, N.S. Flux analysis shows that hypoxia-inducible-factor-1-alpha minimally affects intracellular metabolism in tumor spheroids. *Biotechnology and bioengineering* **2007**, *96*, 1167-1182.

22. Trédan, O.; Galmarini, C.M.; Patel, K.; Tannock, I.F. Drug resistance and the solid tumor microenvironment. *Journal of the National Cancer Institute* **2007**, *99*, 1441-1454.

23. Dewhirst, M.W.; Secomb, T.W. Transport of drugs from blood vessels to tumour tissue. *Nature reviews cancer* **2017**, *17*, 738-750.

24. Duval, K.; Grover, H.; Han, L.-H.; Mou, Y.; Pegoraro, A.F.; Fredberg, J.; Chen, Z. Modeling physiological events in 2D vs. 3D cell culture. *Physiology* **2017**, *32*, 266-277.

25. Kapałczyńska, M.; Kolenda, T.; Przybyła, W.; Zajączkowska, M.; Teresiak, A.; Filas, V.; Ibbs, M.; Bliźniak, R.; Łuczewski, Ł.; Lamperska, K. 2D and 3D cell cultures–a comparison of different types of cancer cell cultures. *Archives of Medical Science* **2018**, *14*, 910-919.

26. Yamada, K.M.; Cukierman, E. Modeling tissue morphogenesis and cancer in 3D. *Cell* **2007**, *130*, 601-610.

27. Yang, T.-M.; Barbone, D.; Fennell, D.A.; Broaddus, V.C. Bcl-2 family proteins contribute to apoptotic resistance in lung cancer multicellular spheroids. *American journal of respiratory cell and molecular biology* **2009**, *41*, 14-23.

28. Desoize, B.; Jardillier, J.-C. Multicellular resistance: a paradigm for clinical resistance? *Critical reviews in oncology/hematology* **2000**, *36*, 193-207.

29. Walsh, C.L.; Babin, B.M.; Kasinskas, R.W.; Foster, J.A.; McGarry, M.J.; Forbes, N.S. A multipurpose microfluidic device designed to mimic microenvironment gradients and develop targeted cancer therapeutics. *Lab on a Chip* **2009**, *9*, 545-554.

30. Abraham, M.C.; Shaham, S. Death without caspases, caspases without death. *Trends in cell biology* **2004**, *14*, 184-193.

31. Kerr, J.F.; Gobe, G.C.; Winterford, C.M.; Harmon, B.V. Anatomical methods in cell death. *Methods in cell biology* **1995**, *46*, 1-27.

32. Majno, G.; La Gattuta, M.; Thompson, T. Cellular death and necrosis: chemical, physical and morphologic changes in rat liver. *Virchows Archiv für pathologische Anatomie und Physiologie und für klinische Medizin* **1960**, *333*, 421-465.

33. Bresciani, G.; Hofland, L.J.; Dogan, F.; Giamas, G.; Gagliano, T.; Zatelli, M.C. Evaluation of spheroid 3D culture methods to study a pancreatic neuroendocrine neoplasm cell line. *Frontiers in endocrinology* **2019**, *10*, 682.

34. Chen, Z.; Ma, N.; Sun, X.; Li, Q.; Zeng, Y.; Chen, F.; Sun, S.; Xu, J.; Zhang, J.; Ye, H. Automated evaluation of tumor spheroid behavior in 3D culture using deep learning-based recognition. *Biomaterials* **2021**, *272*, 120770.

35. Metzger, W.; Rother, S.; Pohlemann, T.; Möller, S.; Schnabelrauch, M.; Hintze, V.; Scharnweber, D. Evaluation of cell-surface interaction using a 3D spheroid cell culture model on artificial extracellular matrices. *Materials Science and Engineering: C* **2017**, *73*, 310-318.

36. Pinto, V.C.; Sousa, P.J.; Cardoso, V.F.; Minas, G. Optimized SU-8 Processing for Low-Cost Microstructures Fabrication without Cleanroom Facilities. *Micromachines* **2014**, *5*, 738-755, doi:10.3390/mi5030738.

CHAPTER 6

Concluding remarks and future perspectives

6.1. Concluding remarks

The use of nanotechnology for developing controlled delivery nanosystems has been asserting its importance in improving the pharmacokinetic profile, biodistribution, stability and *in situ* accumulation of therapeutic agents. Liposomal formulations with encapsulated chemotherapeutic drugs stand out, whose clinical validation resulted in the addition and subsequent improvement of their targeting strategy and therapeutic action. As a result of this evolutionary line, conjugates of magnetic nanoparticles (NPs) and liposomes – the magnetoliposomes – emerged, which, in addition to adding magnetophoretic mobility to lipid systems, allow for the induction of controlled release under external stimuli and the addition of adjuvant treatment modalities (such as localised hyperthermia).

Accordingly, this PhD thesis compiles the analysis and discussion of the obtained results for (1) the development of calcium-substituted magnesium ferrite NPs ($Ca_xMg_{1-x}Fe_2O_4$) and $Ca_xMg_{1-x}Fe_2O_4$-based aqueous (AMLs) and solid magnetoliposomes (SMLs); (2) the optimisation of $Ca_{0.25}Mg_{0.75}Fe_2O_4$ ferrites and SMLs' inherent properties; (3) the development of multi-stimuli-responsive SMLs for doxorubicin(DOX)-controlled release in cancer therapy; (4) 2D, pseudo-3D and 3D Sk-br-3 breast cancer cells culture for the screening of DOX and DOX-loaded SMLs; and (5) design and fabrication of a microfluidic platforms for Sk-br-3 breast cancer spheroids retention in a cell culture microchamber.

Chapter 2 described the preparation of spherical calcium-substituted magnesium ferrite NPs ($Ca_xMg_{1-x}Fe_2O_4$, with x=0.25, 0.50, 0.75) and the influence that the partial replacement of magnesium by calcium in the ferrite structure has on its properties. X-Ray Diffraction (XRD) measurements confirmed the synthesis of pure crystalline ferrite and an increased crystallite size with the higher calcium content. Although all synthesised NPs revealed a superparamagnetic behaviour, they tended to decrease saturation magnetisation (M_s) with the increasing calcium content. Following the NPs' characterisation, they were used in preparing stealth (PEGylated) AMLs and SMLs, which were evaluated, as a proof-of-concept, as curcumin nanocarriers since curcumin-based therapies can be great adjuvants of the classic anticancer treatment to improve its effectiveness. Furthermore, AMLs and SMLs revealed smaller hydrodynamic diameters when $Ca_{0.25}Mg_{0.75}Fe_2O_4$NPs are encapsulated, with values of 131.4±19 nm and 127.3±17 nm, respectively. The integrated analysis of the systems characterisation results revealed that both $Ca_{0.25}Mg_{0.75}Fe_2O_4$ and SMLs enclosing this type of NPs showed more promising results. Thus, these systems were selected to continue developing a fully optimised and functional design.

Thereby, work has progressed towards optimising the individual properties of each of these components. Thus, **chapter 3** described the synthesis, for the first time, of shape-anisotropic $Ca_{0.25}Mg_{0.75}Fe_2O_4$ NPs

and a new method to synthesise SMLs based on these NPs. The formation of these ferrites was confirmed by XRD analysis. In turn, transmission electron microscopy (TEM) analysis distinguishes cubic and slightly rectangular shape NPs with a mean size of 20.8±5.3 nm. The magnetic characterisations revealed an enhancement of 3.86 times in M_s, from 12.98 emu/g (for the spherical NPs) to 50.07 emu/g (for shape-anisotropic NPs with the same proportion of calcium and magnesium ions). The shape-anisotropic $Ca_{0.25}Mg_{0.75}Fe_2O_4$ NPs and the corresponding $Ca_{0.25}Mg_{0.75}Fe_2O_4$-SMLs also revealed a potential for magnetic hyperthermia. These advances were followed by the development of a new method for synthesising SMLs to incorporate these NPs with better magnetic properties and synthesis reproducibility. The lipid formulation used in the proof-of-concept, DPPC-based, exhibits an average hydrodynamic size (by dynamic light scattering) of 117.5±0.5 nm, slightly smaller than the previously obtained 127.3±17 nm, with a reduction also in polydispersity index (PDI). Once again, the high-resolution transmission electron microscopy images (TEM) perfectly distinguished a single SML that revealed a diameter of 116.5±5.5 nm and a lipid bilayer's length of 8.3±1 nm. Several lipid compositions of SMLs (DPPC, DPPC/DSPE-PEG (95:5) and DPPC/Ch (7:3)) have revealed the ability to encapsulate 1×10^{-4} M and 2×10^{-4} M of DOX in the lipid bilayers with great efficiency. Finally, the ability of these SMLs to enhance DOX-controlled release under therapeutic conditions (42 °C and pH=5.5) compared to physiological conditions (37 °C and pH=7.4) was proven. Nonetheless, it was concluded that there is an increased sustained DOX release in PEGylated SMLs, which indicates a prolonged drug delivery period. Overall, the results exceed those previously achieved by showing the new methodology's success in synthesising new shape-anisotropic $Ca_{0.25}Mg_{0.75}Fe_2O_4$NPs and new SMLs.

These preliminary results instigated the need to improve the SMLs to provide them with multi-stimuli-responsive properties for DOX-controlled release in pathological areas under the action of thermal, magnetic, and pH stimuli. Thus, **chapter 4.1** brings together the screening results of three groups of lipid formulations (i) DPPC, (ii) DPPC/DSPC and (iii) DPPC/DOPE, to which CHEMS and DSPE-PEG were added sequentially, resulting in a total of nine studied lipid formulations. It is noteworthy that all the studied lipid formulations revealed a hydrodynamic diameter below 200 nm and PDI below the 0.3 limits, reinforcing the developed method's reproducibility. Nonetheless, only the group (i) and (ii) lipid formulations demonstrated thermosensitivity in the temperature range of interest (38 °C < T_m < 42 °C), while a loss of thermosensitivity was shown for all formulations containing DOPE. Likewise, only the group (i) and (ii) formulations do not show significant variations in their size and PDI upon storage at 4 °C over 30 days, pointing to good general stability. All lipid formulations resulted in SMLs capable of protecting DOX against interaction with human serum albumin (HSA), preventing opsonisation and

increasing its bioavailability. Yet, this protective effect is substantially boosted by including DSPE-PEG in the lipid formulations. Moreover, the DOX release kinetics and profiles were determined to pre-select the lipid formulations that best fit controlled DOX release patterns. Generally, a synergistic effect of a temperature rise (42 °C) with acidic pH (5.5) was found. Notwithstanding, the DPPC and DPPC/DSPC lipid formulations stand out as multi-stimuli-responsive systems (thermo/pH sensitivity) under therapeutic conditions (42 °C and acidic pH). Although DSPE-PEG acts as a DOX diffusion barrier, PEGylated formulations, particularly the DPPC/DSPC/CHEMS/DSPE-PEG, demonstrate an overall potential for a targeted and controlled therapeutic action in tumour environments. Thus, the formulation of DPPC/DSPC/CHEMS/DSPE-PEG was selected for further work since it demonstrates the greatest potential for a controlled therapeutic action in tumour environments.

Following the process of SMLs' lipid formulation optimisation, **Chapter 4.2** was devoted to studying the magnetic component of SMLs, demonstrating the ability of NPs to generate heat by near-infrared (NIR)-induced photothermia, as well as the effects of their increased inclusion on the properties of SMLs. After approximately 10 min of irradiation with an 808 nm laser diode, the NIR-derived heating performance of aqueous suspensions with 1, 2, and 4 mg/mL of NPs registered maximum temperature variations of 9.6±0.4 °C, 11.3±0.6 °C, and 16.5±0.4 °C, respectively. Including these NPs concentrations in 1 mM of the optimised DPPC/DSPC/CHEMS/DSPE-PEG SMLs resulted in the synthesis of SMLs with a superparamagnetic behaviour and mean diameters of 159±3 nm, 143±4 nm and 135±1 nm, as required for biomedical application, for 1, 2, and 4 mg/mM SMLs. However, the 2 mg/1 mM condition was the one that demonstrated a better PDI (0.17±0.0(3)), as well as higher rates of NPs encapsulation per lipid unit, 1.2±0.1 mg/0.52±0.05 mM. The comprehensive evaluation of all the results reveals that the DPPC/DSPC/CHEMS/DSPE-PEG-based SMLs with 2 mg of NPs for 1 mM lipid formulation are optimised systems for controlled, targeted and dual therapy in cancer therapeutics.

In **chapter 5**, the DPPC/DSPC/CHEMS/DSPE-PEG-based SMLs were tested on a relevant breast cancer cell line, the Sk-br-3 breast cancer cell, which was cultured by 2D (monolayer), pseudo-3D (1-week dense spheroids plated on conventional adherent cell culture plates) and 3D (newly formed and 1-week dense spheroids plated on non-adherent cell culture plates) cell culture methods. Different cells' drug sensitivity profiles were identified according to the cellular organisational complexity. 2D Sk-br-3 cancer cell culture revealed higher sensitivity to both DOX and DOX-loaded SMLs treatments since it was the only cell organisation that showed total cell detachment from the culture plates after 24h of the treatments, evidencing cell death. In the pseudo-3D organisation, after 24 h of treatment, live cells were still found, revealing a change in the sensitivity profile relative to monolayer culture. Furthermore, DOX-loaded SMLs

demonstrated a higher number of dead cells at 24 h than free DOX, which points to an earlier therapeutic activity of lipid systems. Regarding Sk-br-3 breast cancer spheroids, newly formed spheroids and 1-week dense spheroids showed similar therapeutic behaviours. Identical to the pseudo-3D organisation, an earlier therapeutic activity of DOX was verified when encapsulated in SMLs, which resulted in the almost total disintegration of the spheroids between 24 h and 48 h. These assays point to an enhanced ability of SMLs to incorporate and release DOX into cells than free DOX, highlighting the practical potential of the developed SMLs developed throughout this PhD project. Finally, the design and fabrication of polydimethylsiloxane (PDMS) microfluidic platforms for Sk-br-3 spheroids retention were essential in establishing a microfluidic cell culture platform for future drug screening. Sk-br-3 spheroids are effectively retained on the rectangular support pillars thar will be essencial for further cell replication and formation of heterogeneous tumour tissue. This platform will continue to be optimised for establishing a spheroids' cell culture to grow a heterogeneous tumour tissue. Also, the miniaturisation and the dynamic supplementation processes (both nutrients and tested drugs) intend not only to establish more realistic biomechanical and biochemical tumour microenvironments for accurate screening but also to study, in real-time, the mechanisms of intratumoral transport of the therapies.

In conclusion, this thesis contributes to a better understanding of multi-responsive solid magnetoliposomes and the importance of establishing suitable *in vitro* cell culture methods for accurate screening. However, as with all such studies, some limitations offer opportunities for further research.

6.2. Future perspectives

This PhD project has fulfilled the main aim of creating knowledge and innovation for applying magnetoliposomes. Nonetheless, some limitations in magnetoliposome optimisation merit further investigation. As a result, this work opened many possibilities for future research.

Regarding superparamagnetic NPs, stability problems were found in terms of aggregation. It is known, however, that the stability of NPs is an essential parameter against aggregation *in vivo* and under alternating magnetic field (AMF) application [1]. Thus, future work should include studies on increasing stability through, for instance, the binding of monomeric stabilisers to NPs' surfaces. These include binding functional groups, such as carboxylates, through the treatment of aqueous solutions of NPs with citric acid and its consequent adsorption to the surface of NPs [2,3]. Another strategy would be to functionalise the NPs with dimercaptosuccinic acid (DMSA) [4,5]. These changes must be accompanied

by assays that ensure the maintenance of other stability properties, such as the chemical identity and crystallinity of the core (investigated by energy dispersive X-ray spectroscopy (EDX) and XRD) and its shape (investigated by atomic force microscope (AFM), HR-TEM, scanning electron microscope (SEM), and XRD). Likewise, equal or greater efficiencies of enclosing NPs per unit of lipid formulation should be guaranteed.

Future work also should also ensure the comprehensive study of AMF-induced magnetic hyperthermia potential with several NPs concentrations and variable magnetic field/frequency combinations, similarly to what was done with NIR-induced photothermal hyperthermia. Likewise, considering that one of the magnetic hyperthermia limitations is the lack of standardised protocols that allow comparison between results, a protocol should be drawn up compiling the most relevant parameters for the assays and allowing its reproduction in *in vitro* assays. Furthermore, studying magnetoliposomes' magnetic responsivity under AMF is also essential to determine the amount of encapsulated magnetic NPs to elevate the temperature to hyperthermia effectively. Moreover, it would be interesting to quantify the possible synergistic effect between NIR-induced photothermal hyperthermia and AMF-induced magnetic hyperthermia in heating magnetic NPs and their impact on drug release.

The biggest challenge for future research will be to implement an integrated and comparative study of the effects of DOX-loaded SMLs on 2D and 3D cell culture methods to explore the underlying mechanisms that govern their therapeutic effects. Ideally, this study should be performed on multiple breast cancer cell lines representing different primary tumours and with multiple functional receptors. In addition to the Sk-br-3 breast cancer cell line, it would be informative to include, for instance, the MCF-7 cell line (non-invasive line, functional estrogen and epidermal growth factor (EGF) receptors) and the MDA-MB-231 (aggressive and metastatic line, which is hormone-independent). The therapeutic effects can be compared by the quantification of the, for instance: (i) cell sensitivity by viable cells quantification after treatment using kits such as the CellQuanti-MTT™ Cell Viability Assay Kit or the CellTiter-Glo® luminescent assay; (ii) cells hypoxic status on different organisational levels using a hypoxia probe, such as LOX-1, which can generate quantifiable oxygen levels signals by fluorescence microscopy [6]; and (iii) association between hypoxia levels with cell dormancy in the G_0 phase, which is related to the resistance of breast cancer cells to treatments [7].

These assays should be performed when optimising the conditions of NIR/AMF-induced hyperthermia (in SMLs and their practical application) to quantify the multifunctional potential of magnetoliposomes. Furthermore, the *in vitro* therapeutic effects should quantify the hyperthermia effects without chemotherapy, chemotherapy effects without hyperthermia and, finally, the combined effect of

chemotherapy and hyperthermia. If the cell culture results indicate a need to improve the targeting abilities of magnetoliposomes, the addition of targeting moieties to the surface of magnetoliposomes can also be explored. This further targeting can be performed by conjugating, for example, arginine (R)–glycine (G)–aspartic acid (RGD) peptides that target cancer cells expressing RGD-binding integrins such as α_5- and α_v-integrins [8] or the aptamer Apt-A6 that can recognise and bind HER-2 receptors on HER-2+ breast cancer cells [9]. Moreover, the potential for magnetic targeting under the action of a permanent magnetic field and its effects on transport across cells should also be evaluated.

Regarding the microfluidic cell culture, a customised temperature-controlled incubator built on the inverted fluorescence microscope should be included. Thus, the process of inclusion and growth of the spheroid until the formation of a tumour tissue would be followed in real-time. After the formation of tumour tissue, it would be interesting to access the pH gradients and hypoxia levels of that tissue to associate them with the therapeutic effects. Thus, pH gradients could be quantified by injecting 2',7'-bis-(2-carboxyethyl)-5-(and-6-)-carboxyfluorescein (BCECF) free acid fluorescent indicator into the microfluidics platform; and the levels of hypoxia could be analysed with the LOX-1probe. Furthermore, it would allow the uptake and clearance of DOX and DOX-loaded SMLs to be monitored by time-lapse fluorescence microscopy (using intrinsic fluorescence of DOX). It should also be acknowledged that the application of optimised DOX-loaded DPPC/DSPC/CHEMS/DSPE-PEG-based SMLs could be explored for other types of cancer and even other types of diseases.

The concluding remarks, in combination with the future perspectives, evidence the complexity of magnetoliposomes and their development and optimisation processes. The versatility and multifunctionality of these systems are their best advantages, as well as their greatest limitations since they require the integration of multidisciplinary expertise. Nonetheless, encouraging multidisciplinarity and interdisciplinarity in the drug discovery paradigm is the key to success in healthcare. This validates the significance of the work completed in this doctoral project and justifies the progression of the research.

6.1. References

1. Laurent, S.; Forge, D.; Port, M.; Roch, A.; Robic, C.; Vander Elst, L.; Muller, R.N. Magnetic iron oxide nanoparticles: synthesis, stabilization, vectorization, physicochemical characterizations, and biological applications. *Chemical reviews* **2008**, *108*, 2064-2110.

2. Sahoo, Y.; Goodarzi, A.; Swihart, M.T.; Ohulchanskyy, T.Y.; Kaur, N.; Furlani, E.P.; Prasad, P.N. Aqueous ferrofluid of magnetite nanoparticles: fluorescence labeling and magnetophoretic control. *The Journal of Physical Chemistry B* **2005**, *109*, 3879-3885.

3. Taupitz, M.; Wagner, S.; Schnorr, J.; Kravec, I.; Pilgrimm, H.; Bergmann-Fritsch, H.; Hamm, B. Phase I clinical evaluation of citrate-coated monocrystalline very small superparamagnetic iron oxide particles as a new contrast medium for magnetic resonance imaging. *Investigative radiology* **2004**, *39*, 394-405.

4. Chaves, S.; Lacava, L.; Lacava, Z.; Silva, O.; Pelegrini, F.; Buske, N.; Gansau, C.; Morais, P.; Azevedo, R. Light microscopy and magnetic resonance characterization of a DMSA-coated magnetic fluid in mice. *IEEE Transactions on magnetics* **2002**, *38*, 3231-3233.

5. Fauconnier, N.; Pons, J.; Roger, J.; Bee, A. Thiolation of maghemite nanoparticles by dimercaptosuccinic acid. *Journal of Colloid and Interface Science* **1997**, *194*, 427-433.

6. Zhang, S.; Hosaka, M.; Yoshihara, T.; Negishi, K.; Iida, Y.; Tobita, S.; Takeuchi, T. Phosphorescent Light–Emitting Iridium Complexes Serve as a Hypoxia-Sensing Probe for Tumor Imaging in Living AnimalsIridium Complexes for Tumor Imaging. *Cancer research* **2010**, *70*, 4490-4498.

7. Flamant, L.; Notte, A.; Ninane, N.; Raes, M.; Michiels, C. Anti-apoptotic role of HIF-1 and AP-1 in paclitaxel exposed breast cancer cells under hypoxia. *Molecular cancer* **2010**, *9*, 1-15.

8. Hynes, R.O. Integrins: bidirectional, allosteric signaling machines. *Cell* **2002**, *110*, 673-687.

9. Powell, D.; Chandra, S.; Dodson, K.; Shaheen, F.; Wiltz, K.; Ireland, S.; Syed, M.; Dash, S.; Wiese, T.; Mandal, T. Aptamer-functionalized hybrid nanoparticle for the treatment of breast cancer. *European journal of pharmaceutics and biopharmaceutics* **2017**, *114*, 108-118.

Appendices

A

Appendix A: Supplementary information of chapter 3

A.1. Photophysical properties of doxorubicin in solution

The behaviour of the drug DOX is determined not only by its molecular structure but also by the nature of solvent interactions established in biological systems. Considering that solvent highly influences the photophysical behaviour of a molecule, the systematic analysis of its spectral features can give relevant physicochemical insight. Therefore, understanding the microenvironment influence on spectroscopic properties of doxorubicin provides information that can be extrapolated to drug-solvent interactions in biological systems.

Solvatochromic methods have been widely used to study solvent effects on photophysical properties (e.g. absorption maxima, emission maxima and Stokes' shift) [1,2]. The multi-parameter Kamlet-Taft {α, β, π*} [3,4] and the Catalán {aSA, bSB, cSP, dSdP} [5] solvent scale, by solvatochromic data analysis, contribute to interactions to the polarity effect on spectroscopic characteristics. Both models, considering non-specific and solute-solvent interaction, give a quantitative description of the solvatochromic shifts [6]. Catalán solvent scale (unlike the Kamlet-Taft solvent scale) has the advantage of separating non-specific solvent effects into two independent parameters (polarizability and dipolarity).

The Kamlet-Taft solvent scale uses the π*, α and β parameters (polarity/polarizability, acidity and basicity, respectively, of a given solvent) to study solute-solvent interactions, following **Equation A.1**. The basicity and acidity (characterised by hydrogen bond acceptor ability and hydrogen bond donor ability, respectively) are specific interactions. In contrast, non-specific interactions include polarity and polarizability, characterised by the solvent's ability (by its dielectric effect) to stabilise a charge or a dipole.

Equation A.1

$$y = y_0 + a_\alpha\,\alpha + b_\beta\,\beta + c_{\pi*}\,\pi*$$

The estimated coefficients y_0, a_α, b_β and c_{π^*} and the corresponding correlation coefficients for the multi-linear regression analyses of the emission maxima, absorption maxima, Stokes' shift and fluorescence

quantum yield, using the Kamlet-Taft solvent scale, are displayed in **Table A.1** The Kamlet-Taft π*, α and β solvatochromic parameters were taken from [7].

The influence of solvents on the same parameters was also studied using the linear solvation energy relationship model of Catalán [8], given by **Equation A.2**, and Catalán parameters were taken from [9,10].

Equation A.2

$$y = y_0 + a_{\mathrm{SA}}\,\mathrm{SA} + b_{\mathrm{SB}}\,\mathrm{SB} + c_{\mathrm{SP}}\mathrm{SP} + d_{\mathrm{SdP}}\mathrm{SdP}$$

Where y_0 is the physicochemical property in the gas phase, SA is the solvent acidity, SB is the solvent basicity, SP is the solvent polarizability, and SdP is the solvent dipolarity. In this model, these solvent parameters are independent (but complementary) and responsible for multiple types of solute-solvent interactions. In this Equation, a_{SA}, b_{SB}, c_{SP} and d_{SdP} are the regression coefficients that describe the sensitivity of the respective parameter to the solute-solvent interaction mechanisms.

Both models consider specific and non-specific interactions, providing a quantitative description of the solvatochromic shifts [6]. However, Catalan's model separates non-specific solvent effects into polarity and polarizability. The results of the multiple regressions are displayed in **Table A.2**. The multi-linear analysis of the obtained λ_{em} data of DOX as a function of {α, β, π*} shows a lower correlation coefficient (R=0.87) when compared to the correlation obtained by the use of {SA, SB, SP, SdP} (R=0.99). This difference is significant since in the Kamlet-Taft model, the solvent (di)polarity and polarizability effects are combined in the π* parameter and in Catalan's model, they are split into SP and SdP parameters. **Table A.1** shows the linear relation between the λ_{em} calculated values using Catalán solvent scale versus the corresponding experimental values. Also, in Kamlet-Taft analysis, if {α, β} are employed as independent variables (**Equation A.3**), the obtained correlation coefficient (R=0.86) is similar to the original fit (R=0.87).

Equation A.3

$$y = y_0 + a_{\alpha}\,\alpha + b_{\beta}\,\beta$$

Table A.1 Estimated coefficients (y_0, a_α, b_β, c_{π^*}), their standard errors and correlation coefficients (R) for the multiple linear regression analysis of λ_{em}, λ_{abs},, $\Delta\tilde{\nu}$ and Φ_F as a function of the Kamlet-Taft solvent scale. The regression coefficients are expressed in nm for λ_{em} and λ_{abs}, in cm^{-1} for $\Delta\tilde{\nu}$ and 10^{-2} for Φ_F.

	y_0	a_α	b_β	c_{π^*}	R
λ_{em}	589.(5)±4	-7.(8)±5	1.(1)±3	3.(3)±6.64	0.87
λ_{em}	591.(7)±1	2.(6)±1	-9.(6)±3		0.86
λ_{abs}	494.(5)±7	-8.(6)±8	11.(4)±6	-16.(2)±11	0.81
$\Delta\tilde{\nu}$	[32.(4) ± 2]×10^{5}	[1.(4) ± 2]×10^{-5}	[-4.(5) ± 1]×10^{-5}	[7.(9) ± 3]×10^{-5}	0.92
Φ_F	0.07±0.02	0.05±0.03	-0.0006±0.0188	-0.0009±0.0266	0.89

In Catalán analysis, the more considerable cSP coefficient estimate value compared to the estimated {aSA, bSB, cSP, dSdP} in the study of λ_{em} (**Equation 3.4**) indicates that the change of λ_{em}maxima can be attributed to a change in polarizability of doxorubicin environment. The relation between y=λ_{em} and the polarizability parameter SP was studied (**Equation 3.5**).

Equation A.4

$$y = y_0 + a_{\mathrm{SA}}\,\mathrm{SA} + b_{\mathrm{SB}}\,\mathrm{SB} + d_{\mathrm{SdP}}\mathrm{SP}$$

Equation A.5

$$y = y_0 + c_{\mathrm{SP}}\mathrm{SP}$$

The correlation coefficient of 0.99 confirms the linear relationship in **Table A.2**. However, only neglecting solvent dipolarity (**Equation A.4**), with {SA, SB, SP} as independent variables) produces a fit (R=0.98) with almost the same quality as the original fit (R=0.99). These results demonstrate that solvent dipolarity can be neglected for minor variations on λ_{em}, but solvent acidity, basicity and polarizability play an active role in the shift of DOX emission maxima.

The multi-linear analysis of λ_{abs} data as a function of {SA, SB, SP, SdP} presents a better correlation (R=0.98) compared to the analysis as a function of {α, β, π*} (R=0.81) (**Table A.2**)

Table A.2 Estimated coefficients (y_0, aSA, bSB, cSP, dSdP), their standard errors and correlation coefficients (R) for the multiple linear regression analysis of λ_{em}, λ_{abs}, $\Delta\tilde{\nu}$ and Φ_F as a function of the Catalán solvent scales. The regression coefficients are expressed in nm for λ_{em} and λ_{abs}, in cm^{-1} for $\Delta\tilde{\nu}$ and 10^{-2} for Φ_F.

	y_0	a_{SA}	b_{SB}	c_{SP}	d_{SdP}	R
λ_{em}	565.(4)±19	1.(1)±1	-2.(2)±4	32.(7)±21	2±5	0.99
λ_{em}	572.(4)±5	1.1±0.7	- 3.(7)±1	25.(4)±7		0.98
λ_{em}	564.(9) ± 5			35.(3)±8		0.89
λ_{abs}	390.(4)±38	9±1	24.78±8.63	114.(7)±41	8.(4)±10	0.98
λ_{abs}	419.(4)±13	9.(5)±1	18.77±3.92	84.(5)±17		0.97
λ_{abs}	489.(5)±7				-4.(3)±9	0.17
$\Delta\tilde{\nu}$	(69 ± 22)×10^{-5}	(-4 ± 1)×10^{-5}	(-11 ± 5)×10^{-5}	(-39 ± 24)×10^{-5}	(-3 ± 6)10^{-5}	0.97
$\Delta\tilde{\nu}$	(59.(6) ± 6)×10^{-5}	(-4 ± 8)×10^{-5}	(-9 ± 1)×10^{-5}	(-29 ± 8)×10^{-5}		0.96
$\Delta\tilde{\nu}$	(34.(5)±3)×10^{-5}				(2 ± 4)×10^{-5}	0.17
Φ_F	0.3±0.2	-0.01 ± 0.01	-0.02±0.03	-0.28±0.18	-0.08±0.07	0.94
Φ_F	0.05±0.02	-0.01 ± 0.01		0.02±0.01	- 0.01±0.03	0.88
Φ_F	0.11±0.05	-0.02±0.01		- 0.09±0.07		0.80

A good linear relationship (R=0.98) was found between the experimental λ_{em} values and the λ_{em} calculated values according to **Equation A.2**, using the estimated values of a_{SA}, b_{SB}, c_{SP} and d_{SdP} (**Figure A.1 A**). Similar to what was verified for λ_{em}, the multi-linear fit of λ_{abs} data as a function of {SA, SB, SP} as independent variables, according to **Equation A.4**, revealed a correlation coefficient of 0.97, which is nearly the same as the original fit (**Figure A.1 B**). The same analysis was made as a function of {SdP}, according to **Equation A.6**, and a poor relationship was found between λ_{abs} and SdP (R=0.17). The results confirm that solvent dipolarity is not critical, primarily in λ_{abs} shifts.

Equation A.6

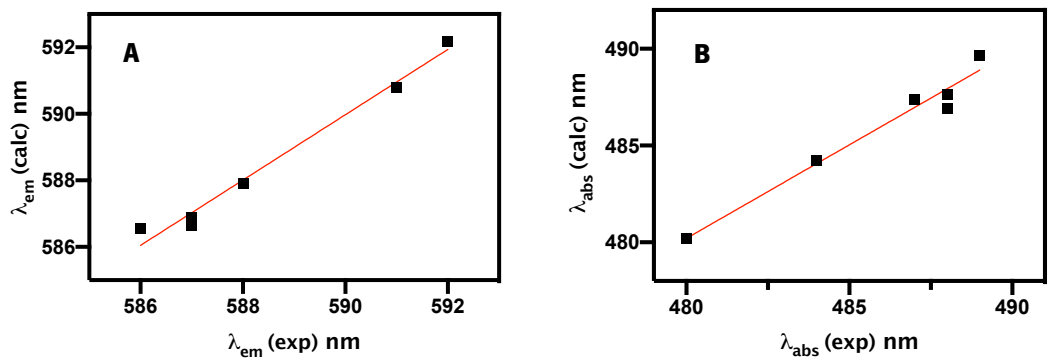
$$y = y_0 + d_{\mathrm{SdP}}\mathrm{SdP}$$

For Stokes' shift ($\Delta\tilde{\nu}$), Kamlet-Taft analysis produces a good fit (R=0.92), but Catalán analysis (R=0.97) outperforms it. **Figure A.1 C** represents the linear relationship between experimental and calculated $\Delta\tilde{\nu}$ obtained by the multiple linear regression analysis according to the Catalán model. In Catalán analysis, if {SA, SB, SP} are used as independent variables in the linear Equation to fit y = $\Delta\tilde{\nu}$ (**Equation A.4**) the correlation coefficient (R=0.96) is similar to the one obtained as a function of {SA, SB, SP, SdP}. This result indicates that solvent dipolarity is not a critical parameter to describe Stokes' shift. This is corroborated by the poor correlation coefficient (R=0.17) obtained by the linear fit of y = $\Delta\tilde{\nu}$ as a function of SdP (**Equation A.6**).

The multi-linear analysis of Φ_F data as a function of {α, β, π^*} is less adequate to describe Φ_F values since it presents a lower correlation (R = 0.89), when compared to the analysis as a function of {SA, SB, SP, SdP} (R=0.94). The linear relationship between experimental and calculated values, according to Catalán solvent scale, is represented in **Figure A.1 D.** The Catálan analysis of Φ_F as a function of {SA, SP, SdP} as independent variables (**Equation A.7**) give rise to a relatively good fit (R=0.88). This result indicates that solvents' basicity does not primarily influence small changes on Φ_F. Furthermore, the same analysis was made as a function of {SA, SP}, with an R-value of 0.80. This result indicates that solvent dipolarity can be neglected for minor Φ_F variations.

Equation A.7

$$y = y_0 + a_{\mathrm{SA}}\,\mathrm{SA} + d_{\mathrm{SdP}}\mathrm{SP} + d_{\mathrm{SdP}}\mathrm{SdP}$$



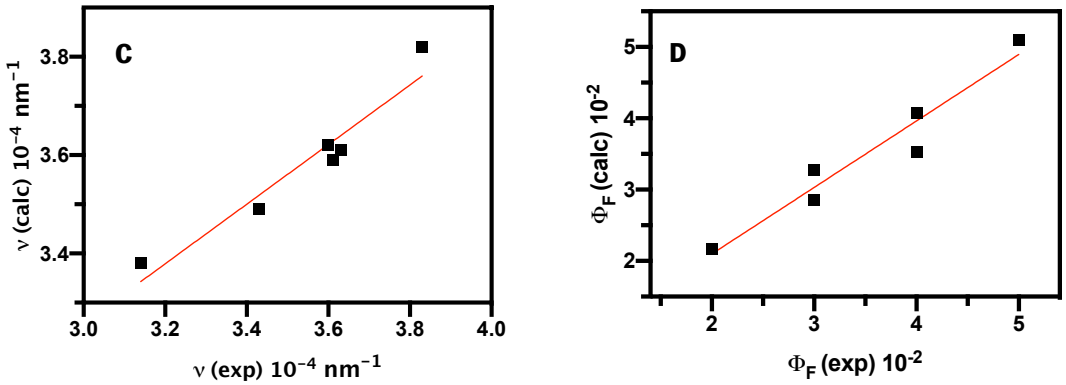


Figure A.1 Linear relationship of the experimental and calculated (A) λ_{em} (R=0.99); (B) λ_{abs} (R=0.98); (C) $\Delta\tilde{\nu}$ (R= 0.97); and (D) Φ_F (R= 0.96) of doxorubicin obtained by the multiple linear regression analysis according to Catalán solvent scale.

A.2. DLS correlation curves of SMLs

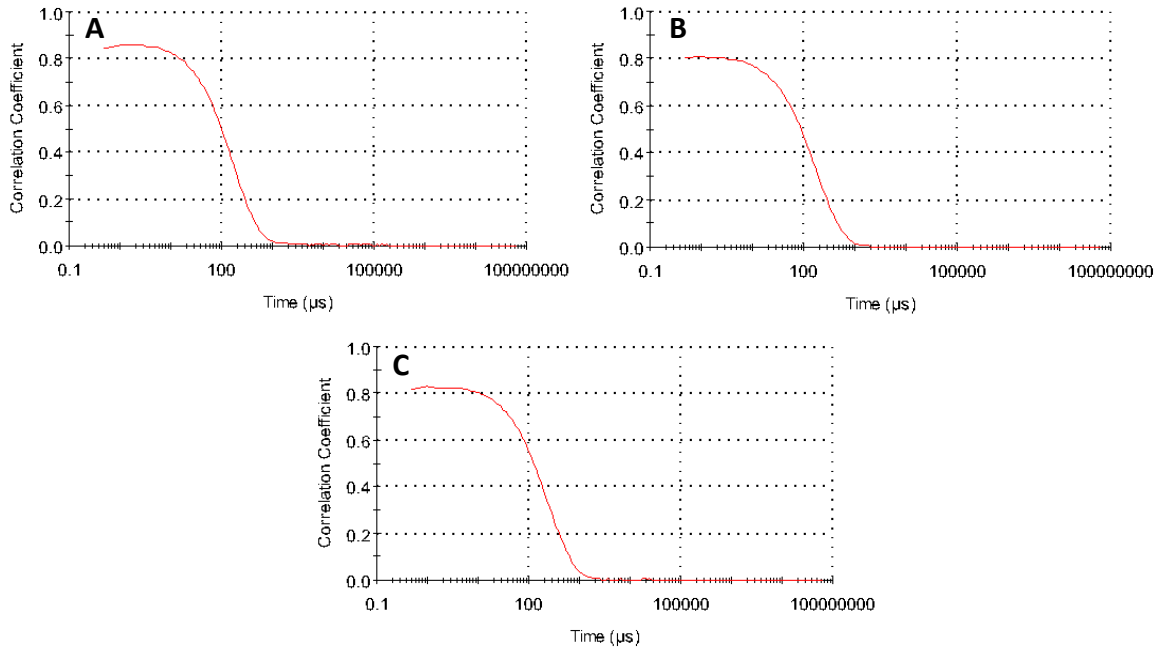


Figure A.2 DLS correlation curves for SMLs. A: SMLs of DPPC; B: SMLs of DPPC/Ch; C: SMLs of DPPC/DSPE-PEG.

A.3. Drug release kinetics and mathematical modelling of release profile

The Weibull model, which is a distribution function, is expressed in terms of the drug fraction accumulated (m) in solution on time t by **Equation A.8** [11]:

Equation A.8

$$m = 1 - exp^{-(t-T_i)^{\frac{b}{a}}}$$

where a is a scale parameter that defines the timescale of the process, T_i represents the latency time of the release process (often being zero), and b is a formal parameter that characterizes the type of curve ($b = 1$ is exponential; $b > 1$ is sigmoid, with ascendant curvature delimited by an inflection point; and $b < 1$ is parabolic, displaying high initial slope and a consistent exponential character).
The first-order kinetic model follows [12]:

Equation A.9

$$F(\%) = M_0 \times (1 - e^{-kt})$$

where $F(\%)$ is the percentage of the released drug, M_0 represents the total amount of the drug released, k represents the first-order rate constant and t the time. Considering that the total drug release varied between experiments, M_0 was regarded as a variable.

The Korsmeyer–Peppas model (power law) is a more comprehensive semi-empirical equation that establishes an exponential relationship between release and time, following **Equation A.10** [13]:

Equation A.10

$$C_t/C_0 = K \cdot t^n$$

where C_0 and C_t are the concentrations at time 0 and t, respectively, K is the rate constant, and n is the transport exponent. When $n < 0.45$, the release mechanism is diffusion-controlled (Fickian release),

$0.45 < n < 0.89$ indicates a combination of diffusion and erosion drug release (non-Fickian release), $0.89 < n < 1$ indicates a relaxation-controlled release, and in the case of $n > 1$, the release is controlled by swelling and chain relaxation. The constant values and coefficient of determination obtained for each model are summarized in **Table A.3** (for DPPC-based SMLs) and **Table A.4** (for DPPC/DSPE-PEG-based SMLs).

Table A.3 Obtained constant values by fitting each mathematical model to the kinetic data and respective coefficient of determination (R^2), according to the temperature and pH variation for DPPC-based SMLs.

pH	Temperature	y_{max}(%) ± SD	Weibull			First-order		Korsmeyer-Peppas		
			B	*a*	R^2	*k*	R^2	*K*	*n*	R^2
5.5	42 °C	25±2	1.18	0.29	0.99	0.35	0.99	10.76	0.30	0.88
	37 °C	9±1	0.89	0.37	0.94	0.34	0.93	3.74	0.28	0.90
7.4	42 °C	6.5±0.2	1.59	0.71	0.96	0.82	0.94	4.66	0.14	0.74
	37 °C	4±1	0.83	0.34	0.88	0.27	0.88	2.64	0.28	0.83

Table A.4 Obtained constant values by fitting each mathematical model to the kinetic data and respective coefficient of determination (R^2), according to the temperature and pH variation for DPPC/DSPE-PEG-based SMLs.

pH	Temperature	y_{max}(%) ± SD	Weibull			First-order		Korsmeyer-Peppas		
			b	*a*	R^2	*k*	R^2	*K*	*n*	R^2
5.5	42 °C	14±1	0.14	0.93	0.99	0.34	0.99	2.570	0.52	0.98
	37 °C	5±1	0.07	2.59	0.95	0.35	0.85	2.83	0.33	0.63
7.4	42 °C	7±3	0.34	0.88	0.87	0.31	0.87	1.87	0.33	0.93
	37 °C	9±1	0.33	1.58	0.97	0.40	0.95	3.37	0.30	0.74

Appendix B: Supplementary information of sub-chapter 4.1

B.1. Interaction with Human Serum Albumin

The calculated variables (following Equation 3.4) for the interaction of DOX-loaded SMLs with HSA are summarized in **Table B.1**.

Table B.1 Dissociation constant (k_d), binding constant ($k_b = \frac{1}{k_d}$) and number of binding locations (n) of liposomes to HSA.

Group		k_d (M)	k_b (M^{-1})	n	R^2
	Free DOX	8.24×10^{-7}	5.26×10^{6}	1.80	0.96
A	DPPC	2.00×10^{-7}	5.00×10^{6}	1.60	0.96
	DPPC/ CHEMS	1.21×10^{-6}	8.25×10^{5}	1.53	0.98
	DPPC/ CHEMS/DSPE-PEG	1.72×10^{-6}	5.81×10^{5}	1.44	0.97
B	DPPC/DSPC	9.22×10^{-7}	1.01×10^{6}	1.67	0.99
	DPPC/DSPC/CHEMS	4.27×10^{-7}	2.12×10^{6}	1.66	0.99
	DPPC/DSPC/CHEMS/DSPE-PEG	8.16×10^{-7}	1.23×10^{6}	1.53	0.98
C	DPPC/DOPE	7.72×10^{-7}	1.30×10^{6}	1.62	0.98
	DPPC/DOPE/CHEMS	2.92×10^{-7}	3.43×10^{6}	1.48	0.98
	DPPC/DOPE/CHEMS/DSPE-PEG	9.90×10^{-7}	1.01×10^{6}	1.46	0.98

B.2. Drug release kinetics and mathematical modelling of the release profile

The DOX release kinetics of all the formulations and release conditions were fitted to three kinetic models: Weibull [12] following **Equation A.8**, first-order [11] following **Equation A.9,** and Korsmeyer-Peppas [13] following **Equation A.10**.

The constant values and coefficient of determination obtained for each model are summarized in **Table B.2** (for DPPC-based SMLs), **Table B.3** (for DPPC/DSPC-based SMLs) and **Table B.4** (for DPPC/DOPE-based SMLs).

Table B.2 Fitting parameters for each mathematical model for the kinetic data and corresponding coefficient of determination (R^2), according to the temperature and pH variation for Group A lipid formulations.

Group A											
	pH	T	y_{max}(%) ± SD	Weibull			First-order		Korsmeyer-Peppas		
				b	*a*	R^2	*k*	R^2	*K*	*n*	R^2
DPPC	5.5	42 °C	25 ± 2	1.18	0.29	0.99	0.35	0.99	10.76	0.30	0.88
		37 °C	9 ± 1	0.89	0.37	0.94	0.34	0.93	3.74	0.28	0.90
	7.4	42 °C	6.5 ± 0.2	1.59	0.71	0.96	0.82	0.94	4.66	0.14	0.74
		37 °C	4 ± 1	0.83	0.34	0.88	0.27	0.88	2.64	0.28	0.83
DPPC/CHEMS	5.5	42 °C	35 ± 5	0.99	0.61	0.98	0.61	0.98	23.84	0.15	0.92
		37 °C	21.1 ± 0.3	0.77	0.72	0.91	0.65	0.91	13.90	0.15	0.89
	7.4	42 °C	23 ± 1	0.75	0.28	0.98	0.23	0.97	5.90	0.37	0.94
		37 °C	18 ± 1	0.92	0.32	0.97	0.31	0.97	7.46	0.29	0.94
DPPC/CHEMS /DSPE-PEG	5.5	42 °C	25 ± 2	4.60	0.01	0.94	0.30	0.83	9.74	0.36	0.65
		37 °C	16 ± 2	2.44	0.07	0.98	0.29	0.87	5.94	0.33	0.70
	7.4	42 °C	17 ± 2	1.53	0.14	0.86	0.25	0.84	4.61	0.36	0.76
		37 °C	11 ± 5	10.0	8.23×10^{-5}	0.97	0.38	0.58	5.51	0.24	0.35

Table B.3 Fitting parameters for each mathematical model for the kinetic data and corresponding coefficient of determination (R^2), according to the temperature and pH variation for Group B lipid formulations.

Group B											
	pH	T	y_{max}(%) ± SD	Weibull			First-order		Korsmeyer-Peppas		
				b	*a*	R^2	*k*	R^2	*K*	*n*	R^2
DPPC/DSPC	5.5	42 °C	40±3	2.11	0.08	0.98	0.30	0.91	14.50	0.31	0.70
		37 °C	24.1±0.9	21.97	1.99	0.98	0.90	0.74	0.50	0.30	0.42
	7.4	42 °C	12.8±0.6	1.57	0.18	0.97	0.35	0.94	6.06	0.27	0.69
		37 °C	14±2	1.66	0.35	0.98	0.85	0.60	12.11	0.19	0.47
DPPC/DSPC/ CHEMS	5.5	42 °C	25±1	0.59	0.55	0.94	0.51	0.64	12.12	0.20	0.96
		37 °C	25.7±0.5	1.11	0.48	0.97	0.45	0.36	19.80	0.10	0.93
	7.4	42 °C	13±1	0.06	0.02	0.74	0.13	0.18	8.89	0.05	0.72
		37 °C	8±1	0.38	0.37	0.98	0.18	0.73	0.24	3.5	0.97
DPPC/DSPC/ CHEMS/ DSPE-PEG	5.5	42 °C	22±3	9.872	0.001	0.97	0.19	0.44	12.83	0.19	0.44
		37 °C	21±1	4.456	0.005	0.95	0.43	0.73	5.86	0.43	0.73
	7.4	42 °C	11±1	1.39	0.15	0.86	0.36	0.78	3.33	0.36	0.78
		37 °C	12±1	1.72	0.15	0.88	0.49	0.92	3.83	0.49	0.92

Table B.4 Fitting parameters for each mathematical model to the kinetic data and corresponding coefficient of determination (R^2), according to the temperature and pH variation for Group C lipid formulations.

Group C											
	pH	T	y_{max}(%) ± SD	Weibull			First-order		Korsmeyer-Peppas		
				b	*a*	R^2	*k*	R^2	*K*	*n*	R^2
DPPC/DOPE	5.5	42 °C	21±1	6.747	0.001	0.98	0.31	0.76	8.79	0.29	0.55
		37 °C	16±2	7.53	6.44×10^{-5}	0.94	0.28	0.67	7.57	0.29	0.45
	7.4	42 °C	17±1	1.68	0.17	0.91	0.31	0.87	6.84	0.28	0.71
		37 °C	8±1	1.68	0.03	0.91	0.08	0.88	1.45	0.64	0.84
DPPC/DOPE /CHEMS	5.5	42 °C	25±2	1.91	0.32	0.99	0.69	0.99	21.2	0.06	0.95
		37 °C	14.6 ± 0.8	1.32	0.23	0.78	0.33	0.77	8.75	0.21	0.73
	7.4	42 °C	15.7± 0.3	3.30	0.03	0.97	0.35	0.90	8.57	0.19	0.81
		37 °C	10±2	10.47	0.001	0.96	0.40	0.76	7.61	0.16	0.65
DPPC/DOPE /CHEMS/ DSPE-PEG	5.5	42 °C	22±3	9.87	0.001	0.97	0.32	0.69	12.83	0.19	0.44
		37 °C	21±2	4.45	0.005	0.95	—	—	5.86	0.43	0.73
	7.4	42 °C	11±1	1.39	0.15	0.85	—	—	3.35	0.36	0.78
		37 °C	18±1	1.54	0.07	0.98	—	—	3.83	0.49	0.92

Appendix C: Supplementary information of chapter 5

C.1. Statistical analysis

Table C.1 Multiple comparisons with control using Dunnett's test

Dunnett's multiple comparisons test	Predicted (LS) mean diff.	95.00% CI of diff.	Significant?	Summary	Adjusted *p* value
1 h					
control vs. SMLs	0.01172	-0.02971 to 0.05314	No	ns	0.8119
control vs. DOX	0.01674	-0.02599 to 0.05947	No	ns	0.6369
control vs. DOX-loaded SMLs	0.04846	0.009049 to 0.08788	Yes	*	0.0117
6 h					
control vs. SMLs	0.0225	0.005216 to 0.08466	Yes	*	0.0225
control vs. DOX	<0.0001	-0.2042 to -0.1248	Yes	****	<0.0001
control vs. DOX-loaded SMLs	0.0071	-0.08710 to 0.01133	Yes	**	0.0071
24 h					
control vs. SMLs	0.0279	-0.08811 to 0.003983	Yes	*	0.0279
control vs. DOX	<0.0001	-0.4130 to 0.3368	Yes	****	<0.0001
control vs. DOX-loaded SMLs	<0.0001	-0.4166 to 0.3415	Yes	****	<0.0001
48 h					
control vs. SMLs	<0.0001	-0.1722 to 0.08271	Yes	****	<0.0001
control vs. DOX	<0.0001	-0.4520 to 0.3725	Yes	****	<0.0001
control vs. DOX-loaded SMLs	<0.0001	-0.4305 to 0.3538	Yes	****	<0.0001

C.2. Establishment of Sk-br-3 breast cancer cell culture on non-adherent plates

Figure C.1 shows a representative image of the effect of DOX-loaded SMLs on Sk-br-3 breast cancer cells seeded on a non-adherent cell culture plate at 4 h after treatment. Several spheroids of smaller dimensions and cellular density are aggregating to dense mass (evidenced by the dark contrast in the upper right corner).

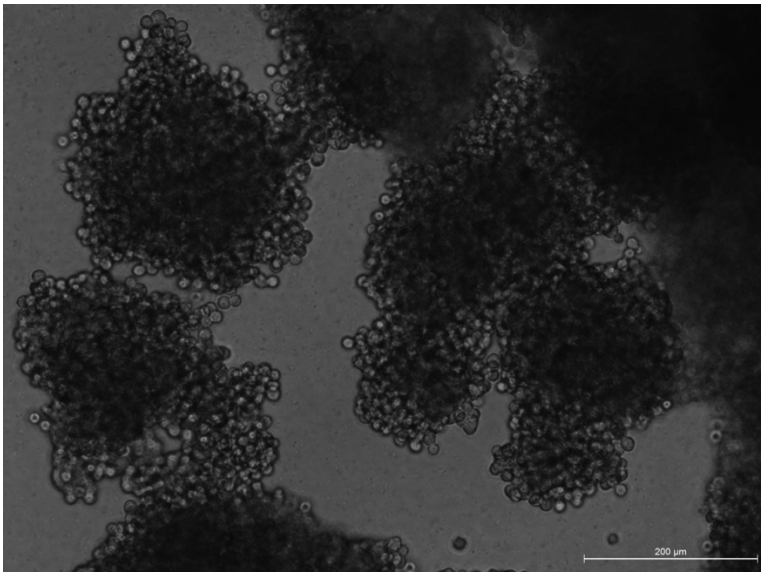


Figure C.1 Representative bright-field microscopy images of DOX-loaded SMLs on Sk-br-3 breast cancer cells seeded on non-adherent cell culture plates (newly formed spheroids) at 4 h.

References

1. Inamdar, S.; Nadaf, Y.; Mulimani, B. Ground and excited state dipole moments of exalite 404 and exalite 417 UV laser dyes determined from solvatochromic shifts of absorption and fluorescence spectra. *Journal of Molecular Structure: THEOCHEM* **2003**, *624*, 47-51.

2. Kawski, A.; Kukliński, B.; Bojarski, P. Excited state dipole moments of 4-(dimethylamino) benzaldehyde. *Chemical Physics Letters* **2007**, *448*, 208-212.

3. Taft, R.W.; Abboud, J.-L.M.; Kamlet, M.J.; Abraham, M.H. Linear solvation energy relations. *Journal of Solution Chemistry* **1985**, *14*, 153-186.

4. Kamlet, M.J.; Abboud, J.L.M.; Abraham, M.H.; Taft, R. Linear solvation energy relationships. 23. A comprehensive collection of the solvatochromic parameters,. pi.*,. alpha., and. beta., and some methods for simplifying the generalized solvatochromic equation. *The Journal of Organic Chemistry* **1983**, *48*, 2877-2887.

5. Catalán, J.; Díaz, C. Extending the Solvent Acidiy Scale to Highly Acidic Organic Solvents: The Unique Photophysical Behaviour of 3, 6-Diethyltetrazine. *European journal of organic chemistry* **1999**, *1999*, 885-891.

6. Marcus, Y. The properties of organic liquids that are relevant to their use as solvating solvents. *Chemical Society Reviews* **1993**, *22*, 409-416.

7. Catalán, J. Toward a generalized treatment of the solvent effect based on four empirical scales: dipolarity (SdP, a new scale), polarizability (SP), acidity (SA), and basicity (SB) of the medium. *The Journal of Physical Chemistry B* **2009**, *113*, 5951-5960.

8. Catalán, J.; López, V.; Pérez, P.; Martin-Villamil, R.; Rodríguez, J.G. Progress towards a generalized solvent polarity scale: The solvatochromism of 2-(dimethylamino)-7-nitrofluorene and its homomorph 2-fluoro-7-nitrofluorene. *Liebigs Annalen* **1995**, *1995*, 241-252.

9. Catalán, J.; Díaz, C. A Generalized solvent acidity Scale: The Solvatochromism of o-tert-Butylstilbazolium Betaine Dye and Its Homomorph o, o′-Di-tert-butylstilbazolium Betaine Dye. *Liebigs Annalen* **1997**, *1997*, 1941-1949.

10. Katritzky, A.R.; Fara, D.C.; Yang, H.; Tämm, K.; Tamm, T.; Karelson, M. Quantitative measures of solvent polarity. *Chemical reviews* **2004**, *104*, 175-198.

11. Noyes, A.A.; Whitney, W.R. The rate of solution of solid substances in their own solutions. *Journal of the American Chemical Society* **1897**, *19*, 930-934.

12. Papadopoulou, V.; Kosmidis, K.; Vlachou, M.; Macheras, P. On the use of the Weibull function for the discernment of drug release mechanisms. *International journal of pharmaceutics* **2006**, *309*, 44-50.

13. Korsmeyer, R.W.; Gurny, R.; Doelker, E.; Buri, P.; Peppas, N.A. Mechanisms of solute release from porous hydrophilic polymers. *International Journal of Pharmaceutics* **1983**, *15*, 25-35.